Quantum Correlations and Complexity: From Spin Chains to Holography

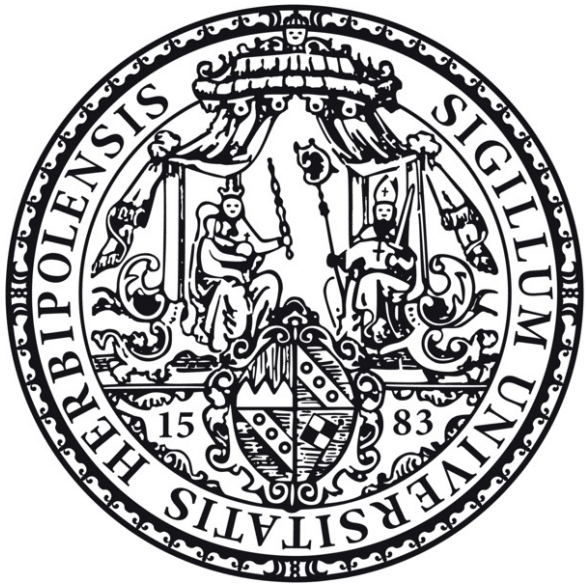

Dissertation zur Erlangung des naturwissenschaftlichen Doktorgrades
an der Fakultät für Physik und Astronomie
der Julius–Maximilians-Universität Würzburg

vorgelegt von

Rathindra Nath Das
aus Nabadwip, Indien

Würzburg, im May 2025

Eingereicht bei der Fakultät für Physik und Astronomie am

Gutachter der Dissertation

1. Gutachter: Prof. Dr. Johanna Erdmenger

2. Gutachter: Prof. Dr. Björn Trauzettel

3. Gutachter:

Prüfer des öffentlichen Promotionskolloquiums

1. Prüfer: Prof. Dr. Johanna Erdmenger

2. Prüfer: Prof. Dr. Björn Trauzettel

3. Prüfer:

4. Prüfer:

5. Prüfer:

Tag des öffentlichen Promotionskolloquiums

Doktorurkunde ausgehändigt am

_____

To my father, Rabindra Nath Das,
my mother, Shobha Sarkar Das,
and my wife, Mampi Biswas Das,
for their unwavering love, support, and guidance.

"You raise me up so I can stand on mountains
You raise me up to walk on stormy seas
I am strong when I am on Your shoulders
You raise me up to more than I can be"

— R. Løvland and B. Graham

Acknowledgements

Countless people have helped bring this dissertation to life. If I inadvertently overlook anyone in the lines that follow, please know that my gratitude is no less sincere.

First and foremost, I owe a profound debt to Prof. Johanna Erdmenger, whose intellectual insight and personal encouragement carried this project from its earliest idea to its final page. I am equally grateful to Prof. Björn Trauzettel—member of my mentoring committee—for his steady guidance and perceptive counsel at every stage of the journey.

A Deutscher Akademischer Austauschdienst (DAAD) scholarship made this work financially feasible, while day-to-day life was enriched by the camaraderie of the entire TP3 group. I am especially indebted to Pablo Basteiro, Saskia Demulder, Giuseppe Di Giulio, and Amelie Mierau for their willing ears, insightful suggestions, and many energising conversations.

The formative training I received from Sudhir Ranjan Jain, Sobhan Kumar Sounda, and Urjit Yajnik laid the bedrock on which this research firmly rests. Over the years, I have benefited from inspiring discussions with many colleagues and collaborators, including—among others—Coraline Bacq, Vijay Balasubramanian, Souvik Banerjee, Aranya Bhattacharya, Satyaki Chowdhury, Bidyut Dey, Moritz Dorband, Sourav Dutta, Haye Hinrichsen, Jonathan Karl, Jani Kastikainen, Taishi Kawamoto, Arnab Kundu, Hong Liu, Archana Maji, Amelie Mierau, Takato Mori, Sara Murciano, Dominik Neuenfeld, Christian Northe, Giuseppe Policastro, Tomaž Prosen, Henri Scheppach, Yanick Thurn, Björn Trauzettel, and Zhuo-Yu Xian. Their insights and encouragement have immeasurably broadened my perspective.

Attendance at a wide array of conferences and workshops likewise shaped my growth; I thank every hosting institution for fostering such stimulating environments. Additional financial support from the ct.qmat Cluster of Excellence (Würzburg–Dresden) was indispensable throughout the doctorate.

Beyond the academic sphere, Nelly Meyer helped me navigate the labyrinthine complexities of German administrative procedures. My parents, Rabindra Nath Das and Shobha Sarkar Das, have been a constant source of strength. Their quiet sacrifices, steadfast belief in the value of education, and willingness to celebrate even the smallest milestones nurtured the resilience that carried me through the most challenging stretches of research. My wife, Mampi Biswas Das, met each twist of this journey with a lot of patience and kindness—cheering each success, lending calm perspective in moments of doubt, and shouldering countless practical burdens so I could focus on science.

Across the miles, my friends in India—Abhilash Mallick and Prandip Saha—were never more than a message or late-night call away. I owe a special debt to all my teachers who first

transformed my curiosity into a passion for scientific inquiry. Their engaging lessons, patient explanations, and early vote of confidence convinced me that pursuing knowledge could be both a calling and a lifelong adventure.

Finally, I am deeply thankful to those who read and critiqued portions of this thesis—especially Mampi Biswas, Saskia Demulder, Jonathan Karl, Yanick Thurn, and Henri Scheppach. Their thoughtful comments have strengthened this thesis in every respect.

Abstract

At the intersection of geometry, dynamics, and information lies a central question in modern theoretical physics: how is the structure of spacetime encoded in quantum correlations and complexity? Over the past two decades, quantum information theory has emerged as both a set of practical tools and a conceptual bridge linking gravitational phenomena to condensed matter and quantum many-body systems. The work presented here is organised around two central themes: fixed-time analyses of quantum correlations in holographic theories and the study of dynamical evolution and quantum complexity in both unitary and nonunitary settings.

In the first part of our study on fixed-time quantum correlations, we pursue a discrete analogue of holography by turning to boundary theories defined on hyperbolic tilings. These are modelled by aperiodic quantum spin chains with the types of couplings determined by substitution rules that reflect the symmetries of the bulk geometry. Using strong-disorder renormalisation group techniques, we extract correlation functions, entanglement entropy, and mutual information in their aperiodic singlet phases. Notably, we find that two-point functions decay with a universal power-law exponent, while the entanglement entropy grows logarithmically. These results support a discrete Ryu–Takayanagi prescription framed in terms of minimal-length geodesics across the tiling, hinting at a geometric encoding of bulk properties within the disordered boundary theory.

In holographic CFTs, we further investigate quantum correlations beyond entanglement entropy. Although von Neumann entropy is commonly used, it captures both quantum and classical correlations in mixed states and vanishes for separable states. To isolate purely quantum effects, we study geometric quantum discord (GQD) as a diagnostic for the factorisation properties of modular partition functions. Our analytical results demonstrate that GQD vanishes if and only if the modular partition function factorises. When applied to the thermofield double (TFD) state, this analysis leads to an information-theoretic derivation of the thermomixed double (TMD) state as the optimal classical approximation to the TFD. Moreover, our approach links the persistence of GQD to the presence of black hole microstates and their imprint on the gravitational path integral, thereby offering deeper insight into the factorisation problem in AdS/CFT.

The second part of the thesis addresses dynamics. We begin with quantum triangular billiards, whose spectral and dynamical properties interpolate between integrability and chaos depending on internal angular parameters. By analysing level spacing ratios, spectral complexity, and the evolution of wavefunctions in the Krylov basis, we observe oscillatory

dynamics in integrable triangles contrasted with a late-time saturation of complexity in chaotic cases—a distinction that reflects differences in the topology of the underlying classical phase space. Furthermore, the variance of Lanczos coefficients and the delocalisation of eigenstates in the Krylov basis trace a sharp transition from order to chaos, establishing a novel connection between classical topology and quantum information dynamics.

We then extend these insights to non-Hermitian systems, where processes such as continuous measurements, open system evolution, or PT-symmetric Hamiltonians induce nonunitary dynamics. By adapting the Lanczos algorithm to non-Hermitian and complex-symmetric Hamiltonians, we examine wavefunction spreading and information flow using Krylov-based measures. Repeated measurements induce a quantum Zeno regime in which time evolution is halted and complexity remains static. In a quench scenario—where the system is driven from Hermitian to non-Hermitian evolution via varying measurement frequencies—we find that the onset of complexity growth is progressively delayed, tending to infinity as the interval between measurements approaches zero. In PT-broken phases, we find localisation phenomena associated with the non-Hermitian skin effect, accompanied by suppressed growth of both complexity and entropy. A newly defined Krylov inverse participation ratio further quantifies this localisation, complementing spread entropy in characterising nonunitary dynamics. To address mixed states and their associated complexities, we develop the concept of the Krylov complexity of purification. By embedding nonunitary processes into an enlarged Hilbert space, we recover unitary evolution. Using three purification schemes, we demonstrate inequalities linking operator and state complexity in both finite- and infinite-dimensional systems. The complexity of a vacuum evolving into a thermal state is equal to the average number of Rindler particles generated across the left and right Rindler wedges. Finally, we demonstrate that the complexity required for a vacuum to evolve into a thermal state equals the average number of Rindler particles created between the corresponding wedges. Furthermore, for the TFD evolving from zero to finite temperature, the state complexity is shown to conform to the Lloyd bound.

Finally, we generalise the Krylov framework to accommodate supercoherent states governed by Lie superalgebras. We construct Krylov lattices for representations of the super Heisenberg–Weyl and $OSp(2|1)$ algebras and use these constructions to compute spread complexity in systems with both bosonic and fermionic degrees of freedom. This extension paves the way for analysing large-charge string states in the planar limit of AdS/CFT, where Krylov paths can be interpreted geometrically as capturing features of the bulk spacetime through which strings propagate, laying the foundation for a complexity-based characterisation of semiclassical string dynamics and its dual gauge theory description.

Zusammenfassung

An der Schnittstelle von Geometrie, Dynamik und Information steht eine zentrale Frage der modernen theoretischen Physik: Wie wird die Struktur der Raumzeit in quantenmechanischen Korrelationen und in Komplexität kodiert? Hierbei hat sich die Quanteninformationstheorie sowohl als praktisches Werkzeug als auch als konzeptionelles Bindeglied zwischen Gravitation, quantenmechanischen Vielteilchensystemen und der Festkörperphysik etabliert. In der vorliegenden Arbeit sollen nun zwei Themenbereiche untersucht werden: die Analyse von Korrelationsfunktionen in holographischen Theorien zu einem festen Zeitpunkt und deren dynamische Entwicklung sowie Komplexität in unitären und nicht-unitären Systemen.

Um Korrelationsfunktionen zu einem festen Zeitpunkt zu untersuchen, gehen wir einem diskreten Analogon der Holographie nach, indem wir Randtheorien auf hyperbolischen Gittern untersuchen. Diese werden durch aperiodische Spin-Ketten beschrieben, wobei die Kopplungsart der Spins untereinander durch Substitutionsregeln gegeben ist, welche die Symmetrien der dualen Geometrie widerspiegeln. Wir bestimmen die Korrelationsfunktionen, die Verschränkungsentropie und die gegenseitige Information in ihren aperiodischen Singulett-Phasen unter Ausnutzung von Techniken aus der Theorie der Renormierungsgruppen. Insbesondere finden wir, dass Zweipunktfunktionen mit einem universellen Potenzgesetz abfallen, während die Verschränkungsentropie logarithmisch wächst. Diese Ergebnisse deuten auf ein diskretes Analogon der Ryu–Takayanagi-Formel hin, gegeben durch minimale Geodäten in der Tesselierung. Dies deutet auf eine geometrische Kodierung von Eigenschaften der Bulktheorie in der Randtheorie hin. Weiterhin untersuchen wir weitere quantenmechanische Korrelationen über die Verschränkungsentropie hinaus. Üblicherweise wird hierfür die von Neumann-Entropie verwendet. Diese misst jedoch sowohl Quanten- als auch klassische Korrelationen in gemischten Zuständen und verschwindet für reine Zustände. Um reine Quanteneffekte zu erfassen, wenden wir uns in dieser Arbeit dem Geometric-Quantum-Discord (GQD) zu. Wir benutzen GQD, um die Faktorisierung von modularen Zustandssummen zu untersuchen. Angewandt auf den Thermofield-Double-Zustand (TFD), führt diese Betrachtung zu einer informationstheoretischen Herleitung des Thermomixed-Double-Zustands (TMD) als optimale klassische Näherung des TFD. Darüber hinaus verknüpft dieser Ansatz das Fortbestehen des GQD mit Mikrozuständen Schwarzer Löcher und deren Einfluss auf das gravitative Pfadintegral, wodurch tiefere Einblicke in das Faktorisierungsproblem innerhalb der AdS/CFT-Korrespondenz gewonnen werden.

Der zweite Teil der Arbeit befasst sich mit dynamischen Systemen. Wir beginnen mit dem Quanten-Dreiecksbillard, dessen spektrale und dynamische Eigenschaften abhängig von

den internen Winkelparametern zwischen Integrierbarkeit und Chaos wechseln. Durch die Analyse von Energieniveaus, spektraler Komplexität und der Zeitentwicklung von Wellenfunktionen in der Krylow-Basis beobachten wir eine oszillierende Dynamik in integrierbaren Billarden im Gegensatz zu einer späten Sättigung der Komplexität in chaotischen Fällen. Dies spiegelt die Unterschiede in der Topologie des zugrunde liegenden klassischen Phasenraums wider. Außerdem weisen die Varianz der Lanczos-Koeffizienten und die Delokalisierung der Eigenzustände in der Krylow-Basis einen scharfen Übergang zwischen Ordnung und Chaos auf, wodurch eine neuartige Verbindung zwischen klassischer Topologie und Quanteninformationsdynamik geschaffen wird.

Wir erweitern diese Erkenntnisse anschließend auf nicht-hermitesche Systeme, in denen Prozesse wie kontinuierliche Messungen, die Zeitentwicklung offener Systeme oder PT-symmetrische Hamiltonoperatoren eine nicht-unitäre Dynamik induzieren. Durch Anpassung des Lanczos-Algorithmus an nicht-hermitesche und komplex-symmetrische Hamiltonoperatoren untersuchen wir die Ausbreitung der Wellenfunktion und den Informationsfluss mit Maßen des Krylowraums. Wiederholte Messungen führen zu einem Quanten-Zeno-Effekt, sodass die Zeitentwicklung gestoppt wird und die Komplexität verschwindet. Bei einem sogenannten Quench, bei dem das System abhängig von den Messintervallen von einem Bereich hermitescher zu einem Bereich nicht-hermiteschen Zeitentwicklung gebracht wird, stellen wir fest, dass sich der Beginn des Anstiegs der Komplexität immer weiter verzögert und gegen unendlich strebt, wenn die Zeit zwischen den Messungen gegen null geht. In Phasen mit gebrochener PT-Symmetrie, finden wir Lokalisierungsphänomene, die mit dem nicht-hermiteschen Skin-Effekt verbunden sind, einhergehend mit unterdrücktem Wachstum von Komplexität und Entropie. Ein neu definiertes inverses Krylow-Partizipationsverhältnis quantifiziert diese Lokalisierung weiter und ergänzt die Krylow-Zustandsentropie bei der Beschreibung nicht-unitärer Dynamik. Um gemischte Zustände und die damit verbundenen Komplexitäten zu behandeln, entwickeln wir das Konzept der Krylow-Komplexität der Purifikation. Durch die Einbettung nicht-unitärer Prozesse in einen erweiterten Hilbert-Raum erhalten wir eine unitäre Zeitentwicklung zurück. Unter Verwendung von drei Purifikationen demonstrieren wir Ungleichheiten zwischen der Komplexität von Operatoren und der Komplexität von Zuständen sowohl in endlich als auch in unendlichdimensionalen Systemen. Wir zeigen insbesondere, dass die erforderliche Komplexität, um eine Zeitentwicklung des Vakuums in einen thermischen Zustand zu erhalten, gleich der durchschnittlichen Anzahl der Teilchen ist, die zwischen den Rindler-Horizonten erzeugt werden. Darüber hinaus wird gezeigt, dass für den TFD-Zustand, bei dem sich die Temperatur von Null zu einem endlichen Wert entwickelt, die Zustandskomplexität der Lloyd-Grenze genügt.

Schließlich verallgemeinern wir Krylow-Techniken, um auch superkohärente Zustände zu berücksichtigen, die mittels Lie-Superalgebren beschrieben werden. Wir konstruieren

Krylow-Gitter für Darstellungen der Super-Heisenberg-Weyl- und $OSp(2|1)$-Algebren und verwenden diese Konstruktionen zur Berechnung der Spread-Komplexität in Systemen mit sowohl bosonischen als auch fermionischen Freiheitsgraden. Diese Erweiterung ebnet den Weg für die Analyse von Stringzuständen mit großer Ladung in der AdS/CFT-Korrespondenz im Grenzfall großer 't Hooft-Kopplung und großem Rang der Eichgruppe, in der Krylow-Pfade geometrisch als Merkmale einer Raumzeit mit propagierenden Strings interpretiert werden können. Hiermit legen wir den Grundstein für eine Charakterisierung der semiklassischen Dynamik von Strings und ihrer dualen eichtheoretischen Beschreibung auf Basis der Komplexität.

Contents

1 Introduction **1**

2 State of the Art **9**

2.1 The AdS/CFT Correspondence 10

2.1.1 Fundamental Ingredients of the Correspondence 14

2.1.2 Mapping AdS/CFT to Spin Chains 19

2.2 Measures of Quantum Correlations 25

2.2.1 Entanglement in Quantum Theories 27

2.2.2 Entanglement in Holography 32

2.2.3 Quantum Discord and the Quantum-Classical Boundary 34

2.3 Quantum Dynamics and Complexity 38

2.3.1 Time Evolution and the Krylov Basis 39

2.3.2 Krylov State Basis and Spread Complexity 41

2.3.3 Krylov Operator Basis and Krylov Complexity 44

3 Quantum Correlations in Holography **49**

3.1 Discrete Holography and Aperiodic Spin Chains 49

3.1.1 Regular Hyperbolic Tilings: Construction, Geometry, and Symmetry 53

3.1.2 Review of SDRG on Aperiodic Spin Chains 61

3.1.3 Two-Point Correlation Functions in Aperiodic Singlet Phases . . . 65

3.1.4 Mutual Information in Aperiodic Spin Chains 70

3.1.5 Piece-wise behaviours and envelopes 74

3.1.6 Aperiodic Spin Chains with Enhanced Symmetries 78

3.1.7 $SO(N)$ aperiodic spin chains 82

3.1.8 Discussion 87

3.2 Geometric Quantum Discord and Holography 89

3.2.1 Geometric Quantum Discord for Pure States 90

3.2.2 Geometric Quantum Discord for the Thermofield Double State . . . 94

3.2.3 Geometric Quantum Discord Probing Black Hole Microstates . . . 97

3.2.4 Discussion 99

4 Quantum Dynamics and Complexity in Spin Chains and Holography **101**

4.1 Chaos, Integrability, and Complexity 102

4.1.1 Triangular Billiards: From Integrable to Non-Integrable Systems . . 104

4.1.2 Spectral Statistics of Triangular Billiards . . . 110
4.1.3 Spectral Complexity . . . 115
4.1.4 Spread Complexity in Triangular Billiards . . . 121
4.1.5 Discussion . . . 127
4.2 Spread Complexity in Non-Hermitian Systems and Purification . . . 130
4.2.1 Measurement-Induced Dynamics and the Zeno Effect . . . 131
4.2.2 Non-Unitary Evolution and Modified Lanczos Methods . . . 132
4.2.3 Complexity and Entropy under Projective Measurements . . . 138
4.2.4 PT-Symmetric Quantum Systems . . . 148
4.2.5 Krylov Complexity of Purification . . . 155
4.2.6 Discussion . . . 170
4.3 Complexity in String Theory and Holography . . . 172
4.3.1 (Super-)Coherent States and Semiclassics . . . 174
4.3.2 Spread Complexity with Fermions . . . 180
4.3.3 Fermionic Heisenberg-Weyl Algebra . . . 181
4.3.4 Spread Complexity with Bosons and Fermions . . . 187
4.3.5 Super-Heisenberg–Weyl Algebra . . . 188
4.3.6 OSp$(2|1)$ or $\mathcal{N} = 1$ SL(2) . . . 192
4.3.7 Spread Complexity in Semiclassical String Settings of $AdS_5 \times S^5$ . . . 200
4.3.8 Discussion . . . 210

5 Conclusion and Outlook 213

Bibliography 221

1 Introduction

Immanuel Kant once famously declared, “There will never be a Newton for the blade of grass,” raising an important question: how can the very laws that govern inanimate matter also orchestrate the emergence of life [1]? From the elegantly simple structure of a single cell to the exuberant tapestry of an entire ecosystem, living systems exhibit a complexity that seems almost impossible to fathom. How, indeed, does nature self-organize—from humble atoms into molecules, from molecules into the tremendous intricacy of life itself? Yet these same fundamental principles appear to govern both the simplest and the most complex structures.

To probe such questions at a deeper level, we draw on the tools of theoretical physics and explore the hierarchy of matter from the smallest hypothesised vibrating strings, through the fundamental particles they compose, up to the atoms that scaffold the visible world. In this microscopic domain, quantum mechanics dictates the behaviour of nature, revealing rules far removed from everyday intuition. In this thesis, we follow that trail, tracing how seemingly simple quantum systems blossom into richly complex states. By quantifying correlations, information spreading, and dynamical complexity, we chart their kinematical structure and elucidate the principles that carry simplicity toward ever-deeper layers of structure.

Quantum mechanics describes how an isolated system evolves in a unitary fashion, without distinguishing between past and future. Nevertheless, our everyday world exhibits a clear arrow of time. How does nature’s inherent time symmetry reconcile with the apparent irreversibility we observe? At the dawn of thermodynamics, pioneers like Sadi Carnot, Rudolf Clausius, William Thomson (Lord Kelvin), and Walther Nernst introduced the laws that describe heat flow and the principle that heat does not move unassisted from cold to hot [2–6]. Their work explained why processes spontaneously progress in one direction and eventually introduced the notion of entropy as a measure of irreversible change [7]. Initially, entropy was a phenomenological concept, but Ludwig Boltzmann revolutionised it with his statistical interpretation: entropy grows because there are countless ways to be disordered, and relatively few ways to remain orderly [8, 9]. His insight reframed irreversibility from a mere observational fact to a probabilistic statement about the configuration space of matter.

Extending these ideas to the quantum level required another ingredient: an information-theoretic perspective. Claude Shannon reimagined entropy in 1948 as an intrinsic measure of uncertainty, a yardstick for the unpredictability or surprise in any probabilistic process—physical or otherwise [10, 11]. His information-theoretic framework not only provided

a universal language for quantifying uncertainty but also paved the way for data compression algorithms, error-correcting codes, and the reliable digital communication systems that underpin today's Internet and computing technologies [10, 12–18]. Then John von Neumann, in his towering work on the mathematical foundations of quantum mechanics, adapted Shannon's classical notion of entropy to the language of density matrices [19, 20]. Thus, von Neumann entropy provided a quantum measure of uncertainty, vanishing for pure states and quantifying genuine quantum mixedness. This unification stands as one of the most profound insights in modern science: a convergence of thermodynamics, classical information theory, and quantum mechanics into a single narrative of how systems evolve and store information.

Moreover, in the late twentieth century, a stunning revelation arose in the realm of high-energy theory: the AdS/CFT correspondence. Originally proposed by Juan Maldacena, this duality weaves together a gravitational theory in an Anti-de Sitter (AdS) spacetime and a conformal field theory (CFT) living on its boundary [21–23]. The holographic principle underlies this relation, insisting that the physics in a (d+1)-dimensional bulk with black holes and gravitational dynamics—can be precisely encoded in a d-dimensional quantum field theory without gravity [21–27]. Early hints of this principle emerged from black hole thermodynamics, where the Bekenstein–Hawking entropy, proportional to the horizon area, offered a partial glimpse of quantum gravity's microscopic degrees of freedom [28–31]. In holography, the entanglement entropy of a region in the boundary conformal field theory is given by the area of a minimal surface in the bulk spacetime, known as the Ryu–Takayanagi surface, which is anchored to the boundary of that region; when the boundary region covers the entire system, this prescription reduces to the black hole entropy formula, identifying the minimal surface with the event horizon and relating quantum entanglement to the geometry of spacetime [32–37].

Yet entropy is not enough to capture all the subtleties of dynamical evolution. In certain scenarios—especially for black holes in near-equilibrium states—entropy saturates, but the geometry behind the event horizon continues to expand [38–41]. This steady growth in the spatial volume of the Einstein–Rosen bridge, even after thermalisation, hints at another quantity altogether: computational complexity. Proposed as "complexity = volume" or "complexity = action," these conjectures assert that the holographic bulk encodes more than just entropic content; it reflects the circuit-depth needed to build the corresponding boundary quantum state from a simple reference [39–53]. The geometry keeps growing despite the constancy of entropy, capturing how the quantum state keeps evolving in an intricate manner—scrambling and rearranging degrees of freedom long after thermal equilibrium is reached [40–43].

One of the recent developments in this chain of works has been the introduction of Krylov complexity in the Heisenberg picture [54], and spread complexity in the Schrödinger

picture [55]. This approach measures how operators or states evolve within a systematically constructed subspace of the Hilbert space: the Krylov subspace. The conceptual seed can be traced back to the work of Alexei Nikolaevich Krylov, a Russian mathematician and naval engineer, whose 1931 investigation into approximate eigenvalue solutions for oscillatory systems introduced the idea of successively applying a matrix A to a vector $\mathbf{b}$, thereby generating the linear span $\mathbf{b}$, $A\mathbf{b}$, $A^2\mathbf{b}$, ... to form a subspace [56, 57]. Krylov's goal was practical—a method to analyze large mechanical systems and determine their vibrational frequencies without fully diagonalising unwieldy matrices. Though originally conceived in the context of naval architecture, his work laid the mathematical foundation for all Krylov-based methods. Decades later, Cornelius Lanczos built on Krylov's insights to develop an iterative algorithm that transforms a large Hermitian matrix into a tridiagonal one within the Krylov subspace [58]. This made eigenvalue approximation dramatically more efficient—an invaluable tool in quantum mechanics, where exact diagonalisation of Hamiltonians is often computationally prohibitive.

Building on this historical foundation, Krylov-based techniques now underpin a wave of research in quantum field theory, condensed matter, and holography, offering powerful tools to quantify how a system's state or operator spreads under time evolution and, in parallel, clarifying how Krylov-based complexities illuminate quantum dynamics across these seemingly disparate arenas [54, 55, 59–82]. They provide a unified framework to study operator growth and state delocalisation across a wide variety of models – from single-particle chaotic billiards [65, 83, 84] to interacting spin networks [85–87], from Hermitian systems to non-Hermitian lattices [63, 69]. Conceptually, these measures offer a fresh perspective on quantum chaos: they signal its presence through the rapid growth and pronounced peaks of complexity, while simultaneously clarifying how chaos manifests through the structure of the Lanczos coefficients and the accompanying basis expansion [54, 55, 65]. They bridge to other concepts like OTOCs and spectral statistics, yet also rectify limitations of those traditional measures by capturing the full time evolution and state-dependent details of complexity growth [54, 55]. Furthermore, Krylov/spread complexity has proven sensitive to features like many-body localisation, integrability, and topological order, revealing new dynamical signatures of these phenomena [64, 65, 87–93]. In non-unitary settings, adapted Krylov methods show how dissipation and amplification alter the growth of complexity, highlighting which aspects of operator dynamics are robust and which are washed out by the environment [63, 69]. All told, these complexity measures deepen our understanding of quantum dynamics by quantifying the "spread" of operators and states in a quantitative way. As research progresses, one can expect Krylov and spread complexity to play an increasing role in characterising phases of matter, diagnosing chaos in experimental quantum simulators, and even drawing analogies to gravitational systems (via holography) where

similar complexity-growth phenomena are hypothesised. This makes Krylov and spread complexity highly relevant topics at the forefront of theoretical condensed matter physics and quantum information, and an essential component in the emerging narrative of how quantum complexity underlies physical thermalisation and structure formation in many-body systems.

Recent advances have established Krylov complexity as an especially compelling candidate for realising the long-standing "complexity = volume/length" conjecture in precise, calculable form. In the AdS_2/CFT_1 correspondence—between Jackiw–Teitelboim gravity and the double-scaled SYK model—it was shown in [94, 95] that the Krylov complexity of the thermofield-double state precisely matches the length of the two-sided JT wormhole: descending one step further into the Krylov basis increases the Einstein–Rosen bridge by a fixed amount, so that boundary operator growth literally measures the wormhole's linear extension. Because the SYK Krylov basis is in one-to-one correspondence with bulk length eigenstates (or fixed "chord numbers"), this constitutes the first parameter-free entry in the holographic complexity dictionary and demonstrates that a purely boundary construct can reproduce a classical bulk geometric quantity. Subsequent work extended this match to finite temperature and incorporated the leading $1/N$ quantum corrections by coupling double-scaled SYK to a two-dimensional sine-dilaton gravity; even in that setting the boundary Krylov (or spread) complexity continues to track the bulk volume, with deviations capturing quantum-field effects atop the classical gravitational saddle [96].

A complementary line of work has established a precise relation between *complexity growth rates* on the boundary and a simple mechanical quantity in the bulk, namely the radial momentum of an infalling probe. The first sharp result appeared in [97], which proved that, for states created by local operators in a two–dimensional CFT, the *spread-complexity rate* coincides with the radial momentum of a particle falling in AdS_3 when both are expressed in the proper–distance coordinate. Parallelly, [75] demonstrated that the *Krylov-complexity rate* enjoys the same identification in generic AdS black-hole geometries: the bulk geodesic momentum reproduces the early-time exponential rise and the universal late-time linear ramp of boundary K-complexity, and for the BTZ background the match is exact against the finite-temperature CFT_2 result. A parallel analysis in [98] confirmed that the spread complexity rate of a boundary CFT equals the radially measured momentum of a freely falling massive particle that starts at the asymptotic boundary with zero velocity. Taken together, these studies weave a coherent narrative: both Krylov and spread complexities not only track the stretching of wormholes but also encode the momentum of objects traversing them, thereby turning boundary operator dynamics into a direct, quantitative probe of bulk interior geometry.

In this thesis, we explore these quantum information perspectives in the context of holography, condensed matter, and a class of quantum dynamical systems. Our investigation

draws on a range of tools—entanglement entropy, quantum discord, and various notions of complexity—to illuminate the relationship between geometry and quantum information. Below is a summary of how the thesis is organised:

Outline:

- **Chapter 2: State of the Art.** In Sec. 2.1, we revisit the AdS/CFT correspondence, highlighting how $(d+1)$-dimensional gravitational dynamics in Anti-de Sitter spacetime correspond to d-dimensional conformal field theories at the boundary. We further outline how, in certain regimes, gravitational theories in $AdS_5 \times S^5$ and their dual CFT can be effectively described by integrable spin chains. In Sec . 2.2, we review key measures of quantum correlations, such as entanglement entropy and quantum discord, emphasising their role in holographic setups. Finally, in Sec . 2.3, we turn to the notions of quantum dynamics and complexity, introducing Krylov and spread complexity as essential tools for characterising the evolution and spreading of states and operators in holographic and quantum systems.

- **Chapter 3: Quantum Correlations in Holography.** We first examine *discrete holography* via hyperbolic tilings, developing boundary theories on *aperiodic spin chains* that preserve dihedral symmetries inherited from the bulk tilings in Sec. 3.1. Correlation functions, entanglement entropy, and mutual information in *aperiodic singlet phases* demonstrate how boundary disorder and symmetry reflect holographic geometry. Moving ahead, in Sec. 3.2, for the continuum AdS_3/CFT_2, we introduce *geometric quantum discord (GQD)* to probe quantum correlations beyond entanglement, pinpointing the Thermo-Mixed Double (TMD) state as the closest quantum-classical approximation to the Thermo-Field Double (TFD). We demonstrate that a non-zero geometric quantum discord signals the presence of underlying wormhole microstates.

- **Chapter 4: Quantum Dynamics and Complexity in Spin Chains and Holography.**
  - **Chaos, Integrability, and Complexity.** We study quantum triangular billiards—a system spanning integrable, pseudo-integrable, and chaotic regimes depending on boundary conditions in Sec. 4.1. By evaluating spectral statistics and spread complexity, we show how wavefunction evolution in the Krylov basis can act as a sensitive marker of chaos, echoing classical phase-space topology.
  - **Spread Complexity in Non-Hermitian Systems and Purification.** Many physical processes involve effective non-Hermitian Hamiltonians, from measured quantum systems to *PT-symmetric* setups that exhibit the non-Hermitian skin effect. In Sec . 4.2, we adapt the Lanczos method to non-unitary evolution,

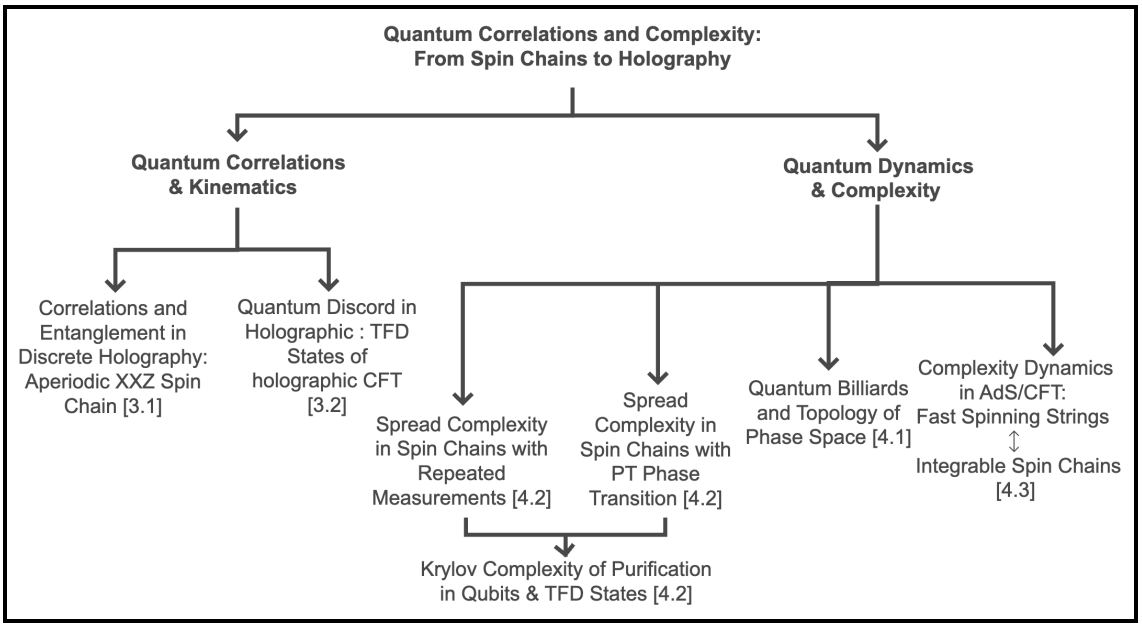

Figure 1.1: Flow chart illustrating the structure of this thesis. The work divides into two main themes. On the left, we analyse quantum correlation measures on constant-time slices. This includes discrete holography in aperiodic XXZ spin chains [3.1] (based on [99]), and the study of geometric quantum discord in thermofield-double states within holographic CFTs [3.2] (based on [100]). On the right, we explore quantum dynamics and complexity. Topics covered include: spread complexity in the quantum chaos and topology of triangular quantum billiards [4.1] (based on [65]); monitored spin chains and the dependence of complexity growth rates on the measurement rate, alongside PT-symmetric spin chains [4.2] (based on [63] and [64]); localisation–delocalisation transitions and Krylov complexity of purifications for qubits and TFD states [4.2] (based on [66]); and the evolution of complexity in AdS/CFT through fast-spinning and integrable spin chains [4.3] (based on [67]). Section numbers are indicated in square brackets.

demonstrating how Krylov and spread complexity capture measurement-induced transitions in complexity dynamics, quantum Zeno effects, and the localisation of states in PT-broken phases. We also introduce the *Krylov complexity of purification*, linking operator complexity and purified state complexity under diverse scenarios (time-independent, time-dependent, and instantaneous purification).

– **Complexity in String Theory and Holography.** Lastly, in Sec. 4.3, we extend spread complexity to fermionic and supersymmetric coherent states in a string-theoretic context, aiming to connect Krylov-based measures with the semiclassical regime of AdS/CFT. These generalisations allow us to probe large-charge superstring states, offering a new perspective on how quantum complexity encodes geometric features of bulk spacetimes.

- **Chapter 5: Conclusion and Outlook.** In Sec . 5, we synthesise the primary results

of the thesis, assessing their broader impact in quantum information, holography, and condensed matter physics. We then propose future directions—ranging from refined Krylov-space diagnostics to measurement-induced phase transition in the holographic settings.

Main results: The key results of this thesis fall into two overarching categories: *(1) fixed time-slice analyses of quantum correlations* and *(2) dynamical studies of quantum complexity*.

(I) Fixed-Time Quantum Correlations

- *Aperiodic Spin Chains and Discrete Holography.* We construct a range of aperiodic quantum spin chains on the boundary of hyperbolic tilings as candidate theories for discrete holography. Via real-space renormalisation group (RG) methods, we characterise correlation functions, entanglement entropy, and mutual information in these aperiodic singlet phases. The entanglement entropy grows logarithmically, with a coefficient interpretable as an "effective central charge," reflecting the symmetry and tiling structure of the bulk. We also propose a discrete analogue of the Ryu–Takayanagi formula, identifying minimal-length discrete geodesics in the tiling as holographic duals of boundary entanglement regions. Although not a direct replication of continuum AdS/CFT physics, these models suggest how discrete setups may open doors to new phenomena and deeper geometrical insights.

- *Geometric Quantum Discord and Factorisation.*

  We introduce an information-theoretic approach using geometric quantum discord (GQD) to detect factorisation properties of modular partition functions in pure states. Our analysis shows that GQD vanishes precisely when the partition function factorises, providing a clean diagnostic of non-factorisation. Applying this to the TFD state of holographic CFTs dual to an eternal AdS black hole clarifies the interpretation of the TMD state of as the closest classical approximation to the TFD state—carrying no quantum correlations. We also connect GQD to black hole microstates, suggesting that these underlie the non-factorisation of the gravitational path integral, thus enhancing our grasp of the factorisation puzzle.

(II) Dynamical Quantum Complexity and Information Scrambling

- *Quantum Triangular Billiards: From Integrable to Chaotic.* We explore spectral and dynamical signatures of chaos in triangular billiards, where internal angles tune

the classical phase space from genus-one tori (integrable) to higher-genus surfaces (pseudo-integrable) or infinite-genus manifolds (chaotic). Key findings include:

  - Increasing average level spacing ratios in chaotic triangles,
  - Late-time linear growth of spectral complexity for integrable while the non-integrable triangles show logarithmic late time growth,
  - Decreasing variance of Lanczos coefficients marking a transition to chaos,
  - Progressive delocalisation of energy eigenstates in the Krylov basis for the integrable to chaotic transition,
  - Enhanced spread complexity in chaotic systems, featuring no recurrences and a clear saturation plateau.

    Notably, we demonstrate a clear link between the topological classification of classical phase space and Krylov-based complexity measures, bridging classical and quantum chaos perspectives.

- *Spread Complexity in Non-Hermitian Systems and Purification.* We develop a bi-Lanczos and complex symmetric approach to handle non-unitary dynamics, particularly in measurement-driven Hamiltonians and *PT-symmetric* setups. Our findings include:
  - Identification of measurement-induced transitions, where repeated projective measurements halt complexity growth (quantum Zeno effect),
  - Localisation phenomena in PT-broken phases appear both in real space and in the Krylov basis, diagnosed by a newly introduced Krylov inverse participation ratio, while showing that spread complexity is not proportionally suppressed by the strength of localisation, whereas spread entropy is.
  - Formulations of purified state complexity, showing how operator complexity bounds translate into constraints on purified evolutions. In examples ranging from finite-dimensional Werner states to infinite-dimensional thermal ensembles (e.g. the TFD state), we observe subadditivity for Krylov complexities—contrasting with certain holographic volume complexity results.

- *Krylov Paths and Geometry.* We generalise the Krylov chain evolution to a path on a multi-dimensional "Krylov lattice" suitable for Lie superalgebras. Through explicit constructions in super Heisenberg–Weyl and OSp(2|1) algebras, we capture separate bosonic and fermionic contributions to complexity in supercoherent states. This framework paves the way for studying large-charge superstring states in $\mathrm{AdS}_5 \times S^5$, where the geometry of the Krylov paths captures the geometry in which the string propagates.

State of the Art 2

Let us review the main pillars that underpin the rapidly advancing field of holography and its deep connections to quantum information theory. Building on the foundational framework of the AdS/CFT correspondence, we discuss its fundamental ingredients and examine how, in specific limits of the parameters of the theory, the one-loop dilatation operator can be mapped to the XXX spin-chain Hamiltonian, with single-trace operators corresponding to spin-chain states in this integrable model. Our aim is to illustrate how this duality naturally connects to notions of entanglement and other quantum correlation measures, and to introduce the core ideas behind Krylov and spread complexity—highlighting their salient features and roles in the holographic paradigm.

We begin in Sec. 2.1 by revisiting the AdS/CFT correspondence, introducing its basic tenets in Sec. 2.1.1. There, we recount how $(d+1)$-dimensional gravitational dynamics in negatively curved spacetimes mirror phenomena in d-dimensional conformal field theories living on flat backgrounds. The bridge between these ostensibly different worlds is furnished by the AdS/CFT dictionary, whose entries allow for a remarkable translation of concepts from geometry into field theory and vice versa. In Sec. 2.1.2, we then highlight how certain low-dimensional instances of AdS/CFT can be mapped to spin-chain models—thereby cementing the notion that methods commonly employed in condensed matter physics can intersect meaningfully with ideas borrowed from quantum gravity.

With this holographic backdrop in place, we turn our attention to the role of quantum correlations in Sec. 2.2. Classical and quantum notions of information have proven indispensable in unravelling the subtleties of black hole thermodynamics, holographic entanglement structures, and the overall fabric of spacetime. In Sec. 2.2.1, we survey key concepts of entanglement in quantum theories, outlining how bipartite measures reveal the nonclassical character of quantum states. This leads seamlessly into Sec. 2.2.2, where we delve into how such measures enter the holographic dictionary—foremost among them being the now-celebrated Ryu–Takayanagi prescription for entanglement entropy. Beyond entanglement, a range of other information-theoretic quantities, from mutual information to relative entropy, have proven equally essential in refining our understanding of holography. Section 2.2.3 extends this exploration further by introducing quantum discord, emphasising its role in clarifying the boundary between quantum and classical correlations and underscoring its significance in holographic setups.

Finally, we review the theme of complexity and the dynamical facets of quantum systems

in Sec. 2.3. Krylov and spread complexity, which quantifies the spread of operators and states in the Hilbert space, have emerged as a new interface connecting holographic scenarios and quantum information. Sections 2.3.1, 2.3.2, and 2.3.3 focus on time evolution and the Krylov basis, illustrating how systematic expansions of state and operator dynamics respectively facilitate a clearer view of how quantum systems spread and evolve. Altogether, the material in this review chapter lays out the "state of the art" in understanding how the AdS/CFT framework, quantum correlations, and the fine details of Krylov and spread complexity can illuminate various facets of quantum gravity. Although a complete theory of quantum gravity remains elusive, these tools—from core concepts in quantum information theory to holographic dictionary entries—attest to the power of holography in furthering our grasp of fundamental physics.

2.1 The AdS/CFT Correspondence

In recent decades, one of the most transformative breakthroughs in theoretical physics has been the conjectured Anti-de Sitter/Conformal Field Theory correspondence. This duality posits an exact one-to-one mapping between a quantum field theory exhibiting conformal symmetry in d dimensions and a string theory—or its low-energy gravitational limit—defined on a background given by the direct product of AdS_{d+1} with a compact manifold $\mathscr{M}_{9-d}$. In this construction, the conformally invariant QFT is realised on the boundary of the AdS space, which itself is conformally flat, while gravitational dynamics take place in the higher-dimensional bulk.

A key strength of AdS/CFT lies in the precise quantitative relationships it establishes. For instance, it provides direct links between the 't Hooft coupling in the gauge theory, the string tension in the dual gravitational description, and the scaling dimensions of local operators. By leveraging these connections, AdS/CFT delivers powerful tools for probing strongly coupled regimes that elude standard perturbative techniques. In particular, the holographic treatment of finite-temperature systems via black hole geometries, along with interpretations in terms of entangled states such as the thermofield double, has yielded profound insights into the interrelations among gravity, thermodynamics, and quantum entanglement.

Developing a comprehensive framework for understanding strongly coupled quantum systems remains a major challenge across multiple domains—ranging from low-energy Quantum Chromodynamics (QCD), which is characterised by quark confinement, to condensed-matter models and certain cosmological scenarios. Although perturbative methods using Feynman diagrams work reliably at high energies in QCD due to asymptotic freedom, they break down at the confining energy scales where quarks are no longer weakly interacting. In the challenging non-perturbative regime, the AdS/CFT correspondence provides a crucial

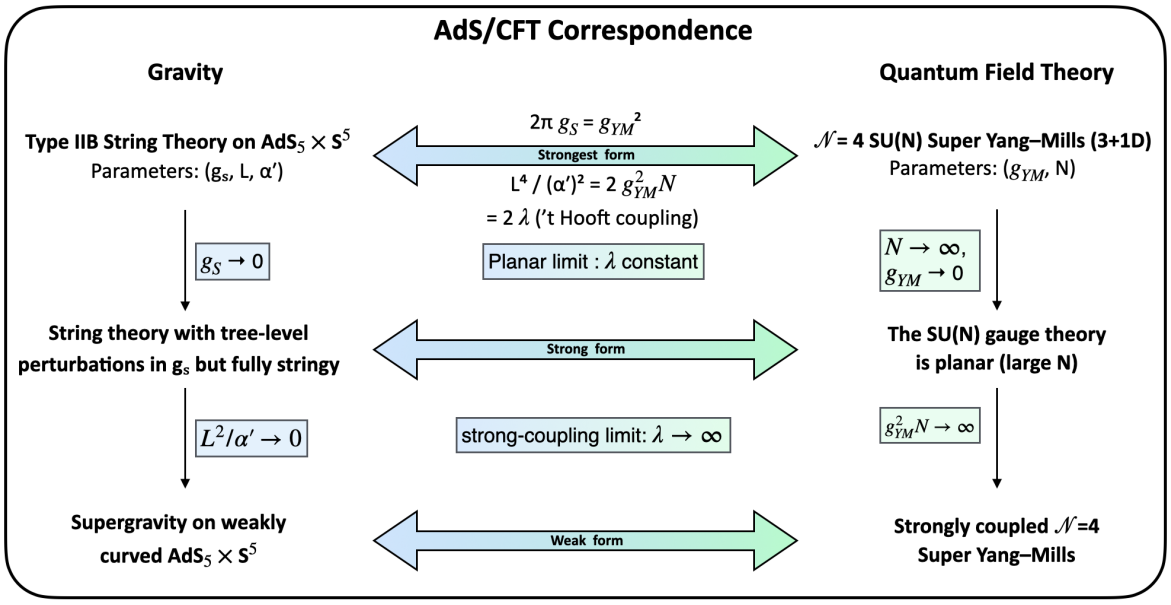

Figure 2.1: Diagrammatic representation of the AdS/CFT correspondence and its successive limiting forms. The duality relates Type IIB string theory on $\mathrm{AdS}_5 \times S^5$ (left, gravity side) to $\mathcal{N} = 4$ $\mathrm{SU}(N)$ Super Yang–Mills theory in four dimensions (right, field theory side). In the strongest form, both sides are fully quantum, with parameter relations $2\pi g_s = g^2_{\mathrm{YM}}$ and $L^4/\alpha'^2 = 2g^2_{\mathrm{YM}}N = 2\lambda$, where λ is the 't Hooft coupling. Taking the planar limit on the field theory side ($N \to \infty$, $g_{\mathrm{YM}} \to 0$, with λ fixed) corresponds to turning off string loops ($g_s \to 0$) but retaining full stringy excitations—this is the strong form of the duality. Further taking $\lambda \to \infty$ (large 't Hooft coupling) maps to the low-energy limit $\alpha'/L^2 \to 0$ on the gravity side, resulting in classical supergravity on $\mathrm{AdS}_5 \times S^5$, known as the weak form of the correspondence. Arrows indicate the direction of the duality and the nature of parameter scaling in each regime.

theoretical bridge: by mapping the strong-coupling domain of a quantum field theory to the weak-coupling regime of a dual string theory, this gauge/string duality supplies a novel toolkit for probing phenomena intractable by conventional perturbative methods, thereby significantly advancing our understanding of strongly interacting systems.

The AdS_5/CFT_4 Example : The $\mathrm{AdS}_5/\mathrm{CFT}_4$ correspondence is the most celebrated example of the holographic principle. It proposes an exact equivalence between two seemingly very different theories: on the gravity side, type IIB superstring theory formulated on a ten-dimensional spacetime that is the direct product of a five-dimensional anti-de Sitter space (AdS_5) and a five-dimensional sphere (S^5); on the field theory side, a four-dimensional conformal field theory—the maximally supersymmetric $\mathcal{N} = 4$ Super Yang–Mills (SYM) theory with gauge group $\mathrm{SU}(N)$ defined on flat Minkowski space $\mathbb{R}^{1,3}$. This duality first emerged from string theory considerations involving D-branes, specifically from analysing the low-energy dynamics of a stack of N parallel D3-branes in type IIB string theory. In one

description, open strings ending on the D3-branes give rise to the $\mathcal{N} = 4$ SYM theory; in the other, the near-horizon geometry of the D3-branes can be shown to be precisely $\mathrm{AdS}_5 \times S^5$, providing a gravitational perspective. This "holographic" nature asserts that a theory of gravity in a higher-dimensional space can be completely encoded in a lower-dimensional quantum field theory without gravity. In this duality, the parameters on both sides are related through the dimensionless 't Hooft coupling λ. On the gauge theory side one defines the 't Hooft coupling as

$$\lambda = g_{\mathrm{YM}}^2 N,$$

where g_{YM} is the Yang–Mills coupling constant, which determines the strength of the interactions between the gauge fields, and N is the rank of the $\mathrm{SU}(N)$ gauge group, which counts the number of "colors" or independent charges in the gauge theory. The 't Hooft coupling λ is dimensionless and serves as the effective expansion parameter in the large-N (planar) limit; when $N \to \infty$ while keeping λ fixed, many Feynman diagrams simplify, and the field theory becomes integrable. On the string-theory side, the 't Hooft coupling λ unifies the fundamental string parameters and the $\mathrm{AdS}_5/\mathrm{S}^5$ geometry via

$$\lambda = 4\pi^2 T^2 = 4\pi N g_s = \frac{R^4}{\alpha'^2}, \tag{2.1}$$

where

- T is the string tension, energy per unit length of the fundamental string, so that $\lambda = 4\pi^2 T^2$ implies large λ corresponds to a high tension and thus to more classical worldsheet dynamics;
- g_s is the dimensionless string coupling controlling genus-expansions, and $\lambda = 4\pi N g_s$ shows that at large N with λ fixed the effective coupling g_s is small, justifying the use of classical supergravity when $\lambda \gg 1$;
- α' is the inverse string tension (the square of the fundamental string length), so that $\lambda = R^4/\alpha'^2$ measures the ratio of the common curvature radius R of AdS_5 and S^5 to the string length.

Accordingly, a large 't Hooft coupling (equivalently $R/\sqrt{\alpha'} \gg 1$) ensures that the spacetime curvature is gentle compared to the string scale, validating the supergravity approximation.

In parallel, one engineers a hierarchy of curvature radii so that AdS_5 remains parametrically large—thereby suppressing α'-corrections—while the internal S^5 radius is kept relatively small (or its volume effectively truncated) to lift the Kaluza–Klein modes to high mass and decouple them from the low-energy spectrum. Hence, in the standard holographic regime

one requires

$$\frac{R_{\mathrm{AdS}_5}}{\sqrt{\alpha'}} \gg 1, \qquad \frac{R_{S^5}}{\sqrt{\alpha'}} \ll \frac{R_{\mathrm{AdS}_5}}{\sqrt{\alpha'}} \tag{2.2}$$

or equivalently a small internal volume. This clear separation of scales guarantees both the reliability of the classical gravity description and a precise correspondence with the dual gauge theory.

A deeper look at the theories together with their symmetries enhances our understanding of the duality. Type IIB superstring theory on $\mathrm{AdS}_5 \times S^5$ is a ten-dimensional theory that is inherently supersymmetric and features chiral fields. When compactified on $\mathrm{AdS}_5 \times S^5$, the background geometry is maximally symmetric: AdS_5 is a maximally symmetric spacetime with constant negative curvature and its isometry group $\mathrm{SO}(2,4)$ is isomorphic to the conformal group in four dimensions, while S^5 is a five-sphere with positive curvature whose isometry group is $\mathrm{SO}(6)$; this latter group turns out to be equivalent to the R-symmetry group of the $\mathscr{N} = 4$ SYM theory, providing a geometrical origin for the internal symmetry transformations of the field theory. Together, the full symmetry of the $\mathrm{AdS}_5 \times S^5$ background is encoded in the supergroup $\mathrm{PSU}(2,2|4)$, which combines the bosonic $\mathrm{SO}(2,4)$ (conformal) and $\mathrm{SO}(6)$ (R-symmetry) symmetries with the appropriate supersymmetries (32 supercharges in total). On the gauge theory side, the $\mathscr{N} = 4$ SYM theory is a four-dimensional conformal field theory with several unique features: it possesses maximal supersymmetry, with 16 real supercharges (organised into 4 complex ones), making it exactly conformal at the quantum level as its beta function vanishes, ensuring that all correlation functions display precise scaling behaviours; it is invariant under the full conformal group $\mathrm{SO}(2,4)$, and it has an R-symmetry $\mathrm{SU}(4) \simeq \mathrm{SO}(6)$ that rotates the four supersymmetry generators among themselves and corresponds exactly to the isometry group of S^5. In addition, in the large N (planar) limit, the theory simplifies dramatically and exhibits integrability that allows for exact computations of anomalous dimensions and other observables. The origin of the duality can be traced back to the study of D3-branes in type IIB string theory. In this setting, D3-branes are extended objects on which open strings can end, and a stack of N D3-branes supports a $U(N)$ gauge theory on its worldvolume; in the low-energy limit, the massive modes decouple, leaving behind $\mathscr{N} = 4$ SYM theory.

The same setup admits two complementary descriptions: a four-dimensional $\mathscr{N} = 4$ SYM theory with coupling g_{YM} and rank N from the open string sector, and a gravitational background $\mathrm{AdS}_5 \times S^5$ from the near-horizon limit of the D3-branes. Notably, the identification $\lambda = \frac{R^4}{\alpha'^2}$ implies that a large curvature radius (relative to the string length) corresponds to a strongly coupled gauge theory. A compelling aspect of the AdS_5/CFT_4 duality is the precise matching of symmetries between the two sides: the conformal symmetry $\mathrm{SO}(2,4)$ of

AdS_5 mirrors exactly the conformal symmetry of the four-dimensional $\mathcal{N} = 4$ SYM theory, ensuring that the scaling behaviour and correlators in the gauge theory remain invariant under conformal transformations; the R-symmetry $\mathrm{SO}(6) \simeq \mathrm{SU}(4)$ of the gauge theory, which governs the rotations among the supercharges and various scalar fields, matches the isometry group of S^5, providing a geometrical interpretation of the internal symmetries in the field theory and enabling the classification of operators according to representations of $\mathrm{SO}(6)$; and finally, both sides preserve 32 supercharges, with the type IIB superstring theory in this maximally supersymmetric background and the $\mathcal{N} = 4$ SYM theory being the unique theories with maximal supersymmetry in their respective dimensions. In summary, the AdS_5/CFT_4 correspondence establishes a deep and powerful connection between a ten-dimensional theory of quantum gravity—type IIB superstring theory on $AdS_5 \times S^5$—and a four-dimensional maximally supersymmetric conformal field theory ($\mathcal{N} = 4$ SYM). The duality is cemented by a detailed matching of parameters: the 't Hooft coupling λ, expressing both the gauge coupling and the number of colors, serves as the bridge between the theories, with g_{YM} and N appearing naturally on the gauge theory side, and T, g_s, α', and R governing the dynamics and geometry on the string theory side through the relations $\lambda = 4\pi^2 T^2 = 4\pi N\, g_s = \frac{R^4}{\alpha'^2}$. The matching of conformal and R-symmetries, along with maximal supersymmetry on both sides, provides compelling evidence for the duality and offers a unique framework for studying strongly coupled gauge theories using gravitational methods.

A later and equally compelling example is provided by the duality between type IIA superstring theory on $\mathrm{AdS}_4 \times \mathbb{C}P^3$ and the three-dimensional $\mathcal{N} = 6$ super Chern–Simons theory with gauge group $\mathrm{SU}(N)_k \times \mathrm{SU}(N)_{-k}$ defined on $\mathbb{R}^{1,2}$. In this correspondence, the 't Hooft coupling $\lambda = N/k$ simultaneously fixes the curvature radii of AdS_4 and $\mathbb{C}P^3$ and determines the effective string tension. At large λ, the string tension scales as $\sqrt{\lambda}$, rendering the worldsheet dynamics essentially classical. Beyond this $\mathrm{AdS}_4/\mathrm{CFT}_3$ example, other holographic dualities exist. In particular, string theories on backgrounds containing AdS_3 are dual to two-dimensional superconformal field theories. Models based on $\mathrm{AdS}_3 \times S^3 \times S^3 \times S^1$ or $\mathrm{AdS}_3 \times S^3 \times T^4$ are distinguished by their rich symmetry and integrability properties. In the chapters that follow, we focus on those correspondences where the boundary description is a gauge theory. We use "gauge/gravity duality" and "AdS/CFT" interchangeably to denote this deep equivalence.

2.1.1 Fundamental Ingredients of the Correspondence

In the sections that follow, we will introduce the main coordinate systems of AdS spacetimes, review the foundational aspects of conformal field theory, and present the Gubser–Klebanov–Polyakov–Witten prescription for relating bulk dynamics to boundary correla-

tors. We will then illustrate black hole solutions in AdS and describe their dual interpretation via the thermofield double state of the boundary CFT.

Anti-de Sitter Spacetimes: Anti–de Sitter (AdS) spacetime is the unique maximally symmetric solution of the vacuum Einstein equations with a negative cosmological constant, $\Lambda < 0$. The Einstein–Hilbert action in $(d+1)$ dimensions is given by

$$S_{\rm EH} = \frac{1}{16\pi G_N}\int_{\mathscr{M}} d^{d+1}x\,\sqrt{-g}\,(R-2\Lambda) - \frac{1}{8\pi G_N}\int_{\partial\mathscr{M}} d^{d}x\,\sqrt{\gamma}\,K, \tag{2.3}$$

where G_N is Newton's constant, R is the Ricci scalar, g denotes the determinant of the metric $g_{\mu\nu}$, and the second term (the Gibbons–Hawking–York boundary term) ensures a well-defined variational principle when the manifold $\mathscr{M}$ is noncompact.

AdS_{d+1} can be represented as the hyperboloid

$$-(X^0)^2 + \sum_{i=1}^{d}(X^i)^2 - (X^{d+1})^2 = -\ell^2, \tag{2.4}$$

embedded in a $(d+2)$-dimensional space with signature $(-,+,\ldots,+,-)$. This embedding makes manifest the isometry group $\mathrm{SO}(d,2)$, which coincides with the conformal group of d-dimensional Minkowski space.

Multiple coordinate systems are used to cover AdS spacetime:

- **Global Coordinates:** With coordinates (ρ,τ,Ω_i), the metric reads

$$ds^2 = \ell^2\Big(-\cosh^2\rho\,d\tau^2 + d\rho^2 + \sinh^2\rho\,d\Omega_{d-1}^2\Big). \tag{2.5}$$

- **Alternate Global Coordinates:** Defined via the transformation $\tilde\rho = \ell\,\sinh\rho$ and $\tilde\tau = \ell\,\tau$, yielding

$$ds^2 = -\Big(1+\frac{\tilde\rho^2}{\ell^2}\Big)d\tilde\tau^2 + \frac{d\tilde\rho^2}{1+\frac{\tilde\rho^2}{\ell^2}} + \tilde\rho^2\,d\tilde\Omega^2. \tag{2.6}$$

- **Poincaré Patch:** With coordinates $(z,t,\vec{x})$, the metric takes the form

$$ds^2 = \frac{\ell^2}{z^2}\Big(dz^2 + \eta_{\mu\nu}\,dx^\mu dx^\nu\Big), \tag{2.7}$$

  where $\eta_{\mu\nu}$ is the flat Minkowski metric and the conformal boundary is located at $z\to 0$.

A Wick rotation in these coordinates produces the Euclidean version of AdS, which is isometric to a hyperbolic space.

Conformal Field Theories: Conformal field theories (CFTs) are quantum field theories invariant under transformations that preserve angles but not necessarily distances. More precisely, conformal transformations are spacetime diffeomorphisms whose effect on the metric can be absorbed by a local rescaling. In a spacetime with metric $g_{\mu\nu}(x)$, such a diffeomorphism acts as

$$g_{\mu\nu}(x) \to e^{2\sigma(x)} g_{\mu\nu}(x). \tag{2.8}$$

In d dimensions, the conformal group is $\mathrm{SO}(d,2)$ (or $\mathrm{SO}(d+1,1)$ in Euclidean signature), matching the isometry group of AdS_{d+1}.

Operators in a CFT are organised into conformal multiplets. A primary operator $\mathscr{O}(x)$ is characterised by its scaling dimension Δ, obeying $\mathscr{O}(\lambda x) = \lambda^{-\Delta}\,\mathscr{O}(x)$, under the rescaling $x^\mu \to \lambda x^\mu$. At the origin it satisfies

$$[D, \mathscr{O}(0)] = -i\,\Delta\,\mathscr{O}(0), \qquad [K_\mu, \mathscr{O}(0)] = 0, \tag{2.9}$$

where D is the dilatation generator, and K_μ are the generators of special conformal transformations. For a scalar representation one may take $D = -i\,x^\nu\partial_\nu$ and $K_\mu = -i\Big(2x_\mu x^\nu\partial_\nu - x^2\partial_\mu\Big)$. Correlation functions of primary operators are therefore strongly constrained by conformal symmetry. For example, the two-point function is given by

$$\langle \mathscr{O}_1(x_1)\mathscr{O}_2(x_2)\rangle = \begin{cases} \dfrac{c_{12}}{|x_1 - x_2|^{2\Delta}}, & \Delta_1 = \Delta_2 \equiv \Delta, \\ 0, & \Delta_1 \neq \Delta_2, \end{cases} \tag{2.10}$$

and the three-point function takes the form

$$\langle \mathscr{O}_1(x_1)\mathscr{O}_2(x_2)\mathscr{O}_3(x_3)\rangle = \frac{C_{123}}{|x_1 - x_2|^{\Delta_1+\Delta_2-\Delta_3}\,|x_2 - x_3|^{\Delta_2+\Delta_3-\Delta_1}\,|x_3 - x_1|^{\Delta_3+\Delta_1-\Delta_2}}. \tag{2.11}$$

In two dimensions the symmetry is further enhanced, as the conformal algebra extends to the infinite-dimensional Virasoro algebra.

The Gubser–Klebanov–Polyakov–Witten Holographic Dictionary

At its core, the AdS/CFT correspondence posits an equivalence between the partition functions of a gravitational theory in AdS and a CFT on its boundary. In its most precise formulation—the Gubser–Klebanov–Polyakov–Witten (GKPW) prescription—this relation

is expressed as

$$e^{-W[\phi_0]} = \left\langle \exp\!\left(\int d^d x\, \mathscr{O}(x)\, \phi_0(x) \right) \right\rangle_{\mathrm{CFT}} = e^{-S_{\mathrm{grav}}[\phi(z,x)]}\Big|_{\lim_{z\to 0}\left(\phi(z,x)\, z^{\Delta-d}\right)=\phi_0(x)}, \tag{2.12}$$

where $W[\phi_0]$ is the generating functional of connected correlators, $\phi_0(x)$ is the source for the operator $\mathscr{O}(x)$, and S_{grav} is the on-shell gravitational action. For a scalar field in the bulk, the asymptotic expansion near the boundary is

$$\phi(z,x) \sim z^{d-\Delta}\, \phi_0(x) + z^{\Delta}\, \langle \mathscr{O}(x) \rangle. \tag{2.13}$$

A direct consequence of this prescription is the relation between the mass m of the bulk scalar and the scaling dimension Δ of the dual operator

$$m^2 \ell^2 = \Delta(\Delta - d), \tag{2.14}$$

which allows for slightly tachyonic (but stable) bulk fields provided $m^2\ell^2 \geq -\frac{d^2}{4}$ (the Breitenlohner–Freedman bound).

While explicit realisations of AdS/CFT emerging from string theory (the "top-down" approach) offer detailed microscopic models, they are often technically involved. An alternative is the "bottom-up" approach, where effective holographic models are constructed based solely on the low-energy spectrum and symmetries, without requiring a complete ultraviolet (UV) completion.

Black Hole Geometries in AdS

The AdS/CFT correspondence naturally extends to finite temperature by relating thermal states in the boundary CFT to black hole solutions in the bulk. In asymptotically AdS spacetimes, black holes are characterised by a Hawking temperature T_{H}, which is identified with the temperature of the dual field theory. For example, in $(2+1)$-dimensional gravity the celebrated Bañados–Teitelboim–Zanelli (BTZ) black hole serves as an important model.

The most general BTZ solution (assuming rotational symmetry and a time-independent ansatz) is given by

$$ds^2 = -\left(-\frac{2M}{k} + r^2 + \frac{J^2}{k^2 r^2}\right) dt^2 + \frac{dr^2}{-\frac{2M}{k} + r^2 + \frac{J^2}{k^2 r^2}} + r^2 \left(\frac{J}{k r^2} dt + d\phi\right)^2, \tag{2.15}$$

where M and J denote the gravitational mass and angular momentum, respectively, and k (which may be set to a fixed value by appropriate rescaling) is related to the Newton constant.

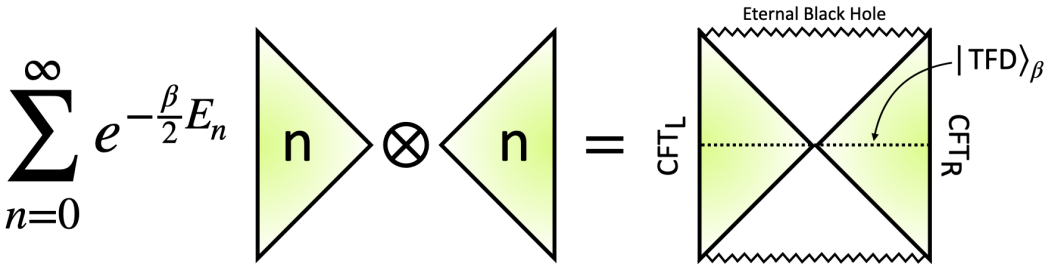

Figure 2.2: The thermofield double (TFD) state, formed by entangling two copies of a conformal field theory (CFT) on a spherical geometry, represents a particular superposition of two initially disconnected spacetimes. This entangled configuration corresponds to a single, connected eternal black hole geometry in the bulk. Figure adapted from [101].

In the nonrotating limit ($J = 0$), the metric simplifies to

$$ds^2 = -\left(r^2 - M\right) dt^2 + \frac{dr^2}{r^2 - M} + r^2 d\phi^2, \tag{2.16}$$

with an event horizon at $r_h = \sqrt{M}$ and a corresponding Hawking temperature

$$T_{\mathrm{BTZ}} = \frac{r_h}{2\pi}. \tag{2.17}$$

Notably, the BTZ geometry has constant negative curvature and can be constructed as a quotient of AdS_{2+1} by a discrete subgroup of its isometry group, resulting in a double-sided black hole geometry with two asymptotically AdS regions.

In higher-dimensional AdS spacetimes, gravitational thermodynamics reveals a phase transition between thermal AdS and AdS black holes. By evaluating the Einstein–Hilbert action on-shell for these configurations, one finds that at a critical temperature (the Hawking–Page temperature) the dominant contribution to the partition function shifts from thermal AdS (interpreted as a gas of thermal radiation) to a large black hole phase. This first-order transition has been linked, via holography, to the deconfinement transition in large-N gauge theories.

Thermofield Double State: Within the framework of the AdS/CFT correspondence, the thermofield double (TFD) state serves as a pivotal construct for understanding the dual description of eternal black holes, such as the maximally extended BTZ solution. The TFD state is formulated in the tensor product Hilbert space $\mathscr{H}_L \otimes \mathscr{H}_R$, representing two non-interacting copies of a conformal field theory (CFT) situated on the distinct asymptotic

boundaries of the AdS spacetime. This state is explicitly given by

$$|\text{TFD}\rangle_\beta = \frac{1}{\sqrt{Z(\beta)}} \sum_n e^{-\frac{\beta E_n}{2}} |E_n\rangle_L \otimes |E_n\rangle_R \,, \tag{2.18}$$

where $Z(\beta) = \sum_n e^{-\beta E_n}$ denotes the partition function at inverse temperature β, and $|E_n\rangle_L$, $|E_n\rangle_R$ are the energy eigenstates corresponding to the left and right CFTs, respectively. The normalisation factor ensures that $\langle\Psi|\Psi\rangle = 1$, confirming that $|\Psi\rangle$ is a pure state in the combined Hilbert space as shown in Fig. 2.2.

By tracing out one of the subsystems, say the right CFT, we obtain a thermal density matrix for the left CFT

$$\rho_L = \text{Tr}_R \left(|\Psi\rangle \langle\Psi| \right) = \frac{e^{-\beta H_L}}{Z(\beta)}, \tag{2.19}$$

where H_L is the Hamiltonian acting on $\mathscr{H}_L$. This reduced density matrix exhibits the canonical thermal form, indicating that the TFD state effectively purifies the thermal state of each individual CFT.

The entanglement inherent in the TFD state manifests through non-vanishing correlators between operators localised on opposite boundaries. These correlations are not merely mathematical artifacts; they correspond to a connected geometric structure in the bulk spacetime—a wormhole or Einstein–Rosen bridge—linking the two asymptotic regions. This profound connection is encapsulated in the *ER=EPR* conjecture, which posits that quantum entanglement (Einstein–Podolsky–Rosen correlations) is fundamentally related to the existence of spacetime wormholes (Einstein–Rosen bridges).

The eternal black hole in AdS spacetime, such as the maximally extended BTZ black hole, provides a concrete realisation of this duality. Its Penrose diagram reveals two asymptotically AdS regions connected through a shared interior, representing the wormhole structure. Each asymptotic region corresponds to one of the two CFTs in the TFD state. The entanglement between these CFTs is thus geometrically realised as the wormhole connecting the two boundaries in the bulk spacetime. This correspondence not only elucidates the thermal properties of the boundary theories but also offers deep insights into the interplay between quantum entanglement and the fabric of spacetime geometry.

2.1.2 Mapping AdS/CFT to Spin Chains

A crucial step in leveraging this duality is to identify specific instances in which both the gauge-theoretic and string-theoretic formulations admit, at least in principle, exact solutions. Such *integrable* models possess a complete set of independent conserved charges—one for every dynamical degree of freedom—so their spectra can be determined non-perturbatively

through techniques like the Bethe ansatz or thermodynamic Bethe equations. The most prominent instance is the planar limit of $\mathcal{N} = 4$ supersymmetric Yang–Mills theory with gauge group $\mathrm{SU}(N)$ and its Type IIB superstring dual on $\mathrm{AdS}_5 \times S^5$, the classic realisation of gauge–gravity duality introduced in [21]. Here supersymmetry and the large global algebra $\mathrm{PSU}(2,2|4)$ combine to produce an infinite tower of commuting charges on both sides of the correspondence, making the system a paradigmatic example of integrability [102, 103]. This setting also illustrates the *holographic principle*, which states that all information contained within a spatial volume can be encoded on its boundary [24, 25].

Integrability in planar $\mathcal{N} = 4$ SYM reveals itself through the spectrum of scaling dimensions. In this limit the dilatation operator acts as the Hamiltonian of an integrable spin chain, so its eigenvalues—the operator dimensions—are obtained from Bethe-ansatz equations rather than from Feynman-diagram resummations. The AdS/CFT correspondence equates the string partition function, evaluated with boundary data $\phi|_{\partial\mathrm{AdS}} = J$, to the generating functional of the boundary CFT, $Z_{\text{string}}\Big[\phi|_{\partial\mathrm{AdS}} = J\Big] = Z_{\text{CFT}}[J]$, where J sources local operators.

In the gauge theory the primary spectrum is fixed by the scaling dimensions $\Delta(\lambda, 1/N)$, which appear as eigenvalues of the dilatation operator $\mathfrak{D}$, a Casimir of $\mathrm{SO}(4,2)$,

$$\mathfrak{D}\,\hat{\mathscr{O}}(x) = \Delta(\lambda, 1/N)\,\hat{\mathscr{O}}(x). \tag{2.20}$$

On the string side an energy eigenstate of energy E in global AdS coordinates corresponds to a local operator with $\Delta = E$. Heavy semiclassical strings at large 't Hooft coupling therefore map to high-dimension operators, while perturbative diagrams dominate at small coupling. Integrability bridges these regimes by providing exact spectral equations valid for every value of λ, giving—at least in the planar limit—an essentially complete solution of a four-dimensional interacting conformal field theory.

Spin Chains, Dilatation Operators, and Integrability in $\mathcal{N} = 4$ SYM

In the planar limit of the AdS/CFT correspondence, one studies single-trace composite operators in four-dimensional $\mathcal{N} = 4$ super Yang–Mills (SYM) theory. This theory enjoys the full superconformal symmetry group $PSU(2,2|4)$, combining conformal invariance, supersymmetry, and an *R*-symmetry described by $\mathfrak{so}(6)$. It contains six real scalars Φ^a (with $a = 1, \ldots, 6$), which are often arranged into three complex fields

$$X = \Phi^1 + i\,\Phi^2, \quad Y = \Phi^3 + i\,\Phi^4, \quad Z = \Phi^5 + i\,\Phi^6.$$

For simplicity, one can focus on two of these complex fields; a prototype single-trace operator then takes the form

$$\mathscr{O}_{J_1,J_2} \;=\; \mathrm{Tr}\Big(ZZXZXX\cdots ZX\Big), \tag{2.21}$$

where the exponents J_1, J_2 respectively record how many times X's and Z's appear inside the trace. In the free theory limit, the classical dimension of this operator is $\Delta_0 = J_1 + J_2$. Quantum corrections to scaling dimensions are governed by the dilatation operator $\mathfrak{D}$, which can be expanded in powers of the 't Hooft coupling $\lambda = g^2_{\mathrm{YM}}\, N$

$$\mathfrak{D} \;=\; \mathfrak{D}^{(0)} \;+\; \lambda\,\mathfrak{D}^{(2)} \;+\; \lambda^2\,\mathfrak{D}^{(4)} \;+\; \ldots.$$

Each $\mathfrak{D}^{(n)}$ preserves the classical quantum numbers such as Lorentz spins and *R*-symmetry charges, ensuring the structure of the theory remains consistent order by order. More generally, within the framework of $\mathscr{N} = 4$ SYM theory, one may also analyze single-trace operators constructed from $\mathscr{N} = 1$ superfields, which can be expressed schematically as

$$\mathscr{O} = \mathrm{tr}\Big(X^{J_X} Y^{J_Y} Z^{J_Z}\, \psi_1^{K_1} \psi_2^{K_2}\Big)\,. \tag{2.22}$$

Here, besides including the three scalar fields from the matter supermultiplets, the operator also involves two spinor components ψ_i from the gaugino supermultiplet. This collection of operators defines an $SU(2|3)$ subsector of the theory [104, 105].

A crucial simplification arises when considering *closed subsectors* of the theory, in which no operators outside that sector mix at a given loop order. One can, for instance, isolate an $\mathfrak{su}(2)$ subsector involving only the two complex scalars X and Z. At one loop in the planar limit, only these fields appear within the corresponding single-trace operator, and no other components of $\mathscr{N} = 4$ SYM can mix in. The correlation functions scale as

$$\langle \mathscr{O}(x)\, \overline{\mathscr{O}}(y)\rangle \;\sim\; |x-y|^{-2\Delta},$$

where Δ includes the quantum corrections to the free-field dimension Δ_0.

Within the $\mathfrak{su}(2)$ sector, the one-loop part of the dilatation operator may be written as [106]

$$\mathscr{D}_{\mathfrak{su}(2)} \;=\; \frac{\lambda}{8\pi^2} \sum_{k=1}^{L} \Big(1 - P_{k,k+1}\Big), \tag{2.23}$$

where $L = J_1 + J_2$ is the total length of the operator and $P_{k,k+1}$ is the permutation exchanging neighboring fields at sites k and $k+1$ in the trace. This operator precisely matches the Hamiltonian of an $\mathrm{XXX}_{1/2}$ Heisenberg spin chain of length L.

By identifying Z with spin-down and X with spin-up, the operator $\mathrm{Tr}(Z^L)$ maps to a

ferromagnetic vacuum in the spin-chain picture, whereas every insertion of X corresponds to a spin flip. Following this convention the operator in (2.21), gets mapped to the state, $|\uparrow\uparrow\downarrow\uparrow\downarrow\downarrow\cdots\uparrow\downarrow\rangle$. One can express the Hamiltonian in terms of Pauli matrices $\vec{\sigma}_k$ acting on site k

$$H_{\text{XXX}} \;=\; \frac{\lambda}{8\pi^2}\sum_{k=1}^{L}\Big(\tfrac{1}{2} \;-\; 2\,\vec{\sigma}_k\cdot\vec{\sigma}_{k+1}\Big). \tag{2.24}$$

Alternatively, letting $\sigma^{\pm}=\sigma^x\pm i\,\sigma^y$ and $\sigma^z=J_0$, one rewrites (2.24) as

$$H_{\text{XXX}} \;=\; \frac{\lambda}{8\pi^2}\sum_{k=1}^{L}\Big[2\Big((J_+)_k(J_-)_{k+1}+(J_-)_k(J_+)_{k+1}\Big) \;+\; (J_0)_k\,(J_0)_{k+1}\Big]. \tag{2.25}$$

Diagonalising this Hamiltonian gives the one-loop anomalous dimensions of the corresponding single-trace operators in the $\mathfrak{su}(2)$ sector [107].

The same idea extends to larger subalgebras of $\mathfrak{psu}(2,2|4)$. For an $\mathfrak{su}(m|n)$ sector, the one-loop dilatation operator is

$$\mathscr{D}_{\mathfrak{su}(m|n)} \;=\; \frac{\lambda}{8\pi^2}\sum_{k=1}^{L}\Big(\frac{m-n-1}{m-n} \;-\; \sum_{A,B} g_{AB}\,(T_A)_k\,(T_B)_{k+1}\Big), \tag{2.26}$$

where T_A are the superalgebra generators, $g_{AB}=\mathrm{Str}(T_AT_B)$ is the Killing form, and the subscript k indicates the operator acts on site k.

As explained in Sec. 2.1, four–dimensional $\mathscr{N}=4$ SYM enjoys the superconformal symmetry group $\mathrm{PSU}(2,2|4)$. Its bosonic part factorises into the *internal* R–symmetry $SU(4)_R$ and the *space–time* conformal group $SU(2,2)\simeq SO(2,4)$. Whether a given closed subsector is described by a *compact* or *non-compact* (super)algebra depends on which generators of the conformal group survive the truncation.

1. Pure-scalar sectors (compact). Single–trace operators built exclusively from the three complex scalars $Z,\ Y,\ X$ are Lorentz scalars and involve no derivatives. Their symmetry reduces to an $SU(3)$ (or $SU(2)$ if only two flavours are kept) inside $SU(4)_R$. Because no element of the conformal algebra acts non-trivially, the effective group manifold is a compact sphere or flag variety, and the dilatation operator maps to a Heisenberg spin chain with compact symmetry $SU(3)$ or $SU(2)$.

2. Adding fermions but no derivatives (still compact). Replacing some scalars by Weyl fermions ψ_α or $\bar{\psi}^{\dot{\alpha}}$ keeps the operators free of space–time dynamics as long as the spinors appear *n*aked. Although each ψ transforms in the $(\frac{1}{2},0)$ representation of $SO(1,3)$, its Lorentz indices are fully contracted inside the trace, so no generator of $SU(2,2)$ remains active. The prototypical example is the closed $\mathfrak{su}(2|3)$ sector whose fundamental multiple $(\mathbf{3}_B\,,\,\mathbf{2}_F)$ defines a *compact* supergroup manifold $SU(2|3)$.

3. Introducing derivatives D_μ (non-compact). The first step towards non-compactness is to act on a scalar or fermion with one or more covariant derivatives, $D^{\{s\}}Z = D_{\mu_1}\dots D_{\mu_s}Z$. Each derivative carries the vector representation $(\frac{1}{2},\frac{1}{2})$ of $SO(1,3)$ and raises the engineering dimension by one. Consequently the dilatation operator must now include the non-compact boosts and dilations that act on these Lorentz indices. The minimal such subsector is the familiar $\mathfrak{sl}(2)$ chain built from $\mathrm{Tr}(D^sZ\,D^tZ\dots)$, whose symmetry algebra is the *non-compact* $\mathfrak{sl}(2,\mathbb{R})\subset\mathfrak{su}(2,2)$.

4. Mixed boson–fermion sectors with derivatives (super-non-compact). If one keeps both derivatives and spinors, the symmetry enhances to a non-compact superalgebra such as $\mathfrak{su}(1,1|2)$ or $\mathfrak{psu}(1,1|2)$. Here the bosonic subalgebra $\mathfrak{sl}(2,\mathbb{R})\oplus\mathfrak{su}(2)$ is non-compact in its first factor, and the fermionic generators transform in mixed Lorentz representations linking the two parts.

5. Summary criterion. Let Q_{int} denote R-charges and $Q_{\text{spacetime}}$ those of $SU(2,2)$. For any closed set of letters $\{\Phi\}$,

$$\text{compact sector} \iff Q_{\text{spacetime}}(\Phi)=0 \iff \text{Lorentz scalars with no derivatives.}$$

Once a letter carries non–zero spin or derivative order, $Q_{\text{spacetime}}(\Phi)\neq 0$; at least one non-compact generator survives, and the group manifold of the subsector becomes non-compact.

In short, the guiding principle can be stated concisely:

> *A subsector remains compact provided it involves only internal $SU(4)_R$ charges. It becomes non-compact as soon as any constituent field or operator carries dynamical Lorentz quantum numbers—such as spin or non–trivial scaling dimension—thereby necessitating the presence of at least some $SU(2,2)$ generators.*

Semiclassical Limit: Coherent States and Fast-Spinning Strings A surprising connection to the string side of AdS/CFT emerges from interpreting the spin-chain states as string states. In [108], one takes a semiclassical limit of the spin-chain Hamiltonian by assigning a coherent state to each site. Concretely, if $\vec{z}_k$ parametrizes the phase-space data at site k, then the single-site coherent state is

$$\big|\vec{z}_k\big\rangle \;=\; \mathscr{N}_k\, D_k(\vec{z}_k)\,\big|\Lambda_k\big\rangle, \tag{2.27}$$

where $\left|\Lambda_k\right\rangle$ is a reference (vacuum) state and $\mathcal{N}_k$ is a normalisation factor ensuring $\langle\vec{z}_k|\vec{z}_k\rangle = 1$. Such coherent states are constructed by applying the displacement operator

$$D_k(\vec{z}_k) \;\equiv\; \exp\Big(z_k\, a_k^\dagger \;-\; \bar{z}_k\, a_k\Big)\,, \tag{2.28}$$

where a_k and $a_k^\dagger$ are the annihilation and creation operators at site k satisfying $[a_k, a_k^\dagger] = 1$, and $\vec{z}_k$ is the displacement parameter at each site. The total spin-chain state is the tensor product

$$\left|\vec{z}\right\rangle \;=\; \bigotimes_{k=1}^{L}\left|\vec{z}_k\right\rangle. \tag{2.29}$$

Applying the path-integral formalism to this construction yields a semiclassical action, which in the continuum (long-wavelength) limit becomes a Landau–Lifshitz sigma model on a worldsheet with coordinate σ. Holographically, these coherent states correspond to classical strings with large angular momentum in AdS. Thus, the space of spin-chain excitations naturally matches the configuration space of spinning strings, tying together integrable spin-chain techniques on the gauge side and semiclassical string descriptions on the gravity side [104, 105].

We further highlight *why* the continuum limit $L \to \infty$ is indispensable for mapping the coherent-state construction to the Landau–Lifshitz (LL) action. The semiclassical regime is characterised by the scaling

$$J = L \;\longrightarrow\; \infty, \qquad \tilde{\lambda} \equiv \frac{\lambda}{J^2} \quad \text{fixed},$$

so that each lattice site acts as a large spin while the collective spin of J sites becomes a macroscopic degree of freedom. Matrix elements of spin operators in the product state fluctuate only by $\mathcal{O}\Big(1/\sqrt{J}\Big)$; relative uncertainties therefore vanish as $J \to \infty$, making coherent states—whose local quantum noise is already minimal—the natural semiclassical variables.

Replacing the discrete site label by $k = J\sigma$ with $\sigma \in [0, 2\pi]$ turns the chain into a continuous world-sheet. For any slowly varying local observable $\mathcal{O}(k)$ one may expand

$$\mathcal{O}(k \pm 1) = \mathcal{O}(\sigma) \pm \frac{1}{J}\,\partial_\sigma \mathcal{O}(\sigma) + \frac{1}{2J^2}\partial_\sigma^2 \mathcal{O}(\sigma) + \ldots,$$

a gradient series that is legitimate only when neighbouring coherent-state parameters differ by $\mathcal{O}(1/J)$, precisely the condition ensured by a smooth field $\vec{n}(\sigma)$.

The overlap $\langle \vec{z}_k | \partial_\tau \vec{z}_k \rangle$ of coherent states then produces a Berry phase,

$$\sum_{k=1}^{J} \frac{1}{2} \cos\theta_k \, \partial_\tau \phi_k = \frac{J}{2} \int_0^{2\pi} d\sigma \, \cos\theta \, \partial_\tau \phi + \mathscr{O}\big(1/J\big),$$

which becomes the Wess–Zumino term in the LL action; this geometric contribution would not emerge from an S_z eigenstate basis. Finally, the exchange term in the Heisenberg Hamiltonian supplies the continuum piece $\tilde{\lambda}(\partial_\sigma \vec{n})^2$. After eliminating the fast angular variable on the string side, the same coefficient reappears, and identifying the lattice spacing with $1/J$ guarantees the match while ensuring that finite-spacing corrections are suppressed by higher powers of $1/J$.

The integrability of the string sigma model enables the use of powerful semiclassical techniques, most notably the finite-gap construction. This method allows one to characterize entire families of classical string solutions by means of algebraic spectral curves, whose moduli capture the conserved charges such as energy and angular momenta. In the semiclassical limit, these energies match with the scaling dimensions Δ of operators on the gauge theory side in the strong coupling regime $\lambda \gg 1$.

A particularly tractable subsector is the $\mathfrak{su}(2)$ sector, wherein string solutions are restricted to motion on $\mathbb{R} \times S^3 \subset \mathrm{AdS}_5 \times \mathrm{S}^5$. Operators with large R-charge J and scaling dimension Δ but fixed $\Delta - J$ correspond to classical string states with angular momentum J and energy $E = \Delta$. The prototypical example is the BMN string—a point-like object orbiting a great circle of S^5 at light speed—which corresponds to the ground state of the spin-chain corresponding to the operator $\mathrm{tr}(X^J)$ and satisfies the BPS condition $E - J = 0$.

To summarise, the dilatation operator in planar $\mathscr{N} = 4$ SYM can be recast as a spin-chain Hamiltonian, illustrating the integrable nature of the theory. At one loop, this identification is especially transparent in the $\mathfrak{su}(2)$ sector, where the $\mathrm{XXX}_{1/2}$ Heisenberg chain describes the scalar excitations. In broader sectors, one finds analogous spin-chain descriptions with larger superalgebra symmetries. Finally, taking a semiclassical continuum limit connects the spin-chain perspective to fast-rotating string solutions on the AdS side, thereby furnishing a remarkable example of the AdS/CFT correspondence in action.

2.2 Measures of Quantum Correlations

As the preceding discussion has laid out, the AdS/CFT correspondence furnishes a remarkably fertile framework in which gravitational dynamics and quantum field theory are brought into precise and often surprising dialogue. Yet, over the past two decades, this duality has not only deepened our understanding of gauge theories and string dynamics, but has also revealed a

profound resonance with ideas originating in quantum information (QI) theory. What was once considered a peripheral toolkit has now moved to the center of gravity in holographic research, as notions such as entanglement, quantum complexity, and information recovery have emerged as indispensable in probing the fabric of spacetime itself.

Quantum mechanics departs fundamentally from classical physics through the phenomenon of *entanglement*. While classical intuition suggests that a composite system may be understood by isolating its non-interacting subsystems, analysing them separately, and then recombining the results, this intuition breaks down in the quantum regime. In quantum theory, subsystems may exhibit nonlocal correlations even in the absence of direct interactions. This nonlocality manifests as stronger-than-classical correlations that cannot be explained by any local hidden variable theory, providing a clear departure from classical statistical descriptions. Schrödinger emphasised this point by noting that knowledge of the whole does not entail knowledge of its parts [109].

> *"When two systems, of which we know the states by their respective representatives, enter into temporary physical interaction due to known forces between them, and when after a time of mutual influence the systems separate again, then they can no longer be described in the same way as before, viz. by endowing each of them with a representative of its own. I would not call that 'one' but rather 'the' characteristic trait of quantum mechanics, the one that enforces its entire departure from classical lines of thought. By the interaction the two representatives (or ψ-functions) have become* ***entangled****."*

The Einstein-Podolsky-Rosen (EPR) paradox [110] was an early attempt to highlight this peculiar feature of quantum mechanics, raising the question of whether quantum theory could be considered a complete description of physical reality. Building on these ideas, Bell [111] introduced his famous inequalities to distinguish quantum correlations from any classical local hidden variable theory. Experiments violating Bell inequalities confirmed that entanglement enables correlations exceeding classical bounds, thus establishing that nature cannot be explained by local realism alone.

Over time, entanglement came to be understood as a valuable resource within quantum information theory (QIT). The development of tasks such as quantum teleportation, superdense coding, and secure quantum communication [112] highlighted that entanglement is not merely a curious phenomenon but rather a powerful tool. Indeed, the ability to harness entanglement underpins many advanced quantum technologies, including prospective quantum computers that promise exponential speed-ups for specific classes of problems.

Although the concept of entanglement initially emerged from thinking about finite- dimensional systems such as qubits, it extends well beyond this realm. For instance, topological

field theories in $(2+1)$ dimensions, which seemingly lack local propagating degrees of freedom, can display intricate patterns of *topological order* that become visible through the study of topological entanglement entropy [113]. In more conventional many-body systems, entanglement encodes complicated correlation structures in the ground and low-lying excited states of quantum Hamiltonians, enabling novel ways to characterize and classify quantum phases.

Entanglement has also emerged as a cornerstone in high-energy physics, particularly within the framework of the AdS/CFT correspondence [21], which posits a duality between a gravitational theory in an asymptotically AdS spacetime (the bulk) and a conformal field theory (CFT) defined on its boundary. One of the most striking insights in this context is the Ryu-Takayanagi (RT) proposal [32, 33], subsequently generalised covariantly by Hubeny, Rangamani, and Takayanagi (HRT) [35], which identifies the entanglement entropy of a boundary region with the area of an extremal surface in the bulk. Swingle [114] and Van Raamsdonk [115, 116] expanded upon these ideas to suggest that spacetime geometry might itself emerge from the entanglement patterns of the boundary theory. The suggestive slogan "ER = EPR" [117] captures this provocative viewpoint, positing a deep connection between Einstein-Rosen bridges (wormholes) and entangled states. In sum, entanglement provides a unifying language bridging quantum information, condensed matter, and high-energy physics, shaping our understanding of quantum reality at both the smallest and largest scales.

2.2.1 Entanglement in Quantum Theories

A natural and widely adopted framework for studying entanglement in many-body quantum systems involves discretising space into a lattice, where each site α carries its own local Hilbert space $\mathscr{H}_\alpha$. The total Hilbert space of the system is then given by the tensor product over all lattice sites

$$|\Psi\rangle \in \bigotimes_\alpha \mathscr{H}_\alpha. \tag{2.30}$$

To probe the quantum correlations within such a system, one introduces a bipartition of the lattice into a subset of sites A—which may consist of one or several disjoint blocks—and its complement A^c. This induces a corresponding factorisation of the full Hilbert space

$$\bigotimes_\alpha \mathscr{H}_\alpha \cong \mathscr{H}_A \otimes \mathscr{H}_{A^c}. \tag{2.31}$$

Such a decomposition is foundational in the study of entanglement, as it defines the interface across which quantum correlations are quantified.

Upon restricting attention to region A, we effectively trace over the degrees of freedom residing in A^c, thereby producing a reduced description that captures the entanglement

between the two regions. Given a global pure state $|\Psi\rangle$, the reduced density matrix for A is obtained by tracing out the complement

$$\rho_A = \mathrm{Tr}_{A^c}\left(|\Psi\rangle\langle\Psi|\right). \tag{2.32}$$

While $|\Psi\rangle$ is pure, the reduced state ρ_A will generally be mixed, reflecting a loss of information due to the partial trace. A state is said to be pure when it can be written as $\rho = |\psi\rangle\langle\psi|$, in which case it satisfies $\mathrm{Tr}(\rho^2) = 1$. More generally, a mixed state corresponds to a probabilistic mixture of pure states

$$\rho = \sum_i p_i |\psi_i\rangle\langle\psi_i|, \quad \sum_i p_i = 1, \tag{2.33}$$

with $\mathrm{Tr}(\rho^2) < 1$ characterising the presence of classical or quantum uncertainty.

The most fundamental measure of bipartite entanglement in this setting is the von Neumann entropy of the reduced density matrix ρ_A

$$S_A = -\mathrm{Tr}(\rho_A \log \rho_A). \tag{2.34}$$

If we diagonalize ρ_A with eigenvalues λ_i, this entropy admits the explicit expression

$$S_A = -\sum_i \lambda_i \log \lambda_i, \tag{2.35}$$

making clear that entanglement is intimately tied to the spectrum of ρ_A. For global pure states, the entanglement entropy is symmetric under exchange of subsystems: $S_A = S_{A^c}$. This property reflects the mutual nature of entanglement between A and its complement.

In the specific case of a bipartite Hilbert space $\mathscr{H}_A \otimes \mathscr{H}_B$, a pure state $|\psi\rangle$ is called *separable* if it factorises as $|\psi\rangle = |\psi_A\rangle \otimes |\psi_B\rangle$. Otherwise, the state is entangled. Any such pure bipartite state admits a Schmidt decomposition

$$|\psi\rangle = \sum_i \lambda_i |i_A\rangle \otimes |i_B\rangle, \tag{2.36}$$

where the $|i_A\rangle$ and $|i_B\rangle$ form orthonormal bases for subsystems A and B, respectively. The real, non-negative Schmidt coefficients λ_i satisfy the normalisation condition $\sum_i \lambda_i^2 = 1$. The entanglement entropy is then computed from the squared Schmidt coefficients, which correspond to the eigenvalues of the reduced density matrix, confirming that the entanglement structure of pure states is entirely encoded in their Schmidt spectra.

Rényi Entropies, Modular Hamiltonians, and Scaling of Entanglement

The quantitative study of entanglement in quantum systems extends far beyond the von Neumann entropy. A central family of entanglement measures is given by the Rényi entropies,

$$S_A^{(q)} \;=\; \frac{1}{1-q}\log \mathrm{Tr}\Big(\rho_A^q\Big), \tag{2.37}$$

which, as the parameter q approaches 1, reduce to the familiar von Neumann entropy. Since different values of q emphasize different parts of the eigenvalue spectrum of the reduced density matrix ρ_A, the Rényi entropies serve as versatile diagnostic tools that are often more tractable analytically or numerically, and can signal phase transitions or capture subtle aspects of topological order.

A related and illuminating concept is that of the *modular Hamiltonian*, defined by

$$K_A \;=\; -\log \rho_A, \tag{2.38}$$

so that the reduced density matrix takes the form of a thermal state at unit temperature

$$\rho_A \;=\; \frac{e^{-K_A}}{\mathrm{Tr}(e^{-K_A})}. \tag{2.39}$$

From this viewpoint, the expression for the Rényi entropy becomes

$$S_A^{(q)} \;=\; \frac{1}{1-q}\log \mathrm{Tr}\Big(e^{-qK_A}\Big), \tag{2.40}$$

which closely resembles a free-energy-like quantity. Insights into the structure of K_A not only deepen our understanding of how information is encoded in a given subsystem but also establish connections between entanglement and thermodynamics.

In the realm of many-body physics, it is well established that ground states of local, gapped Hamiltonians frequently exhibit an *area law*, meaning that their entanglement entropy scales with the surface area (or the perimeter in lower dimensions) of the subsystem rather than its volume. This behaviour is intuitively understood as a consequence of the typically exponential decay of correlations in such systems, ensuring that only degrees of freedom near the boundary of A contribute significantly to the entanglement. Nevertheless, there are notable exceptions. In systems at criticality—where correlations decay only algebraically—the entanglement entropy may display logarithmic growth, as observed in $(1+1)$-dimensional conformal field theories. Moreover, topologically ordered phases can produce subleading corrections that carry essential topological information. Hence, the scaling behaviour of

entanglement provides a powerful diagnostic for identifying and characterising novel phases of matter.

When transitioning from discrete lattice models to continuum quantum field theories (QFTs), one typically considers a partition of a Cauchy slice Σ into a region A and its complement. In continuum settings, the entanglement entropy often diverges in the ultraviolet (UV) due to the infinite number of degrees of freedom at arbitrarily short distances. A standard way to regulate these divergences is by introducing a short-distance cutoff ϵ_{UV}. The leading divergence in the entanglement entropy then commonly scales with the area of the boundary ∂A of the region, mirroring the area-law behaviour observed in lattice systems.

Entanglement in Continuum Quantum Field Theories

While the discussion above addressed bipartite entanglement in systems with finite-dimensional Hilbert spaces, extending these notions to quantum field theories (QFTs) introduces significant conceptual challenges. In continuum theories, the Hilbert space is inherently infinite-dimensional—an expression of the infinitely many degrees of freedom present at every point in space. As a result, the naïve tensor product factorisation, $\mathscr{H} \neq \mathscr{H}_A \otimes \mathscr{H}_B$, which underpins the standard treatment of entanglement in lattice systems, becomes problematic. Furthermore, in relativistic QFTs one encounters modes at arbitrarily short distances, thereby complicating the definition of a sharply localised entangling surface.

A key consequence of these ultra-violet (UV) modes is that the entanglement entropy in QFTs generally exhibits a universal UV divergence. To control these divergences, one typically introduces a short-distance cutoff, denoted by ϵ_{UV}, which effectively renders the local Hilbert spaces finite-dimensional. This regularisation allows for the extension of many entanglement properties familiar from finite systems into the continuum, even though the removal of the cutoff would cause the entanglement entropy to diverge. Importantly, the structure of these divergences encodes deep information about the underlying QFT.

UV Divergences and Area Laws in d Dimensions For a QFT in its ground state in d dimensions, it has been established that the entanglement entropy of a spatial subregion A obeys an area law. In particular, one finds

$$S(\rho_A) \;=\; c\,\frac{\mathrm{Area}(\partial A)}{\epsilon_{\mathrm{UV}}^{d-2}} \;+\; \mathscr{O}\Big(\epsilon_{\mathrm{UV}}^{d-1}\Big), \tag{2.41}$$

where ∂A denotes the entangling surface and c is a numerical constant. In a scale-invariant theory, the divergence can be expressed in terms of the dimensionless ratio $L_A/\epsilon_{\mathrm{UV}}$, where L_A is the characteristic size of A, so that the leading divergence scales as $\Big(L_A/\epsilon_{\mathrm{UV}}\Big)^{d-2}$.

In odd spacetime dimensions, the entanglement entropy admits an expansion of the form

$$S(\rho_A) \;=\; c_{d-2}\left(\frac{L_A}{\epsilon_{\mathrm{UV}}}\right)^{d-2} \;+\; c_{d-4}\left(\frac{L_A}{\epsilon_{\mathrm{UV}}}\right)^{d-4} \;+\cdots+\; (-1)^{\frac{d-1}{2}}\, c_{\mathrm{odd}} \;+\; \mathscr{O}\Big(\epsilon_{\mathrm{UV}}\Big), \quad (2.42)$$

where c_{odd} is a universal, regulator-independent constant. In contrast, in even spacetime dimensions one obtains

$$S(\rho_A) \;=\; c_{d-2}\left(\frac{L_A}{\epsilon_{\mathrm{UV}}}\right)^{d-2} + c_{d-4}\left(\frac{L_A}{\epsilon_{\mathrm{UV}}}\right)^{d-4} +\cdots+ (-1)^{\frac{d-2}{2}}\, c_{\mathrm{even}}\, \log\Big(\frac{L_A}{\epsilon_{\mathrm{UV}}}\Big) \;+\; \mathscr{O}\Big(\epsilon_{\mathrm{UV}}\Big). \quad (2.43)$$

Here, the coefficient c_{even} multiplies a characteristic logarithmic divergence. These universal coefficients, c_{odd} and c_{even}, are often identified with the central charges of the theory and encapsulate intrinsic, UV-insensitive physical information.

The Special Case of $d = 2$ CFTs

Two-dimensional conformal field theories (CFTs) stand out due to the powerful constraints imposed by conformal invariance. In $d = 2$, instead of obeying an area law, the entanglement entropy exhibits a universal logarithmic divergence. Exploiting methods such as the replica trick, one can compute the Rényi entropies for the vacuum state exactly:

$$S^{(\alpha)}(\rho_A) \;=\; \frac{c}{6}\,\frac{\alpha+1}{\alpha}\;\log\Big(\frac{L_A}{\epsilon_{\mathrm{UV}}}\Big), \quad (2.44)$$

where c is the central charge of the CFT. Analytic continuation in the Rényi index α yields the von Neumann entropy,

$$S(\rho_A) \;=\; \frac{c}{3}\,\log\Big(\frac{L_A}{\epsilon_{\mathrm{UV}}}\Big). \quad (2.45)$$

This logarithmic scaling is a hallmark of two-dimensional field theories and underpins many of the significant results discussed in Chapters 3 and 4.

Beyond serving as a computational tool, entanglement measures have proven crucial in unveiling the structural properties of QFTs. A prominent example is the irreversibility of renormalisation group (RG) flows: in $d = 2$, Zamolodchikov's c-theorem asserts that the central charge decreases monotonically along RG flows. More recent work by Casini and Huerta has provided an alternative demonstration based on the strong subadditivity of entanglement entropy, a method that generalises to $d = 3$ and forms the basis for the F-theorem. Ongoing efforts continue to extend these entanglement-based approaches to higher dimensions, highlighting the deep interplay between quantum information theory and the fabric of quantum field theories.

2.2.2 Entanglement in Holography

Entanglement, being a cornerstone of quantum mechanics, quantum field theories, and especially conformal field theories (CFTs), naturally prompts us to inquire whether its universal characteristics can be realised as a gravitational dual. In holographic CFTs—typically distinguished by a large central charge or, equivalently, a large rank N of the gauge group—one expects that certain quantum informational measures should have geometric counterparts in the bulk. It is, however, crucial to note that only a subset of states in the CFT, namely those with well-defined bulk duals, correspond to classical geometric configurations.

A landmark result bridging these two perspectives is encapsulated in the Ryu-Takayanagi (RT) prescription. According to this proposal, for a subregion A of a d-dimensional holographic CFT, the entanglement entropy is determined by the area of a codimension-2 extremal surface γ_A in the $(d+1)$-dimensional bulk, via

$$S(\rho_A) \;=\; \frac{\mathrm{Area}(\gamma_A)}{4\,G_N^{(d+1)}}\,, \tag{2.46}$$

where $G_N^{(d+1)}$ is Newton's constant in the bulk. Here, γ_A is required to be homologous to the boundary region A (i.e., $\partial\gamma_A = \partial A$) and, in the event multiple extremal surfaces exist, the one with the minimal area is selected. Because the surface γ_A extends deep into the AdS bulk, its area typically exhibits divergences near the boundary that parallel the UV divergences encountered in the corresponding field theory.

This geometric picture not only supplies a direct method to compute entanglement entropy but also unifies it with black hole thermodynamics. For instance, when the entangling region A is taken to be the entire boundary of a static black hole geometry, the appropriate RT surface simply wraps the event horizon, thereby reproducing the Bekenstein-Hawking entropy,

$$S_{\mathrm{BH}} = \frac{k_B c^3 A}{4\hbar G_N} \propto \frac{A}{4\,G_N}, \tag{2.2}$$

where k_B is Boltzmann's constant, c is the speed of light, and G_N is Newton's gravitational constant. Since $G_N \propto l_{\mathrm{p}}^2$, this expression implies that the entropy of a black hole is determined by its surface area measured in Planck units.

To illustrate these ideas concretely, consider an $\mathrm{AdS}_3/\mathrm{CFT}_2$ setup. In one scenario (schematically depicted in Fig. 2.3a), A represents a connected interval on a constant-time slice of the boundary, and the corresponding minimal surface γ_A (shown in blue) extends into the bulk. In the presence of a black hole, if one chooses A to cover the entire boundary circle S^1, then the minimal surface wraps the black hole horizon (indicated by the dotted green line), thus encoding the horizon's entropy.

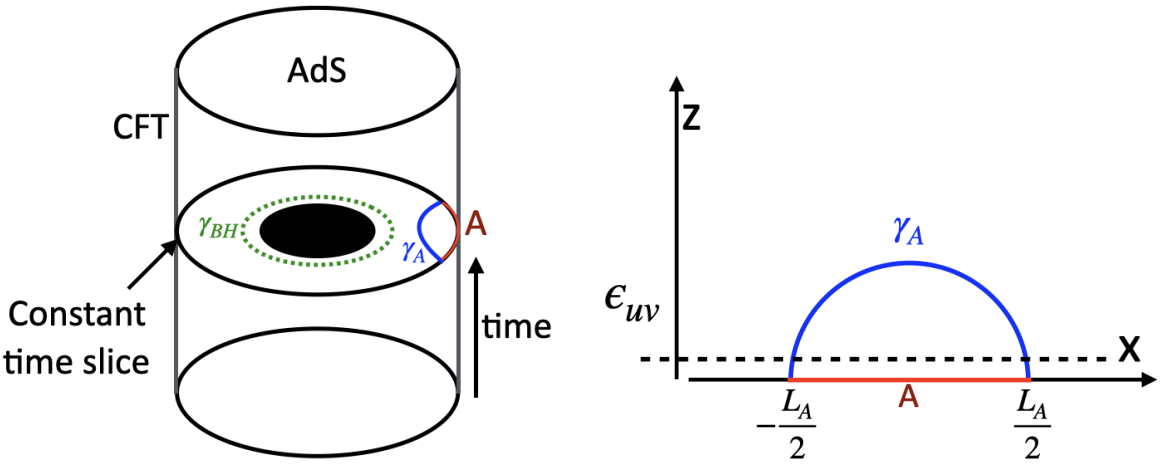

Figure 2.3: Left: Illustration of the Ryu–Takayanagi (RT) prescription for calculating holographic entanglement entropy using equation (2.63) in the context of AdS_3/CFT_2, possibly with a black hole in the bulk. We consider a static spacetime such that the RT surface γ_A (shown in blue) lies on a constant-time slice of AdS, while the entangling region A (in red) corresponds to a connected interval on the boundary circle of the CFT. When the entangling region covers the entire circle, i.e., $A = S^1$, and a black hole is present, the minimal RT surface γ_{BH} (dotted green) wraps the horizon and yields the Bekenstein–Hawking entropy via equation (2.2). **Right:** Diagram representing the RT computation in pure AdS_3 using Poincaré coordinates, with a UV cutoff ϵ_{UV}. The entangling region A is defined by the interval $x \in [-L_A/2, L_A/2]$, and the corresponding RT surface γ_A—a geodesic—extends into the bulk along the holographic direction z. This setup leads to the entanglement entropy given in equation (2.65), which matches the result of equation (2.62). Figure adapted from [118].

A more detailed example is provided in Fig. 2.3b, where empty AdS_3 is described using Poincaré coordinates with an explicit UV cutoff ϵ_{UV}. Here, the entangling region is defined as the interval $x \in \left[-\frac{L_A}{2}, \frac{L_A}{2}\right]$, and the RT surface is the geodesic anchored at the boundary endpoints $\partial A = \{-L_A/2,\ L_A/2\}$. Exploiting time-translation symmetry in static configurations allows us to place the geodesic on a constant-time slice, so its "area" reduces to its length

$$|\gamma_A| = 2\,\ell\,\ln\!\left(\frac{L_A}{\epsilon_{\text{UV}}}\right). \tag{2.47}$$

Substituting this into Eq. (2.63) yields

$$S(\rho_A) \;=\; \frac{\ell}{2\,G_N^{(3)}}\,\ln\!\left(\frac{L_A}{\epsilon_{\text{UV}}}\right), \tag{2.48}$$

and by invoking the Brown-Henneaux relation $c = \frac{3\ell}{2\,G_N^{(3)}}$, one obtains

$$S(\rho_A) \;=\; \frac{c}{3}\,\ln\!\Big(\frac{L_A}{\epsilon_{\mathrm{UV}}}\Big), \tag{2.49}$$

which coincides precisely with the entanglement entropy derived directly within a two-dimensional CFT (cf. Eq. (2.45)). This striking match not only demonstrates the efficacy of the holographic approach but also underscores how a geometric calculation in the bulk reproduces the universal UV behaviour found in the dual field theory.

In summary, the RT prescription not only provides a powerful computational tool for determining entanglement entropy in holographic CFTs but also exemplifies the deep interplay between quantum information theory and gravitational dynamics in the framework of AdS/CFT.

2.2.3 Quantum Discord and the Quantum-Classical Boundary

Quantum correlations lie at the heart of quantum information theory. Entanglement entropy, introduced in the last section, offers a precise measure of quantum correlations for *pure* bipartite states. However, when dealing with *mixed* states, entanglement entropy captures both classical ad quantum correlations present—classical correlations become intertwined with the quantum ones, creating subtleties absent in pure-state scenarios. To address this deficiency, the concept of *quantum discord* was introduced in Refs. [119–121] as a measure capable of detecting quantum correlations even in the absence of entanglement. Quantum discord can be viewed as the most general identifier of "non-classical" correlations, reducing to other well-known measures (e.g. negativity, entanglement of formation) in specific limits.

In fact, the significance of quantum discord goes beyond pure bipartite states: even separable (i.e. non-entangled) mixed states can exhibit certain quantum features that are otherwise overlooked by entanglement measures [122]. This broader recognition that "quantumness" persists in mixed states has spurred intense interest in quantum discord, its operational meanings, and its potential applications—even in contexts such as holography, where a complete role for quantum discord remains open-ended. Figure 2.6a sketches a hierarchy of quantum correlation measures, highlighting that quantum discord $Q(\rho)$ is generally nonzero for a strictly larger set of mixed states than those captured by entanglement measures alone.

Classical versus Quantum Correlations

Before introducing quantum discord, it is instructive to review the basic distinctions between classical and quantum correlations. These differences emerge already when comparing

classical random variables with quantum states, and they underscore why quantum systems can exhibit correlations that have no classical counterpart.

A discrete classical system of dimension d is described by a probability distribution $\mathbf{p} = \{p_i\}_{i=1}^{d}$ defined over a phase space with d distinct outcomes. In this framework, observables are simply real-valued functions, and the measurement of an observable f yields the expectation value $\sum_i p_i f_i$. When considering a bipartite classical system with subsystems A and B, the joint state is given by a probability distribution $\mathbf{p}^{AB} = \{p_{ij}\}$ on the Cartesian product of the individual phase spaces. The marginal distributions for each subsystem, $\mathbf{p}^A$ and $\mathbf{p}^B$, are obtained by summing over the appropriate complementary indices. By contrast, a quantum system of dimension d is represented by a density operator ρ acting on a d-dimensional Hilbert space. Observables are Hermitian operators O, and the expectation value in the state ρ is computed as $\mathrm{Tr}(\rho\, O)$. Pure quantum states are given by projectors $|\psi\rangle\langle\psi|$ while mixed states appear as convex combinations of pure states. The intrinsic non-commutative nature of quantum observables, along with the superposition principle, endows quantum systems with richer correlation structures compared to classical ones.

For a composite quantum system with subsystems A and B having Hilbert spaces $\mathscr{H}^A$ and $\mathscr{H}^B$, the joint state resides in the tensor product space $\mathscr{H}^{AB} = \mathscr{H}^A \otimes \mathscr{H}^B$. A state ρ^{AB} is termed *separable* if it can be expressed as a convex combination of product states,

$$\rho^{AB} = \sum_i p_i\, \rho_i^A \otimes \rho_i^B, \tag{2.50}$$

which is indicative of classical correlations between the subsystems. If no such decomposition exists, the state is *entangled* and exhibits quantum correlations that can exceed classical bounds. Notably, even separable states can sometimes possess signatures of non-classicality, highlighting that entanglement is not the sole source of quantum correlations.

Three Relevant Classes of Bipartite States. A particularly useful classification of bipartite states ρ^{AB} distinguishes the degree to which each subsystem carries classical or quantum information [123, 124]:

- *Classical-Classical (c-c) States:* Both subsystems are described by orthonormal bases of classical states. These states can be written as

$$\chi^{(\mathrm{c-c})} = \sum_{m,n} \lambda_{mn} \left|\phi_m^A\right\rangle\!\left\langle\phi_m^A\right| \otimes \left|\phi_n^B\right\rangle\!\left\langle\phi_n^B\right|,$$

  and they exhibit purely classical correlations (with zero quantum discord).

- *Quantum-Classical (q-c) or Classical-Quantum (c-q) States:* In these states, one

subsystem (say, B) is represented by a classical basis while the other subsystem (A) is allowed to be in a general quantum state. They take the form

$$\chi^{(\mathrm{q-c})} \;=\; \sum_m \lambda_m \, \rho_m^A \otimes \left|\phi_m^B\right\rangle\!\left\langle\phi_m^B\right|,$$

or, equivalently, one may define the corresponding classical-quantum (c-q) states with the roles reversed. In either case, the resulting quantum discord vanishes.

- *Quantum-Quantum (q-q) States:* This is the most general category, where both subsystems are in arbitrary quantum states. Such states are expressed as

$$\chi^{(\mathrm{q-q})} \;=\; \sum_{m,n} \lambda_{mn} \; \rho_m^A \otimes \rho_n^B.$$

Typically, these states exhibit nonzero quantum discord, reflecting intrinsic quantum correlations beyond mere entanglement.

Schematic representations, such as that in Figure 2.6b, illustrate the hierarchical inclusion $(\mathrm{c}-\mathrm{c}) \subset (\mathrm{q}-\mathrm{c})/(\mathrm{c}-\mathrm{q}) \subset (\mathrm{q}-\mathrm{q})$, signifying that only the classical-classical states are devoid entirely of quantum correlations.

Two Paths to Mutual Information and the Origin of Discord

In classical information theory [125], the notion of mutual information quantifies how much the knowledge of one random variable reduces the uncertainty about another. One standard definition is

$$I(A:B) \;=\; H(A) + H(B) - H(A,B), \tag{2.51}$$

where $H(\cdot)$ denotes the Shannon entropy. Equivalently, this can be expressed as

$$I(A:B) \;=\; H(A) - H(A \mid B), \tag{2.52}$$

with $H(A \mid B)$ representing the conditional entropy – that is, the residual uncertainty about A once B is known. In the classical realm, these two formulations are equivalent and capture the full extent of the correlations between A and B.

When one moves to quantum systems, probabilities are replaced by density matrices and Shannon entropy by the von Neumann entropy. A direct analogue of Eq. (2.71) then defines the *quantum mutual information* as

$$I(A:B)_\rho \;=\; S(\rho_A) + S(\rho_B) - S(\rho_{AB}), \tag{2.53}$$

which encompasses all correlations—both classical and quantum—present in the bipartite state ρ_{AB}. However, the second classical form, Eq. (2.72), does not translate straightforwardly into the quantum context because the concept of conditional entropy becomes ambiguous when measurements, which generally disturb the state, are involved.

One way to resolve this ambiguity is by acknowledging that gaining information about a quantum system invariably requires performing a measurement. For a bipartite state ρ_{AB}, consider a complete set of rank-one projectors $\{\Pi_k^B\}$ acting on subsystem B. Upon measuring B, the probability for obtaining outcome k is given by

$$q_k \;=\; \mathrm{Tr}\Big[(\mathbb{I}_A \otimes \Pi_k^B)\,\rho_{AB}\,(\mathbb{I}_A \otimes \Pi_k^B)^\dagger\Big], \tag{2.54}$$

and the corresponding post-measurement state of A becomes

$$\rho_k^A \;=\; \frac{1}{q_k}\,\mathrm{Tr}_B\Big[(\mathbb{I}_A \otimes \Pi_k^B)\,\rho_{AB}\,(\mathbb{I}_A \otimes \Pi_k^B)^\dagger\Big]. \tag{2.55}$$

Based on this, one defines the *quantum conditional entropy* by minimising over all such local projective measurements on B

$$S(A \mid B) \;=\; \min_{\{\Pi_k^B\}\in\mathscr{M}^B} \sum_k q_k\, S(\rho_k^A). \tag{2.56}$$

This minimisation procedure reflects the optimal strategy for learning about subsystem A while causing minimal disturbance due to the measurement on B.

Consequently, one may define an alternative, measurement-induced mutual information as

$$J(A:B) \;=\; S(\rho_A) - S(A \mid B), \tag{2.57}$$

which captures the *classical* correlations that can be locally extracted by measuring B. By its very construction, the conventional quantum mutual information in Eq. (2.73) includes all correlations, so their difference isolates the purely quantum contributions

$$Q(A:B) \;=\; I(A:B) - J(A:B). \tag{2.58}$$

This quantity $Q(A:B)$ is known as the *quantum discord* [119–121] and is intrinsically asymmetric, meaning that the value depends on whether one measures B or A. Notably, for pure bipartite states, the discord reduces to the von Neumann entanglement entropy, while for mixed states it reveals the presence of quantum correlations that can exist even when the state is separable.

Several important properties follow:

- *Non-negativity:* $Q(A:B) \geq 0$, with equality if and only if the state is classical-quantum (or equivalently, quantum-classical) from the perspective of the measured subsystem. In particular, $Q(A:B) = 0$ for states belonging to the sets $\Omega^{(\mathrm{q-c})}$ or $\Omega^{(\mathrm{c-q})}$, as well as for fully classical-classical $(\mathrm{c-c})$ states.

- *Equivalence with Entanglement Entropy in Pure States:* For pure states ρ_{AB}, the quantum discord coincides with the von Neumann entropy of either reduced density matrix, thus mirroring the fact that in pure bipartite systems, entanglement completely accounts for quantum correlations.

- *Generality:* Unlike entanglement measures based solely on separability, quantum discord can be nonzero for separable mixed states. This demonstrates that discord captures a broader class of quantum correlations beyond those signified by entanglement alone.

2.3 Quantum Dynamics and Complexity

Building on our discussion of holographic duality and entanglement measures, we now focus on the dynamics of quantum complexity using Krylov subspace techniques. Originally introduced by Aleksey N. Krylov in 1931 [56] and later independently refined by Cornelius Lanczos [126], these methods construct an orthonormal basis by repeatedly applying a matrix (or Hamiltonian) to a reference vector, thereby reducing high-dimensional problems to tractable Krylov subspaces. Such strategies are indispensable in large-scale scientific computing, efficiently addressing linear systems, eigenvalue problems, and spectral estimates for sparse or structured matrices [57, 127, 128].

Interest in Krylov methods has surged due to their successful applications in understanding quantum ergodicity, nonequilibrium thermalisation, and quantum chaos [129, 129–131]. In the context of quantum many-body dynamics, the iterative application of the Hamiltonian or Liouvillian naturally generates a reduced Krylov space that captures essential features of operator spreading and time evolution. This approach, often referred to as the recursion method [132–134], not only bypasses full diagonalisation of exponentially large Hilbert spaces but also provides a quantitative framework for assessing operator growth. A seminal development in this context emerged in Ref. [135], where the authors formulated an *operator growth hypothesis* that correlates the structure of Krylov subspaces with the spectral properties distinguishing integrable, nonintegrable, and chaotic dynamics. In that work, they introduced *Krylov complexity* as a quantitative measure of how an initially simple operator spreads within the operator space, providing a means to bound a potential quantum Lyapunov exponent. More recently, Ref. [55] extended these ideas to the Schrödinger evolution of quantum states, demonstrating that an optimal choice of Krylov basis minimizes complexity. This measure,

termed *spread complexity*, quantitatively captures the dispersion of an initial state under the evolution governed by the system Hamiltonian. In the following part, we detail the mathematical foundations underlying Krylov subspace methods. This review provides the backbone for our later discussions on operator growth and spread complexity, and it will be particularly valuable in the second half of the thesis.

2.3.1 Time Evolution and the Krylov Basis

One of the key objectives in studying quantum many-body dynamics is to understand how an initially simple object—a state $|\psi(0)\rangle$ or an operator $\hat{O}(0)$—spreads in its respective Hilbert space (or space of operators) as time evolves under a Hamiltonian $\hat{H}$. A particularly natural and computationally efficient way to track this process is by constructing the so-called *Krylov basis*, sometimes referred to via the Lanczos approach. This basis spans precisely the subspace that is dynamically accessed under time evolution of the chosen initial state or operator.

Although the Krylov basis is not unique, its construction is guided by applying the Gram–Schmidt orthogonalisation procedure to successively generated vectors (or nested commutators) of the Hamiltonian. The resulting framework not only offers insight into the system's dynamics but also provides a foundation for defining measures of complexity, particularly *Krylov complexity*. In what follows, we first review the Schrödinger and Heisenberg pictures of quantum mechanics, then outline the Lanczos algorithm for states and operators, and finally discuss universal growth bounds in operator dynamics.

Schrödinger and Heisenberg Pictures

Quantum mechanics admits several mathematically equivalent formulations. Two of the most commonly employed frameworks are the *Schrödinger picture* and the *Heisenberg picture*. In the Schrödinger picture, the state vectors $|\psi(t)\rangle$ encapsulate the full time dependence of the system, evolving according to the time-dependent Schrödinger equation, while observables remain fixed. In contrast, in the Heisenberg picture the time dependence is shifted to the observables $O(t)$ that evolve via the Heisenberg equation of motion, with the quantum states remaining constant. Despite these differing assignments of time dependence, both pictures ultimately yield the same physical predictions and measurable outcomes, underscoring the internal consistency and versatility of the quantum formalism.

Schrödinger Picture In the Schrödinger picture, the time evolution of an initial normalised state $|\psi(t_0)\rangle$ at $t = t_0$ is governed by the Schrödinger equation

$$i\hbar \frac{\partial}{\partial t} |\psi(t)\rangle \;=\; \hat{H}\; |\psi(t)\rangle\,. \tag{2.59}$$

For a time-independent Hamiltonian, the solution can be written as

$$|\psi(t)\rangle \;=\; \hat{U}_{t-t_0}\; |\psi(t_0)\rangle \;=\; e^{-\,i\,\hat{H}\,(t-t_0)}\; |\psi(t_0)\rangle\,, \tag{2.60}$$

where $\hat{U}_{t-t_0} = e^{-i\hat{H}(t-t_0)}$ is the unitary time-evolution operator. Setting $t_0 = 0$ for simplicity and expanding the exponential yields

$$|\psi(t)\rangle \;=\; \sum_{n=0}^{\infty} \frac{(-\,i\,t)^n}{n!}\, \hat{H}^{\,n}\; |\psi(0)\rangle \;=\; \sum_{n=0}^{\infty} \frac{(-\,i\,t)^n}{n!}\; |\psi_n\rangle\,, \tag{2.61}$$

with $|\psi_n\rangle = \hat{H}^{\,n}\; |\psi(0)\rangle$. This series reveals that repeated applications of $\hat{H}$ generate the directions in Hilbert space accessible to $|\psi(0)\rangle$ over time.

Heisenberg Picture In the Heisenberg picture the roles are reversed: states are fixed (up to initial preparation) and operators $\hat{O}(t)$ carry the time dependence. The operator evolution is governed by

$$i\hbar \frac{d}{dt}\, \hat{O}(t) \;=\; i\hbar \frac{\partial}{\partial t}\, \hat{O}(t) \;+\; \Big[\hat{O}(t),\, \hat{H}\Big]. \tag{2.62}$$

Neglecting any intrinsic time dependence of $\hat{O}$, the solution (with $\hbar = 1$) is given by

$$\hat{O}(t) \;=\; \hat{U}_t^{\dagger}\, \hat{O}\, \hat{U}_t \;=\; e^{\,i\,\hat{H}\,t}\, \hat{O}\, e^{-\,i\,\hat{H}\,t}. \tag{2.63}$$

Both pictures yield the same expectation values. For example, if $|\psi(t)\rangle_S$ denotes the Schrödinger-picture state and $\hat{O}(t)_H$ the Heisenberg-picture operator, then

$$\langle\psi(t)|\, \hat{O}\, |\psi(t)\rangle_S \;=\; \langle\psi(0)|\, e^{\,i\,\hat{H}\,t}\, \hat{O}\, e^{-\,i\,\hat{H}\,t}\, |\psi(0)\rangle \;=\; \langle\psi|\, \hat{O}(t)\, |\psi\rangle_H.$$

Thus, the choice of picture is one of convenience. The Baker–Haussdorff lemma is crucial for rewriting the time-evolved operator

$$\hat{O}(t) = e^{\,i\,\hat{H}\,t}\, \hat{O}\, e^{-\,i\,\hat{H}\,t}$$

as an infinite series of nested commutators

$$e^{\hat{B}}\,\hat{A}\,e^{-\hat{B}} \;=\; \hat{A} \;+\; \Big[\hat{B},\,\hat{A}\Big] \;+\; \frac{1}{2!}\Big[\hat{B},\,[\hat{B},\,\hat{A}]\Big] \;+\; \frac{1}{3!}\Big[\hat{B},\,[\hat{B},\,[\hat{B},\,\hat{A}]]\Big] \;+\; \ldots. \tag{2.64}$$

This allows us to express

$$\hat{O}(t) \;=\; \sum_{n=0}^{\infty} \frac{(i\,t)^n}{n!}\,\tilde{O}_n, \tag{2.65}$$

where $\tilde{O}_n$ represents the n-fold nested commutator of $\hat{O}$ with $\hat{H}$. In this way, the analogy between state and operator evolution becomes manifest when operators are viewed as vectors in an appropriate auxiliary space.

2.3.2 Krylov State Basis and Spread Complexity

We begin by applying the Lanczos algorithm to the set of vectors $\left\{\hat{H}^n\,|\psi(0)\rangle\right\}_{n=0}^{\infty}$, generated by the Hamiltonian $\hat{H}$ acting on the normalised initial state $|\psi(0)\rangle$. Owing to the hermiticity of $\hat{H}$, we can freely move $\hat{H}$ between the ket and bra, a property that will significantly streamline the construction of the Krylov basis.

In the state picture, we construct the Krylov subspace by repeatedly applying the Hamiltonian to $|\psi(0)\rangle$ and then orthogonalising the resulting set via the Gram–Schmidt procedure. By convention, we label the initial basis vector as $|K_0\rangle \equiv |\psi(0)\rangle$.

The next vector is generated by acting with $\hat{H}$ on $|K_0\rangle$ and then removing the component along $|K_0\rangle$ itself,

$$|z_1\rangle = \hat{H}\,|K_0\rangle - a_0\,|K_0\rangle\,, \quad \text{with} \quad a_0 = \langle K_0|\hat{H}|K_0\rangle. \tag{2.66}$$

Normalising this, we set

$$|K_1\rangle = \frac{|z_1\rangle}{\sqrt{\langle z_1|z_1\rangle}}. \tag{2.67}$$

Proceeding in this manner, one would normally subtract projections onto all previously constructed vectors; however, the power of the Lanczos algorithm lies in its recursion relation, which requires only the two most recent orthonormal vectors. Specifically, one proves by induction that the iterative step can be written as

$$|z_{n+1}\rangle = \Big(\hat{H} - a_n\Big)\,|K_n\rangle - b_n\,|K_{n-1}\rangle\,, \quad |K_{n+1}\rangle = \frac{|z_{n+1}\rangle}{b_{n+1}}, \quad \langle K_n|K_m\rangle = \delta_{nm}, \tag{2.68}$$

with the Lanczos coefficients defined by

$$a_n = \langle K_n|\hat{H}|K_n\rangle, \qquad b_n = \sqrt{\langle z_n|z_n\rangle}, \quad \text{with } b_0 \equiv 0. \tag{2.69}$$

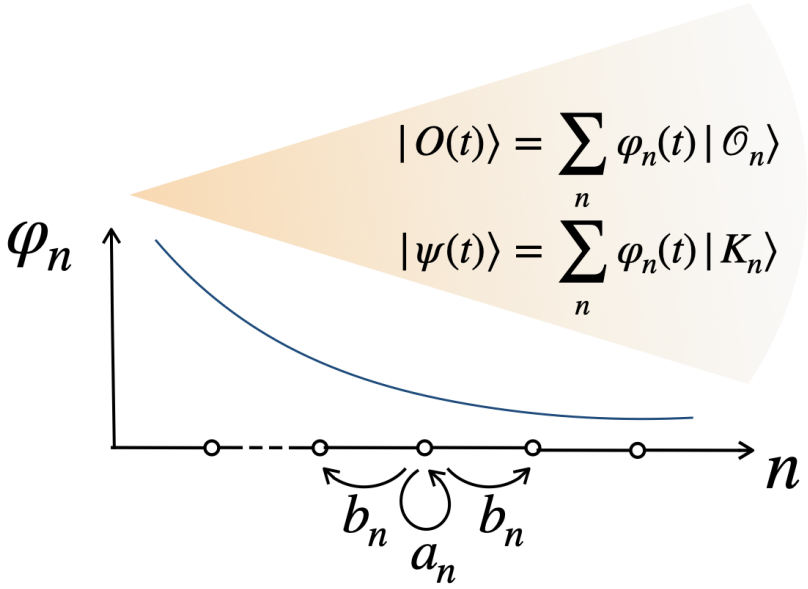

Figure 2.4: Effective one-dimensional Krylov chain representation of quantum dynamics: The time-evolved state $|\psi(t)\rangle$, or an operator state $|O(t)\rangle$ in the context of operator dynamics, can be expressed as a superposition over an orthonormal Krylov basis $\{|K_n\rangle\}$ (or operator basis $\{|\mathcal{O}_n\rangle\}$), with time-dependent amplitudes $\varphi_n(t)$. These amplitudes evolve according to a tight-binding-like recursion relation governed by the Lanczos coefficients a_n (on-site potentials) and b_n (nearest-neighbor hopping amplitudes), reflecting the tridiagonal form of the Hamiltonian in the Krylov basis. The illustration captures this effective dimensional reduction: an originally high-dimensional quantum system is mapped to a one-dimensional chain where complexity and spreading are encoded in the profile of $\varphi_n(t)$ across sites labeled by Krylov depth n. A hypothetical probability distribution is sketched on this figure.

An alternative form of the recursion, which demonstrates the tridiagonal structure of $\hat{H}$ in the Krylov basis, is given by

$$\hat{H}\,|K_n\rangle = a_n\,|K_n\rangle + b_{n+1}\,|K_{n+1}\rangle + b_n\,|K_{n-1}\rangle\,. \tag{2.70}$$

This relation implies that the matrix elements $H_{nm} := \langle K_n|\hat{H}|K_m\rangle$ form a tridiagonal matrix with diagonal entries a_n and off-diagonals b_n. Remarkably, this mapping is far more than a formal convenience—it encodes a powerful dimensional reduction: any quantum system, regardless of the complexity or dimensionality of its Hilbert space, is effectively projected onto a *one-dimensional tight-binding chain*, with the Lanczos coefficients a_n and b_n acting as local on-site potentials and nearest-neighbor hopping amplitudes, respectively (see Fig. 2.4). This Krylov chain captures the full dynamics of the initial state under the Hamiltonian $\hat{H}$, allowing for a compressed yet faithful description of quantum evolution.

It is important to note that the set $\{\hat{H}^n\,|\psi(0)\rangle\}$ may not be linearly independent. In such cases, the recursive process terminates after a finite number of steps, say L; the resulting

Krylov basis then spans an L-dimensional subspace of the Hilbert space that captures the part explored by the time evolution.

The true power of this construction becomes apparent when one expresses the time-evolved state in this basis. In the Schrödinger picture, the state evolves according to $|\psi(t)\rangle = e^{-i\hat{H}t}\,|\psi(0)\rangle$. Expanding $|\psi(t)\rangle$ in the Krylov basis,

$$|\psi(t)\rangle = \sum_{n=0}^{L-1} \phi_n(t)\ |K_n\rangle\,, \tag{2.71}$$

the coefficients $\phi_n(t)$ represent the probability amplitudes for the state to be found in each basis vector, satisfying the normalisation condition $\sum_{n=0}^{L-1} |\phi_n(t)|^2 = 1$. Substituting the expansion (2.71) into the Schrödinger equation,

$$i\frac{\partial}{\partial t}\,|\psi(t)\rangle = \hat{H}\,|\psi(t)\rangle\,, \tag{2.72}$$

and using the tridiagonal form (2.70) for $\hat{H}\,|K_n\rangle$, we obtain a set of coupled differential equations for the amplitudes

$$i\,\frac{\partial \phi_n(t)}{\partial t} = a_n\,\phi_n(t) + b_{n+1}\,\phi_{n+1}(t) + b_n\,\phi_{n-1}(t). \tag{2.73}$$

Here, we adopt the convention that $\phi_{-1}(t) = 0$ and $b_L = 0$.

In addition to providing a numerically efficient description of time evolution, the Krylov basis is central to defining measures of quantum complexity. In particular, the *spread complexity* is defined as the average position in Krylov space,

$$C_S(t) = \sum_n n\,|\phi_n(t)|^2, \tag{2.74}$$

which quantifies how extensively the state spreads over the basis. The probabilities $|\phi_n(t)|^2$ not only determine $C_S(t)$ but also give rise to the *spread entropy* in the Schrödinger picture,

$$S_S(t) = -\sum_n |\phi_n(t)|^2 \ln |\phi_n(t)|^2. \tag{2.75}$$

We can also characterize this distribution in terms of its moments

$$C_K^{(\alpha)}(t) = \sum_{n=0}^{N-1} n^\alpha |\phi_n(t)|^2. \tag{2.76}$$

For $\alpha = 1$, this moment coincides with the spread complexity defined in Eq. 2.74; however, higher moments prove valuable as they accentuate aspects of the dynamics that are indicative

of chaos [55, 136].

A different and complementary procedure to obtain the Lanczos coefficients involves the moment recurrence method. Starting with the *return amplitude*

$$S(t) = \langle \psi(t) | \psi(0) \rangle, \tag{2.77}$$

one defines the nth moment as

$$\mu_n = \frac{1}{i^n} \lim_{t \to 0} \frac{d^n}{dt^n} S(t). \tag{2.78}$$

Since $S(0) = 1$ by normalisation, the zeroth moment is $\mu_0 = 1$. With these moments in hand, the Lanczos coefficients a_n and b_n can be computed through a recursive algorithm. One introduces intermediate quantities $\mathsf{M}_k^{(n)}$ and $\mathsf{L}_k^{(n)}$ defined as

$$\begin{aligned} \mathsf{M}_k^{(0)} &= (-1)^k \mu_k, \quad \mathsf{L}_k^{(0)} = (-1)^{k+1} \mu_{k+1}, \\ \mathsf{M}_k^{(n)} &= \mathsf{L}_k^{(n-1)} - \mathsf{L}_{n-1}^{(n-1)} \frac{\mathsf{M}_k^{(n-1)}}{\mathsf{M}_{n-1}^{(n-1)}}, \\ \mathsf{L}_k^{(n)} &= \frac{\mathsf{M}_{k+1}^{(n)}}{\mathsf{M}_n^{(n)}} - \frac{\mathsf{M}_k^{(n-1)}}{\mathsf{M}_{n-1}^{(n-1)}}, \quad k \geq n. \end{aligned} \tag{2.79}$$

Finally, the Lanczos coefficients are given by

$$b_n = \sqrt{\mathsf{M}_n^{(n)}}, \quad a_n = -\mathsf{L}_n^{(n)}. \tag{2.80}$$

Once the coefficients are determined, one can solve the Schrödinger equation within the Krylov subspace as in Eq. (2.73) to obtain the Krylov wavefunctions and thereby evaluate the spread complexity.

Both the direct construction via the Lanczos algorithm and the moment recurrence method provide complementary approaches to capture the essential dynamics of a state as it evolves under $\hat{H}$. In particular, these techniques illuminate how the complexity of the state increases over time, a feature that becomes especially significant in studies of thermalisation, chaos, and quantum information spreading.

2.3.3 Krylov Operator Basis and Krylov Complexity

An analogous construction applies to the Heisenberg evolution of an operator $\hat{O}(t)$. Since $\hat{O}$ is not a vector in the original Hilbert space, we promote it to a state in an auxiliary Hilbert space of operators by endowing the space $\mathscr{A}$ of bounded operators on $\mathscr{H}$ with an appropriate

inner product. For example, one may define

$$\langle A|B\rangle = \omega\Big(A^\dagger\, B\Big)\,, \tag{2.81}$$

where ω is a positive, normalised linear functional. In many-body contexts at finite temperature, a common choice is to use the thermal (Wightman) inner product

$$(A \mid B)_\beta = \left\langle e^{\frac{\beta}{2}\hat{H}}\, A^\dagger\, e^{-\frac{\beta}{2}\hat{H}}\, B \right\rangle_\beta, \tag{2.82}$$

which ensures that $\mathscr{A}$ becomes a Hilbert space (up to possible issues with null vectors).

In this framework, the operator $\hat{O}$ is mapped to a ket $|O\rangle$ (or equivalently denoted as $\mid O)$). Its time evolution is generated by the Liouvillian super-operator $\mathscr{L} \equiv [\hat{H}, \cdot\,]$, so that the time-evolved operator is expressed as

$$\hat{O}(t) = e^{i\,\mathscr{L}\,t}\,\hat{O}. \tag{2.83}$$

We now apply the Lanczos algorithm to the set of operator-states $\{\mathscr{L}^n\,\hat{O}\}$. For Hermitian operators—thanks to the properties of the chosen inner product (for example, the Wightman inner product defined in (2.82))—one can show that $\left(\hat{O} \mid \mathscr{L}\hat{O}\right) = 0$, so that all diagonal Lanczos coefficients vanish ($a_n = 0$). Consequently, the recursion relation simplifies considerably.

Constructing the Operator Krylov Basis. We set the first basis vector as $\mid \mathscr{O}_0) \equiv \mid \hat{O})$, and, following the Lanczos prescription, define $\mid z_1) = \mathscr{L} \mid \mathscr{O}_0)$, with normalisation

$$\mid \mathscr{O}_1) = \frac{\mid z_1)}{b_1}, \quad b_1 = \sqrt{(z_1 \mid z_1)}. \tag{2.84}$$

More generally, the iterative procedure is given by

$$\mid z_n) = \mathscr{L} \mid \mathscr{O}_{n-1}) - b_{n-1} \mid \mathscr{O}_{n-2}), \quad \mid \mathscr{O}_n) = \frac{\mid z_n)}{b_n}, \quad b_n = \sqrt{(z_n \mid z_n)}, \tag{2.85}$$

with the convention $b_0 = 0$. It follows that the basis $\{\mid \mathscr{O}_n)\}$ is orthonormal, $(\mathscr{O}_n \mid \mathscr{O}_m) = \delta_{nm}$. The resulting tridiagonal representation of the Liouvillian is

$$\mathscr{L} \mid \mathscr{O}_n) = b_{n+1} \mid \mathscr{O}_{n+1}) + b_n \mid \mathscr{O}_{n-1}), \tag{2.86}$$

so that, in the Krylov basis $\mathscr{L}$ has the following matrix form,

$$\mathscr{L}_{nm} := (\mathscr{O}_n \mid \mathscr{L} \mid \mathscr{O}_m) = \begin{pmatrix} 0 & b_1 & 0 & 0 & \cdots \\ b_1 & 0 & b_2 & 0 & \cdots \\ 0 & b_2 & 0 & b_3 & \cdots \\ 0 & 0 & b_3 & 0 & \ddots \\ \vdots & \vdots & \vdots & \ddots & \ddots \end{pmatrix}. \tag{2.87}$$

This, like state spreading, maps the operator dynamics onto a one-dimensional tight-binding chain, as illustrated in Fig. 2.4.

Time Evolution in the Operator Krylov Basis. Expressing the time evolution of the operator within this basis, we write

$$\mid O(t)) = \sum_n i^n \, \phi_n(t) \mid \mathscr{O}_n), \tag{2.88}$$

where the probability amplitudes $\phi_n(t)$ are real and satisfy the initial condition $\phi_n(0) = \delta_{n,0}$. Substituting the expansion into the Heisenberg evolution equation,

$$\frac{d}{dt} \mid O(t)) = i \, \mathscr{L} \mid O(t)),$$

and using the tridiagonal form (2.86), one obtains the set of coupled differential equations

$$\frac{\partial \phi_n(t)}{\partial t} = b_n \, \phi_{n-1}(t) - b_{n+1} \, \phi_{n+1}(t). \tag{2.89}$$

These equations govern the operator dynamics in the Krylov basis and, together with the normalisation of the amplitudes, $\sum_n |\phi_n(t)|^2 = 1$, fully determine the evolution of $\hat{O}(t)$.

Krylov Operator Complexity. Using the expansion (2.88), one may define a measure of complexity for operator growth, analogous to the spread complexity in the state picture. The *Krylov operator complexity* is given by

$$K_O(t) = \sum_n n \, |\phi_n(t)|^2, \tag{2.90}$$

which quantifies the average number of Krylov basis elements contributing to $\hat{O}(t)$. A more extensive exploration of how these coefficients b_n evolve and how they characterize the dynamical complexity of the operator is presented in subsequent chapters.

In summary, by mapping operators onto an auxiliary Hilbert space and applying the

Lanczos algorithm to the sequence $\{\mathscr{L}^n\hat{O}\}$, we construct an orthonormal Krylov operator basis. The tridiagonal form of the Liouvillian in this basis and the ensuing differential equations for the expansion coefficients provide a powerful framework for analysing operator growth and for defining measures such as Krylov operator complexity.

This definition can be interpreted in terms of a fictitious particle hopping on a one-dimensional chain (the *Krylov chain*) with sites labeled by the index n and hopping amplitudes given by the Lanczos coefficients $\{b_n\}$. The index n serves as a measure of the "complexity level." Therefore, the average position $\langle n\rangle$ on this chain reflects the extent to which the state or operator has spread from its initial configuration.

Under the universal growth hypothesis (1.59), if $b_n \sim \alpha\, n$, the system behaves like a tight-binding model on a semi-infinite chain with linearly increasing hopping amplitudes. In many chaotic systems, this results in an exponential rise of complexity at intermediate times, with the rate $\lambda_K = 2\alpha$ serving as a quantum analogue of the classical Lyapunov exponent. At finite temperature, this growth is consistent with bounds on chaos such as the Maldacena–Shenker–Stanford bound, $\lambda \leq 2\pi/\beta$.

Quantum Correlations in Holography 3

Building on the previous reviews, this chapter explores quantum correlations within the holographic framework through two complementary works. On one hand, we examine quantum information in discrete holography by constructing boundary spin chain Hamiltonians whose aperiodic couplings reflect the inflation rules underlying the bulk tiling of the hyperbolic plane. On the other hand, we investigate geometric quantum discord (GQD) in holographic conformal field theories as an indicator of non-factorisation in the partition function and as a diagnostic tool for probing wormhole microstates.

In the first part, we establish a framework for a holographic duality on a discretised hyperbolic geometry. Here, a boundary spin chain Hamiltonian is constructed with couplings patterned after the inflation rules that determine the bulk tiling. The boundary spins are organised into multiplets under a finite dihedral symmetry, capturing the remnant conformal invariance. By applying strong-disorder renormalisation group techniques, we demonstrate that the ground state resides in an aperiodic singlet phase; in this phase, two-point correlation functions decay with a power law of exponent one. Furthermore, when the spins are in the fundamental representation of $SO(N)$, the system is gapless and the effective central charge extracted from the entanglement entropy scales as $\ln N$, reflecting the number of local degrees of freedom. We also obtain an analytical expression for the mutual information, revealing that it does not undergo a phase transition at any finite separation.

In the second part, we propose using geometric quantum discord (GQD) as an information-theoretic indicator of non-factorisation in quantum systems with holographic duals. Our analysis shows that a nonzero GQD implies that the corresponding partition function fails to factorise, a result that holds both for generic pure states and for the thermofield double state—a state with a well-established holographic dual. This observation leads to a novel interpretation of the thermomixed double state as the best classical approximation to the Einstein–Rosen bridge, linking the persistence of quantum discord to the existence of wormhole microstates.

3.1 Discrete Holography and Aperiodic Spin Chains

Over the past few decades, the holographic principle [24, 25] and its most celebrated realisation via the Anti-de Sitter/Conformal Field Theory (AdS/CFT) correspondence [21–23] have revolutionised high-energy physics. These frameworks establish a precise dictionary between

gravitational theories in $d+1$ dimensions and strongly coupled d-dimensional conformal field theories, with quantum information measures—such as entanglement entropy [32, 33, 35], mutual information [137], Rényi entropies, and relative entropy [138–140]—playing a central role in refining this correspondence.

Motivated by the undeniable success of these continuous approaches and the experimental progress in realising hyperbolic geometries [141–143], researchers have increasingly turned to the challenge of formulating holographic dualities in discrete settings. This shift not only aims to harness the computational and numerical advantages of discrete systems but also to bridge theory with experiment—addressing common criticisms that the predictions of traditional AdS/CFT, aside from notable outcomes like the Kovtun-Son-Starinets (KSS) bound [144–146] (which aligns with experimental observations [147]), are too few to be compelling.

Within the program of discrete holography [148–159], the focus is on constructing dualities based on discrete spaces—graphs, tilings, and lattices—with particular emphasis on the prototypical $\mathrm{AdS}_3/\mathrm{CFT}_2$ case. In this context, regular hyperbolic tilings [160–162] are extensively employed to discretize two-dimensional hyperbolic spaces. Characterised by their Schläfli symbol $\{p, q\}$, which denotes a tiling in which q regular p-gons meet at each vertex, these tessellations inherit a significant number of the symmetries of their continuous counterparts. Intriguingly, such tilings can be generated through a systematic process known as inflation [163], whereby recursive replacement rules induce an aperiodic structure along the boundary of finite hyperbolic domains.

This emergent aperiodicity has been exploited in recent studies—for instance, in [157]—to propose explicit boundary Hamiltonians. In these models, the couplings between nearest-neighbor spins are arranged to follow exactly the aperiodic sequences generated by the inflation process, yielding an aperiodically modulated interaction pattern. Specifically, a spin-$1/2$ $SU(2)$ aperiodic XXX chain was analysed via strong-disorder renormalisation group (SDRG) techniques [164, 165]. Under appropriate assumptions, its ground state was shown to factorise into an *aperiodic singlet phase* (ASP), consisting of singlet pairs formed between spins at arbitrarily large, irregular distances. Moreover, a significant class of $\{p, q\}$ modulations necessitates at most two decimation steps in the SDRG procedure, allowing a distinction between two families of singlets—depending on whether an even or an odd number of decimation steps has been applied. The entanglement entropy of a given interval in these systems exhibits a piecewise linear scaling with subsystem size, accompanied by a logarithmic envelope that conforms to predictions from conformal field theory [166, 167]. Here, the discrete parameters contribute only as a multiplicative prefactor, interpreted in terms of an effective central charge following the approach in [168]. An exact tensor network (TN) representation of the ground state has also been constructed, thereby providing a discrete

hyperbolic geometric realisation of the ASP.

Beyond these technical achievements, the investigation of discrete holography is driven by both practical and conceptual motivations. On the one hand, discretised models promise enhanced experimental accessibility and the use of robust numerical techniques; on the other, they offer a fresh perspective on the limitations and potential extensions of the holographic principle itself. Discrete dualities may illuminate open questions in continuous AdS/CFT by introducing computational methods that are inherently attuned to the discrete nature of experimental systems. Furthermore, the enrichment of the holographic dictionary with intrinsically discrete entries finds support in quantum matter theories, where lattice restrictions give rise to excitations absent in continuum models [169]. This dual incentive—both applied and theoretical—underscores the exciting prospects for advancing our understanding of holographic dualities in regimes where discreteness is fundamental.

In [99], we extend the investigation of aperiodic spin chains whose modulations arise from the boundary aperiodic sequence generated by the inflation rule for a $\{p, q\}$ bulk tiling. A natural question—especially from the perspective of holographic dualities—is whether one can realize a regime populated by a large number of spin degrees of freedom. This inquiry is inspired by continuous AdS/CFT, where the large N limit (with N associated to the gauge group $SU(N)$ on the boundary) is indispensable for the saddle-point approximation on the gravity side.

To emulate this feature in a discrete setup, we propose two symmetry-based constructions. The first construction is motivated by the fact that, in continuous AdS/CFT, the boundary CFT operators transform covariantly under the irreducible representations of the bulk isometry (i.e., the conformal) group. In our discretised framework [157], after performing a radial truncation of the $\{p, q\}$ tilings, the residual symmetry is given by the dihedral group D_n (with $n = p, q$), which is the symmetry group of a regular polygon.[1] This observation motivates the definition of a spin chain where the local spin degrees of freedom are organised into multiplets that transform covariantly under D_n.

The second construction involves aperiodic spin chains with a global $SO(N)$ symmetry. Here, we choose $SO(N)$ rather than $SU(N)$ to ensure both a gapless phase [175, 176] and the stabilisation of the aperiodic singlet phase (ASP).[2] In this context, the symmetry is implemented globally (in contrast to the gauge symmetry usually considered in holography [180]), which is consistent with standard analyses of spin chains. We further extend the strong-disorder renormalisation group (SDRG) procedure to derive the ASP in these models. To the best of our knowledge, spin chains with these symmetry properties have not been

[1] For infinite tilings and, if one excludes reflection transformations, these symmetry groups become examples of so-called *Fuchsian groups*. Such groups have been studied in condensed matter physics; see [170–174].

[2] For a holographic Kondo model involving an $SU(N)$ spin defect, see [177–179].

previously examined in the presence of aperiodic modulations.

For chains exhibiting $SO(N)$ symmetry, one may also explore the $N \to \infty$ limit. Interestingly, we find that the effective central charge computed from the entanglement entropy diverges as $\ln N$ when $N \to \infty$, thereby capturing the information encoded in the number of degrees of freedom. Although our approach is motivated by the AdS/CFT correspondence, we stress that our results do not replicate features observed in continuous holographic setups. In particular, our analysis does not involve any notion of strong coupling—a hallmark of continuous boundary theories such as the SYK model [181–183]—and the large N limit considered here is fundamentally different from that in conventional AdS/CFT, since $SO(N)$ acts as a global symmetry and the spin variables transform in the fundamental representation rather than in the adjoint. Nonetheless, these findings are expected to contribute to a deeper understanding of the discrete holographic framework developed in [157] and may serve as a basis for future work toward establishing a duality that incorporates a dynamical bulk theory.

A separate but related discussion concerns spin chains endowed with dihedral symmetry. In these models, the residual spacetime symmetry D_n (which can be regarded as a vestige of the continuous conformal symmetry) comes with an additional tunable parameter $n = p, q$ that does not appear in the conventional conformal algebra. This extra degree of freedom allows us to explore the limit $n \to \infty$, a scenario lacking a direct analogue in continuous AdS/CFT. Because the number of irreducible representations of D_n grows proportionally with n, the effective central charge is rescaled by a factor linear in n; hence, for appropriate modulations, one can access a regime characterised by a large effective central charge.

Our investigation leads to three main results:

1. For aperiodic coupling modulations associated with hyperbolic $\{p, q\}$ tilings, we generalise the findings of [184] regarding correlation functions to incorporate two families of singlets emerging from the SDRG procedure. In particular, for spins paired into the same singlet, the two-point correlation function decays as a power law with an exponent equal to one. The corresponding prefactors depend on the tiling parameters p and q as well as on the particular SDRG decimation family.

2. We extend the analysis of entanglement entropy in ASPs presented in [157] by deriving exact analytical expressions for the non-universal additive constants in the enveloping functions. These results allow us, for the first time, to compute the mutual information in ASPs. In the case of adjacent intervals, the mutual information displays a piecewise linear behaviour accompanied by a logarithmic envelope, in agreement with the form predicted by CFT calculations [185]. For disjoint intervals, while a piecewise linear behaviour persists, no enveloping function is observed. Moreover, as a function of the distance d between subsystems, the mutual information decays in a manner

characterised by finite intervals of vanishing mutual information interspersed with peaks of nonzero amplitude; notably, no phase transition (i.e. no critical distance d_c beyond which the mutual information strictly vanishes) is detected, in contrast with continuous AdS/CFT results [137].

3. We generalise the SDRG procedure to $SO(N)$-invariant aperiodic Hamiltonians with spin degrees of freedom in the fundamental representation of $SO(N)$. By computing the entanglement entropy of an interval in such chains, we demonstrate that the effective central charge grows as $\ln N$ in the limit $N \to \infty$.

3.1.1 Regular Hyperbolic Tilings: Construction, Geometry, and Symmetry

Regular hyperbolic tessellations provide a powerful framework for discretising two- dimensional hyperbolic space. Unlike the familiar lattices of Euclidean or spherical geometries, these tilings exist in a regime defined by constant negative curvature. This unique geometric setting yields not only a complete covering of space without gaps or overlaps but also imparts a rich and intricate symmetry structure. Such tilings have deep connections with several branches of mathematics—including Riemann surface theory, group theory, number theory, topology, and algebraic geometry [170, 171, 173, 186–194]—and they play a central role in emerging approaches to discrete holography. In particular, the systematic construction of these tilings by means of inflation rules [157, 163, 168] produces aperiodic patterns on the asymptotic boundary, offering a tantalising link between bulk geometry and boundary physics.

Poincaré Disk from AdS_{2+1}

A natural starting point to study these tilings is provided by the geometry of Anti-de Sitter (AdS) spacetime in $(2+1)$ dimensions. By considering AdS in global coordinates

$$\{\rho, t, \phi\} \in [0, 1) \times \mathbb{R} \times [0, 2\pi),$$

and restricting to a constant time slice, one obtains a two-dimensional spatial section that is isomorphic to hyperbolic space. Explicitly, the induced metric on the corresponding Poincaré disk is given by

$$ds^2 = (2L_{\text{AdS}})^2 \frac{d\rho^2 + \rho^2 d\phi^2}{(1-\rho^2)^2}\,, \tag{3.1}$$

where L_{AdS} denotes the AdS radius. As $\rho \to 1$, the conformal boundary of the disk emerges, signaling the transition between the finite interior and the idealised asymptotic boundary—a feature that has important ramifications in holographic dualities. The Poincaré disk, defined by

$$\mathbb{D}^2 = \{z = x + iy \in \mathbb{C} \mid x^2 + y^2 < 1\}\,, \tag{3.2}$$

serves as a canonical model for two-dimensional hyperbolic geometry. The metric on $\mathbb{D}^2$ is expressed as

$$ds^2 = \frac{(2L_{\text{AdS}})^2}{(1-|z|^2)^2}\, dz\, d\bar{z} = (2L_{\text{AdS}})^2 \frac{dx^2 + dy^2}{(1-x^2-y^2)^2}\,, \tag{3.3}$$

which emphasises the role of the conformal factor that distinguishes hyperbolic from Euclidean geometry. One of the remarkable features of the Poincaré disk is that its isometries are realised by Möbius transformations. These transformations take the form

$$f(z) = \frac{az+b}{cz+d}\,, \quad a,b,c,d \in \mathbb{C}, \quad ad - bc = 1\,, \tag{3.4}$$

and they generate the group $\mathrm{PSU}(1,1) = \mathrm{SU}(1,1)/\{\pm 1\}$, which is isomorphic to $\mathrm{PSL}(2,\mathbb{R})$ [195]. This group symmetry underpins many of the distinctive geometric properties of hyperbolic space. Geodesics in the Poincaré disk are represented by circular arcs that intersect the boundary at right angles, or by diameters, and the hyperbolic distance between any two points $z_1, z_2 \in \mathbb{D}^2$ is calculated via

$$d_{\mathbb{D}^2}(z_1,z_2) = \ell\ \operatorname{arcosh}\left(1 + \frac{2|z_1 - z_2|^2}{(1-|z_1|^2)\,(1-|z_2|^2)}\right) = 2\ell\ \operatorname{arctanh}\left(\frac{|z_1 - z_2|}{|1 - z_1\overline{z_2}|}\right)\,, \tag{3.5}$$

or, equivalently, expressed in polar coordinates with $z_j = \rho_j e^{i\phi_j}$,

$$d_{\mathbb{D}^2}(z_1,z_2) = \ell\ \operatorname{arcosh}\left(1 + \frac{2\big(\rho_1^2 + \rho_2^2 - 2\rho_1\rho_2\cos(\phi_1 - \phi_2)\big)}{(1-\rho_1^2)\,(1-\rho_2^2)}\right)\,. \tag{3.6}$$

The fact that these distances are invariant under $\mathrm{PSU}(1,1)$ reflects the underlying homogeneity and isotropy of the hyperbolic plane. Alternative formulations using the upper half-plane model [196] or the Cayley transform [197, 198] further illustrate the mathematical richness of these constructions.

Tiling the Poincaré Disk

The discretisation of the Poincaré disk is achieved by covering it with regular polygonal tiles. Each tiling is characterised by the Schläfli symbol $\{p, q\}$, where p is the number of edges

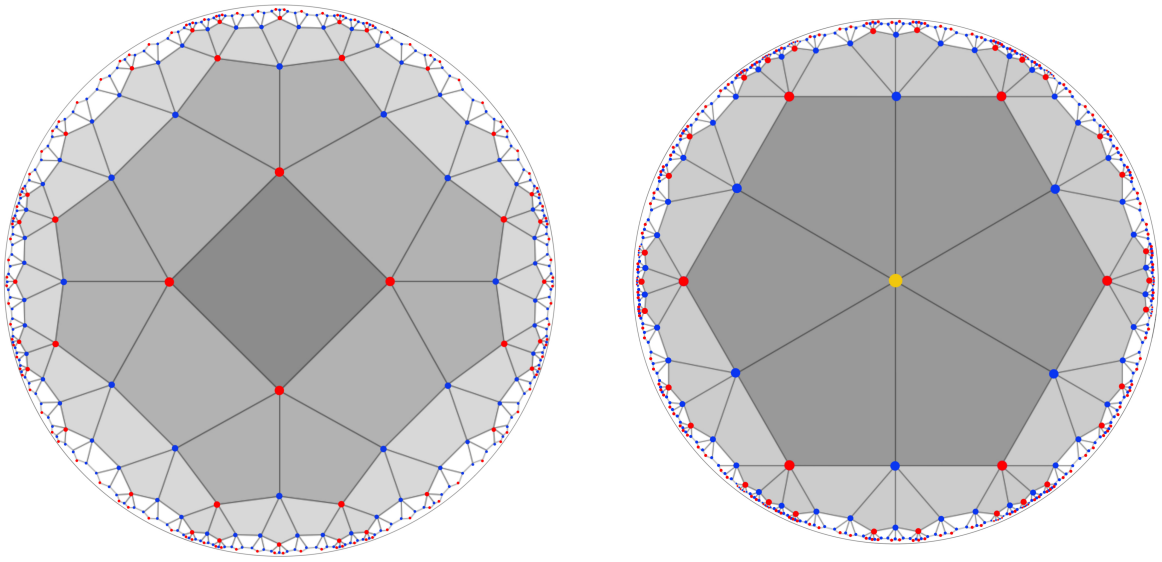

(a) (b)

Figure 3.1: Illustration of hyperbolic $\{p, q\}$ tiling construction via inflation rules. Vertices labeled as a, b, and c are colored red, blue, and yellow, respectively. In panel (3.1a), a polygon-centered $\{4, 5\}$ tiling is shown: starting from the seed $aaaa$ and applying the inflation rule $a \mapsto babab$ as given in (3.18), the vertices forming the outer boundary of the second layer are generated. In panel (3.1b), a vertex-centered $\{4, 6\}$ tiling is depicted: beginning at a central vertex of type c, the inflation rule $c \mapsto abababababab$ in (3.18) produces the vertices along the boundary of the first layer. Figure taken from [99].

per polygon and q is the number of polygons that meet at each vertex. In order for a tiling to represent hyperbolic space, the condition

$$(p-2)(q-2) > 4 \tag{3.7}$$

must be satisfied; this condition ensures that the interior angles of the polygons are sufficiently small so that the total angle around any vertex is less than 2π. There are two natural approaches to constructing such tilings. One may start with a polygon centered at the origin and add successive layers outward—this is referred to as a *polygon-centered* tiling. Alternatively, the construction may begin from a vertex at the center, leading to a *vertex-centered* tiling. These configurations are illustrated in Fig. 3.1. If the construction is iterated indefinitely, the entire Poincaré disk is tessellated, and the resulting infinite tiling possesses a symmetry group given by the hyperbolic triangle group $\Delta(p, q, 2)$ [160–162]. When restricted to orientation-preserving transformations, these groups form a subset of Fuchsian groups [188].

The hyperbolic tessellations introduced above are not invariant under the entire isometry group $\mathrm{PSU}(1,1) \cong \mathrm{PSL}(2,\mathbb{R})$ but rather under a discrete subgroup thereof.

Every $\{p, q\}$ tiling can be further subdivided into a network of right-angled hyperbolic (Schwarzian) triangles—what we refer to as hyperbolic triangulations. In fact, by allowing the third angle to be arbitrary, i.e. π/r, one obtains a more general class of hyperbolic triangulations whose full isometry group is given by the triangle group

$$\Delta(p, q, r) = \langle x, y, z \mid x^2 = y^2 = z^2 = (xy)^p = (yz)^q = (zx)^r = e \rangle \,,$$

as discussed in [161, 188]. This presentation encapsulates the maximal set of symmetries achievable for such triangulations, although for many applications only the orientation-preserving subgroup (e.g. the von Dyck group in the special case $r = 2$) is relevant.

In parallel, the discrete symmetries of hyperbolic tessellations are also naturally described by Fuchsian groups. These groups, defined as discrete subgroups of $\mathrm{PSL}(2, \mathbb{R})$ (or, equivalently, $\mathrm{PSU}(1, 1)$), act properly discontinuously on $\mathbb{D}^2$. More precisely, for any point $z \in \mathbb{D}^2$ the orbit

$$\mathscr{F} \cdot z = \{f(z) \mid f \in \mathscr{F}\}$$

is discrete, meaning that each point in the orbit is isolated, and the identity is isolated in the group topology. We recall:

- **(Fuchsian Group)** A subgroup $\mathscr{F} \subset \mathrm{PSL}(2, \mathbb{R})$ is called Fuchsian if its action on $\mathbb{D}^2$ is properly discontinuous.
- **(Fundamental Region)** A set $\mathscr{R} \subset \mathbb{D}^2$ is a fundamental region for $\mathscr{F}$ if $\bigcup_{f \in \mathscr{F}} f(\mathscr{R}) = \mathbb{D}^2$ and the interiors of distinct translates do not overlap.

Fuchsian groups are further classified by the nature of their limit set $\Lambda(\mathscr{F})$: groups of the first kind satisfy $\Lambda(\mathscr{F}) \cong S^1$, while those of the second kind have a limit set that is a proper, nowhere dense subset of S^1.

For practical computations, however, one must introduce a UV cutoff by truncating the infinite tessellation to a finite number of layers. This truncation reduces the full Fuchsian symmetry to a finite residual group, typically the dihedral group D_n, defined by

$$D_n = \langle r, s \mid r^n = s^2 = e,\ rs = sr^{-1} \rangle \,, \tag{3.8}$$

where r represents a rotation by $2\pi/n$ and s a reflection. In a polygon-centered tiling we set $n = p$, whereas for vertex-centered tilings $n = q$. The inclusion of reflections in D_n enriches the representation theory available for applications such as discrete holography (see Sec. 3.1.6).

Thus, the overall picture is one in which the infinite hyperbolic tessellation of $\mathbb{D}^2$ carries a rich continuous structure described by a Fuchsian group (and more generally by triangle

groups in the case of hyperbolic triangulations), while a practical, finite representation of the tiling is endowed with the residual discrete symmetry of a dihedral group. Moreover, the aperiodic structures emerging from inflation rules [157, 163, 168] encode information from the bulk geometry onto the boundary, a feature that is central to recent developments in discrete holography.

For the group D_n is defined in (3.8), we present its complete set of irreps. For an integer n, the total number of inequivalent irreducible representations is given by $\lceil n/2 \rceil + 3$ when n is even, $\lceil n/2 \rceil + 1$ when n is odd, where $\lceil \cdot \rceil$ denotes the ceiling function. In the even case, there exist four one-dimensional representations, whereas for odd n there are only two one-dimensional irreps; the remaining $\lceil n/2 \rceil - 1$ irreps are two-dimensional [199, 200]. We consider only those irreps that are inequivalent, meaning they cannot be related by any change of basis. Their definitions are determined by how they act on the group generators.

For even n, denote the one-dimensional irreps by Φ_l with $l = 1, 2, 3, 4$. Their actions on the generators r and s are given by

$$\Phi_1(r) = 1\,, \qquad \Phi_1(s) = 1\,, \tag{3.9}$$

$$\Phi_2(r) = -1\,, \qquad \Phi_2(s) = 1\,, \tag{3.10}$$

$$\Phi_3(r) = 1\,, \qquad \Phi_3(s) = -1\,, \tag{3.11}$$

$$\Phi_4(r) = -1\,, \qquad \Phi_4(s) = -1\,. \tag{3.12}$$

When n is odd, only Φ_1 and Φ_3 (as defined in (3.9)–(3.12)) continue to form irreps of D_n.

The remaining irreps are two-dimensional. We label these by $m = 1, \ldots, \lceil n/2 \rceil - 1$. In a basis where the representation $\rho_m(r)$ is diagonal, their actions on the generators are expressed as

$$\rho_m(r) = \begin{pmatrix} e^{2\pi \mathrm{i} m/n} & 0 \\ 0 & e^{-2\pi \mathrm{i} m/n} \end{pmatrix}\,, \tag{3.13}$$

$$\rho_m(s) = \begin{pmatrix} 0 & 1 \\ 1 & 0 \end{pmatrix}\,. \tag{3.14}$$

It is important to note that all the representations in (3.9)–(3.12) and (3.13)–(3.14) are unitary. These irreps are employed in Sec. 3.1.6 to specify the transformation rules of the multiplets, which constitute the fundamental building blocks of the D_n-invariant Hamiltonian in (3.75).

Inflation Rules and Finite Symmetry in $\{p, q\}$ Tilings

In this part, we describe in detail the procedure for generating hyperbolic $\{p, q\}$ tilings of the Poincaré disk $\mathbb{D}^2$ through inflation rules, and we discuss the corresponding symmetries that persist in truncated (finite) tilings. This construction not only offers a systematic method to obtain arbitrarily large patches of the tiling, but it also encodes significant geometric and combinatorial information in the form of an aperiodic boundary sequence.

We begin with a seed tile, which is a polygon centered at the origin of $\mathbb{D}^2$. This central polygon, chosen for its high symmetry, serves as the "zeroth layer" in our construction. When the tiling is generated by successively adding concentric layers of polygons around this central tile, the tiling is referred to as *polygon-centred*. An alternative construction, which takes a vertex at the origin as the starting point, gives rise to a *vertex-centred* tiling. In the polygon-centred case, the central p-gon preserves its dihedral symmetry D_p, while in vertex-centred tilings the symmetry is that of D_q (where q is the number of tiles meeting at a vertex). These two constructions are illustrated in Fig. 3.9, which shows examples of both polygon-centred and vertex-centred tilings.

Each new layer of the tiling is generated through an *inflation rule*, a substitution process applied iteratively to the vertices on the boundary of the current finite tiling. At the initial stage, the boundary vertices of the central polygon are uniformly labelled using a chosen symbol. For polygon-centred tilings with $p > 3$, we typically assign the label a to each vertex, so that the seed word is $w_0 = a^p$. This seed word encapsulates the inherent symmetry of the central tile and serves as the starting point for subsequent inflation steps.

During an inflation step, a new layer of vertices is added around the current boundary. Crucially, the vertices on the new boundary are distinguished by how they connect to the previous layer. Those vertices that remain unconnected to an inner layer are labelled a, while those that are connected by an edge to the previous layer are labelled b. In the special case when $p = 3$, an auxiliary label d is introduced in the seed (with $w_0 = d^3$), but this label quickly vanishes after the first inflation step, resulting in a binary asymptotic sequence.

The inflation rule for a general hyperbolic tiling with $p > 3$ and arbitrary q is then formulated as follows:

$$\sigma_{\{p,q\}} : \begin{cases} a \mapsto a^{p-4}\, b\, (a^{p-3}b)^{\,q-3}\,, \\ b \mapsto a^{p-4}\, b\, (a^{p-3}b)^{\,q-4}\,, \\ c \mapsto (a^{p-3}b)^{\,q}\,, \end{cases}$$

where the third label c is used primarily in the context of vertex-centred tilings (with seed $w_0 = c$); after one iteration, however, the sequence effectively becomes binary (i.e., involving

only a and b labels). Similarly, for $\{3, q\}$ tilings the inflation rule adapts to

$$\sigma_{\{3,q\}} : \begin{cases} a \mapsto a^{\,q-5} b, \\ b \mapsto a^{\,q-6} b, \\ d \mapsto a^{\,q-4} b. \end{cases}$$

In each case, these substitution rules prescribe how each vertex at the boundary of the existing tiling is to be replaced, thereby generating the vertices of the next layer. The resulting sequence of labels, when read along the boundary, contains encoded information about the construction parameters p and q, and in the asymptotic limit the boundary is described by the infinite aperiodic sequence $\mathscr{S}_{\{p,q\}}$.

Examples and Matrix Representation To illustrate the inflation process, consider a few explicit examples:

Example 1: The $\{3, 7\}$ Tiling. For a $\{3, 7\}$ tiling, the inflation rule becomes

$$\sigma_{\{3,7\}} : \begin{cases} a \mapsto aab, \\ b \mapsto ab, \\ d \mapsto aaab, \end{cases}$$

where the auxiliary label d in the seed (e.g., $w_0 = d^3$) disappears after one iteration. The associated inflation matrix, considering only the substitutions for a and b, is

$$M_{\{3,7\}} = \begin{pmatrix} 2 & 1 \\ 1 & 1 \end{pmatrix}.$$

Its Perron-Frobenius eigenvalue is $\lambda_+ = \frac{3+\sqrt{5}}{2} = \tau^2$, where $\tau = \frac{1+\sqrt{5}}{2}$ is the golden ratio. In this sense, the inflation rule for $\{3, 7\}$ is equivalent to applying the Fibonacci substitution rule twice.

Example 2: The $\{5, 5\}$ Tiling. For a $\{5, 5\}$ tiling, the inflation rule reads

$$\sigma_{\{5,5\}} : \begin{cases} a \mapsto abaa\, baab, \\ b \mapsto abaa\, b, \end{cases}$$

with the corresponding inflation matrix

$$M_{\{5,5\}} = \begin{pmatrix} 5 & 3 \\ 3 & 2 \end{pmatrix}. \tag{3.15}$$

It can be shown that $M_{\{5,5\}} = M_{\{3,7\}}^2 = M_{\text{Fib}}^4$, thereby linking the asymptotic sequences of the $\{5,5\}$ tiling to those of the $\{3,7\}$ tiling and the Fibonacci rule. The Perron–Frobenius eigenvalue corresponding to (3.15) is $\lambda_+ = \frac{7+\sqrt{5}}{2} = \tau^4$.

Example 3: The $\{6,4\}$ Tiling. For a polygon-centered $\{6,4\}$ tiling, the seed word is $w_0 = a^6$ and the inflation rule is given by

$$\sigma_{\{6,4\}} : \begin{cases} a \mapsto aa\,b\,aaa\,b, \\ b \mapsto aa\,b, \end{cases}$$

leading to the inflation matrix

$$M_{\{6,4\}} = \begin{pmatrix} 5 & 2 \\ 2 & 1 \end{pmatrix}. \tag{3.16}$$

The largest Perron–Frobenius eigenvalue for (3.16) is $\lambda_+ = 3 + 2\sqrt{2} = (1+\sqrt{2})^2$, which is the square of the silver ratio.

The inflation procedure can be practically implemented by introducing an inflation matrix defined for $p > 3$ and $q > 3$

$$M_{\{p,q\}} = \begin{pmatrix} (p-3)(q-3)+p-4 & (p-3)(q-4)+p-4 \\ q-2 & q-3 \end{pmatrix}. \tag{3.17}$$

In this matrix, the entry $(M_{\{p,q\}})_{ij}$ (with $i,j \in \{a,b\}$) counts how many times the symbol i appears in the substitution word assigned to the symbol j, according to the general inflation rules,

$$\sigma_{\{p,q\}} = \begin{cases} a \mapsto a^{p-4}b(a^{p-3}b)^{q-3}, \\ b \mapsto a^{p-4}b(a^{p-3}b)^{q-4}, \\ c \mapsto (a^{p-3}b)^{q}, \end{cases} \tag{3.18}$$

which determines the replacement rule for every boundary vertex as a new layer is appended to the tiling for a general $\{p,q\}$ tiling.

Inflation matrices allow us to quantitatively characterise the asymptotic aperiodic sequence $\mathscr{S}_{\{p,q\}}$ that emerges from the inflation process. In particular, the dominant (Perron–Frobenius)

eigenvalue λ_+ of $M_{\{p,q\}}$ determines the scaling factor of the sequence upon each inflation step. Furthermore, the components of the normalised right eigenvector, $\mathbf{v}_+ = (p_a, p_b)^t$ with $p_a + p_b = 1$, and the normalised left eigenvector, $\mathbf{u}_+ = (l_a, l_b)^t$ (normalised such that $\mathbf{u}_+ \cdot \mathbf{v}_+ = 1$), encode the relative frequencies and typical lengths associated with the symbols a and b in $\mathscr{S}_{\{p,q\}}$.

For a more comprehensive discussion on these aspects, see [157, 163, 184, 201]. Notably, these parameters play a central role when applying the strong-disorder renormalisation group (SDRG) technique to aperiodic spin chains, a topic that will be revisited in the following section.

3.1.2 Review of SDRG on Aperiodic Spin Chains

In this section we present an in-depth overview of the strong disorder renormalisation group (SDRG) method as applied to aperiodic spin chains. We focus on how SDRG is used to derive entanglement entropy results in aperiodic singlet phases (ASP) [201, 202] and recast the procedure in a systematic framework that facilitates its extension to models with novel aperiodic modulations. In such cases—where the SDRG fixed point is described by an ASP—the dependence of the piecewise entanglement entropy for a block of consecutive sites on the subsystem size is determined exclusively by the characteristics of the modulation [157, 201]. The explicit form of the aperiodic Hamiltonian enters only via an overall prefactor given by the singlet entropy, s_0, which in turn influences the effective central charge.

As demonstrated in [163, 168] and reviewed in Sec. 3.1.1, an aperiodic structure can be identified at the boundary of a finite $\{p, q\}$ tiling obtained through an inflation procedure. This observation motivated the proposal in [157] that theories defined on such boundaries could naturally exhibit aperiodic features. Consequently, aperiodic spin chains with modulations that mirror the bulk discretisation were introduced as candidate boundary theories, with their ground state and entanglement properties analysed via SDRG. In what follows, we review the core SDRG techniques [164, 165, 203, 204] that form the backbone of our analysis and set the stage for the extensions presented later in the manuscript.

We consider an infinite chain described by the following spin Hamiltonian with nearest-neighbour interactions:

$$H_{\{p,q\}} = \sum_{i\in\mathbb{Z}} J_i \, h\Big(\vec{\sigma}_i \cdot \vec{\sigma}_{i+1}; \theta_i\Big) \,. \tag{3.19}$$

Here, $\vec{\sigma}_i$ represents the local spin degrees of freedom at site i, with the dot denoting the Euclidean scalar product. The interaction strengths, $J_i \in \{J_a, J_b\}$, and the additional parameters, $\theta_i \in \{\theta_a, \theta_b\}$, are arranged along the chain according to the aperiodic sequence $\mathscr{S}_{\{p,q\}}$. Although one may consider a larger set of aperiodically distributed parameters, for clarity

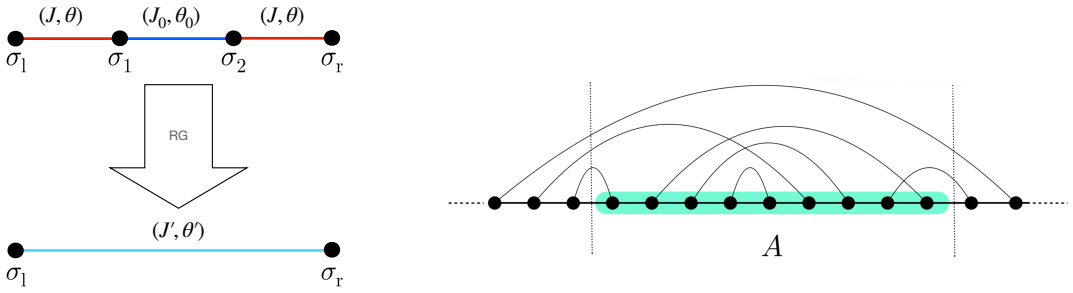

(a) (b)

Figure 3.2: (3.2a) Illustration of a basic decimation step within the SDRG procedure for aperiodic spin chains. At low energies, the two spins σ_1 and σ_2, which are strongly coupled via the bond (J_0, θ_0), are removed from the chain and replaced by an effective coupling (J', θ') that connects the neighboring spins σ_l and σ_r. The relative strength of the new coupling (J', θ') in the renormalised chain is determined in a later analysis. (3.2b) Diagram showing the distribution of singlets in an aperiodic singlet phase as generated by the SDRG process. The entanglement entropy for a region A is computed by counting the singlets that are cut by the boundary between A and its complement B. In this example, three singlets are severed. Figure taken from [99].

we restrict our discussion to these two. Moreover, we assume that the Hamiltonian (3.19) operates in a gapless regime [157], which in turn implies that the underlying homogeneous model is critical [157, 184, 205].

The SDRG is a real-space renormalisation technique designed to tackle non-homogeneous quantum chains. In our analysis of aperiodic modulations, we may assume without loss of generality that $J_b > J_a$ and define the coupling ratio $r \equiv \frac{J_a}{J_b}$. At low energies, the SDRG process involves iteratively decimating blocks of spins that are linked by the stronger bonds (J_b), thus renormalising the couplings of the remaining bonds. Figure 3.2a illustrates a fundamental decimation step for a two-spin block, where the notation is slightly modified (taking $J_b = J_0$ and $J_a = J$, with an analogous redefinition for θ_i). With each decimation, the couplings evolve as

$$r \to r' \to r'' \to \cdots \to r^* \quad \text{and} \quad \theta_i \to \theta_i' \to \theta_i'' \to \cdots \to \theta_i^* \quad (i \in \{a, b\}) \,,$$

with r^* and θ_i^* being the fixed points of the SDRG flow. When these fixed points depend on the initial parameters, the modulation is called *m*arginal; conversely, if the fixed points are independent of the starting values, the modulation is classified as *r*elevant. In the latter case, the SDRG yields asymptotically exact predictions for the ground state [184, 203].

Typically, the SDRG may decimate blocks of more than two spins. Here, we concentrate on cases in which only two-spin blocks are decimated. In such blocks, one projects onto the ground state of the local Hamiltonian $h\left(\vec{\sigma}_1 \cdot \vec{\sigma}_2; \theta_b\right)$ from (3.19). When this ground state is

non-degenerate, the two-spin block is projected onto a singlet state. Repeated decimation that exclusively produces singlets eventually drives the system to a fixed point where the ground state is a product of singlet bonds spanning arbitrary distances—a phase known as the *a*periodic singlet phase (ASP) [201] (see Fig. 3.2b).

A striking feature of the SDRG when applied to Hamiltonians of the form (3.19) is that the original aperiodic sequence is recovered after a finite number of decimation steps. This periodic recurrence allows the entire SDRG procedure to be formulated in terms of repeated *s*equence-preserving transformations. Specifically, if the initial sequence is restored after k steps, one refers to the SDRG as exhibiting a k-cycle. In our subsequent discussion, the case of a two-cycle is especially important. In a two-cycle SDRG, one can associate two distinct 2×2 deflation matrices, M_1^{-1} and M_2^{-1}, corresponding to the two decimation steps that combine to reform the original sequence (cf. Sec. 3.1.1). Since $M_1 \neq M_2$, their action naturally distinguishes between two classes of singlets, which we label as *even* and *odd* based on the number of SDRG steps required for decimation. Quantitatively, the procedure is characterised by the eigenvalues and eigenvectors of the matrices $M_1 M_2$ and $M_2 M_1$. Denote by $\lambda_+^{(12)}$ the larger eigenvalue common to both products. The corresponding right eigenvectors,

$$(p_a^{(e)}, p_b^{(e)})^{\mathrm{t}} \quad \text{and} \quad (p_a^{(o)}, p_b^{(o)})^{\mathrm{t}} ,$$

are normalised such that $p_a^{(i)} + p_b^{(i)} = 1$, with $i = e, o$.

$$(p_a^{(e)}, p_b^{(e)})^{\mathrm{t}} \quad \text{and} \quad (p_a^{(o)}, p_b^{(o)})^{\mathrm{t}} ,$$

are normalised such that $p_a^{(i)} + p_b^{(i)} = 1$ with $i = e, o$. Similarly, we denote the left eigenvectors by

$$(l_a^{(e)}, l_b^{(e)})^{\mathrm{t}} \quad \text{and} \quad (l_a^{(o)}, l_b^{(o)})^{\mathrm{t}} ,$$

with the normalisation $l_a^{(i)} p_a^{(i)} + l_b^{(i)} p_b^{(i)} = 1$ for $i = e, o$ [157].

To extend the entanglement entropy findings of spin-$\frac{1}{2}$ aperiodic XXX chains [157] to a broader class of Hamiltonians described by (3.19), the following conditions must be met:

1. The system must be critical; for the modulations induced by the sequences $\mathscr{S}_{\{p,q\}}$, this requires the underlying homogeneous model to be gapless.
2. The modulation enforced by $\mathscr{S}_{\{p,q\}}$ must be relevant.
3. The SDRG flow must be characterised by either a one-cycle or a two-cycle modulation.
4. The ground state of the Hamiltonian (3.19) must be in an ASP.

It is important to note that these criteria stem both from the dynamics encoded in the function h and the inherent properties of the aperiodic modulation. Remarkably, based solely on

the modulation properties, it was shown in [157] that only the following classes of $\{p, q\}$ modulations fulfill conditions 1–4: $\{6, q\}$ with $q \geqslant 4$, $\{5, 4\}$, $\{5, 5\}$, $\{3, 7\}$, and $\{3, 8\}$. Our analysis henceforth concentrates on these modulations in combination with the Hamiltonian (3.19).

When the Hamiltonian satisfies conditions 1–4, the entanglement entropy of a block comprising L consecutive sites can be determined by a simple counting argument. In the ASP, the entanglement entropy is computed by tallying the number of singlets shared between the subsystem A and its complement B [206] (see Fig. 3.2b). Denoting this number by $n_{A:B}$, the total entanglement entropy is obtained by multiplying $n_{A:B}$ by the single-singlet entropy, s_0. Due to the inhomogeneity introduced by the aperiodic sequence, $n_{A:B}$ depends on the position of the block within the infinite chain. Thus, we consider an averaged number, $\bar{n}_{A:B}$, over all possible positions. Although this average is strictly a density, we refer to it as a total number for notational convenience. The entanglement entropy is then given by

$$S_A(L) = s_0\, \bar{n}_{A:B}(L)\,. \tag{3.20}$$

Here, $\bar{n}_{A:B}(L)$ is a function of the modulation parameters p and q, and it is independent of the explicit form of h in (3.19). Its analytic expression is detailed in 3.1.5. As shown in [157], the entanglement entropy exhibits a piecewise linear behaviour as a function of L. In particular, for two-cycle SDRG, one can identify two logarithmic envelopes:

$$S_{\text{env}}^{(i)}(L) = \frac{c_{\text{eff}}}{3} \ln L + \kappa_i, \quad i = e, o, \qquad c_{\text{eff}} = \frac{12 p_b^{(e)} l_b^{(e)} s_0}{\ln \lambda_+^{(12)}}\,. \tag{3.21}$$

Although c_{eff} is inspired by the central charge concepts in conformal field theory [166, 207], it is not a true CFT central charge but rather a parameter characterising the entanglement scaling. Both the additive constants κ_i and c_{eff} depend on the modulation parameters p and q, and their analytic forms—together with the reasoning for the even (e) and odd (o) labeling—are derived in 3.1.5. In the case of a one-cycle SDRG, these two envelopes merge into a single logarithmic curve [157, 201].

A further representation of the ground state for an aperiodic spin chain is provided by tensor networks (TN). In [157], the SDRG procedure was exploited to construct a TN that exactly reproduces the ground state of a spin-$\frac{1}{2}$ aperiodic XXX chain. This network not only reflects the symmetry of the ground state but also encodes its entanglement structure, thereby mapping it onto a discrete hyperbolic geometry. Importantly, this TN construction can be generalised to the ground states of Hamiltonians of the form (3.19). For any aperiodic spin chain with a relevant modulation specified by $\mathscr{S}_{\{p,q\}}$, the TN graph remains identical to that discussed in [157]; the sole difference lies in the contribution of a single network cut to the

entanglement entropy (i.e., the bond dimension), which is sensitive to the explicit structure of h in (3.19).

In [157], the methods discussed above were applied to the spin-$\frac{1}{2}$ aperiodic XXX chain. For this model, the Hamiltonian is given by (3.19) with

$$h\Big(\vec{\sigma}_i \cdot \vec{\sigma}_{i+1}; \theta_i\Big) = \vec{\sigma}_i \cdot \vec{\sigma}_{i+1} \quad (i \in \mathbb{Z}) \,,$$

and the local spin operators are represented as

$$\vec{\sigma}_i = (\sigma_i^{(x)}, \sigma_i^{(y)}, \sigma_i^{(z)})^{\mathrm{t}} \,,$$

with the entries being the familiar Pauli matrices. It was argued that for this specific model the requisite conditions 1–4 are satisfied, and all sequences $\mathscr{S}_{\{p,q\}}$ induce a relevant modulation. Consequently, when the ground state is an ASP, the entanglement entropy for a block of L consecutive sites is given by (3.20) with $s_0 = \ln 2$, corresponding to the entropy of an EPR pair. In Sec. 3.1.6 we extend this analysis to a broader class of Hamiltonians that accommodate a larger number of degrees of freedom at each site.

3.1.3 Two-Point Correlation Functions in Aperiodic Singlet Phases

In this section we detail the derivation of two-point correlation functions for spin degrees of freedom belonging to the same singlet in aperiodic singlet phases (ASPs) as governed by the general aperiodic Hamiltonian (3.19). Our analysis focuses exclusively on two-point functions. We begin by recapitulating the one-cycle SDRG results originally obtained in a condensed matter framework [184] and subsequently extend the analysis to the more complex two-cycle SDRG case. In the latter, distinct two-point functions emerge corresponding to the different singlet generations introduced previously. In all cases, the correlations decay with a power law featuring an exponent equal to unity, and all nontrivial dependence on the Schläfli parameters p and q appears solely in the constant prefactor.

Moreover, drawing from [157], we conclude the section by discretising well-established holographic relations between boundary correlators and bulk geometric quantities [208], showing that the effective scaling dimension of boundary operators is increased by the discretisation. A physical interpretation of this outcome from the bulk perspective is also provided.

One-Cycle SDRG: A Review

We begin by summarising the derivation presented in [184] for a one-cycle SDRG, originally worked out for the spin-$\frac{1}{2}$ XXX Hamiltonian. Under the assumption that the conditions 1–4 are fulfilled for Hamiltonians of the form (3.19), the results generalise to our broader setting. In the ASP, the ground state is constructed as a product of singlets connecting spins over arbitrary distances, and the dominant contribution to the two-point function comes from spins that are paired in the same singlet—while all other correlations decay exponentially.

Let us define the averaged two-point correlation function as

$$C^{\alpha\beta}(\Lambda) \equiv \overline{\langle \sigma_i^{\alpha} \sigma_{i+\Lambda}^{\beta} \rangle} = \delta_{\alpha\beta}\, C(\Lambda)\,, \tag{3.22}$$

where Λ is the typical length of a singlet and the Kronecker delta reflects the symmetry of (3.19). In this setup, the overall correlation between two spins within a singlet is the product of the intrinsic singlet correlation, denoted c_0, and the density (or number) of singlets produced in a given SDRG step. If we denote by Λ_j the characteristic length of a singlet in the jth generation, its density scales as $\rho_j \sim 1/\Lambda_j$ [184]. Hence, the two-point correlation function for the jth generation is approximated by

$$C(\Lambda_j) \approx c_0\,(\rho_j - \rho_{j+1}) = \frac{c_0}{\Lambda_j}\left(1 - \frac{\Lambda_j}{\Lambda_{j+1}}\right). \tag{3.23}$$

For a one-cycle SDRG, the ratio Λ_j/Λ_{j+1} tends to a constant value, which we denote by $\sigma(p,q)$ in the large-j limit. Accordingly, the two-point correlation becomes

$$C(\Lambda_j) = c_0\,\sigma(p,q)\,\frac{1}{\Lambda_j}\,, \tag{3.24}$$

demonstrating a power-law decay with an exponent of unity and with all modulation effects encoded in the prefactor.

Two-Cycle SDRG Correlations

A broad class of $\{p,q\}$ modulations—discussed in detail in [157]—induces a two-cycle SDRG leading to an ASP. In this scenario, the sequence-preserving transformation M_2M_1 breaks the SDRG process into alternating *even* and *odd* generations, each characterised by its own typical singlet length Λ_j and corresponding density ρ_j. A detailed derivation of these results is provided in [157]; for the reader's convenience, we present here a concise summary of the key expressions.

In the two-cycle scenario, the aperiodic sequence is reproduced only after the combined

application of two consecutive renormalisation group (RG) transformations, namely M_1^{-1} followed by M_2^{-1}. Following the notation introduced in [157], we denote the largest eigenvalue of the product M_2M_1 by $\lambda_+^{(12)}$; note that in general this eigenvalue does not factorise as the product of the largest eigenvalues of M_2 and M_1 individually, because these transformations do not commute.

We define the 0-th generation as the distribution of strong bonds in the original chain. Then, for $k \in \mathbb{N}$, the *even* generations (with index $j = 2k$) of singlets are obtained by applying the inverse transformation $(M_1M_2)^{-1}$ to the $(k-1)$-th even generation, whereas the *odd* generations (with index $j = 2k-1$) are generated by applying $(M_2M_1)^{-1}$ to the $(k-1)$-th odd generation.

A scaling factor, denoted by $\tilde{\lambda}$, is required to relate the singlet distributions between the first odd and even generations (i.e. between $k = 1$ and $k = 2$). This factor is not equal to $\lambda_+^{(12)}$ because the first and second generations are connected by a single application of M_1, nor is it given by the largest eigenvalue of M_1 alone—since M_1 does not by itself determine the asymptotic bond distribution of the even generations. The determination of $\tilde{\lambda}$ was addressed in [157].

It is important to note that the typical length Λ, which characterises the distance between two spins forming a singlet, varies with the generation. One can assign independent scaling behaviours for the even and odd generations. As derived in [157], singlets in the k-th generation correspond to the strong bonds of the $(k-1)$-th generation and therefore their characteristic lengths are given by

$$\Lambda_{2k-1} = l_b^{(e)} \left(\lambda_+^{(12)}\right)^{k-1}, \tag{3.25}$$

$$\Lambda_{2k} = l_b^{(o)} \left(\lambda_+^{(12)}\right)^{k-1} \tilde{\lambda}\,, \tag{3.26}$$

where $l_b^{(e)}$ and $l_b^{(o)}$ are the b-th components of the left eigenvectors associated with $\lambda_+^{(12)}$ for the matrices M_1M_2 and M_2M_1, respectively. Moreover, since the first generation of singlets coincides with the original strong-bond distribution, one has $\Lambda_1 = l_b^{(e)}$. This convention explains the superscripts in (3.25) and (3.26): the typical length of the odd generations is determined by the strong bonds in the preceding even generation (via $l_b^{(e)}$), and vice versa.

Similarly, the concentration of singlets in the k-th generation is given by

$$\rho_{2k-1} = p_b^{(e)} \left(\lambda_+^{(12)}\right)^{-k+1}, \tag{3.27}$$

$$\rho_{2k} = p_b^{(o)} \left(\lambda_+^{(12)}\right)^{-k+1} \tilde{\lambda}^{-1}\,, \tag{3.28}$$

where $p_b^{(e)}$ and $p_b^{(o)}$ denote the b-th components of the right eigenvectors of M_1M_2 and M_2M_1

(both associated with $\lambda_+^{(12)}$), respectively. As demonstrated in [157], the scaling factor $\tilde{\lambda}$ can be expressed in terms of these eigenvector components:

$$\tilde{\lambda} = \frac{2p_b^{(o)}\lambda_+^{(12)}}{\lambda_+^{(12)}\left(1-2p_b^{(e)}\right)-1}\,. \tag{3.29}$$

The expressions above are crucial for calculating two-point correlation functions in aperiodic singlet phases (ASPs), as discussed in detail in Sec. 3.1.3 for the case of two-cycle modulations $\{6,q\}$. For completeness, we now present the results for two additional modulations, specifically those associated with $\{5,4\}$ and $\{3,8\}$, which fall within the domain of validity of (3.36). By inserting the typical lengths and concentrations defined above into (3.36), one obtains for the $\{5,4\}$ modulation:

$$C_{\{5,4\}}(\Lambda_j) = \begin{cases} \dfrac{c_0}{6}\left(5-\dfrac{7}{\sqrt{3}}\right)\dfrac{1}{\Lambda_{2k}}\,, & j=2k\,, \\[2ex] c_0\left(\dfrac{13}{2}-\dfrac{11}{\sqrt{3}}\right)\dfrac{1}{\Lambda_{2k-1}}\,, & j=2k-1\,, \end{cases} \tag{3.30}$$

and for the $\{3,8\}$ modulation:

$$C_{\{3,8\}}(\Lambda_j) = \begin{cases} c_0\left(\dfrac{5}{2}-\dfrac{4}{\sqrt{3}}\right)\dfrac{1}{\Lambda_{2k}}\,, & j=2k\,, \\[2ex] \dfrac{c_0}{6}\left(9-5\sqrt{3}\right)\dfrac{1}{\Lambda_{2k-1}}\,, & j=2k-1\,, \end{cases} \tag{3.31}$$

where c_0 is the constant appearing in the two-point correlation function expressions.

In the two-cycle framework, nonvanishing correlations occur only between spins within the same generation. Thus, the two-point correlator for the jth generation can be estimated by

$$C(\Lambda_j) \approx c_0\,(\rho_j - \rho_{j+1})\,. \tag{3.32}$$

Since we are exclusively counting the singlets produced in generation j, the difference here is taken with respect to the immediately following generation, avoiding any overcounting from intermediate stages. Based on equations (3.25)–(3.26) and (3.27)–(3.28), we can express the singlet densities as

$$\rho_{2k} = \frac{p_b^{(o)}\,l_b^{(o)}}{\Lambda_{2k}}\,, \qquad \rho_{2k-1} = \frac{p_b^{(e)}\,l_b^{(e)}}{\Lambda_{2k-1}}\,. \tag{3.33}$$

Substituting these expressions into (3.32) and using the fact that

$$p_b^{(e)}\,l_b^{(e)} = p_b^{(o)}\,l_b^{(o)} \equiv p_b\,l_b \quad \text{(independent of parity)}\,,$$

we obtain

$$C(\Lambda_j) = \frac{c_0\, p_b\, l_b}{\Lambda_j}\left(1 - \frac{\Lambda_j}{\Lambda_{j+1}}\right). \tag{3.34}$$

The factor Λ_j/Λ_{j+1} converges to a constant that depends on the parity of the generation. Specifically, one finds

$$\frac{\Lambda_{2k}}{\Lambda_{2k+1}} = \frac{l_b^{(o)}\,\tilde{\lambda}}{l_b^{(e)}\,\lambda_+^{(12)}} \equiv \alpha^{(e)}\,, \qquad \frac{\Lambda_{2k-1}}{\Lambda_{2k}} = \frac{l_b^{(e)}}{l_b^{(o)}\,\tilde{\lambda}} \equiv \alpha^{(o)}\,, \tag{3.35}$$

with the auxiliary parameter $\tilde{\lambda}$ defined in 3.1.3 (see also equation (3.29)). Consequently, the final form of the two-point correlation function in the two-cycle case is

$$C(\Lambda_j) = \begin{cases} \dfrac{c_0\, p_b\, l_b\, \left(1 - \alpha^{(e)}_{(p,q)}\right)}{\Lambda_{2k}}\,, & j = 2k\,, \\[2ex] \dfrac{c_0\, p_b\, l_b\, \left(1 - \alpha^{(o)}_{(p,q)}\right)}{\Lambda_{2k-1}}\,, & j = 2k-1\,. \end{cases} \tag{3.36}$$

In the limit of a one-cycle SDRG, one has $\tilde{\lambda}^2 = \lambda_+^{(12)}$ and $l_b^{(o)} = l_b^{(e)}$, yielding $\alpha^{(o)} = \alpha^{(e)}$ and reducing (3.36) to (3.24). Notably, the spatial dependence—namely, the inverse scaling with Λ_j—remains identical in both cases, with the modulation parameters p and q affecting only the overall prefactors.

For an explicit illustration, consider the family of $\{6, q\}$ modulations. As demonstrated in [157], these two-cycle, relevant modulations yield closed-form expressions for the quantities $p_b^{(o)}$, $p_b^{(e)}$, $l_b^{(o)}$, $l_b^{(e)}$, $\tilde{\lambda}$, and $\lambda_+^{(12)}$ for all $q \geq 4$. In this case, the prefactors in (3.36) depend on q via

$$1 - \alpha^{(e)}_{(6,q)} = \frac{2\left(q^2 - \left(\sqrt{q^2-5q+6}+4\right)q + 3\sqrt{q^2-5q+6}+2\right)}{3q-10}\,, \tag{3.37}$$

$$1 - \alpha^{(o)}_{(6,q)} = \frac{2}{\sqrt{q^2-5q+6}+q-2}\,. \tag{3.38}$$

Additional examples for two-cycle modulations yielding ASPs can be found in 3.1.3.

It is worth emphasising that the ASP reached via this SDRG scheme exhibits a highly factorised structure: the full density matrix decomposes into a product of singlet density matrices. Consequently, all odd-point correlation functions vanish, and even-point functions factorise into products of two-point correlations. Given that the local Hilbert space is two-dimensional, the sole nontrivial operators are the Pauli matrices (and the identity), so the two-point functions, as determined above, completely characterise the correlation structure.

Holographic Boundary Correlations

Within the AdS/CFT correspondence, the two-point function for a boundary operator O_Δ, with scaling dimension $\Delta \gg 1$, is expressed in terms of the bulk geodesic distance $\gamma(x, y)$ between boundary points x and y as [208, 209]

$$\langle O_\Delta(x) O_\Delta(y) \rangle \propto \exp\left[-\Delta \frac{\gamma(x, y)}{L_{\text{AdS}}}\right]. \tag{3.39}$$

For simplicity, we have omitted the subtleties arising from cutoff-dependent evaluations of the geodesic endpoints. In our discrete setting, it is natural to assume that (3.39) holds, with the discrete geodesic length γ given in [157] as a function of the edge length $s(p, q)$, the asymptotic scaling factor $\lambda_+(p, q)$ (see Sec. 3.1.1), and a parity function $\nu(p, q)$. Replacing $\gamma(x, y)$ with its discrete counterpart leads to an effective two-point function

$$\langle O_\Delta(x) O_\Delta(y) \rangle_{\text{discr}} \propto \frac{1}{|x - y|^{2\Delta_{\text{eff}}(p,q)}}, \qquad \Delta_{\text{eff}}(p, q) = \frac{\Delta\, s(p, q)\, \nu(p, q)}{L_{\text{AdS}} \ln \lambda(p, q)}, \tag{3.40}$$

where $|x - y|$ counts the number of sites on the discrete boundary between x and y. A comparison of Δ_{eff} with the original scaling dimension Δ reveals that the ratio $\Delta_{\text{eff}}/\Delta$ exceeds unity for all allowed values of p and q.

This increase in the effective scaling dimension can be physically interpreted in the following manner. In the continuum, fluctuations of the bulk geodesic about its saddle-point configuration induce only minor corrections. However, in the discrete framework such fluctuations necessarily extend over an entire edge (of length $\sim L_{\text{AdS}}$) because a deviation from the geodesic must traverse one of the adjacent tiles. As a result, the scalar field dual to O_Δ becomes more strongly confined to the discrete geodesic, which is akin to an increase in the effective mass. Given that for large Δ one typically has $\Delta \approx m L_{\text{AdS}}$, a higher effective mass directly translates into a larger scaling dimension, in full agreement with (3.40).

3.1.4 Mutual Information in Aperiodic Spin Chains

In this section we analyze the mutual information $I(A_1 : A_2)$ between two subsystems A_1 and A_2 embedded in aperiodic singlet phases (ASPs). Our discussion begins with a brief review of the random singlet phase results for spin chains as presented in [210]. We then introduce new findings for ASPs, focusing on both one-cycle and two-cycle strong disorder renormalisation group (SDRG) modulations. In particular, we show that for adjacent intervals the mutual information displays a piecewise linear dependence with logarithmic envelopes whose parameters are determined solely by the effective central charge and non-universal constants (cf. (3.21)). Furthermore, we extend our study to disjoint intervals, separated by a

distance d, and compare these findings with continuum AdS/CFT predictions [137].

Review of Mutual Information in Random Singlet Phases

The analysis in [210] considered two disjoint blocks A_1 and A_2, containing L_1 and L_2 consecutive sites, respectively, separated by a block B_1 of d sites, with the remainder of the chain denoted as B_2. In that study the exchange couplings J_i are drawn from a random distribution, and the system is driven into a random singlet phase [211], where the ground-state entanglement structure is essentially the same as in an ASP [201, 211].

Mutual information is defined by

$$I(A_1 : A_2) = S_{A_1}(L_1) + S_{A_2}(L_2) - S_{A_1 \cup A_2}(L_1, L_2, d)\,, \tag{3.41}$$

and it was argued that in the singlet phase, all correlations between A_1 and A_2 originate from singlet bonds connecting the two regions. In fact, if $\bar{n}_{A_1:A_2}$ represents the average number of such connecting singlets, then one finds

$$I(A_1 : A_2) = 2\, s_0\, \bar{n}_{A_1:A_2}\,, \tag{3.42}$$

where s_0 is the contribution of a single singlet to the entropy. To overcome the challenge of calculating the entanglement entropy for disjoint regions in non-homogeneous chains, the quantity $S_{A_1 \cup A_2}$ is reexpressed as a linear combination of entropies of contiguous regions, namely those of $A_1 \cup B_1$, $B_1 \cup A_2$, B_1, and $A_1 \cup B_1 \cup A_2$. This manipulation yields the formula

$$I(A_1 : A_2) = S_{B_1 \cup A_1}(L_1 + d) + S_{B_1 \cup A_2}(L_2 + d) - S_{B_1}(d) - S_{B_1 \cup A_1 \cup A_2}(L_1 + L_2 + d)\,. \tag{3.43}$$

Because the entanglement entropy for a single interval in an ASP is given by (3.20), the above expression can be fully determined once these single-interval results are known.

Mutual Information in ASP: New Results

We now present new results for the mutual information in ASPs, emphasising the role of both one-cycle and two-cycle SDRG modulations. Depending on whether the intervals are adjacent or separated by a finite distance d, distinct analyses are required.

Adjacent Intervals

For two adjacent intervals, one sets $d = 0$ in (3.43). By introducing the parametrisation

$$L_1 \equiv L\,, \quad L_2 \equiv aL \quad (a > 0)\,,$$

the mutual information simplifies to

$$I(A_1 : A_2) = S_{A_1}(L) + S_{A_2}(aL) - S_{A_1 \cup A_2}((1+a)L)\,. \tag{3.44}$$

As established in [157], each of the entropic terms in (3.44) exhibits a piecewise linear behaviour in $\ln L$ with logarithmic enveloping functions of the form

$$S^{(i)}_{\text{env}}(L) = \frac{c_{\text{eff}}}{3} \ln L + \kappa_i\,, \tag{3.45}$$

where c_{eff} and κ_i depend on the modulation parameters. After combining the various contributions, one finds that the mutual information has enveloping functions given by

$$I^{(i)}_{\text{env}}(A_1 : A_2) = \frac{c_{\text{eff}}}{3} \ln L + \beta^{(i)}\,, \quad i = 1, \ldots, k\,, \quad k \in \{2, 3, 4, 6\}\,, \tag{3.46}$$

with the set of additive constants $\{\beta^{(i)}\}$ determined by the details of the SDRG cycle and the ratio a. In particular, for one-cycle modulations, the number of distinct envelopes is 2 when $a = 1$ and 3 when $a \neq 1$, while for two-cycle modulations these numbers double to 4 and 6, respectively (see Table 3.1). In 3.1.5 the explicit expressions for the constants $\beta^{(i)}$ are derived. Figure 3.3 illustrates representative plots for modulations such as $\{6, 4\}$ and $\{6, 6\}$.

	one-cycle	two-cycle
$a = 1$	2	4
$a \neq 1$	3	6

Table 3.1: Number of logarithmic envelopes (i.e., different additive constants $\beta^{(i)}$) appearing in the mutual information of two adjacent intervals in an ASP.

Disjoint Intervals

In the case of two disjoint intervals ($d \neq 0$), the extra length scale d in (3.43) complicates the analytic structure of the resulting expression. In this situation, the additive contributions originating from the floor functions in the single-interval entanglement entropy (see 3.1.5) do not permit a simple factorisation into an overall $\ln L$ envelope. Nonetheless, since closed

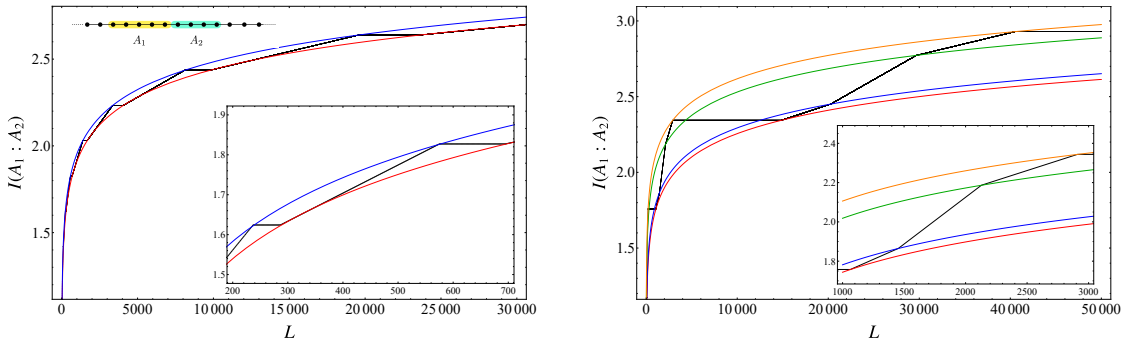

(a) $\{6, 4\}$, $a = 1$.

(b) $\{6, 6\}$, $a = 1$.

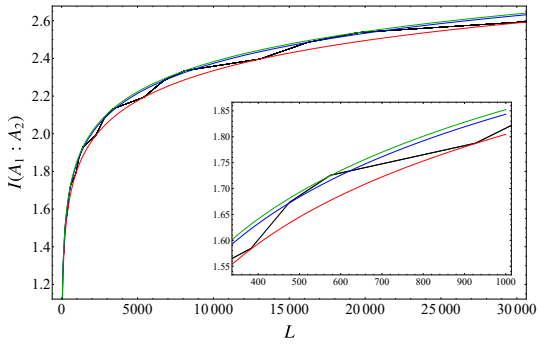

(c) $\{6, 4\}$, $a = \frac{1}{2}$.

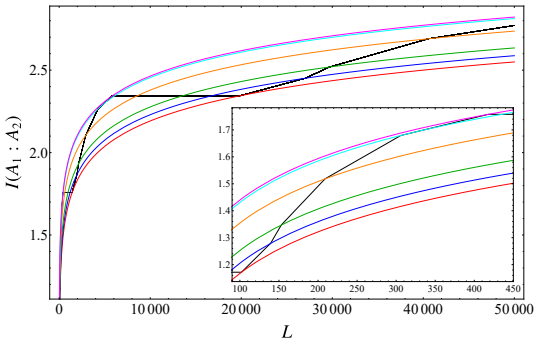

(d) $\{6, 6\}$, $a = \frac{1}{2}$.

Figure 3.3: Mutual information $I(A_1 : A_2)$ computed for two contiguous intervals of lengths $L_1 \equiv L$ and $L_2 \equiv aL$ within an ASP, using various $\{p, q\}$ aperiodic modulations. For clarity, all plots assume $s_0 = \ln 2$ as specified in (3.42). The four panels correspond to the four scenarios listed in Table 3.1, illustrating both one- and two-cycle modulations as well as cases with equal and different subsystem sizes. Figure taken from [99].

analytic forms are available for each entropic term, one can directly evaluate the mutual information as a function of the separation d. Figure 3.4 displays typical outcomes for a $\{6, 4\}$ modulation, for both equal and unequal intervals.

The key observation is that $I(A_1 : A_2)$ decays in a piecewise linear manner as a function of d, with characteristic intervals where the mutual information vanishes identically. However, these regions of zero mutual information are interspersed with finite peaks or hills; the peaks are sharper for equal-length intervals and become smoother when the interval sizes differ. Unlike holographic predictions based on the Ryu-Takayanagi formula—where mutual information drops sharply to zero beyond a critical distance [137]—our ASP analysis shows that singlet contributions at arbitrarily large distances ensure that $I(A_1 : A_2)$ never remains zero for all d beyond any finite critical value.

In the holographic setting, the mutual information between two intervals in a conformal field theory is known to vanish discontinuously after a critical separation due to a first-order phase transition in the corresponding Ryu-Takayanagi minimal surface [32, 33, 137]. In con-

trast, the ASP results presented here display a gradual (piecewise linear) decay, reflecting the fact that singlets exist on all scales in the ASP. Therefore, while the enveloping logarithmic behaviour in adjacent intervals mimics the functional form obtained from continuum CFT calculations [185, 212–214], the discrete nature of the ASP necessarily implies a nonvanishing mutual information at arbitrarily large separations.

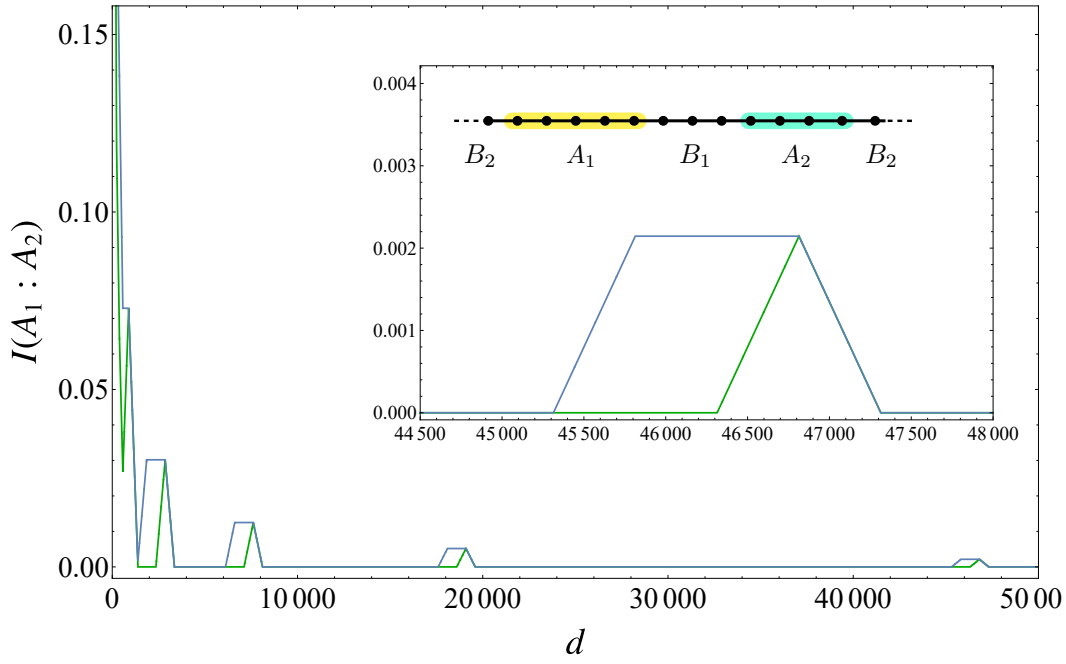

Figure 3.4: Displayed is the mutual information $I(A_1 : A_2)$ between two contiguous intervals of lengths $L_1 \equiv L$ and $L_2 \equiv aL$ in an ASP, computed under various $\{p, q\}$ aperiodic modulation schemes. All plots use $s_0 = \ln 2$ as stated in (3.42) for consistency. The four panels illustrate the four different scenarios listed in Table 3.1, covering both one- and two-cycle modulations and depicting cases with equal as well as different subsystem sizes. Figure taken from [99].

In summary, our findings confirm that the modulation parameters p and q enter exclusively through the effective central charge and a non-universal additive constant, and that the number of envelope functions depends on both the SDRG cyclicity and the ratio of subsystem sizes. Moreover, these features provide a natural framework to compare ASP results with both random singlet and holographic CFT predictions.

3.1.5 Piece-wise behaviours and envelopes

In this part, we present detailed analytic derivations for the logarithmic envelope functions of the piece-wise entanglement entropy and mutual information in aperiodic spin chains exhibiting ASPs.

Envelopes for the entanglement entropy

We consider a sub-system consisting of L consecutive sites embedded in an infinite chain. Its entanglement entropy is given by Eq. (3.20). To establish the envelope forms, we focus on the average number of sites belonging to a singlet that is shared between the sub-block A of length L and its complement B, denoted by $\bar{n}_{A:B}(L)$. The entanglement entropy (and its envelope) then follows by simply multiplying $\bar{n}_{A:B}(L)$ by s_0.

An exact formula for $\bar{n}_{A:B}(L)$ as a function of L was initially derived in [201] for single-cycle SDRGs and generalised to two-cycle SDRGs in [157]. We concentrate on the latter, which inherently captures the former as a special case. For subsequent purposes, let us examine $\bar{n}_{A:B}(aL)$ where $a > 0$ is a real parameter. As reported in [157], it reads

$$\bar{n}_{A:B}(aL) = 2\, p_b^{(e)}\, l_b^{(e)}\, \nu(aL) + \frac{2\,aL\left(\lambda_+^{(12)}\right)^{-\frac{\nu(aL)}{2}}}{\lambda_+^{(12)}-1} \times \begin{cases} \lambda_+^{(12)}\left(p_b^{(e)} + \tilde{\lambda}^{-1}\, p_b^{(o)}\right) & \nu(aL) \text{ even}, \\ \sqrt{\lambda_+^{(12)}}\left(p_b^{(e)} + \lambda_+^{(12)}\,\tilde{\lambda}^{-1}\, p_b^{(o)}\right) & \nu(aL) \text{ odd}, \end{cases} \tag{3.47}$$

where

$$\nu(aL) \equiv \left(\left\lfloor \frac{\ln\left(\frac{aL}{l_b^{(e)}}\right)}{\ln \lambda_+^{(12)}} \right\rfloor + \left\lfloor \frac{\ln\left(\frac{aL}{\tilde{\lambda}\, l_b^{(o)}}\right)}{\ln \lambda_+^{(12)}} \right\rfloor + 2 \right), \tag{3.48}$$

and the parameters $p_b^{(e)}$, $l_b^{(e)}$, $p_b^{(o)}$, $l_b^{(o)}$, and $\lambda_+^{(12)}$ (together with $\tilde{\lambda}$) are specified in Sec. 3.1.2 and 3.1.3 for the $\{p, q\}$ modulations that generate ASPs. As demonstrated in [157], the function in Eq. (3.47) exhibits a piece-wise linear profile when viewed as a function of L. We refer to the points of non-analytic behaviour as *breaking points*. Their explicit expressions, reported in [157], are given by Λ_{2k-1} in Eq. (3.25) and Λ_{2k} in Eq. (3.26), collectively denoted as Λ_k if one wishes to address both sequences at once.

For two-cycle SDRGs, these two sets of breaking points lead to two distinct envelope functions, differing by a constant offset. The derivation method for these envelopes (including the additive offset) is as follows. First, we evaluate $\bar{n}_{A:B}(aL)$ at $L = \Lambda_{2k-1}$ and $L = \Lambda_{2k}$, requiring us to insert these points into Eq. (3.48). Next, we check whether $\nu(aL)$ in Eq. (3.48) can be expressed in a way that extracts k from the floor functions. If so, and if $\bar{n}_{A:B}(aL)$ from Eq. (3.47) remains smooth at $L = \Lambda_{2k-1}$ or $L = \Lambda_{2k}$, the resulting expressions define the corresponding envelopes.

Even breaking points. Let us start by focusing on the sequence $L = \Lambda_{2k}$. Substituting this into $\nu(aL)$ yields

$$\nu\Big(a\,\Lambda_{2k}\Big) \;=\; 2k \;+\; \left\lfloor \frac{\ln a}{\ln \lambda_+^{(12)}} \right\rfloor \;+\; \left\lfloor \frac{\ln\left(\frac{a\,l_b^{(e)}}{\tilde{\lambda}\,l_b^{(o)}}\right)}{\ln \lambda_+^{(12)}} \right\rfloor \tag{3.49}$$

$$= \; 2\,\frac{\ln \Lambda_{2k}}{\ln \lambda_+^{(12)}} \;+\; 2 \;-\; 2\,\frac{\ln l_b^{(e)}}{\ln \lambda_+^{(12)}} \;+\; \left\lfloor \frac{\ln a}{\ln \lambda_+^{(12)}} \right\rfloor \;+\; \left\lfloor \frac{\ln\left(\frac{a\,l_b^{(e)}}{\tilde{\lambda}\,l_b^{(o)}}\right)}{\ln \lambda_+^{(12)}} \right\rfloor \tag{3.50}$$

$$\equiv \; 2\,\frac{\ln \Lambda_{2k}}{\ln \lambda_+^{(12)}} \;+\; 2 \;-\; 2\,\frac{\ln l_b^{(e)}}{\ln \lambda_+^{(12)}} \;+\; \xi_e, \tag{3.51}$$

where we have employed Eq. (3.26) to relate k and Λ_{2k}, and have introduced ξ_e as a shorthand for the terms that do not depend on k once a and the modulation parameters have been specified. Because $\nu(a\Lambda_{2k})$ has a fixed parity for any fixed a, one of the two branches in Eq. (3.47) will apply, dictated by ξ_e in Eq. (3.51). Substituting $L = \Lambda_{2k}$ into Eq. (3.47), we get

$$\bar{n}_{A:B}\Big(a\,\Lambda_{2k}\Big) \;=\; \frac{4\,p_b^{(e)}\,l_b^{(e)}}{\ln \lambda_+^{(12)}}\,\ln \Lambda_{2k} \;+\; \tilde{\kappa}_e(a), \tag{3.52}$$

with

$$\tilde{\kappa}_e(a) \;\equiv\; 2\,p_b^{(e)}\,l_b^{(e)}\left(2 \;-\; 2\,\frac{\ln l_b^{(e)}}{\ln \lambda_+^{(12)}} \;+\; \xi_e\right) \tag{3.53}$$

$$+ \;\; \frac{2\,a\,l_b^{(e)}\,\lambda^{-\frac{\xi_e}{2}-1}}{\lambda_+^{(12)} - 1} \;\times\; \begin{cases} \lambda_+^{(12)}\left(p_b^{(e)} + \tilde{\lambda}^{-1}\,p_b^{(o)}\right) & \xi_e \text{ even}, \\ \sqrt{\lambda_+^{(12)}}\left(p_b^{(e)} + \lambda_+^{(12)}\,\tilde{\lambda}^{-1}\,p_b^{(o)}\right) & \xi_e \text{ odd}. \end{cases}$$

Equation (3.52) is thus one of the two *exact envelopes* of $\bar{n}_{A:B}(aL)$ in Eq. (3.47). If we set $a = 1$ and multiply it by s_0 (see Sec. 3.1.2), we recover the envelope with $i = e$ in Eq. (3.21). Its constant term can be deduced from Eq. (3.53) upon taking $a = 1$, namely $\kappa_e \equiv s_0\,\tilde{\kappa}_e(a = 1)$.

Odd breaking points. Similarly, for $L = \Lambda_{2k-1}$, a direct computation provides

$$\bar{n}_{A:B}\Big(a\,\Lambda_{2k-1}\Big) \;=\; \frac{4\,p_b^{(e)}\,l_b^{(e)}}{\ln \lambda_+^{(12)}}\,\ln \Lambda_{2k-1} \;+\; \tilde{\kappa}_o(a), \tag{3.54}$$

where

$$\tilde{\kappa}_o(a) \equiv 2\,p_b^{(e)}\,l_b^{(e)}\left(2 - 2\,\frac{\ln\left(l_b^{(o)}\,\tilde{\lambda}\right)}{\ln\lambda_+^{(12)}} + \xi_o\right) + \frac{2\,a\,l_b^{(o)}\,\tilde{\lambda}\,\lambda^{-\frac{\xi_o}{2}-1}}{\lambda_+^{(12)}-1} \times \begin{cases} \lambda_+^{(12)}\left(p_b^{(e)} + \tilde{\lambda}^{-1}\,p_b^{(o)}\right) & \xi_o \text{ even}, \\ \sqrt{\lambda_+^{(12)}}\left(p_b^{(e)} + \lambda_+^{(12)}\,\tilde{\lambda}^{-1}\,p_b^{(o)}\right) & \xi_o \text{ odd}. \end{cases} \tag{3.55}$$

and

$$\xi_o \equiv \left\lfloor \frac{\ln a}{\ln\lambda_+^{(12)}} \right\rfloor + \left\lfloor \frac{\ln\left(\frac{a\,\tilde{\lambda}\,l_b^{(o)}}{l_b^{(e)}}\right)}{\ln\lambda_+^{(12)}} \right\rfloor. \tag{3.56}$$

Equation (3.54) thus provides the second envelope for the piece-wise function in Eq. (3.47). Setting $a = 1$ and multiplying by s_0 returns the envelope with $i = o$ in Eq. (3.21), with the corresponding additive constant $\kappa_o = s_0\,\tilde{\kappa}_o(a = 1)$ (cf. Eq. (3.55)).

Envelopes for the mutual information

We now apply the envelopes derived in Eq. (3.21) to determine analogous envelope functions for the mutual information of two blocks of consecutive sites. When the two blocks are adjacent and have lengths L and aL, Eq. (3.43) simplifies to Eq. (3.44). In this general setting with $a \neq 1$, three separate length scales arise: L, aL, and $(a+1)L$. For two-cycle modulations, this leads to six families of breaking points at

$$L = \Lambda_{2k},\ L = \Lambda_{2k-1},\ L = \Lambda_{2k}/a,\ L = \Lambda_{2k-1}/a,\ L = \Lambda_{2k}/(a+1),\ L = \Lambda_{2k-1}/(a+1),$$

with $k \in \mathbb{N}$. Similar computations to those in the previous subsection (substituting each set of these breaking points into Eq. (3.44)) yield six distinct envelope functions, each corresponding to one family of breaking points.

Denoting these envelopes by $I_{\text{env}}^{(i)}(L, a)$, one obtains

$$I_{\text{env}}^{(i)}(L, a) = \frac{c_{\text{eff}}}{3}\,\ln L + \beta^{(i)}, \quad i = 1, \ldots, 6, \tag{3.57}$$

where their additive constants emerge from

$$\beta^{(1)} = \frac{s_0}{2}\Big(\tilde{\kappa}_e(1) + \tilde{\kappa}_e(a) - \tilde{\kappa}_e(a+1)\Big), \tag{3.58}$$

$$\beta^{(2)} = \frac{s_0}{2}\Big(\tilde{\kappa}_o(1) + \tilde{\kappa}_o(a) - \tilde{\kappa}_o(a+1)\Big), \tag{3.59}$$

$$\beta^{(3)} = \frac{s_0}{2}\Big(\tilde{\kappa}_e(1/a) + \tilde{\kappa}_e(1) - \tilde{\kappa}_e\big(1+1/a\big)\Big) + \frac{c_{\text{eff}}}{6}\ln a, \tag{3.60}$$

$$\beta^{(4)} = \frac{s_0}{2}\Big(\tilde{\kappa}_o(1/a) + \tilde{\kappa}_o(1) - \tilde{\kappa}_o\big(1+1/a\big)\Big) + \frac{c_{\text{eff}}}{6}\ln a, \tag{3.61}$$

$$\beta^{(5)} = \frac{s_0}{2}\Big(\tilde{\kappa}_e\big(1/(a+1)\big) + \tilde{\kappa}_e\big(a/(a+1)\big) - \tilde{\kappa}_e(1)\Big) + \frac{c_{\text{eff}}}{6}\ln(a+1), \tag{3.62}$$

$$\beta^{(6)} = \frac{s_0}{2}\Big(\tilde{\kappa}_o\big(1/(a+1)\big) + \tilde{\kappa}_o\big(a/(a+1)\big) - \tilde{\kappa}_o(1)\Big) + \frac{c_{\text{eff}}}{6}\ln(a+1), \tag{3.63}$$

employing Eqs. (3.53) and (3.55) for $\tilde{\kappa}_e$ and $\tilde{\kappa}_o$, respectively, and recalling that c_{eff} is defined in Eq. (3.21), while s_0 is introduced in Sec. 3.1.2 (where it depends on the Hamiltonian in Eq. (3.19)). These six results appear in Eq. (3.46) (with a notational shift $I^{(i)}_{\text{env}}(L,a) \equiv I^{(i)}_{\text{env}}(A_1 : A_2)$).

When $a = 1$, certain breaking-point sequences merge, leaving just four families. This reflects the fact that only two independent length scales remain in that specific scenario. Furthermore, when the SDRG has a single cycle (rather than two), the two sets of breaking points Λ_{2k-1} and Λ_{2k} merge into one unified set, halving the total number of envelope functions. Thus, the logic behind the analytic envelope derivation corroborates the content of Table 3.1.

Finally, let us comment on the mutual information for disjoint intervals, where $d \neq 0$. In this setting, one is interested in the mutual information as a function of d for fixed L_1 and L_2; see also Fig. 3.4. According to Eq. (3.43), eight families of breaking points occur $d = \Lambda_{2k}$, $d = \Lambda_{2k-1}$, $d = \Lambda_{2k} - L_1$, $d = \Lambda_{2k-1} - L_1$, $d = \Lambda_{2k} - L_2$, $d = \Lambda_{2k-1} - L_2$, $d = \Lambda_{2k} - L_1 - L_2$, $d = \Lambda_{2k-1} - L_1 - L_2$, where $k \in \mathbb{N}$ and the Λ_k values are given by Eqs. (3.25), (3.26). However, inserting such points into Eq. (3.43) requires evaluating entanglement entropies at arguments like Λ_k + (constant). Because of the floor functions and the logarithmic terms in Eq. (3.48), one can no longer cleanly factor out k in this context. Hence, no well-defined envelope function emerges for the mutual information of disjoint sub-systems. Consequently, no straightforward envelope analogous to that for adjacent intervals can be identified in this case.

3.1.6 Aperiodic Spin Chains with Enhanced Symmetries

In this section we extend the analysis of aperiodic spin chains by incorporating additional symmetry structures inspired by the continuous AdS/CFT correspondence. By leveraging symmetry principles, we construct two families of models and study their strong disorder renormalisation group (SDRG) properties. In the particular case when the ground state lies in an aperiodic singlet phase (ASP), we investigate the entanglement entropy, mutual information, and two-spin correlation functions.

Within the AdS/CFT framework the boundary operators transform covariantly under the conformal group, which coincides with the isometry group of AdS spacetime. This symmetry matching is one of the hallmarks of holographic duality. In the discrete holographic construction presented in [157] and reviewed in Sec. 3.1.1, the finite hyperbolic $\{p, q\}$ tiling exhibits a discrete symmetry group D_n, where the integer n is naturally identified with either p (for polygon-centered tilings) or q (for vertex-centered tilings). This observation motivates the definition of aperiodic spin chains whose local degrees of freedom are organised into multiplets transforming under irreducible representations of D_n.

A further feature of continuous AdS/CFT is the emergence of a large N limit, as in the case of $SU(N)$ gauge theories. In our discrete setup we incorporate a similar notion by considering spin chains with a global $SO(N)$ symmetry where the spin degrees of freedom are given by the generators of $SO(N)$ in the fundamental representation. (It is important to note that this implementation of a large number of degrees of freedom is distinct from the conventional large N gauge limit, since the symmetry here remains global.) The choice of $SO(N)$, rather than $SU(N)$ in the adjoint, is key to attaining a critical aperiodic spin chain with an ASP at the SDRG fixed point.

D_n–Symmetric Spin Chain Hamiltonians

We now detail the construction of aperiodic spin chain models that are invariant under the dihedral group D_n, embodying the intrinsic symmetry of the underlying finite hyperbolic tiling. Our aim is to generalise the familiar spin-$\frac{1}{2}$ XXX Hamiltonian

$$H^{\mathrm{XXX}}_{\{p,q\}} = \sum_i J_i \, \vec{\sigma}_i \cdot \vec{\sigma}_{i+1} \,, \tag{3.64}$$

(which corresponds to a specific instance of Eq. (3.19) with $h(\vec{\sigma}_i \cdot \vec{\sigma}_{i+1}, \theta_i) = \vec{\sigma}_i \cdot \vec{\sigma}_{i+1}$) so that its spin degrees of freedom are arranged into multiplets transforming in irreps of D_n.

The representation theory of the dihedral group D_n is completely known: its irreducible representations are either one- or two-dimensional. In fact, when n is even there are four one-dimensional irreps, while for odd n only two exist. We denote by $\vec{\sigma}_l$ the one-dimensional multiplets (with $l = 1, \ldots, 4$ or $l = 1, 2$, depending on the parity of n). Under the action of a generator $\lambda \in \{r, s\}$ of D_n, these multiplets transform as

$$U_l(\lambda) \, \vec{\sigma}_{i,l} \, U_l(\lambda^{-1}) = \Phi_l(\lambda) \, \vec{\sigma}_{\lambda(i),l} \,, \tag{3.65}$$

where $U_l(\lambda)$ is the unitary operator acting on the ith site and $\lambda(i)$ denotes the transformed site index. For the purpose of our construction we retain only those one-dimensional irreps that are invariant under the rotation generator r (i.e. those with a trivial phase), which in the

notation of 3.1.1 correspond to Φ_1 and Φ_3. We adopt the unified labels

$$\Phi_+ \equiv \Phi_1\,, \qquad \Phi_- \equiv \Phi_3\,,$$

and accordingly relabel the associated spin degrees of freedom as $\vec{\sigma}_{i,+}$ and $\vec{\sigma}_{i,-}$. Their transformation laws become

$$U_\pm(r)\,\vec{\sigma}_{i,\pm}\,U_\pm(r^{-1}) = \vec{\sigma}_{r(i),\pm}\,, \qquad U_\pm(s)\,\vec{\sigma}_{i,\pm}\,U_\pm(s^{-1}) = \pm\vec{\sigma}_{s(i),\pm}\,. \tag{3.66}$$

Here, the action of the reflection generator s distinguishes a scalar (for the $+$ multiplet) from a pseudo-scalar (for the $-$ multiplet). In constructing invariant Hamiltonian terms, one may consider, for instance,

$$\left(\vec{\sigma}_{i,l}\cdot\vec{\sigma}_{i+1,l}\right)^{\mathscr{P}_1} \quad \text{or} \quad \left(\vec{\sigma}_{i,l_1}\cdot\vec{\sigma}_{i+1,l_2}\right)^{2\mathscr{P}_2}\,, \tag{3.67}$$

with $\mathscr{P}_1, \mathscr{P}_2 \in \mathbb{N}_0$ and $l_1 \neq l_2$. To maintain an analogy with the XXX chain we restrict our attention to the cases $\mathscr{P}_1 = 1$ and $\mathscr{P}_2 = 0$.

We now turn to the two-dimensional irreps of D_n, of which there are $\lceil \frac{n}{2} \rceil - 1$. At each site we introduce the two-component object

$$\vec{T}_{i,m} \equiv \begin{pmatrix} \vec{\tau}_{i,m} \\ \vec{\tilde{\tau}}_{i,m} \end{pmatrix}\,, \qquad m = 1, \ldots, \lceil \tfrac{n}{2} \rceil - 1\,, \tag{3.68}$$

and define the invariant bilinear (or "scalar product") as

$$\vec{T}^{\dagger}_{i,m}\cdot\vec{T}_{i+1,m} = \vec{\tau}_{i,m}\cdot\vec{\tau}_{i+1,m} + \vec{\tilde{\tau}}_{i,m}\cdot\vec{\tilde{\tau}}_{i+1,m}\,. \tag{3.69}$$

The transformation properties under the action of the generators of D_n are given by

$$U_m(r)\,\vec{T}_{i,m}\,U_m(r^{-1}) \;=\; \rho_m(r)\begin{pmatrix} \vec{\tau}_{r(i),m} \\ \vec{\tilde{\tau}}_{r^{-1}(i),m} \end{pmatrix} = \begin{pmatrix} e^{\frac{2\pi i m}{n}}\,\vec{\tau}_{r(i),m} \\ e^{\frac{-2\pi i m}{n}}\,\vec{\tilde{\tau}}_{r^{-1}(i),m} \end{pmatrix}\,, \tag{3.70}$$

$$U_m(s)\,\vec{T}_{i,m}\,U_m(s^{-1}) \;=\; \rho_m(s)\begin{pmatrix} \vec{\tau}_{s(i),m} \\ \vec{\tilde{\tau}}_{s(i),m} \end{pmatrix} = \begin{pmatrix} \vec{\tilde{\tau}}_{s(i),m} \\ \vec{\tau}_{s(i),m} \end{pmatrix}\,, \tag{3.71}$$

where $\rho_m(r)$ and $\rho_m(s)$ are the representation matrices in the mth two-dimensional irrep (see 3.1.1). The differing positions of $\vec{\tau}_{i,m}$ and $\vec{\tilde{\tau}}_{i,m}$ under r motivate interpreting them as analogous to right- and left-moving components under discrete rotations. Invariant bilinear

terms can then be formed by considering expressions such as

$$\vec{T}^{\dagger}_{i,m}\, g^{(m)}\, \vec{T}_{i+1,m}\,, \tag{3.72}$$

where $g^{(m)}$ is a coupling matrix. Requiring invariance under D_n, one must have

$$\rho_m^{-1}(\lambda)\, g^{(m)}\, \rho_m(\lambda) = g^{(m)} \quad \forall\, \lambda \in D_n\,. \tag{3.73}$$

By Schur's lemma, $g^{(m)}$ must then be proportional to the identity, and we set $g^{(m)} = \mathbf{1}_m$ without loss of generality.

In constructing our model the local Hilbert space is organised as follows

$$\mathscr{H}_n = \bigotimes_{i\in\mathbb{Z}} \left[\mathscr{H}_{i,+} \otimes \mathscr{H}_{i,-} \bigotimes_{m=1}^{\lceil n/2\rceil - 1} \left(\mathscr{G}_{i,m} \otimes \tilde{\mathscr{G}}_{i,m} \right) \right], \tag{3.74}$$

where the one-dimensional degrees of freedom $\vec{\sigma}_{i,\pm}$ act on $\mathscr{H}_{i,\pm}$, and the two-dimensional objects $\vec{T}_{i,m}$ act on $\mathscr{G}_{i,m}$ and $\tilde{\mathscr{G}}_{i,m}$. As each constituent Hilbert space is two-dimensional, the total local Hilbert space has dimension $2^{2\lceil \frac{n}{2}\rceil}$.

Combining the invariant bilinear terms for the one-dimensional multiplets (with $\mathscr{P}_1 = 1$) and the two-dimensional multiplets (with $g^{(m)} = \mathbf{1}_m$), we propose the Hamiltonian

$$H^{\text{dih}}_{\{p,q\}} = \sum_i \left[J_i^{(+)}\, \vec{\sigma}_{i,+} \cdot \vec{\sigma}_{i+1,+} + J_i^{(-)}\, \vec{\sigma}_{i,-} \cdot \vec{\sigma}_{i+1,-} + \sum_{m=1}^{\lceil \frac{n}{2}\rceil - 1} J_i^{(m)}\, \vec{T}^{\dagger}_{i,m} \cdot \vec{T}_{i+1,m} \right]. \tag{3.75}$$

Here, all couplings $J_i^{(+)}$, $J_i^{(-)}$, and $J_i^{(m)}$ are modulated aperiodically according to the sequence $\mathscr{S}_{\{p,q\}}$. By construction, Eq. (3.75) is manifestly invariant under the dihedral group D_n (see Eqs. (3.66) and (3.70)–(3.71)). Moreover, it may be interpreted as a direct sum of $2\lceil \frac{n}{2}\rceil$ independent spin-$\frac{1}{2}$ XXX Hamiltonians (cf. Eq. (3.64)), each acting on a separate two-dimensional Hilbert space in the decomposition (3.74).

This decomposition has significant implications when the chain flows to an ASP under SDRG. In that case, the entanglement entropy for each copy is given by Eq. (3.20) with $s_0 = \ln 2$, so that the overall effective central charge is rescaled to

$$c_{\text{eff}}^{\text{total}} = 2\lceil \frac{n}{2} \rceil\, c_{\text{eff}}\,, \tag{3.76}$$

with c_{eff} defined in Eq. (3.21). In our discrete holographic perspective the parameter n (which may be chosen as p or q) controls the aperiodic modulation of the couplings; in the limit $n \to \infty$ the boundary theory has an increasingly large number of local degrees of freedom and the corresponding bulk tiling approaches either a $\{\infty, q\}$ or a $\{p, \infty\}$ geometry. Notably,

this tunable parameter does not have an analog in conventional continuous AdS/CFT.

An interesting instance is provided by the infinite family of $\{6, q\}$ modulations with $q \geq 4$. In the spin-$\frac{1}{2}$ case the effective central charge was computed in [157] as

$$c_{\text{eff}}(6, q) = \frac{6 - 2q + \sqrt{q^2 - 5q + 6}}{\ln\left(2q - 5 + 2\sqrt{q^2 - 5q + 6}\right)} \frac{6 \ln 2}{6 - 2q} . \tag{3.77}$$

While $c_{\text{eff}}(6, q)$ decays as $1/\ln q$ for $q \to \infty$, the inclusion of D_q symmetry via Eq. (3.75) rescales the effective central charge by a factor of q, yielding a markedly different large-q behaviour.

Finally, since the Hamiltonian in Eq. (3.75) is a sum of independent spin-$\frac{1}{2}$ XXX models, the analysis of two-point correlation functions presented in Sec. 3.1.3 applies directly. In practice, only degrees of freedom belonging to the same multiplet (and, more restrictively, the same component within the multiplet) exhibit nonvanishing correlations. Consequently, correlators such as $\langle \sigma_{i,+} \sigma_{i+r,+} \rangle$ or $\langle \tilde{\tau}_{i,m} \tilde{\tau}_{i+r,m} \rangle$ are computed using Eqs. (3.24) and (3.36) with the coefficient $c_0 = -1$ remaining unaltered, as it depends solely on the two-point functions of the Pauli matrices.

In summary, by arranging the local degrees of freedom into multiplets of the dihedral group, the Hamiltonian in Eq. (3.75) not only inherits the geometric symmetry of the underlying hyperbolic tiling but also enables the exploration of regimes with a large number of local degrees of freedom. This framework permits a straightforward adaptation of the results for entanglement and correlation properties developed for spin-$\frac{1}{2}$ aperiodic XXX chains.

3.1.7 $SO(N)$ aperiodic spin chains

In this subsection, we investigate a class of aperiodic spin chains exhibiting a global $SO(N)$ symmetry. We shall explicitly construct their Hamiltonians in a regime where the conditions outlined in Sec. 3.1.2 are satisfied. Under these circumstances, the entanglement entropy of a contiguous block of sites and its corresponding envelopes take the forms specified in (3.20) and (3.21), respectively, with the constant s_0 given by $s_0 = \ln N$. An analogous conclusion holds for the mutual information discussed in Sec. 3.1.4, again featuring $s_0 = \ln N$. As a direct implication, when $N \to \infty$, the effective central charge of these models diverges logarithmically, which is consistent with the proliferation of degrees of freedom (DOFs).

We focus on an aperiodic chain whose Hamiltonian is formally given by (3.19). In

particular, we choose the local interaction h to be [215]

$$h\Big(\vec{\sigma}_i \cdot \vec{\sigma}_{i+1}, \theta\Big) = \cos\theta\, \vec{\sigma}_i \cdot \vec{\sigma}_{i+1} + \sin\theta \left(\vec{\sigma}_i \cdot \vec{\sigma}_{i+1} + \frac{2\Big(\vec{\sigma}_i \cdot \vec{\sigma}_{i+1}\Big)^2}{N-2} \right), \qquad N > 2\,. \tag{3.78}$$

Here, $\vec{\sigma}_i$ comprises $N(N-1)/2$ generators of the $SO(N)$ group in the fundamental representation (for an elementary overview of Lie groups and their representations, see [216]). Concretely,

$$\vec{\sigma}_i = \left(\sigma_i^{(1)}, \sigma_i^{(2)}, \ldots, \sigma_i^{\left(\frac{N(N-1)}{2}\right)} \right)^{\mathrm{t}}. \tag{3.79}$$

The resulting Hamiltonian enjoys global $SO(N)$ invariance, manifest in the invariance under the following unitary representation acting on each spin DOF

$$\vec{\sigma}_i \;\to\; U_{\vec{k}}^{\dagger}\, \vec{\sigma}_i\, U_{\vec{k}}\,, \quad U_{\vec{k}} \;\equiv\; e^{\,\mathrm{i}\sum_{j\in\mathbb{Z}} \vec{k}\cdot\vec{\sigma}_j}\,,$$

where $\vec{k}$ is an $N(N-1)/2$-dimensional real vector of parameters. This symmetry can be verified by observing that the Hamiltonian in (3.19) and (3.78) commutes with every component of $\sum_{j\in\mathbb{Z}} \vec{\sigma}_j$. Moreover, one can show that the form in (3.78) is actually the most general $SO(N)$-invariant nearest-neighbor Hamiltonian [215, 217], since higher powers of $\Big(\vec{\sigma}_i \cdot \vec{\sigma}_{i+1}\Big)$ can be reduced to combinations of $\Big(\vec{\sigma}_i \cdot \vec{\sigma}_{i+1}\Big)$ and $\Big(\vec{\sigma}_i \cdot \vec{\sigma}_{i+1}\Big)^2$.

In what follows, we assume that the coupling θ in (3.78) remains uniform across the chain; hence, the only aperiodic modulation arises from the hopping parameters J_i in (3.19). When $J_i = J$, the model is homogeneous. For the corresponding $SO(N)$ chain at homogeneous couplings, a phase diagram was derived in [217], showing that the system is critical in the two intervals $\pi/4 \leqslant \theta \leqslant \pi/2$ and $-\pi/2 \leqslant \theta \leqslant -\pi/4$. By restricting θ to these critical regimes, and imposing aperiodic modulations J_i prescribed by $\mathscr{S}_{\{p,q\}}$, condition 1 of Sec. 3.1.2 (criticality of the unperturbed chain) is satisfied.

Previous studies [215] dealt with $SO(N)$-invariant spin chains in disordered settings, and an appropriate strong-disorder RG (SDRG) procedure was introduced. Below, we extend that analysis to the aperiodic case. Concretely, we focus on the sequences $\mathscr{S}_{\{p,q\}}$ with $\{p,q\} = \{6,q\}$, $\{5,4\}$, $\{5,5\}$, $\{3,7\}$, or $\{3,8\}$. These particular sequences ensure that the emergent SDRG involves either one-cycles or two-cycles, so that only two-spin blocks appear throughout the entire RG flow. To obtain an aperiodic singlet-product (ASP) ground state, we require that the local Hamiltonian (3.78) has a singlet as its ground state. By examining the decomposition of two fundamental $SO(N)$ representations (where the fundamental representation of $SO(N)$ is self-conjugate), one finds three possible irreps: dimension $(N+2)(N-1)/2$, dimension $N(N-1)/2$, and a one-dimensional representation

(the singlet). It was shown in [215] that the singlet is the ground state of (3.78) if $-3\pi/4 < \theta < \arctan\left(\frac{N-2}{N+2}\right)$. Therefore, for $-\pi/2 \leqslant \theta \leqslant -\pi/4$, the aperiodic chains introduced here satisfy conditions 3 and 4 of Sec. 3.1.2 as well.

Mathematically, it is worth noting that self-conjugate irreps always contain singlets [216]. While $SO(N)$ and $SU(2)$ both have self-conjugate fundamental representations, the fundamental representation of $SU(N)$ with $N > 2$ is not self-conjugate, implying that in such $SU(N)$ models, the tensor product of two fundamentals does not include any singlet. Hence, Hamiltonians analogous to (3.19) with $SU(N)$ generators in the fundamental representation would not yield ASPs for $N > 2$.

To judge whether our chosen modulations from $\mathscr{S}_{\{p,q\}}$ are relevant, we look at the flow of the coupling constants under SDRG. A second-order perturbative treatment [215] shows that, when a two-spin block is decimated, the couplings are renormalised according to

$$J' \cos\theta' \;=\; f_1(N)\,\frac{J^2\,(\cos\theta)^2}{J_0\Big(g(N)\;-\;\tan\theta_0\Big)}\,,\;\; J'\sin\theta' \;=\; f_2(N)\,\frac{J^2\,(\sin\theta)^2}{J_0\Big(1\;-\;\tan\theta_0\Big)}\,, \tag{3.80}$$

where

$$f_1(N) \;\equiv\; \frac{4}{N(N+2)}, \qquad f_2(N) \;\equiv\; -\frac{4}{N^2}, \qquad g(N) \;\equiv\; \frac{N-2}{N+2}. \tag{3.81}$$

In these expressions, J_0 and θ_0 are the couplings within the two-spin block just before its decimation, while J and θ represent the couplings connecting that block to the remaining chain, and J', θ' are the renormalised quantities (see also Fig. 3.2). Since there are two independent terms in (3.78), J and θ each flow non-trivially during the decimation step.

For $SO(N)$-invariant aperiodic chains, the explicit coupling flows emerge from (3.80) by adapting arguments originally applied in [157, 184, 203]. By way of illustration, take $\mathscr{S}_{\{6,q\}}$ with $q \geq 4$. This family accommodates both two-cycle ($q > 4$) and one-cycle ($q = 4$) SDRGs. Following the steps in Sec. 3.3 of [157] and adjusting them to the Hamiltonian (3.19), (3.78), one obtains, after a sequence-preserving transformation, the following renormalised couplings

$$\begin{aligned}
J'_a \cos\theta'_a &= J_a^{q-1}\, J_b^{2-q}\, \frac{f_1(N)^{2q-5}\left(\cos\theta_a\right)^{q-1}}{\Big[\cos\theta_b\left(g(N)-\tan\theta_b\right)\Big]^{q-2}\Big[g(N)+B\Big(N,\theta_a,\theta_b\Big)\Big]^{q-3}}, \\
J'_a \sin\theta'_a &= J_a^{q-1}\, J_b^{2-q}\, (\tan\theta_a)^{q-3}\, \frac{f_2(N)^{2q-5}\left(\sin\theta_a\right)^{q-1}}{\Big[\cos\theta_b\left(1-\tan\theta_b\right)\Big]^{q-2}\Big[1+B\Big(N,\theta_a,\theta_b\Big)\Big]^{q-3}},
\end{aligned} \tag{3.82}$$

and

$$J_b' \cos\theta_b' = J_a^{q-2}\, J_b^{3-q}\, \frac{f_1(N)^{2q-7}\left(\cos\theta_a\right)^{q-2}}{\left[\cos\theta_b\left(g(N)-\tan\theta_b\right)\right]^{q-3}\left[g(N)+B\Big(N,\theta_a,\theta_b\Big)\right]^{q-4}},$$
$$J_b' \sin\theta_b' = J_a^{q-2}\, J_b^{3-q}\,(\tan\theta_a)^{q-4}\, \frac{f_2(N)^{2q-7}\left(\sin\theta_a\right)^{q-2}}{\left[\cos\theta_b\left(1-\tan\theta_b\right)\right]^{q-3}\left[1+B\Big(N,\theta_a,\theta_b\Big)\right]^{q-4}}, \tag{3.83}$$

where

$$B\Big(N,\theta_a,\theta_b\Big) \;=\; (\tan\theta_a)^2\left(\frac{N+2}{N}\right)\frac{\left(g(N)-\tan\theta_b\right)}{\left(1-\tan\theta_b\right)},$$

with f_1, f_2, g given by (3.81). Observe that, in each sequence-preserving step, several strong bonds may be decimated simultaneously, so (3.80) must be recombined appropriately to generate (3.82)–(3.83) (see [157, 184, 203] for details). An important point is that even if θ is initially homogeneous across the chain, an effective aperiodicity for θ itself can arise under the flow.

Our primary interest lies in the behaviour of $r = J_a/J_b$ and of the angles θ_a, θ_b. From (3.82)–(3.83), one can evaluate the RG fixed points by examining

$$\tan\theta_i' \;=\; \left(\frac{f_2(N)}{f_1(N)}\right)^{2\,(q-k_i)+1}\left[\frac{(\tan\theta_a)^2\,(g(N)-\tan\theta_b)}{(1-\tan\theta_b)}\right]^{q-k_i+1}\left[\frac{g(N)+B\Big(N,\theta_a,\theta_b\Big)}{1+B\Big(N,\theta_a,\theta_b\Big)}\right]^{q-k_i}, \tag{3.84}$$

where $i = a, b$ and $k_a = 3$, $k_b = 4$. Within the interval $-\pi/2 \leqslant \theta \leqslant -\pi/4$, one obtains an unstable fixed point at $\theta_a = \theta_b = -\pi/4$ and a stable fixed point at $\theta_a = \theta_b = -\pi/2$. In addition, the ratio r renormalizes according to

$$r' \;=\; r\,C\Big(q,N,\theta_a,\theta_b\Big), \tag{3.85}$$

with $C\Big(q,N,\theta_a,\theta_b\Big)$ derivable from (3.82)–(3.83). Crucially, $C(q,N,\theta_a,\theta_b) < 1$ for $-\pi/2 \leqslant \theta_{a,b} \leqslant -\pi/4$, $q \geq 4$, and $N > 2$. Hence $r' < r$, driving $r \to 0$ upon iteration. Consequently, these aperiodic modulations are relevant (fulfilling condition 2 in Sec. 3.1.2), pushing the system toward a new aperiodicity-induced RG fixed point. Analogous conclusions hold for the other $\{p, q\}$ pairs listed at the start of this section.

It is also worth highlighting that these disorder-driven fixed points are attractive in r, whereas the fixed points of the corresponding homogeneous models are repulsive with respect to r. This implies that any small deviation from homogeneity, i.e. $r \neq 1$, is sufficient to shift the system to the new, aperiodic fixed point. Such behaviour emerges in both the

$SO(N)$ model considered here and in the $SU(2)$ XXX aperiodic chain discussed in Sec. 3.1.2 (see also Sec. 3 of [157] for a detailed explanation of the fixed-point structure).

Summarising our findings thus far: starting from any J_a, J_b, the ratio $r = J_a/J_b$ flows to zero (via (3.85)), while a uniform $-\pi/2 \leqslant \theta \leqslant -\pi/4$ under RG either remains at $\theta = -\pi/4$ if that is the initial value or flows to $\theta = -\pi/2$ otherwise. In both cases, the aperiodic chain described by (3.19), (3.78), and the specific modulations just discussed meets all four conditions of Sec. 3.1.2, ensuring it belongs to an ASP. Therefore, its entanglement entropy follows (3.20) and its mutual information follows (3.42). The only undetermined constant is s_0. A direct calculation [206] shows that $s_0 = \ln N$. This modifies the effective central charge introduced in (3.20) so it depends on N. In fact, the effective central charge diverges logarithmically as $N \to \infty$, which differs from the typical power-law growth in N exhibited by standard AdS_3/CFT_2 in continuum contexts [23, 26, 180]. Since the role of N in the spin chain differs from its role in conventional continuous AdS/CFT descriptions, a discrepancy of this sort should not be surprising.

Next, let us briefly comment on two-point correlation functions for spins bound in the same singlet, following the arguments in Sec. 3.1.3. As stated there, for any ASP we can write the two-point functions of spins in the same singlet through (3.36), which involves a model-dependent constant c_0. For $SO(N)$ aperiodic chains with local interactions (3.78), one has $c_0 = -2/N$. Consequently, altering the Hamiltonian to a different aperiodic model does not affect the dependence of correlation functions on p and q; it simply modifies c_0.

Finally, a remark regarding the tensor-network (TN) interpretation of the ground states of these $SO(N)$ aperiodic chains: as mentioned in Sec. 3.1.2, one must choose a relevant aperiodicity fully determined by $\mathscr{S}_{\{p,q\}}$. Thus, the TN graph structure that exactly represents the ASP ground state remains the same as in [157], except that one must update the bond dimension to N. In other words, the maximal entanglement for each tensor leg—previously $\ln 2$ in the $SU(2)$ chain—now becomes $\ln N$. Aside from this bond-dimension change, the construction of the TN follows precisely as described in [157], and all key properties remain intact [218]. The geometry of this TN reflects the correlations in the boundary ground state, providing a geometric underpinning for the entanglement entropy, as well as a simple interpretation of the mutual information. For example, each peak in Fig. 3.4 corresponds to a TN leg stretching across the bulk between two spins forming a singlet, thereby contributing to the mutual information whenever both spins lie in the specified intervals. While we do not observe a sharp transition analogous to continuum AdS/CFT, the geometric meaning of these peaks in the TN picture remains transparent.

3.1.8 Discussion

In this Section we have explored infinite spin chains with couplings modulated aperiodically by sequences that characterize the boundaries of regular hyperbolic tilings of the Poincaré disk. These models, introduced in [157], serve as an initial step toward realising a holographic duality in which the bulk is described by a regular hyperbolic tiling. The principal findings of our study can be summarised as follows.

We have developed a comprehensive framework for analysing aperiodic singlet phases (ASPs) at strong-disorder renormalisation group (SDRG) fixed points. This framework relies on the conditions 1-4 specified in Sec. 3.1.2, which encompass criticality, gaplessness, a specific cyclic behaviour under SDRG transformations, and the existence of an ASP. In particular, these conditions guarantee that the entanglement entropy is given directly by (3.20). Moreover, for an aperiodic Hamiltonian of the form (3.19)—with the function h and the spin degrees of freedom left generic—these criteria ensure that one can straightforwardly compute both the correlation functions and the mutual information.

Within this setup, we have obtained the two-point correlation function for spins within the same singlet in an ASP, thereby extending the results of [184] to cases where the SDRG exhibits a two-cycle behaviour. Our analysis reveals that the correlation function decays as a power law with the spin separation, with an exponent equal to one, as expressed in (3.36). Additionally, we have adapted a continuum AdS/CFT result—which relates the correlation functions of boundary operators with large scaling dimensions ($\Delta \gg 1$) to bulk geodesics [208, 209]—to our discrete framework, where the bulk is modeled by a hyperbolic tiling. This modification, detailed in (3.40), effectively associates the correlation function with a scaling dimension larger than Δ.

Our work also introduces new analytic results for the mutual information between blocks of consecutive sites in these aperiodically modulated spin chains, as summarised in (3.43). These results generalise those of [210] from the context of random couplings to that of aperiodic modulations. Consistent with previous studies on the entanglement entropy [157, 201, 202], the mutual information is found to exhibit a piecewise linear behaviour. For adjacent subsystems, the logarithmic enveloping functions given in (3.46) differ only by an additive constant, whose analytic expression has been determined (cf. 3.1.5). These envelopes agree with the behaviour predicted by conformal field theory [185, 212–214], featuring a prefactor that reproduces the modulation-dependent effective central charge in (3.20). We also show that the number of such envelopes depends on the relative sizes of the subsystems and on whether the ASP originates from a one-cycle or a two-cycle SDRG (see Table 3.1 on page 72). When considering disjoint intervals, our findings indicate that the mutual information decays as a function of the number d of sites separating the regions. More specifically, as d increases,

intervals with vanishing mutual information become increasingly extended, interspersed by isolated peaks (see Fig. 3.4). However, owing to the long-range connections inherent in the ASP, no finite separation d_c exists beyond which the mutual information remains identically zero—thus, the sharp phase transition observed in continuous AdS/CFT is absent in the discrete setup.

Motivated by key features of continuous AdS/CFT—namely, the matching of symmetries between the bulk and boundary, and the large-N limit—we have also investigated two concrete models that satisfy the conditions 1-4 of Sec. 3.1.2. In the first model, a spin-1/2 XXX chain is considered in which the local spins form multiplets transforming covariantly under the dihedral group D_n (cf. (3.75)). In this case the effective central charge found in [157] is rescaled by a factor linear in n, and for $\{6, q\}$ modulations in the large $n = q$ limit the rescaled effective central charge grows with q. In the second model, we analyze an aperiodic Hamiltonian with a global $SO(N)$ symmetry, as given in (3.78). Here the effective central charge diverges as $\ln N$ when $N \to \infty$, a behaviour that reflects the increasing number of local degrees of freedom.

It is crucial to note that, while our research is inspired by the program of discrete holography, the present spin-chain models do not reproduce all features of holographic duality. In particular, these models lack a strong-coupling limit—a fundamental aspect of traditional holographic dualities—and they do not possess a gauge symmetry, featuring instead a global $SO(N)$ symmetry. Nevertheless, by pursuing this line of investigation, we have identified several promising directions for future work aimed at incorporating these essential features.

One promising direction is to consider models that incorporate elements of the Sachdev-Ye-Kitaev (SYK) paradigm [181, 182], as exemplified by chains studied in [219]. In the low-energy, large-N regime, the $(0 + 1)$-dimensional SYK model—describing N strongly interacting Majorana fermions—is exactly solvable and characterised by an effective Schwarzian action. Moreover, this model is conjectured to be holographically dual [182, 220, 221] to Jackiw-Teitelboim (JT) dilaton gravity [222, 223]. Introducing aperiodicities into SYK-like chains could thus offer new perspectives on discrete holographic duality while extending the known holographic properties of the SYK model and JT gravity.

Another exciting prospect is to extend the tensor-network (TN) description developed in [157] to finite-temperature aperiodic spin chains. In the continuous AdS/CFT framework, thermal CFT states are dual to black holes in asymptotically AdS spacetimes [22]. Therefore, a TN realisation for aperiodic spin chains at finite temperature might naturally reveal the emergence of event horizons in the discrete bulk without resorting to ad hoc modifications of the network.

Finally, the incorporation of dynamical degrees of freedom in the bulk represents a key step towards constructing a bona fide discrete holographic duality. In this context, the framework

of *edge length dynamics* [224], originally developed for p-adic AdS/CFT [225–228] and designed for tree graphs, offers a promising route. This approach allows for fluctuating edge lengths in graphs that discretize hyperbolic space and leads to a discrete, graph-theoretic version of the Einstein-Hilbert action, whereby probabilistic weights are assigned to different edge configurations. Generalising this method to hyperbolic tilings with closed loops could provide the necessary ingredients to introduce bulk dynamics into the discrete holography program.

3.2 Geometric Quantum Discord and Holography

As highlighted in our discussion on discrete holography, the AdS/CFT correspondence [21–23] has driven major progress in high-energy physics by revealing a deep relationship between gravity, quantum field theory, and geometry—as encapsulated in the holographic principle [24, 25, 229]—with quantum information measures such as entanglement entropy [32, 33, 35] and complexity [38–40] serving as key tools in refining this connection.

Yet, there are instances where this bulk/boundary mapping appears to lead to paradoxes. A striking example is the so-called *thermofield double* (TFD) state, formed by taking a weighted sum over energy eigenstates of two copies of a CFT, which is holographically dual to an eternal two-sided black hole in AdS [230]. One can view the TFD as a purification of the thermal state describing the black hole exterior at finite temperature. On the boundary side, the CFT Hilbert space factorises as $\mathscr{H}_{\text{TFD}} = \mathscr{H}_L \otimes \mathscr{H}_R$, consistent with the absence of direct interactions between the left and right CFTs. In the bulk, however, the eternal black hole is a smooth geometry with a non-traversable Einstein–Rosen bridge connecting the two asymptotic regions. This wormhole structure is often interpreted as a classical signature of the quantum entanglement linking the left and right CFTs, giving rise to the maximally entangled TFD state—an idea encapsulated by the phrase ER = EPR [116, 117, 231]. From this viewpoint, the bulk geometry does not split in the same way the boundary Hilbert space does, prompting what is referred to as the *factorisation puzzle*.

It is evident that black holes introduce correlations between both sides in the TFD description, with the two CFTs maximally entangled. However, the TFD itself is an extremely fine-tuned pure state with zero von Neumann entropy. By contrast, a realistic black hole is a large thermodynamic object, whose microscopic degrees of freedom account for an enormous entropy. Consequently, one is led to suspect that the actual black hole state should be mixed, with any decoherence hidden from a typical boundary observer. In line with this reasoning, [232] has proposed that, to a low-energy one-sided observer, a typical two-sided black hole is better represented by a so-called *thermomixed double* (TMD)—a classically correlated state devoid of quantum entanglement. While such a state still violates factorisation

in the bulk, it encodes only classical Shannon correlations, suggesting that supplementary quantum correlations beyond ordinary entanglement entropy may be required to resolve the factorisation dilemma.

This motivates the study of broader quantum information measures capable of revealing correlations beyond those captured by entanglement entropy. One such measure is quantum discord [233–235], which remains nonzero even when other common measures—such as entanglement of formation or entanglement negativity—vanish, as shown in analyses of isotropic states [234, 236, 237]. Unfortunately, quantum discord is difficult to calculate in general, as it involves an optimisation over all possible projective measurements, and is thus NP complete [238]. This hurdle has led to the introduction of *geometric quantum discord* (GQD) [239, 240], which is simpler to compute yet still satisfies the property that non-zero GQD implies non-zero quantum discord [239], and furthermore serves as an upper bound on entanglement negativity [241].

In the present work, we propose utilising GQD as an accessible indicator of boundary non-factorisation, as it cleanly encapsulates the presence of purely quantum correlations in general pure states. Specifically, we demonstrate that GQD can be expressed in terms of the second Rényi entropy of an associated classical state, revealing that it coincides with the "geometric measure of quantum correlation" introduced in [242]. Moreover, we show that a non-zero GQD in a holographic state implies a breakdown of factorisation in the boundary, signaled by a failure of the thermal partition function to factorise, with the TFD state serving as a prime example. Within this picture, the TMD state of [232] emerges as a "best classical approximation to the TFD," while our arguments extend naturally to other states describing black holes, including those formed by collapse. We also provide a brief discussion of how GQD might be computed directly from bulk considerations. Finally, we compare our proposal with the non-exactness criterion of [243], clarifying the distinct ways these approaches diagnose the factorisation issue.

3.2.1 Geometric Quantum Discord for Pure States

Calculating quantum discord in explicit settings often proves to be highly non-trivial, owing to the need to perform a minimisation over all possible projective measurements (see (2.56)). This challenge typically restricts analyses to numerical approaches, and even defining quantum discord in quantum field theories remains subtle, as the notion of projective measurements does not straightforwardly extend to field-theoretic contexts (though see [244, 245] for recent progress). To circumvent these complications, [239] introduced *geometric quantum discord* (GQD), reviewed in [240], defined through a minimisation over states rather than

measurements:

$$Q^{(2)}(A:B) \;=\; \min_{\chi\in\Omega_0}\Big\|\rho_{AB}-\chi\Big\|^2, \tag{3.86}$$

where ρ_{AB} is the density matrix for the combined system, $\|X\|^2 = \mathrm{Tr}(X^2)$ denotes the Hilbert–Schmidt norm, and Ω_0 is the space of zero-discord states. Such zero-discord states take the quantum-classical (q-c) form

$$\chi^{\text{q-c}} \;=\; \sum_k q_k\,\rho_k^A \otimes \Big|\phi_k^B\Big\rangle\Big\langle\phi_k^B\Big|, \tag{3.87}$$

where $q_k \geq 0$, $\sum_k q_k = 1$, and $\langle\phi_k^B \mid \phi_l^B\rangle = \delta_{kl}$. Meanwhile, each ρ_k^A describes the quantum state of subsystem A. [3] Reference [239] established that $Q^{(2)}(A:B)$ being non-zero characterizes precisely the same scenarios in which the quantum discord (2.58) also remains non-zero. In other words, GQD vanishes if and only if quantum discord does so. From the perspective of the norm definition, one can interpret the q-c state that achieves the minimum in (3.86) as the "closest" approximation (in the Hilbert–Schmidt sense) to ρ_{AB}.

Here and throughout the remainder of this discussion, we specialise to pure states $\rho_{AB} = |\psi\rangle\langle\psi|$, given their central importance in quantum field theories and in holography. A bipartite pure state $|\psi\rangle$ in the Hilbert space $\mathscr{H}_{AB}$ admits a Schmidt decomposition of the form

$$|\psi\rangle \;=\; \sum_k \lambda_k \Big|\phi_k^A\Big\rangle\Big|\phi_k^B\Big\rangle, \tag{3.88}$$

which in turn implies

$$\rho_{AB} \;=\; \sum_{k,l} \lambda_k\,\lambda_l \Big|\phi_k^A\Big\rangle\Big|\phi_k^B\Big\rangle\Big\langle\phi_l^A\Big|\Big\langle\phi_l^B\Big|, \tag{3.89}$$

where the λ_k are Schmidt coefficients that characterize the entanglement in $|\psi\rangle$. Specifically, the eigenvalues of either reduced density matrix $\rho_{B/A} = \mathrm{Tr}_{A/B}(\rho_{AB})$ are λ_k^2.

We proceed by evaluating the Hilbert–Schmidt norm of ρ_{AB} (3.89) minus a generic q-c state (3.87), obtaining

$$\Big\|\rho_{AB} \;-\; \chi^{\text{q-c}}\Big\| \;=\; 1 \;-\; 2\sum_k \lambda_k^2\,q_k\,\mathrm{Tr}_A\Big(\rho_k^A\Big) \;+\; \sum_k q_k^2\,\mathrm{Tr}_A\Big(\rho_k^A\,\rho_k^A\Big). \tag{3.90}$$

Since $\mathrm{Tr}_A\Big(\rho_k^A\Big) = 1$ by definition, the last term requires additional care. The quantity $\mathrm{Tr}(\rho^2)$, often referred to as the purity, takes a value of 1 if and only if ρ is pure; otherwise, it falls

[3] If one instead chose to measure subsystem A, one would swap ρ_k with $|\,\phi_k\rangle\langle\phi_k\,|$. In that case, the relevant states become classical–quantum (c-q).

strictly between 0 and 1. Minimising (3.90) with respect to q_k by setting its derivative to zero yields

$$q_k \;=\; \frac{\lambda_k^2}{\mathrm{Tr}\big(\rho_k^A\,\rho_k^A\big)}, \tag{3.91}$$

yet one must ensure that the result remains valid under purity considerations. Indeed, if ρ_k^A is not pure, directly substituting (3.91) into (3.90) can produce unphysical (negative) values in the norm expression. An explicit calculation of (2.55) and (2.54) for the Schmidt form (3.88) shows that

$$q_k \;=\; \lambda_k^2 \quad \text{and} \quad \rho_k^A \;=\; \big|\phi_k^A\big\rangle\!\big\langle\phi_k^A\big|. \tag{3.92}$$

In other words, each ρ_k^A must itself be pure. Conceptually, one can see this from the fact that, for pure states, $Q(A:B) \equiv S(\rho_A)$, reflecting the fact that $S(A \mid B) = 0$ for a pure ρ_{AB}. When $S(A \mid B) = 0$, the individual entropies $S(\rho_k^A)$—weighted by q_k—must vanish, which requires each ρ_k^A to be pure, consistent with (3.92).

By substituting (3.92) back into (3.90), one finds that the GQD for the pure state (3.88) becomes

$$Q^{(2)}(A:B) \;=\; 1 \;-\; \sum_k \lambda_k^4. \tag{3.93}$$

Meanwhile, the quantum discord of a pure state ρ_{AB} takes the well-known form $Q(A:B) = S(\rho_A)$, which is generally non-zero. Since the Schmidt coefficients obey $\sum_k \lambda_k^2 = 1$ and $0 \le \lambda_k^2 \le 1$, (3.93) vanishes if and only if there exists a single $\lambda_{k^*} = 1$ (and thus all other $\lambda_{k\neq k^*} = 0$). From the perspective of the Schmidt decomposition (3.88), this pattern corresponds exactly to a product state with zero entanglement, implying $Q(A:B) = S(\rho_A) = 0$.

Our results indicate yet another noteworthy conclusion: the particular q-c state that realizes the minimum in the Hilbert–Schmidt norm is

$$\chi_0^{\text{q-c}} \;=\; \sum_k \lambda_k^2 \big|\phi_k^A\big\rangle\!\big\langle\phi_k^A\big| \;\otimes\; \big|\phi_k^B\big\rangle\!\big\langle\phi_k^B\big| \;\widehat{=}\; \chi_0^{\text{c-c}}\,, \tag{3.94}$$

which is, in fact, a classical-classical (c-c) state. In other words, although the minimisation in (3.86) *a priori* spans the entire family Ω_0 of zero-discord states, it effectively enforces the zero-discord state $\chi^{\text{q-c}}$ to be c-c. This result naturally aligns with the measure $\bar{Q}^{(2)}(A:B)$ introduced in [242]—sometimes referred to as the "geometric measure of quantum

correlations"—defined as

$$\bar{Q}^{(2)}(A:B) \;=\; \min_{\chi\,\in\,\Lambda_0} \frac{\big\|\rho_{AB} \;-\; \chi\big\|^2}{\big\|\rho_{AB}\big\|^2}\,, \tag{3.95}$$

which closely resembles (3.86), except that the minimisation there is taken over the subset Λ_0 of c-c states of the general form

$$\chi^{\text{c-c}} \;=\; \sum_{k,l} q_{kl}\, \big|\phi_k^A\big\rangle\!\big\langle\phi_k^A\big| \;\otimes\; \big|\phi_l^B\big\rangle\!\big\langle\phi_l^B\big|\,. \tag{3.96}$$

Given that $\Lambda_0 \subset \Omega_0$, one might expect a more restricted minimisation domain. Nevertheless, for a pure state ρ_{AB}, $Q^{(2)}(A:B)$ and $\bar{Q}^{(2)}(A:B)$ can be viewed as effectively equivalent, because the unique state that minimizes $Q^{(2)}(A:B)$ in fact lies within Λ_0. By contrast, in the mixed-state setting, the two measures generally differ. An illustrative example is provided by the isotropic two-spin state

$$\rho_{\text{iso}} \;=\; \frac{1-z}{4}\,\mathbb{I}_4 \;+\; \frac{z}{2}\,\Big(\,|00\rangle \;+\; |11\rangle\Big)\,\Big(\,\langle 00| \;+\; \langle 11|\Big), \tag{3.97}$$

for which the GQD evaluates to

$$Q^{(2)}_{\text{iso}}(A:B) \;=\; \frac{z^2}{2}. \tag{3.98}$$

The state (3.87) minimising the geometric discord in this case is

$$q^{\text{iso}}_{0/1} = \tfrac{1}{2}, \quad \rho_0^{A,\,\text{iso}} = \begin{bmatrix} \frac{1+z}{2} & 0 \\ 0 & \frac{1-z}{2} \end{bmatrix}, \quad \rho_0^{B,\,\text{iso}} = \begin{bmatrix} \frac{1-z}{2} & 0 \\ 0 & \frac{1+z}{2} \end{bmatrix}. \tag{3.99}$$

Since these ρ_i^A are generically mixed for general z, the minimising q-c state is not c-c and thus differs from the one that would minimize $\bar{Q}^{(2)}(A:B)$. As a consistency check, note that for $z=1$, the above isotropic state (3.97) itself becomes pure, causing both measures to coincide.

Finally, let us emphasize that the expression for $Q^{(2)}(A:B)$ in (3.93) can alternatively be written in terms of the second Rényi entropy,

$$S^{(k)}(\rho) \;=\; \frac{1}{1-k}\,\ln\,\text{Tr}\Big(\rho^k\Big) \quad \text{for} \quad k=2\,, \tag{3.100}$$

which leads to

$$Q^{(2)}(A:B) \;=\; 1 \;-\; e^{-\,S^{(2)}\left(\chi_0^{\text{q-c}}\right)}. \tag{3.101}$$

By defining the modular Hamiltonian $H_{\text{mod}} \equiv -\,\ln\,\chi_0^{\text{q-c}}$, we can write

$$Q^{(2)}(A:B) \;=\; 1 \;-\; \frac{Z\left(2\,H_{\text{mod}}\right)}{\left(Z\left(H_{\text{mod}}\right)\right)^2}, \tag{3.102}$$

where $Z(H_{\text{mod}})$ is a partition function obtained by substituting $\beta H \mapsto H_{\text{mod}}$. Hence, whenever the modular partition function does not factorise, one infers that A and B share non-zero quantum correlations. Put another way, working in the Schmidt basis lays bare the non-factorising nature of a quantum system via the non-factorisation of its modular partition function. Moreover, in light of the replica trick [166, 207], this reformulation suggests a concrete path to computing GQD in field-theoretic contexts.

3.2.2 Geometric Quantum Discord for the Thermofield Double State

In this section, we specialize to a holographic context and apply the GQD formalism to the Thermofield Double (TFD) state. Our goal is twofold: first, to place the results of the preceding sections within the wormhole scenario of [232], and second, to show how computing the GQD via (3.86) offers a clear boundary-based diagnostic for non-factorisation. Along the way, we review both TFD and TMD (thermomixed double) states, and then provide a fresh perspective on the role of TMD as it emerges in holographic settings.

A TFD state is constructed from two copies of a CFT and takes the form

$$|\text{TFD}\rangle \;=\; \frac{1}{\sqrt{Z(\beta)}}\sum_n e^{-\beta\,\frac{E_n}{2}}\,\left|n_L\right\rangle\left|n_R\right\rangle^*, \tag{3.103}$$

where $Z(\beta) = \sum_n e^{-\beta E_n}$ represents the thermal partition function at inverse temperature β. The states $|n_i\rangle$ have energy eigenvalues $E_{n,i}$, satisfying $E_{n,L} = E_{n,R}$, and we define $E_n = \frac{1}{2}\left(E_{n,L} + E_{n,R}\right)$. The notation $|n_R\rangle^*$ indicates application of an anti-unitary operation, commonly chosen as $\Theta \equiv \mathscr{C}\mathscr{P}\mathscr{T}$, so that $|n_R\rangle^* = \Theta\,|n_R\rangle$. [4] The coefficients $p_n = \frac{1}{\sqrt{Z(\beta)}}\,e^{-\beta\,\frac{E_n}{2}}$ serve as the Schmidt coefficients of (3.103).

[4] In most field-theoretic contexts $\mathscr{C}\mathscr{P}\mathscr{T}$ is used, but any anti-unitary operator can be factored as $V\,K$, with K denoting complex conjugation. Since time-reversal also involves complex conjugation, Θ can generally be identified with $\mathscr{T}$ up to a unitary transformation.

In a holographic interpretation, the pure TFD state above describes an eternal, two-sided AdS black hole. Nevertheless, [232] notes that once the black hole interacts with its surrounding spacetime, dynamical decoherence processes force the overall description into a mixed state by transforming quantum correlations into classical ones. Crucially, from the viewpoint of a single-sided low-energy observer, the black hole should appear thermal both before and after such decoherence. One can see how any quantum information carried by TFD's delicate phase structure becomes effectively randomised: suppose we append phases α_n to each term in (3.103),

$$\left|\mathrm{TFD}\right\rangle_{\alpha} \;=\; \sum_{n} p_n \, \mathrm{e}^{\mathrm{i}\alpha_n} \left|n_L\right\rangle \left|n_R\right\rangle^{*}, \tag{3.104}$$

where these phases are interpreted as arising from the time evolution generated by $H_L + H_R$, with $H_{L/R}$ being the respective boundary Hamiltonians. The local observer cannot detect the global jump in time coordination across the horizon [246], implying that arbitrary choices for $\{\alpha_n\}$ are physically indistinguishable from her perspective. Consequently, it is natural to consider an ensemble average over all possible phases.

This averaging procedure produces the so-called *thermomixed double* (TMD) state [232], given by

$$\rho_{\mathrm{TMD}} = \frac{1}{N} \sum_{\{\alpha\}} |\mathrm{TFD}\rangle_{\alpha\,\alpha}\langle\mathrm{TFD}| \,, \tag{3.105}$$

where N normalizes the sum over all configurations of phases. Because the CFT spectrum is typically chaotic and random, one obtains

$$\rho_{\mathrm{TMD}} \;=\; \sum_{n} p_n^2 \left|n_L\middle\rangle\middle\langle n_L\right| \otimes \left|n_R\middle\rangle\middle\langle n_R\right| , \tag{3.106}$$

by using $\frac{1}{N}\sum_{\{\alpha\}} \mathrm{e}^{\mathrm{i}(\alpha_n - \alpha_m)} \;=\; \delta_{nm}$. The final result describes a two-sided black hole that has lost any quantum entanglement with the environment, leaving only classical correlations behind—a fully decohered state from the perspective of interactions with its surroundings.

We can now address the GQD of the TFD state by directly substituting its Schmidt coefficients, p_n, into our prior result (3.93). This yields

$$Q^{(2)}(L:R) \;=\; 1 \;-\; \sum_{n} p_n^4 \,, \tag{3.107}$$

which indicates that each realisation of the TFD state exhibits quantum correlations between L and R.[5] While it is well known that the TFD state contains quantum correlations (EPR

[5] A parallel calculation would emerge if one employed the phase-shifted state $|\mathrm{TFD}\rangle_{\alpha}$ in place of $|\mathrm{TFD}\rangle$,

pairs) as diagnosed by the entanglement entropy, a striking feature here is the *precise c-c state* identified by the minimisation procedure within the GQD calculation. From our generic pure-state analysis, (3.94), we recognize that this c-c state is exactly the TMD state:

$$\chi_0^{\text{c-c}} \;=\; \sum_n p_n^2\, |n_L\rangle\langle n_L| \otimes |n_R\rangle\langle n_R| \;=\; \rho_{\text{TMD}}\,. \tag{3.108}$$

Remarkably, this derivation hinges solely on quantum information principles and does not presuppose any specific gravitational interpretation, as in [232]. Thus, we gain a fresh perspective on the TMD state: it emerges naturally as *the classical approximation of the TFD state that lacks all EPR-type quantum correlations.* Geometrically, this corresponds to having only classical correlations across the horizon.

Substituting the explicit coefficients p_n allows one to rewrite $Q^{(2)}(L:R)$ in terms of the thermal partition function $Z(\beta)$. The result,

$$Q^{(2)}(L:R) \;=\; 1 \;-\; \frac{\sum_n e^{-2\beta E_n}}{Z^2(\beta)} \;=\; 1 \;-\; \frac{Z(2\beta)}{Z^2(\beta)}, \tag{3.109}$$

echoes the Euclidean path integral formulations presented in [232, 243, 247]. Indeed, [232, 243] established that

$$\text{Tr}\big(\rho_{\text{TMD}}^k\big) \;=\; \frac{Z(k\beta)}{Z^k(\beta)}\,, \tag{3.110}$$

and applying the connection between GQD and the second Rényi entropy (3.101) naturally reproduces (3.109). Section 3.2.3 further explains how (3.109) can arise from self-averaging of black hole microstates. Note that, as (3.102) clarifies, expressing $Q^{(2)}(L:R)$ via the thermal partition function does not apply to *generic* pure states; usually one must employ the *modular* partition function. In the TFD's special case, the entanglement spectrum is thermal, so the standard thermal partition function substitutes for the modular one.

Equation (3.109) highlights several important points. First, $Q^{(2)}(L:R)$ does not generally vanish, implying (by [239]) non-zero quantum discord. This is consistent with the TFD being pure and thus having discord $Q(L:R) = S(\rho_L)$, where ρ_L is thermal and thus nontrivial. Second, $Q^{(2)}(L:R)$ vanishes precisely if $Z(2\beta) = Z^2(\beta)$, signifying factorisation. In the $\beta \to \infty$ limit, $|\text{TFD}\rangle$ degenerates into the product state $|0_L\rangle|0_R\rangle$, annihilating any shared EPR pairs. Geometrically, this high-temperature limit erases the black hole interior, so there is no ER bridge to sustain non-factorisation in the bulk.

Hence, our principal lesson is that non-vanishing quantum discord directly reflects non-factorisation. In the TFD scenario, as per (3.102) and (3.109), one finds that discord is

because the phases drop out when computing the norm.

linked to a failure of the thermal (or modular) partition function to split into separate factors. At $\beta \to \infty$, which effectively zeroes the temperature and eliminates the wormhole region, $Q^{(2)}(L:R)$ and $Q(L:R)$ both drop to zero. More broadly, our general pure-state relation (3.101) supports the correspondence:

$$\text{non-zero quantum discord} \quad \Longrightarrow \quad \text{non-factorisation attributable to quantum correlations.}$$

Of course, classical correlations may also introduce non-factorisation, but in that case $\rho_{\mathrm{TFD}_\alpha}$ becomes ρ_{TMD} by discarding off-diagonal (quantum) components.

In summary, consider a pure state ρ_{AB}, and let us ask whether its (modular) partition function factorises. Though proving factorisation (or otherwise) can be challenging in standard holographic systems—where few direct boundary arguments exist—our findings propose a new computational route. By selecting the c-c state $\rho_{AB}^{\text{c-c}}$ that best approximates ρ_{AB}, one can check (3.101) to see if the associated modular partition function factorises. If it does not factorise for $\rho_{AB}^{\text{c-c}}$, it likewise will not factorise for ρ_{AB}, since both states share the same Schmidt data. This effectively reinterprets the presence of wormhole-like features (non-factorisation) in terms of second Rényi entropies of the classical approximation to ρ_{AB}.[6]

Geometrically, one can view the observed quantum correlations in GQD as subleading $1/N$-effects that are invisible to a low-energy observer. The TFD state, along with its phase-shifted version (3.104) and the TMD state, yield identical predictions for simple operators [246], so it takes high-energy (order-N) probes to distinguish them [248]. The non-zero quantum correlations differentiating TFD from TMD hence appear as $\frac{1}{N}$ corrections.

Lastly, it is interesting that (3.101) fixes the GQD through the second Rényi entropy, for which [249] offers a bulk dual in terms of cosmic branes with tension $T_n = \frac{n-1}{4nG_N}$. These branes backreact on the geometry by producing conical defects of angle $\Delta\phi = 2\pi\frac{n-1}{n}$. When the conical defect disappears, this cosmic brane becomes tensionless and recovers the minimal Ryu–Takayanagi surface [249]. In particular, if $n = 2$, the tension is $T_2 = \frac{1}{8G_N}$, generating a conical defect of $\Delta\phi = \pi$. This strongly hints that the bulk dual of GQD aligns with such cosmic brane geometries.

3.2.3 Geometric Quantum Discord Probing Black Hole Microstates

We have seen that quantum correlations persist precisely when the partition function fails to factorise, i.e. whenever $Z(2\beta) \neq Z^2(\beta)$. In this section, we connect that observation with the

[6] Although factorisation can also arise from purely classical correlations, the GQD approach sidesteps direct evaluation of partition functions by isolating quantum contributions through its minimisation scheme. Hence, it makes the role of genuine quantum correlations transparent.

role of black hole microstates $|\text{TFD}\rangle_\alpha$ introduced in Sec. 3.2.2, following [246]. A particular specification of phases $\{\alpha\}$ determines how left and right boundary times synchronise, effectively deciding how the left and right edges of the geometry are identified with the bulk. Interpreting the GQD in this context amounts to contrasting one specific microstate $|\text{TFD}\rangle_\alpha$ with the TMD state (3.105), which aggregates all microstates into an ensemble average. Crucially, the overlap between the TMD state and any given microstate governs the sign structure that appears in the GQD calculation. Although (3.109) looks like $1 - \text{Tr}(\rho_{\text{TMD}}^2)$, it is actually the cross term

$$\left\| \rho_{\text{TFD}_\alpha} - \rho_{\text{TMD}} \right\|^2 \;=\; 1 \;-\; 2\,\text{Tr}\Big(\rho_{\text{TFD}_\alpha}\,\rho_{\text{TMD}}\Big) \;+\; \text{Tr}\Big(\rho_{\text{TMD}}^2\Big) \tag{3.111}$$

that encodes how phases affect the result. As these phases average out (a phenomenon sometimes referred to as self-averaging), they do not modify the final GQD value.

To see this averaging explicitly, consider the overlap between a generic microstate ρ_{TFD_β} and the TMD state

$$\text{Tr}\Big(\rho_{\text{TFD}_\beta}\,\rho_{\text{TMD}}\Big) \;=\; \frac{1}{N}\sum_{\{\alpha\}} {}_\beta\langle\text{TFD}|\,\text{TFD}\rangle_\alpha \;{}_\alpha\langle\text{TFD}|\,\text{TFD}\rangle_\beta\,. \tag{3.112}$$

Up to $\frac{1}{N}$-suppressed terms, each microstate is approximately orthogonal to the rest, so ${}_\beta\langle\text{TFD}|\text{TFD}\rangle_\alpha \simeq \delta_{\alpha\beta}$. However, precisely because of $\frac{1}{N}$ corrections, it is not valid to commute the phase summation with the approximate orthogonality. This is where the non-factorising behaviour emerges. Concretely, before using the near-orthogonality approximation, one has

$${}_\beta\langle\text{TFD}|\text{TFD}\rangle_\alpha \;=\; \sum_n p_n^2\, \mathrm{e}^{\mathrm{i}(\alpha_n-\beta_n)}, \tag{3.113}$$

and employing $\frac{1}{N}\sum_{\{\alpha\}} \mathrm{e}^{\mathrm{i}(\alpha_n-\alpha_m)} = \delta_{nm}$ in (3.112) reveals that only the term $\sum_n p_n^4$ survives. Analogously, higher-order overlaps of a single microstate with powers of ρ_{TMD} take a similar form

$$\begin{aligned}\text{Tr}\Big(\rho_{\text{TFD}_\beta}\,\rho_{\text{TMD}}^n\Big) &= \frac{1}{N^n}\sum_{\{\alpha\}_1,\ldots,\{\alpha\}_n} {}_\beta\langle\text{TFD}|\text{TFD}\rangle_{\alpha_1}\ldots{}_{\alpha_n}\langle\text{TFD}|\text{TFD}\rangle_\beta \\ &= \sum_m p_m^{2(n+1)} \;=\; \frac{Z\big((n+1)\beta\big)}{Z^{\,n+1}(\beta)},\end{aligned} \tag{3.114}$$

matching the pattern discussed in [250, 251] for astrophysical black holes. There, unitarity implies that realistic black holes also admit a pure-state representation (before decoherence sets in), mirroring what we have here for an eternal black hole. By comparing (3.114) with the results of [250, 251] in the large-mass limit $m_n \gg M$, one sees that a similar "best classical

approximation"—reminiscent of the TMD—applies to black holes formed by collapse, even though our explicit discussion focuses on an eternal geometry.

From a bulk perspective, (3.114) can be viewed as *state averaging* (or *microstate averaging*) [252–254], in contrast to *ensemble averaging* typically invoked for replica wormholes. The sum over phases in (3.113) illustrates precisely this state-averaging mechanism. The normalisation factor $\frac{1}{N}$ in the definition of ρ_{TMD} (3.105) is essential, indicating there are N such microstates, each associated with a distinct choice of phases, and hence yielding $S = \ln N$ at the thermodynamic level [232].

Moreover, these higher overlaps in (3.114), closely related to higher-order spectral form factors [247], naturally arise when generalising the squared Hilbert–Schmidt norm to an nth Schatten norm.[7] In particular, for a Hermitian matrix X, the nth Schatten norm is

$$\|X\|_{(n)} \;=\; \Big[\mathrm{Tr}\Big(\sqrt{X^\dagger X}^{\,n}\Big)\Big]^{\frac{1}{n}} \;=\; \Big[\mathrm{Tr}\Big(X^n\Big)\Big]^{\frac{1}{n}}, \tag{3.115}$$

so setting $X = \rho_{\text{TFD}_\alpha} - \rho_{\text{TMD}}$ leads schematically to

$$\|\rho_{\text{TFD}_\alpha} - \rho_{\text{TMD}}\|^n_{(n)} \;=\; 1 \;+\; \#_1 \frac{Z(2\beta)}{Z^2(\beta)} \;+\; \cdots + \;\#_n \frac{Z(n\beta)}{Z^n(\beta)}, \tag{3.116}$$

where the constants $\#_k$ ensure this expression vanishes precisely if all partition functions factorise ($Z(k\beta) = Z^k(\beta)$ for $1 \leq k \leq n$). Every intermediate ratio of partition functions thus reflects quantum correlation contributions. Similar to (3.101), one can rewrite these ratios in terms of higher Rényi entropies $S^{(n)}$. On the gravitational side, such quantities can again be computed by introducing cosmic branes with suitable tension [249], reinforcing the connection between GQD and the geometry of black holes.

3.2.4 Discussion

This section introduced a geometric measure of quantum correlations, known as geometric quantum discord (GQD) (3.86), as a new means of diagnosing non-factorisation on the boundary. We performed explicit GQD calculations for both generic pure states and the thermofield double (TFD) as a concrete holographic system, demonstrating that a non-zero GQD reflects a failure of the associated partition function to factorise—whether that be a modular partition function in the generic case or a thermal one for the TFD. Within the TFD framework, we showed that wormholes in the bulk are closely tied to GQD, thereby indicating non-factorisation from a dual geometric viewpoint. Moreover, the thermomixed double (TMD) state arose as the unique classical-approximation state that minimizes GQD for

[7] The Hilbert–Schmidt norm corresponds to $n = 2$ as a special case.

the TFD, thus serving as the *closest classical state* to the TFD, in a way that does not require holographic arguments. In fact, our general pure-state analysis suggests this emergence of classical approximations is a generic feature of minimising GQD. This perspective offers a new lens on the factorisation puzzle, especially regarding the TFD's subtle correlations. We also showed that two geometric correlation measures, $Q^{(2)}(A:B)$ (3.86) and $\bar{Q}^{(2)}(A:B)$ from [242], coincide for pure states.

Furthermore, our results demonstrated a direct link between non-zero GQD and the replica wormholes that arise upon state averaging in the path integral, signaled by a non-exact symplectic form. We illustrated this through a quantum-mechanical Hamiltonian whose ground state is precisely the TFD, thereby furnishing an independent argument for the appearance of wormhole microstates and the associated non-factorisation. In addition, we drew parallels between higher-order overlaps of wormhole microstates introduced in [250, 251] and the more general Schatten norms, which extend the familiar Hilbert–Schmidt norm. Although these norms likely admit an information-theoretic interpretation akin to GQD, explicit developments in this direction remain to be pursued.

Looking to the future, several avenues emerge from the results presented in this section. First, extending geometric quantum discord (GQD) to field-theoretic contexts—particularly to two-dimensional conformal field theories—may prove fruitful, given the possible use of replica methods hinted at by (3.101) and efforts to define projective measurements in QFT [244, 245]. One might also seek a bulk realisation of GQD through cosmic branes. Second, as noted in [247], the TMD state (3.105) considered here—labeled the *old TMD*—describes the plateau region of the spectral form factor, while a *new TMD* variant has been linked to the dip regime. Determining the GQD for this new TMD may shed light on partial decoherence in black hole dynamics and transitions between the dip and plateau phases. Finally, exploring GQD beyond the entanglement entropy framework for mixed states remains a compelling challenge, since GQD for mixed states typically does not produce a strictly classical (c-c) minimising state. Although holography frequently treats pure states, one can generate mixed states via double bipartitions of pure states, making it worthwhile to contrast GQD with entanglement negativity—such as in the BTZ black hole setting [255]—and to investigate how $Q^{(2)}(A_1:A_2)$ behaves in these scenarios.

Overall, geometric quantum discord presents a powerful framework for dissecting the quantum correlations in holographic states and diagnosing their non-factorisation. We anticipate that further explorations will refine our understanding of how quantum information theory interweaves with the holographic principle, potentially revealing richer facets of the factorisation puzzle and the role of wormholes as emergent phenomena in gravity.

Quantum Dynamics and Complexity in Spin Chains and Holography

4

In the first part of this thesis, we laid the groundwork in fixed-time quantum correlations by constructing a discrete analogue of holography via aperiodic quantum spin chains on hyperbolic tilings and by studying holographic CFTs using geometric quantum discord (GQD) to isolate purely quantum effects. We now shift our focus to the dynamical aspects of quantum systems, marking the beginning of the second part of this thesis. This new chapter is devoted to exploring the evolution of quantum spin chains, many-body quantum dynamical systems, and holographic models, with particular emphasis on the role of Krylov space methods in characterising state complexity and entropy growth.

A central theme of this chapter is the analysis of quantum dynamics using Krylov subspace techniques. We begin by investigating quantum triangular billiards—systems whose spectral and dynamical properties bridge the gap between integrability and chaos. These differences are closely linked to variations in the underlying classical phase space topology, as will be discussed in further detail.

Building on these insights, we extend our study to non-Hermitian systems. In this context, processes such as continuous measurement, open-system evolution, and $\mathscr{P}\mathscr{T}$-symmetric Hamiltonians induce nonunitary dynamics. By adapting the Lanczos algorithm to non-Hermitian and complex-symmetric Hamiltonians, we examine how wavefunctions spread and how information flows using Krylov-based measures. To address the dynamics of mixed states and to map nonunitary dynamics to unitary evolution, we advance the concept of Krylov complexity of purification. By embedding nonunitary processes within an enlarged Hilbert space, we recover unitary evolution and, through three distinct purification schemes, derive inequalities linking operator and state complexity.

Finally, we extend the Krylov framework to encompass supercoherent states governed by Lie superalgebras. By constructing Krylov lattices for representations of higher-rank algebras, we compute spread complexity in systems containing both bosonic and fermionic degrees of freedom. This extension opens avenues for analysing large-charge string states in the planar limit of AdS/CFT, thus laying the groundwork for a complexity-based characterisation of semiclassical string dynamics and its dual gauge theory description.

In summary, this chapter systematically explores the dynamical evolution of quantum systems through Krylov subspace methods. By developing rigorous measures such as Krylov state and operator complexity and introducing novel diagnostics for nonunitary and

supercoherent dynamics, we reveal deep connections between quantum complexity, chaos, and holographic principles. The insights gained here not only advance our understanding of quantum dynamics in various settings but also provide a unifying framework that bridges traditional quantum many-body physics with modern holographic theories.

4.1 Chaos, Integrability, and Complexity

Chaos and integrability in quantum systems continue to pose challenging open questions. Their distinction is traditionally made through spectral statistics [256]; maximally chaotic systems exhibit level correlations resembling those of random matrix ensembles, while integrable systems typically display uncorrelated, Poisson-distributed spectra [257–266]. Despite these clear-cut definitions at the extremes, many quantum systems manifest behaviour that lies between the integrable and maximally chaotic limits, and a rigorous quantification and characterisation of such intermediate regimes remains elusive. Early-time dynamics can be partially probed through out-of-time-ordered correlators (OTOCs), which exhibit Lyapunov-like growth in chaotic systems with the growth rate bounded by unitarity [267, 268]. Prior investigations have addressed the integrable-to-chaotic transition by utilising complementary local and global quantum statistical measures [269–272]. In the present work, we introduce spread complexity [55] as a novel tool to distinguish among integrable, chaotic, and intermediate "pseudo-integrable" dynamics [273, 274].

To explore these regimes, we focus on triangular quantum billiards [273], where the dynamical type is controlled by tuning just a few parameters. In the classical scenario, a free particle moves inside a billiard, bouncing elastically off the boundaries; quantum mechanically, the dynamics are governed by the two-dimensional Schrödinger equation with a vanishing potential in the interior and an infinitely repulsive potential at the boundaries [274–282]. Although these billiards are not strongly chaotic—the classical Lyapunov exponent is zero due to a linear divergence of initially close trajectories, and the Kolmogorov–Sinai entropy is zero [264, 274, 283, 284]—they can still display ergodic and mixing properties [285–287]. Moreover, replacing the vertices of a polygonal billiard with disks renders the system ergodic, K-mixing, and Bernoulli [288]. The degree of integrability or chaos in these billiards is controlled by their internal angles. An equilateral triangle is classically integrable, as its motion can be solved by quadratures through conserved quantities, whereas triangles with generic rational angles are pseudo-integrable—exhibiting trajectory splitting at the vertices that prevents any global coordinate transformation from yielding constant momenta [273]. Such systems yield quantum spectra that, while exhibiting level repulsion characteristic of chaos, retain an exponential tail in the level spacing distribution typical of integrability [289, 290]. In contrast, triangles with irrational angles typically exhibit mixing dynamics with

spectral statistics analogous to those from the Gaussian Orthogonal Ensemble (GOE) [264]. Furthermore, the symmetry properties of the triangle—for instance, whether it is isosceles or right-angled—have a significant impact on its dynamics. A comprehensive review of these aspects and a tabulation of the integrable, pseudo-integrable, and non-integrable triangles considered in this study is provided in the next subsection.

Generally, chaotic systems produce spectral correlations, whereas integrable theories yield uncorrelated spectra. An integral transform of spectral density correlations, referred to as "spectral complexity," was introduced in [291] and subsequently applied to analyze the stadium billiard [292]. In Sec. 4.1.2, we analyze key spectral properties—namely, the level spacing ratio (LSR), the spectral form factor (SFF), and spectral complexity (SC) [291]—and compare them with analytical predictions for Poisson and GOE spectra. Our analysis reveals that generic pseudo-integrable and non-integrable triangles possess level spacings and LSRs that closely resemble those of the GOE [264, 289], with deviations arising from numerical Hilbert space truncation and scarring effects. In contrast, symmetry plays a more pronounced role in certain cases; isosceles pseudo-integrable and non-integrable triangles often exhibit Poisson-like LSRs due to the statistical independence of eigenvalues corresponding to states of even and odd parity, although when these sectors are analysed separately, GOE-like statistics emerge. Right triangles, meanwhile, display deviations from GOE behaviour that are more intricate to characterise. Additionally, integrable triangles tend to have lower-than-Poisson average LSRs, partly as a consequence of spectral degeneracies. Our analytical work shows that for non-degenerate Poisson spectra, late-time spectral complexity increases linearly, whereas GOE spectra lead to logarithmic growth that eventually saturates in a finite-dimensional Hilbert space. Energy level degeneracies, on the other hand, contribute to a quadratic increase in spectral complexity. These trends are reflected in our findings: integrable triangles, characterised by significant spectral degeneracies, exhibit quadratic late-time SC growth, while generic pseudo-integrable and non-integrable triangles display logarithmic growth with eventual saturation. Notably, isosceles triangles present linear SC growth, closely resembling the Poisson case, yet their symmetric and anti-symmetric sectors diverge markedly, reflecting an overall Poisson-like spectral behaviour coexisting with GOE-like structures in individual sectors.

Chaos is also expected to facilitate the rapid scrambling of information [293] and accelerate the spreading of operators [294, 295], in contrast to integrable dynamics. A measure of operator spread proposed in [135] demonstrates universal early-time behaviour [61, 79, 135, 296–302] and captures signatures of late-time chaos [87, 91, 303–305]. Moreover, chaos is hypothesised to be more efficient at transporting generic initial states throughout the Hilbert space compared to integrable dynamics. To quantify this transport, the notion of "spread complexity" was introduced in [55]. This concept measures the extent of the wavefunction's

spread in a unique minimising basis—the Krylov basis—in which the Hamiltonian is brought to tridiagonal form. For Random Matrix Theories that model maximal chaos, the density of states determines the tridiagonal (Lanczos) coefficients analytically [306, 307]. Consequently, the time dependence of spread complexity offers a direct quantification of information spreading and chaotic dynamics in quantum systems [136, 307].

4.1.1 Triangular Billiards: From Integrable to Non-Integrable Systems

In classical billiards, a frictionless particle moves within a bounded domain and experiences elastic collisions at the boundaries. In the quantum version, the wave function of a free particle evolves within a two-dimensional domain bounded by an infinite potential barrier. To investigate these systems, we numerically solve the Schrödinger equation

$$-\nabla^2\psi_j = \mathscr{E}_j\psi_j, \quad j = 0, 1, 2, \ldots, \tag{4.1}$$

subject to Dirichlet boundary conditions, i.e., $\psi_j(x_\partial) = 0$ for every point x_∂ on the boundary of the triangular region. Without loss of generality, we set the particle mass to $m = \frac{1}{2}$, adopt natural units with $\hbar = 1$, and normalize each triangle to have unit area. For every billiard considered, we compute the lowest $D_0 = 1000$ energy levels, $\{\mathscr{E}_j\}_{j=0}^{D_0-1}$, and, in the case of isosceles triangles, we further resolve the spectrum into symmetric and antisymmetric sectors corresponding to the inherent reflection symmetry.

Topology and Ergodicity of Triangular Billiards

The geometry of a triangular billiard decisively influences the phase space available to a classical particle, thereby determining whether the dynamics are integrable, pseudo-integrable, or chaotic [274–277]. A classical particle's state is described by its position, $q = (x, y)$, and its direction of motion, θ, while the magnitude of its momentum remains constant. Upon reaching the boundary of the triangle, the particle reflects according to the law of specular reflection [273, 308].

A particularly convenient way to understand these reflections is through an *unfolding procedure*: instead of reflecting the trajectory at the boundary, one reflects (or replicates) the entire billiard table across the corresponding side and continues the trajectory in the reflected copy as shown for an example of a rectangular billiard in Fig. 4.1. When the triangle's interior angles are rational multiples of π, the particle's path covers only a finite number of these replicas before recurring [273, 274, 308]. The union of all these copies forms a continuous surface called the *translation surface* (or invariant surface), which is compact in

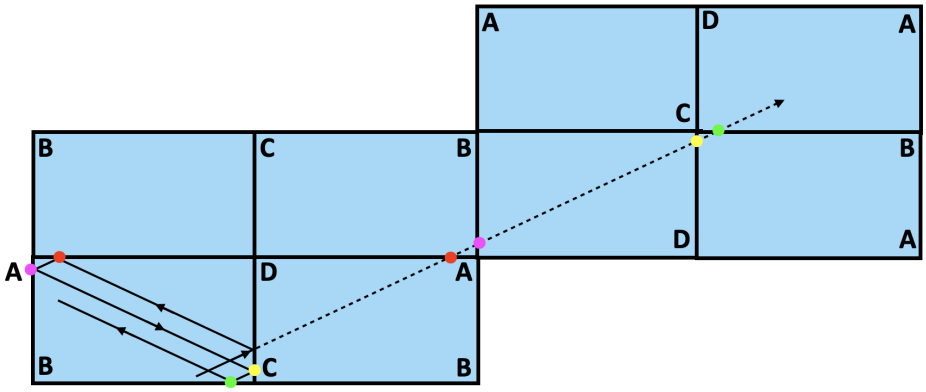

Figure 4.1: Illustration of the unfolding procedure applied to a polygonal billiard. The image depicts the original billiard table alongside several of its reflected copies, arranged to form a continuous tiling. Each reflected domain is generated by reflecting the original billiard across its edges, thereby constructing a translation surface on which the particle's dynamics are recast as straight-line motion. The dashed trajectory, which crosses seamlessly from one reflected copy to the next, represents the path of the particle in the unfolded region—this path is equivalent to the trajectory the particle follows within the original billiard. Notably, four distinct orientations of the rectangle are required to tile the entire surface uniquely.

the case of rational billiards.

For a triangle with rational internal angles expressed as $\left\{\frac{p_1}{q_1}\pi, \frac{p_2}{q_2}\pi, \frac{p_3}{q_3}\pi\right\}$, with each $p_i, q_i \in \mathbb{Z}^+$ chosen to be relatively prime, the genus g of the translation surface is given by [308]

$$g = 1 + \frac{\mathcal{N}}{2}\sum_{i=1}^{3}\left(\frac{p_i - 1}{q_i}\right), \tag{4.2}$$

where $\mathcal{N}$ is the least common multiple of $\{q_1, q_2, q_3\}$. Triangles that yield a translation surface of genus one correspond to classically integrable systems, in accordance with Arnold's criterion [273, 309]; the dynamics are confined to an n-torus in the presence of n conserved quantities. In contrast, when the resulting surface has genus greater than one, the system is termed *pseudo-integrable*. In these cases, despite momentum conservation in the reflected and stitched-together billiard, trajectories that meet at particular vertices diverge into different handles of the surface [273]. Finally, if even one interior angle is irrational, the translation surface becomes non-compact with infinite genus—homeomorphic to the so-called Loch Ness Monster, a unique orientable surface with one end [310]. Such irrational triangles exhibit chaotic features such as level repulsion [264], even though nearby trajectories only separate linearly.

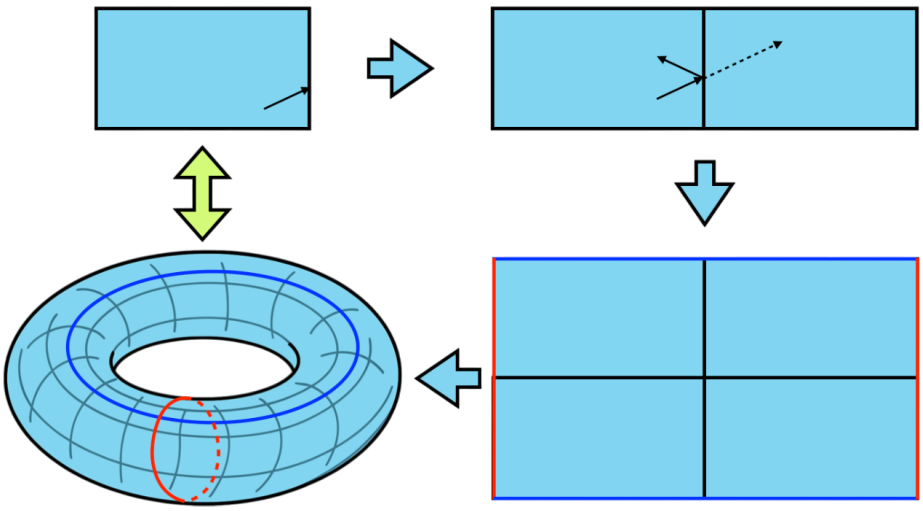

Figure 4.2: Illustration of how a rectangular billiard domain can be transformed into a torus through edge identifications. The top row shows the original rectangle (top left), followed by a reflection scheme that generates a replicated tiling (top right). By "gluing" opposite edges of this tiled region together, one obtains a torus geometry, as indicated at the bottom.

Unfolding Procedure and Construction of Translation Surfaces

To rigorously connect the billiard geometry with its dynamical properties, we employ the unfolding method. In this procedure, rather than reversing the particle's velocity at each collision with a boundary, one reflects the entire billiard table across that side. Consequently, each reflection produces a new copy of the polygon, and the billiard trajectory unfolds into a straight line traversing these copies.

For a rational billiard, the finite order of the dihedral group generated by reflections ensures that after a finite number, say N, of copies (with N typically being twice the least common multiple of the denominators of the angles), the unfolded polygons tile a closed region in the plane. Parallel edges of these copies are naturally paired via translations, which, upon identification, yields a flat surface with a well-defined translation structure.

Edge Identification and Genus Computation

After constructing the unfolded assembly, the next step is to glue the copies along corresponding edges. This identification results in a flat surface whose interior is locally Euclidean, except at a finite number of singular points—these arise at the vertices of the polygons. Specifically, if several copies of a vertex with angle α_i coincide, the total cone angle at the resulting singular point is $\Theta = m_i\alpha_i$, with m_i being the number of copies meeting at that point; by construction, $m_i\alpha_i$ is an integer multiple of 2π. There are two common approaches to compute the genus g of the translation surface:

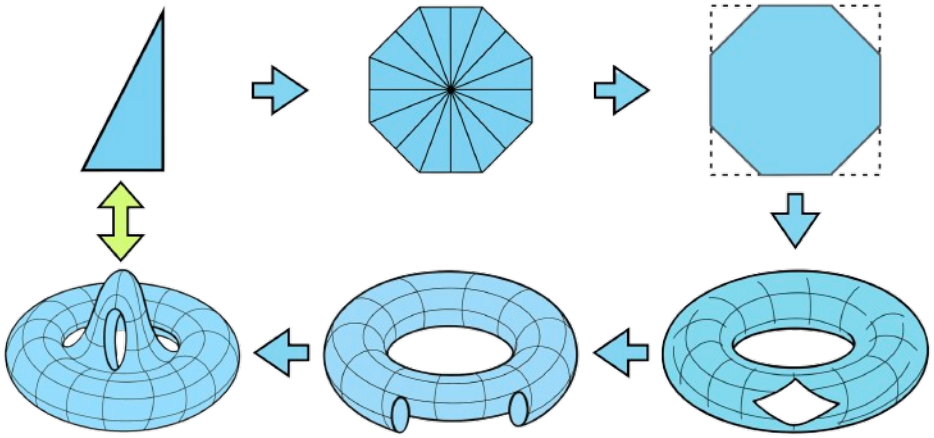

Figure 4.3: Illustration of how the triangle with $\left(\frac{\pi}{2}, \frac{\pi}{8}, \frac{3\pi}{8}\right)$ interior angles can be unfolded and then mapped into a higher-genus surface by pairwise edge identifications. In the top row, the triangle is reflected repeatedly around its edges, producing an octagonal tiling. In the bottom row, these edges are "glued" together to form a surface with two holes (genus two).

Euler Characteristic Method: Denote the number of faces by F (equal to the number of copies N), the number of distinct edges after pairing by E, and the number of vertices by V. Then the Euler characteristic is

$$\chi = V - E + F, \tag{4.3}$$

and for a closed orientable surface, it is related to the genus via

$$\chi = 2 - 2g. \tag{4.4}$$

Angle Deficit (Gauss–Bonnet) Method: Alternatively, one may focus on the singular points. For each cone singularity with total angle Θ, define its order as

$$k = \frac{\Theta}{2\pi} - 1. \tag{4.5}$$

Then the Gauss–Bonnet theorem for flat surfaces gives

$$2g - 2 = \sum_i k_i, \tag{4.6}$$

where the sum is over all singularities. For example, an unfolded rectangle (with interior angles $\frac{\pi}{2}$) produces a torus (genus 1) when opposite sides are identified (see Fig. 4.2); a right triangle with angles $\left(\frac{\pi}{2}, \frac{\pi}{8}, \frac{3\pi}{8}\right)$ unfolds into 8 copies that can be assembled into a regular octagon, which upon appropriate edge identifications yields a surface of genus 2 (see Fig. 4.3).

In general, for a rational polygon with interior angles $\{\alpha_i\}$, the unfolding involves N copies of the polygon and the resulting translation surface captures the topological nature of the billiard. Notably, the topology—summarised by the genus—serves as an indicator of the underlying dynamics: a genus-one surface implies integrability, higher genus signals pseudo-integrability, and the emergence of an infinite genus in the presence of any irrational angle correlates with chaotic behaviour.

Symmetry and Fine-Tuning Effects

The dynamical properties of triangular billiards are further modulated by symmetry considerations and parameter fine-tuning. For instance, isosceles triangles possess a reflection symmetry along their altitude; as a consequence, the Hamiltonian commutes with the reflection operator, and all energy eigenstates can be classified as symmetric or antisymmetric (see Fig. 4.4). The spectral statistics and ergodic properties may differ significantly when analysed within these individual symmetry sectors compared to the full spectrum [264].

Additionally, fine-tuning a triangle, such as by setting one of its angles to $\frac{\pi}{2}$ in an otherwise irrational triangle, can have profound effects on the dynamics. Right triangular irrational billiards, for example, are known to exhibit weak (though not strong) mixing properties [311–313], while still maintaining ergodicity [264].

To summarise, the translation surface corresponding to a rational billiard is constructed through the following steps:

1. **Unfolding:** Reflect the billiard polygon across its sides to obtain a finite collection of copies (typically $N = 2 \times \mathrm{lcm}(q_i)$), over which the billiard trajectory becomes a straight line.

2. **Edge Identification:** Pair corresponding parallel edges via translations to form a closed, orientable flat surface; the interior is flat except at isolated cone singularities.

3. **Genus Computation:** Determine the topological genus of the surface either by the Euler characteristic,
$$\chi = V - E + F, \qquad \chi = 2 - 2g,$$
or via the Gauss–Bonnet theorem that accounts for the cumulative angle deficits at the singular points:
$$2g - 2 = \sum_i \left(\frac{\Theta_i}{2\pi} - 1 \right).$$

As an illustrative example, consider a regular n-gon with interior angles $\frac{(n-2)\pi}{n}$. The associ-

ated translation surface has genus

$$g = \begin{cases} \left\lfloor \frac{n}{4} \right\rfloor, & \text{if } n \text{ is even,} \\ \frac{n-1}{2}, & \text{if } n \text{ is odd.} \end{cases}$$

This framework establishes a clear connection between the geometric properties of the billiard and the integrability of the classical dynamics, thereby providing a basis for interpreting the corresponding quantum spectral features.

In summary, by combining numerical solutions of the Schrödinger equation with a detailed topological analysis of the corresponding translation surfaces, we are able to classify triangular billiards into integrable, pseudo-integrable, and non-integrable regimes. This classification, which also takes into account the effects of symmetry and fine-tuning, lays a solid foundation for further exploration of quantum chaos in billiard systems.

	g	Isosceles	Right	General
I	1	$\{\frac{1}{3}, \frac{1}{3}, \frac{1}{3}\}_1$, $\{\frac{1}{2}, \frac{1}{4}, \frac{1}{4}\}_2$	$\{\frac{1}{2}, \frac{1}{3}, \frac{1}{6}\}_3$	—
PI	2	$\{\frac{2}{5}, \frac{2}{5}, \frac{1}{5}\}_4$, $\{\frac{1}{5}, \frac{1}{5}, \frac{3}{5}\}_5$	$\{\frac{3}{8}, \frac{1}{8}, \frac{1}{2}\}_6$, $\{\frac{2}{5}, \frac{1}{10}, \frac{1}{2}\}_7$	—
	3	$\{\frac{3}{7}, \frac{3}{7}, \frac{1}{7}\}_8$	$\{\frac{5}{12}, \frac{1}{12}, \frac{1}{2}\}_9$	$\{\frac{1}{3}, \frac{1}{4}, \frac{5}{12}\}_{10}$
	4	$\{\frac{1}{9}, \frac{4}{9}, \frac{4}{9}\}_{11}$	$\{\frac{4}{9}, \frac{1}{18}, \frac{1}{2}\}_{12}$	$\{\frac{1}{4}, \frac{1}{6}, \frac{7}{12}\}_{13}$
	5	$\{\frac{5}{11}, \frac{5}{11}, \frac{1}{11}\}_{14}$	$\{\frac{9}{20}, \frac{1}{20}, \frac{1}{2}\}_{15}$	$\{\frac{4}{15}, \frac{1}{15}, \frac{2}{3}\}_{16}$
	6	$\{\frac{6}{13}, \frac{6}{13}, \frac{1}{13}\}_{17}$	$\{\frac{11}{24}, \frac{1}{24}, \frac{1}{2}\}_{18}$	$\{\frac{5}{16}, \frac{7}{16}, \frac{1}{4}\}_{19}$
NI	∞	—	$\{\frac{(-1+\sqrt{5})}{8}, \frac{(5-\sqrt{5})}{8}, \frac{1}{2}\}_{20}$, $\{\frac{(6-\sqrt{5})}{8}, \frac{(-2+\sqrt{5})}{8}, \frac{1}{2}\}_{21}$	$\{\frac{(3-\sqrt{5})}{5}, \frac{3}{5}, \frac{(-1+\sqrt{5})}{5}\}_{22}$, $\{\frac{(-2+\sqrt{5})}{8}, \frac{3}{4}, \frac{(4-\sqrt{5})}{8}\}_{23}$
NI	∞	$\{\frac{1}{4\sqrt{2}}, \frac{1}{4\sqrt{2}}, \frac{(4-\sqrt{2})}{4}\}_{24}$ $\{\frac{1}{2\sqrt{2}}, \frac{1}{2\sqrt{2}}, \frac{\sqrt{2}-1}{\sqrt{2}}\}_{25}$	—	$\{\frac{(1+\sqrt{2})(3-\sqrt{5})}{4(3+\sqrt{2})}, \frac{(1+\sqrt{5})}{4}, \frac{(3-\sqrt{5})}{2(3+\sqrt{2})}\}_{26}$ $\{\frac{(-1+\sqrt{5})}{8}, \frac{(5-\sqrt{5})}{16}, \frac{(13-\sqrt{5})}{16}\}_{27}$

Table 4.1: A total of 27 distinct triangular billiards are examined in this study. Each triangle is labeled as $\{\frac{p_1}{q_1}, \frac{p_2}{q_2}, \frac{p_3}{q_3}\}_\kappa$, where the internal angles are given by $p_i\pi/q_i$, and κ serves as an integer index for reference. The triangles are categorised as follows: I denotes integrable, PI stands for pseudo-integrable, and NI indicates non-integrable triangles; the genus g refers to that of the associated translation surface. All three known integrable triangles are represented in the dataset. Notably, the triangle $\{\frac{1}{2}, \frac{1}{4}, \frac{1}{4}\}_2$ is both right-angled and isosceles. Furthermore, all triangles yielding translation surfaces of genus one or two are either isosceles or right-angled. The first subgroup of non-integrable triangles includes those with a single rational angle, while the second subgroup consists entirely of triangles with no rational angles.

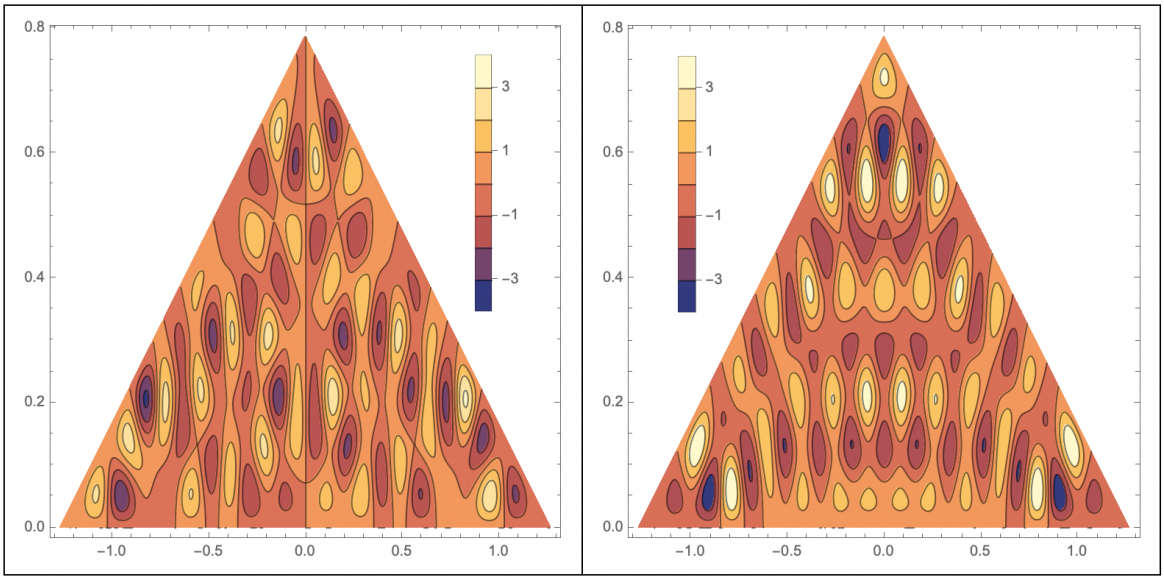

Figure 4.4: 94th (left) and 96th (right) energy eigenstate of κ=24 (irrational isosceles) triangle. The left (right) panel shows a symmetric (an anti-symmetric) eigenstates with respect to the reflection axis. Figure taken from [65].

4.1.2 Spectral Statistics of Triangular Billiards

The extent of quantum chaos in a system is determined by the short-range correlations and local fluctuations in its energy eigenvalues. In our work, we compare the spectral characteristics of triangular billiards with those expected for chaotic random matrix ensembles (RMTs), independent of the non-universal, coarse-grained density profile. In triangular billiards the spectral density is influenced by geometric attributes (e.g., the triangle's area and perimeter), so that the coarse-grained profile is not uniform. A standard method to examine local spectral properties involves an unfolding procedure [261] that maps the raw eigenvalues $\{\mathscr{E}_j\}$ onto a new set $\{e_j\}$ with unit density. Specifically, if $\bar{\rho}(E)$ denotes a density of states smoothed over a scale larger than the mean level spacing, the unfolded levels are obtained via

$$e_j = \bar{N}(\mathscr{E}_j), \quad \forall j, \tag{4.7}$$

with

$$\bar{N}(\mathscr{E}_j) = \int_{-\infty}^{\mathscr{E}_j} dE\, \bar{\rho}(E)$$

being the cumulative count of states below energy $\mathscr{E}_j$. While this procedure guarantees a macroscopically uniform spectrum with preserved local fluctuations, it also modifies the underlying Hamiltonian and can yield different outcomes for dynamical properties such as wavefunction spreading. Consequently, we follow an alternative approach as described in [256, 264, 314–319].

For the case of triangular billiards, the cumulative number of energy levels below $\mathscr{E}$ asymptotically follows the generalised Weyl formula [264, 314, 320]:

$$\bar{N}(\mathscr{E}) = \frac{A\mathscr{E} - L\sqrt{\mathscr{E}}}{4\pi} + \frac{\pi}{24}\left(\frac{1}{\alpha} + \frac{1}{\beta} + \frac{1}{\gamma} - \frac{1}{\pi}\right), \tag{4.8}$$

where α, β, and γ denote the internal angles, A is the triangle's area (set to 1 in our analysis), and

$$L = A\,\frac{\sqrt{2}\,(\sin\alpha + \sin\beta + \sin\gamma)}{\sqrt{\sin\alpha\,\sin\beta\,\sin\gamma}}$$

represents its perimeter. When $\mathscr{E} \gg (L/A)^2$, the spectral staircase becomes nearly linear, i.e., $\bar{N}(\mathscr{E}) \approx A\mathscr{E}/(4\pi)$. Thus, by restricting our study to energies above a threshold $\mathscr{E}_M \gg (L/A)^2$, we avoid the need for unfolding. We therefore consider the truncated spectrum

$$\{\mathscr{E}_j\}_{j=M}^{D_0-1} \quad \text{with} \quad D \equiv D_0 - M, \tag{4.9}$$

where our numerical experiments indicate that the Weyl formula linearizes for indices $j \gtrsim 50$ (hence we set $M = 50$) out of a total $D_0 = 1000$ levels. Subsequently, we shift and rescale this truncated spectrum so that its mean energy is zero and its overall range is unity:

$$E_j = \frac{\mathscr{E}_{j+M} - \bar{\mathscr{E}}}{\mathscr{E}_{D_0-1} - \mathscr{E}_M}, \quad \bar{\mathscr{E}} = \frac{1}{D}\sum_{j=M}^{D_0-1}\mathscr{E}_j. \tag{4.10}$$

This normalisation facilitates a consistent comparison of spectral statistics across different triangular billiards.

Level Spacing Ratio

A robust measure of local spectral fluctuations that remains independent of the unfolding procedure is the Level Spacing Ratio (LSR) [321, 322]. Using the truncated levels defined in (4.9), we introduce the consecutive spacing

$$s_j = \mathscr{E}_{j+1} - \mathscr{E}_j, \quad j = 1, 2, \ldots, D-1.$$

The LSR for level j is then defined as

$$r_j = \min\left\{\frac{s_j}{s_{j+1}}, \frac{s_{j+1}}{s_j}\right\}, \quad r_j \in [0,1], \tag{4.11}$$

and the average LSR is given by

$$\bar{r} = \frac{1}{D_0 - 1} \sum_{j=1}^{D_0-1} r_j. \tag{4.12}$$

A perfectly regular spectrum would yield $\bar{r} = 1$, whereas larger fluctuations result in smaller values. In particular, uncorrelated (Poisson) spectra produce $\bar{r}_{\text{Poisson}} \approx 0.3863$, while the GOE is characterised by $\bar{r}_{\text{GOE}} \approx 0.5307$ [321]. In cases where degeneracies are present, some ratios may become undefined (i.e., $0/0$). To address this, such ill-defined ratios are replaced uniformly by either 0 or 1, allowing us to derive lower and upper bounds on $\bar{r}$.

Figure 4.5 summarizes the average LSR for our set of 27 triangles. The observed hierarchy is as follows:

- **Generic triangles** (4 non-integrable and 4 pseudo-integrable), which lack symmetry or fine-tuning of angles, exhibit average LSR values that conform to GOE statistics, indicating strong chaotic behaviour.
- **Right-angled triangles** (6 pseudo-integrable and 2 non-integrable) feature average LSRs that are slightly below the GOE expectation.
- **Isosceles triangles** (6 pseudo-integrable and 2 non-integrable) display average LSRs near the Poisson value. However, when resolved into their symmetric and antisymmetric components (see Fig. 4.6), each sector individually approaches GOE statistics, signaling robust internal correlations despite their combined Poisson-like behaviour.
- The **three integrable triangles** show the lowest average LSRs, consistent with large fluctuations in level spacing arising from substantial spectral degeneracies. Here, the reported values are given as bounds obtained by substituting all undetermined $0/0$ ratios with 0 or 1.

Overall, higher average LSRs are indicative of chaotic systems with pronounced level repulsion, whereas Poissonian (uncorrelated) spectra lead to lower average LSR values. Although the average LSR is a useful metric, a more detailed characterisation is obtained by analysing the full distribution of level spacing ratios.

Level-Spacing-Ratio Distributions

Here we detail the probability distributions $P(r)$ of the level spacing ratios for the triangular billiards. These distributions offer a more nuanced picture of the spectral fluctuations than the average LSR alone. According to [321], the LSR distribution for a Poissonian spectrum

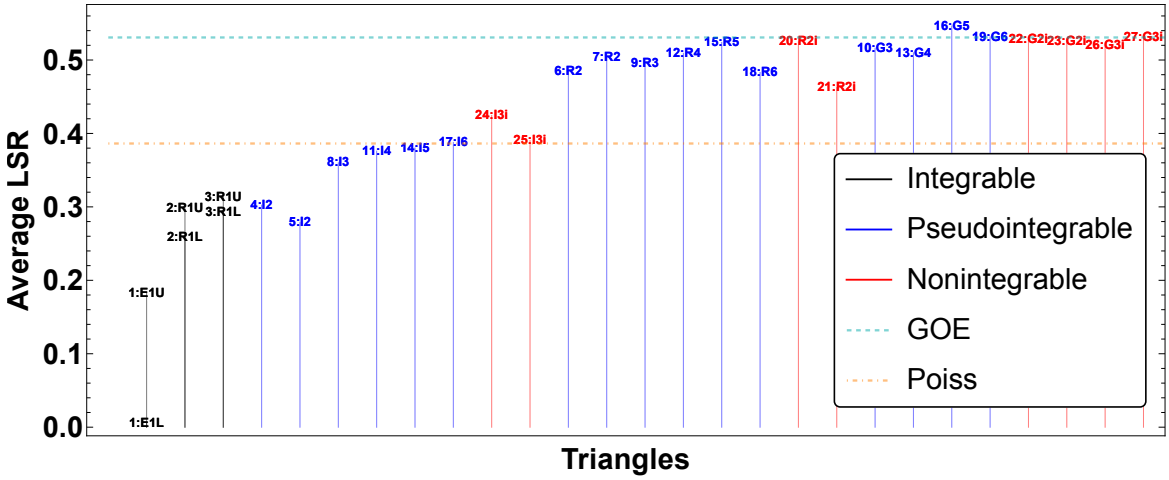

Figure 4.5: Level spacing ratios (LSR) for all 27 triangles. Labels follow the notation $\kappa : Tg$, where κ is the triangle index (see Table 4.1), T indicates the triangle type (E for equilateral, I for isosceles, R for right, G for general), and g is the genus of the translation surface. For irrational triangles (infinite genus), g is replaced by $2i$ or $3i$ for triangles with 2 and 3 irrational angles, respectively. The sky blue dashed line denotes the GOE average LSR, while the orange dot-dashed line indicates the Poisson value. Integrable and isosceles triangles tend to approach the Poisson result, whereas generic and right triangles align with GOE statistics. For the three integrable cases (displayed in black on the far left), two labels are provided to indicate the lower and upper average LSRs, corresponding to the two choices for handling ill-defined ratios. Figure taken from [65].

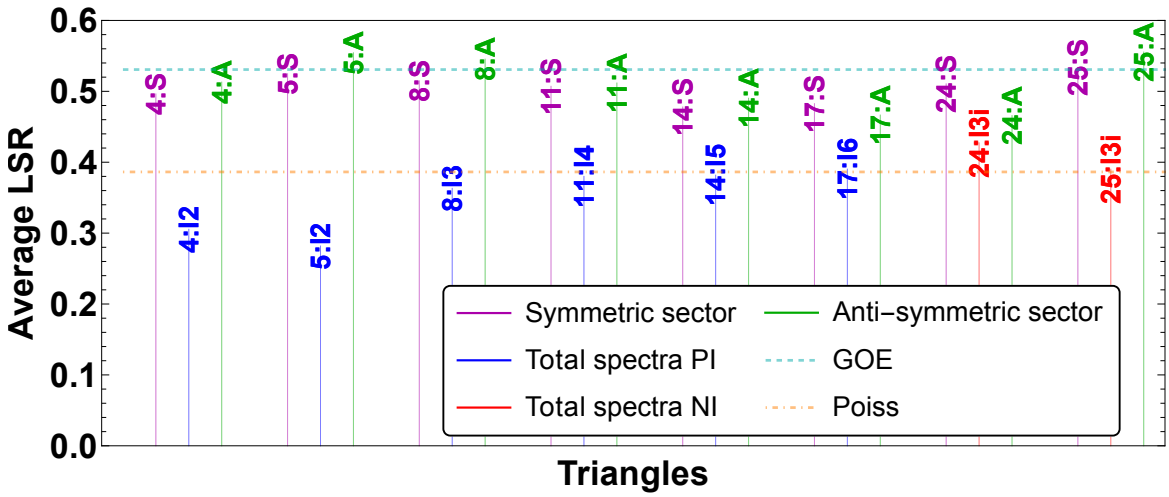

Figure 4.6: Level spacing ratios (LSR) for isosceles triangles, with data points labeled analogously to Fig. 4.5. Here, the designations κ:S and κ:A refer to the symmetric and antisymmetric sectors of the triangle indexed by κ. Although the aggregate spectrum for isosceles triangles exhibits average LSR values closer to the Poisson limit, the separated symmetric and antisymmetric sectors display average LSRs approximating the GOE result. Figure taken from [65].

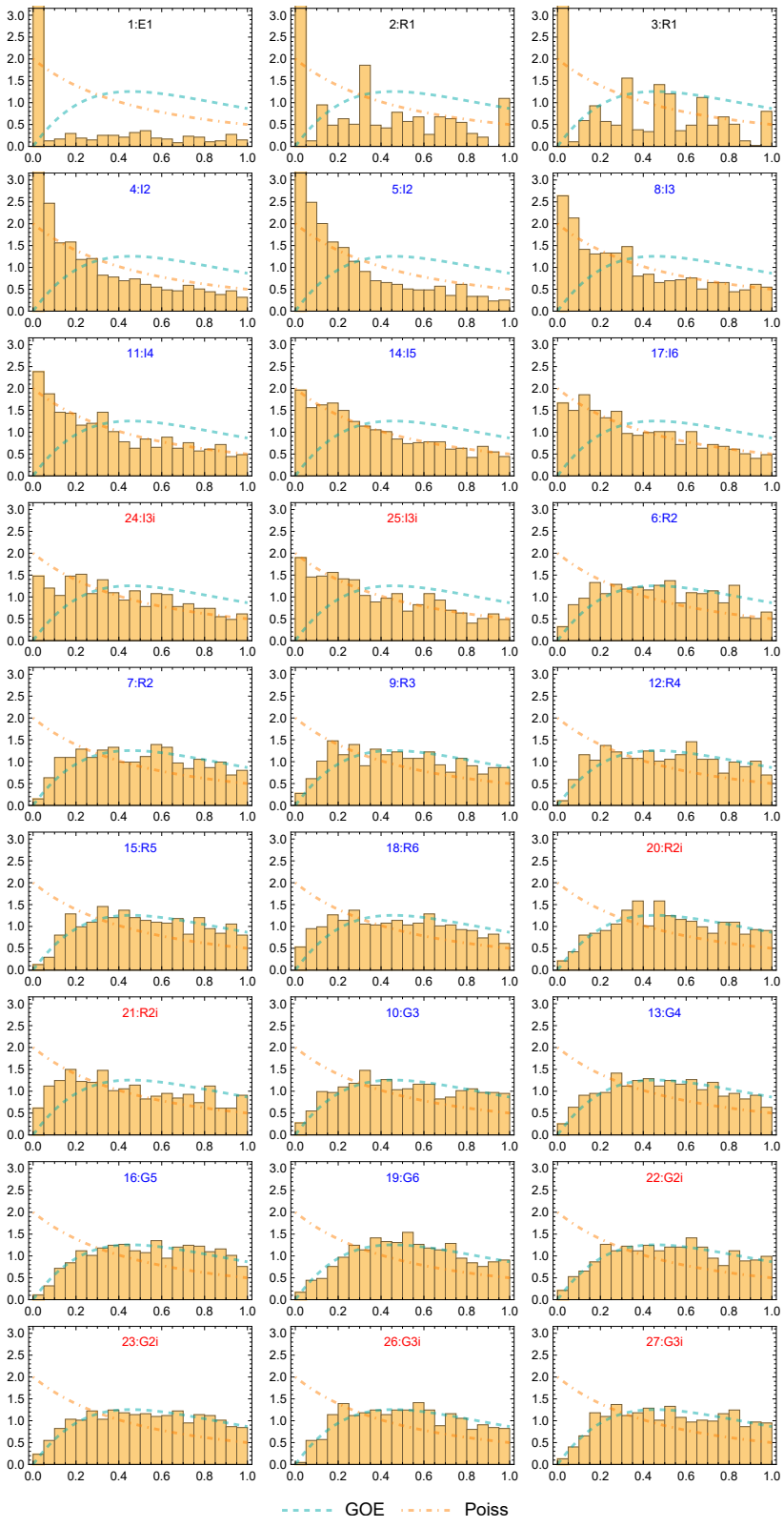

Figure 4.7: LSR distributions for all 27 triangles. The horizontal axis represents the level spacing ratio r, while the vertical axis shows the probability distribution $P(r)$. Triangle labels and legends correspond to those in Fig. 4.5. Figure taken from [65].

is given by

$$P_{\text{Poiss}}(r) = \frac{2}{(1+r)^2}\,\Theta(1-r), \tag{4.13}$$

while the GOE prediction is approximated by

$$P_{\text{GOE}}(r) = \frac{27}{4}\,\frac{r+r^2}{(1+r+r^2)^{5/2}}\,\Theta(1-r). \tag{4.14}$$

Here, $\Theta(1-r)$ denotes the Heaviside step function ensuring that $r \in [0,1]$. Notably, $P_{\text{Poiss}}(0) \neq 0$ reveals that Poisson spectra do not exhibit level repulsion, whereas $P_{\text{GOE}}(0) = 0$ is indicative of the repulsion present in chaotic spectra.

Figure 4.7 shows $P(r)$ for all 27 triangles. It is evident that none of the integrable or isosceles triangles manifest level repulsion, with their $P(r)$ distributions approaching the Poisson form. In contrast, both non-isosceles rational and general triangles show distributions that are closer to the GOE prediction, consistent with a higher degree of chaos. These observations are in full agreement with the average LSR results presented in Fig. 4.5.

Figure 4.8 presents the LSR distributions for the symmetric and antisymmetric sectors of the isosceles triangles. Although the total spectrum of isosceles triangles yields a $P(r)$ that trends toward the Poisson distribution, when the spectrum is decomposed into its symmetric and antisymmetric parts, both sectors exhibit level repulsion, with distributions approaching the GOE prediction. These results further corroborate the sector-resolved average LSR findings shown in Fig. 4.6.

4.1.3 Spectral Complexity

In this section we provide an overview of spectral complexity, a measure originally formulated as the holographic dual of the Einstein-Rosen (ER) bridge volume [291]. According to the AdS/CFT correspondence, the ER bridge for an eternal black hole is dual to the thermofield double (TFD) state in the doubled Hilbert space of the boundary conformal field theory [230]:

$$|\text{TFD}(t)\rangle = \frac{1}{\sqrt{Z_\beta}} \sum_j e^{-(\beta/2+it)E_j}\,|E_j\rangle_L\,|E_j\rangle_R\,, \quad Z_\beta = \sum_j e^{-\beta E_j}. \tag{4.15}$$

Alternatively, one may consider a single-copy description by forming a superposition of energy eigenstates,

$$|\psi(t)\rangle = \frac{1}{\sqrt{Z_\beta}} \sum_j e^{-(\beta/2+it)E_j + i\theta_j}\,|E_j\rangle\,, \tag{4.16}$$

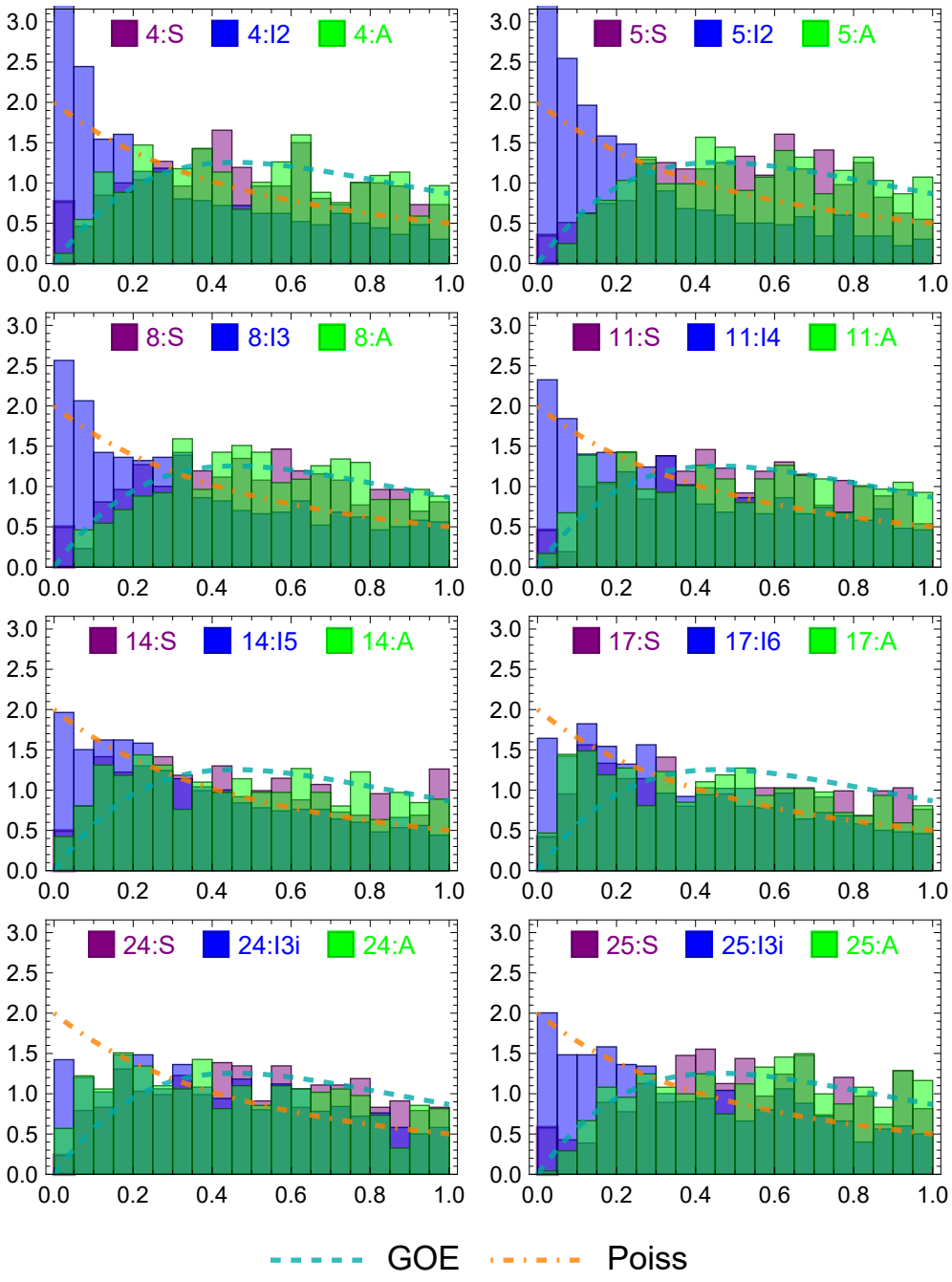

Figure 4.8: LSR distributions for 8 isosceles triangles. Here, the horizontal axis indicates the LSR r and the vertical axis represents the distribution $P(r)$. Labels and legends follow those in Fig. 4.6. Figure taken from [65].

where arbitrary phases θ_j can always be absorbed by redefining the eigenstates. In fact, the inner products between states at different times satisfy

$$\langle \mathrm{TFD}(t_1)|\mathrm{TFD}(t_2)\rangle = \langle\psi(t_1)|\psi(t_2)\rangle = Z_\beta^{-1}\sum_j e^{-(\beta - i(t_1-t_2))E_j},$$

so that the two constructions are equivalent in their time correlations.

To capture the cumulative time evolution, we form a mixed state by averaging the pure-state evolution over the time interval $[0, t]$:

$$\rho(t) = \frac{1}{t}\int_0^t dt' \; |\psi(t')\rangle\langle\psi(t')| \,. \tag{4.17}$$

In [291], spectral complexity is defined in terms of the purity of $\rho(t)$:

$$C_S(t) = t^2\left(\mathrm{Tr}[\rho(t)^2] - \frac{Z_{2\beta}}{Z_\beta^2}\right) = \sum_{j\neq k}\left[\frac{\sin\left(\frac{t}{2}(E_j - E_k)\right)}{Z_\beta\,(E_j - E_k)/2}\right]^2 e^{-\beta(E_j+E_k)}. \tag{4.18}$$

In time, the decreasing purity (i.e. loss of coherence) signals that the rate of complexity growth becomes sub-quadratic, with $C_S(t) \lesssim t^2$ at later times.

At early times the complexity exhibits a transition from quadratic to linear growth. At late times, its behaviour is strongly influenced by the underlying spectral statistics: chaotic (GOE-like) spectra tend to saturate or grow very slowly due to level repulsion, whereas integrable spectra, which lack level repulsion, lead to a more rapid growth of spectral complexity. This behaviour reflects the enhanced ergodicity in the time evolution of the TFD state in chaotic systems.

For our quantum billiards, we employ the truncated spectrum defined in (4.9) to compute both the spectral form factor (SFF) and the spectral complexity (SC). The SFF is given by

$$\mathrm{SFF}(t) = \sum_{j,k}^{D}\exp\Big[it(E_j - E_k)\Big] = \int dE\, dE'\, \rho(E)\,\rho(E')\, e^{it(E-E')}, \tag{4.19}$$

where the spectral density is defined as

$$\rho(E) = \sum_{j=1}^{D}\delta(E - E_j), \tag{4.20}$$

with the normalisation $\int dE\,\rho(E) = D$. In the absence of degeneracies, the long-time limit of the SFF reaches a plateau of height D, reflecting the $j = k$ contributions in (4.19) [323–325]. At inverse temperature $\beta = 0$, the spectral complexity for our truncated spectrum takes the

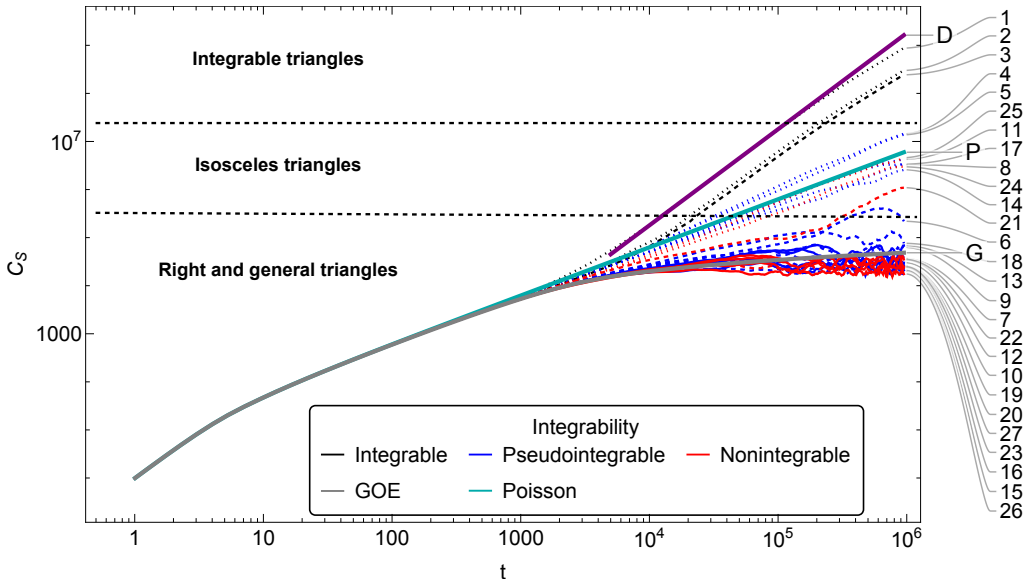

Figure 4.9: Spectral complexity for all 27 triangular billiards. The numbers on the right indicate the triangle index κ as defined in Table 4.1. The labels P, G, and D represent our analytical predictions for Poisson (linear in t at late times), GOE (logarithmic in t at late times), and degenerate (quadratic in t at late times) spectral complexity, respectively, with the degeneracy matching that in the equilateral triangle 1. Dotted lines correspond to isosceles triangles, dashed lines to right-angled triangles, and solid lines (except the three denoted P, G, and D) to general triangles. Figure taken from [65].

form

$$C_S(t) = \sum_{j\neq k}^{D} \left[\frac{\sin\left(\frac{t}{2}(E_j - E_k)\right)}{D\,(E_j - E_k)/2}\right]^2 = \int dE\, dE'\, \rho(E)\,\rho(E') \left[\frac{\sin\left(\frac{t}{2}(E - E')\right)}{D\,(E - E')/2}\right]^2 . \quad (4.21)$$

For a non-degenerate spectrum, since $\sin^2\left(\frac{t}{2}(E_j - E_k)\right) \leq 1$, the complexity is upper bounded by $\left(\frac{2}{\Delta E_{\min}}\right)^2$, where $\Delta E_{\min}$ is the minimal level spacing. Because our spectrum is rescaled to have unit width, $\Delta E_{\min}$ scales as $1/D$. In contrast, for spectra with degeneracies, taking the limit $E_j - E_k \to 0$ in (4.21) reveals that the spectral complexity grows as $\frac{d}{D^2}\, t^2$ at late times, with

$$d = \sum_{j\neq k} \delta_{E_j, E_k}.$$

Assuming that the SFF reaches a plateau value D for non-degenerate spectra, the relation between the SFF and SC can be expressed as [136, 291]

$$C_S(t) = \frac{2}{D^2} \int_0^t dt' \int_0^{t'} dt'' \Big(\mathrm{SFF}(t'') - D\Big). \quad (4.22)$$

To illustrate these concepts, we first consider the cases of Poisson and GOE statistics. In

the energy regime where the cumulative number of states grows linearly (cf. (4.23)) the coarse-grained spectral density is constant:

$$\bar{\rho}(E) = \frac{d\bar{N}}{dE} = D. \tag{4.23}$$

One then determines the behaviour of the SFF and SC by averaging (4.19) and (4.21) over Poisson or GOE ensembles, which replaces the product $\rho(E)\rho(E')$ by the ensemble-averaged two-point correlation function.

For an integrable system with uncorrelated levels, the two-point function is given (at large D) by [261]

$$\langle \rho(E)\rho(E') \rangle = \bar{\rho}(\bar{E})\delta(s) + \left(1 - \frac{1}{D}\right)\bar{\rho}(E)\bar{\rho}(E'), \tag{4.24}$$

with $\bar{E} = (E + E')/2$ and $s = E - E'$. Substituting this into (4.19) yields

$$\mathrm{SFF}(t) = \left[(D-1)D\ \mathrm{sinc}^2\left(\frac{t}{2}\right) + D\right] \approx \begin{cases} 4D^2\,\mathrm{sinc}^2\left(\frac{t}{2}\right), & t \ll \sqrt{D} \\ D, & \sqrt{D} \ll t\,, \end{cases} \tag{4.25}$$

where $\mathrm{sinc}(t) = \sin(t)/t$. The SFF descends quadratically from a maximum value of order D^2, reaching a plateau at D for $t \sim \sqrt{D}$. For Poisson spectra, where exact degeneracies are absent for finite D, evaluating (4.22) gives the spectral complexity

$$C_S(t) = 4\left(1 - \frac{1}{D}\right)\left[\mathrm{Ci}(t) + t\ \mathrm{Si}(t) - \log(t) + \cos(t) - \gamma - 1\right] \approx \begin{cases} t^2, & t \ll 1, \\ 2\pi t, & 1 \ll t, \end{cases} \tag{4.26}$$

with $\mathrm{Ci}(t) = -\int_t^\infty dz\ \cos(z)/z$, $\mathrm{Si}(t) = \int_0^t dz\ \sin(z)/z$, and γ denoting Euler's constant. Thus, for Poisson-distributed spectra, the complexity grows linearly at late times.

For spectra exhibiting GOE correlations, the two-point function is modified to

$$\langle \rho(E)\rho(E') \rangle = \bar{\rho}(\bar{E})\delta(s) + \bar{\rho}(E)\bar{\rho}(E')\Big[1 - Y_2(\pi D s)\Big], \tag{4.27}$$

where the GOE cluster function, valid in the large-D limit, is given by [259–261, 323, 326]

$$Y_2(x) = \mathrm{sinc}^2(x) + \frac{1}{x}\left(\mathrm{Si}(x) - \frac{\pi}{2}\,\mathrm{sgn}(x)\right)(\mathrm{sinc}(x) - \cos(x)). \tag{4.28}$$

Because $Y_2(\pi D s)$ is localised around $s = 0$ with width $\sim 1/D$, one can approximate the

SFF by

$$\mathrm{SFF}(t) \approx \begin{cases} 4D^2 \,\mathrm{sinc}^2\left(\frac{t}{2}\right), & t \ll D^{2/3}, \\ \frac{t}{\pi}, & D^{2/3} \ll t \ll D, \\ D, & t \gg D. \end{cases} \tag{4.29}$$

Thus, after a dip occurring at $t \sim D^{2/3}$, the SFF increases linearly until reaching the plateau at D. Using this behaviour in (4.22) and incorporating the localisation properties of the cluster function, one obtains the spectral complexity for a GOE spectrum:

$$C_S(t) = 4\left[\mathrm{Ci}(t) + t\ \mathrm{Si}(t) - \log(t) + \cos(t) - \gamma - 1\right] + D\, C_1\left(\frac{t}{\pi D}\right), \tag{4.30}$$

$$\approx \begin{cases} t^2, & t \ll 1, \\ 2\pi t, & 1 \ll t \ll D, \\ \frac{2}{3}\pi^2 D\ \log\left(\frac{t}{\pi D}\right), & t \gg D, \end{cases} \tag{4.31}$$

where

$$C_1(u) = \frac{\pi^2}{3} \begin{cases} u\left(\frac{17}{12}u^2 - 4u - 1\right) + (1 - \frac{u}{2})(u+1)^2 \log(u+1), & u < 2, \\ \log\left(u^2 - 1\right) - (u^2 - 3)u\ \coth^{-1}(u) + (u-6)u + \frac{4}{3}, & u > 2. \end{cases} \tag{4.32}$$

Thus, for GOE-correlated spectra the late-time growth of spectral complexity is logarithmic in t.

The analytical results derived above demonstrate that for a fixed spectral density, spectra without correlations (Poisson) lead to a more rapid increase of spectral complexity at late times than those with GOE correlations (see Fig. 4.9). It should be noted that these formulas apply in the leading large-D limit for spectra rescaled to a bounded interval; in this regime the minimum level spacing $\Delta E_{\min}$ vanishes, rendering the bound $\left(\frac{2}{\Delta E_{\min}}\right)^2$ trivial. Figure 4.9 illustrates the late-time behaviour of the spectral complexity for our set of triangular billiards:

- **Generic triangles** (4 non-integrable and 4 pseudo-integrable), which lack any special symmetry or fine-tuning, display slow late-time growth akin to the GOE prediction.
- **Right-angled triangles** (6 pseudo-integrable and 2 non-integrable) similarly exhibit slow growth, but they tend to reach marginally higher late-time values.
- **Isosceles triangles** (6 pseudo-integrable and 2 non-integrable) follow a nearly linear growth at late times, consistent with Poisson statistics. However, as shown in Fig. 4.10,

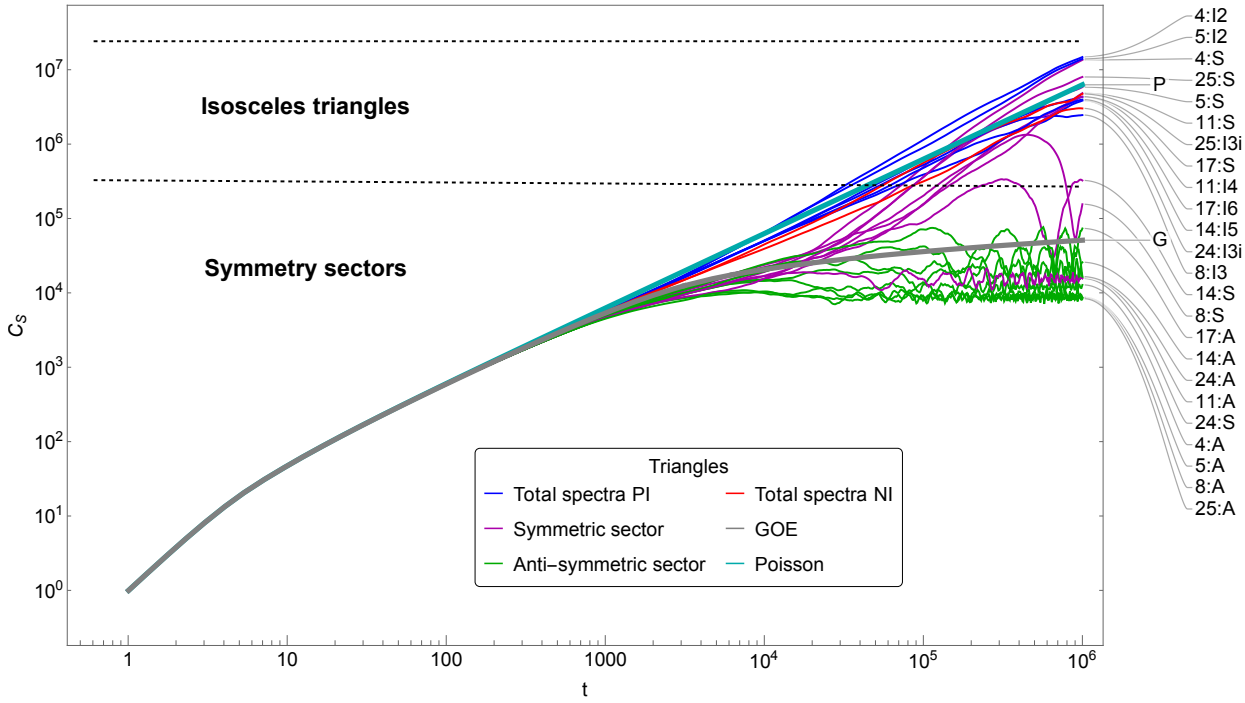

Figure 4.10: Spectral complexity for the symmetric and antisymmetric sectors of isosceles triangles. The labels P and G denote the expected Poissonian and GOE behaviours, respectively. While the overall isosceles spectra exhibit linear growth at late times, the antisymmetric sectors more closely follow the GOE behaviour; in contrast, the symmetric sectors show an extended period of linear growth before decelerating, and in some cases, even decrease toward the GOE profile. Both sectors display pronounced oscillations at late times. Figure taken from [65].

when the isosceles spectrum is partitioned into its symmetric and antisymmetric sectors, the antisymmetric components align more closely with GOE behaviour, while the symmetric sectors maintain a prolonged period of linear growth before eventually decelerating or even decreasing toward the GOE trend. Both sectors exhibit significant late-time oscillations. It remains an open question why the two sectors diverge so markedly despite similar average LSRs (cf. Fig. 4.6).

- Finally, the three integrable triangles with pronounced spectral degeneracies exhibit quadratic growth of spectral complexity at late times, as anticipated.

4.1.4 Spread Complexity in Triangular Billiards

In this section, we demonstrate how various Krylov space diagnostics—such as the spread complexity, the variance of the Lanczos coefficients, and the inverse participation ratio (IPR) of energy eigenstates in the Krylov basis—can distinguish between integrable and chaotic dynamics in triangular billiards [91, 327–329]. Since the Hilbert space of these systems is

infinite-dimensional, for practical computations we restrict our analysis to the $D = 1000$ lowest energy eigenstates. In this truncated basis, the initial state is chosen to be uniformly spread, i.e.,

$$|\psi(0)\rangle = \frac{1}{\sqrt{D}} \sum_{j=0}^{D-1} e^{i\theta_j} |E_j\rangle, \tag{4.33}$$

where the phases θ_j are arbitrary. The state evolves in time according to

$$|\psi(t)\rangle = e^{-iHt}|\psi(0)\rangle.$$

Note that if the initial state has support on n energy eigenstates, then the Krylov subspace generated by H will have dimension at most n. Our choice of a uniform linear superposition maximizes the effective dimension of the Krylov space; we have confirmed that using random phases leads to qualitatively similar dynamics.

Variance of the Lanczos Coefficients

An observed indicator of chaotic behaviour is the (inverse) relation between the classical Lyapunov exponent and the variance of the Lanczos coefficients [84]. Although polygonal billiards have vanishing classical Lyapunov exponents [274], recent studies suggest that the variance of the Lanczos coefficients may serve as a signature that discriminates between integrable and chaotic quantum dynamics [84, 307, 330, 331]. We define the standard deviations as follows:

$$\sigma(a_n) = \sqrt{\sum_n \Big[x_n\Big]^2 - \left(\sum_n x_n\right)^2}, \quad \text{with } x_n = a_{n+1} - a_n, \tag{4.34}$$

$$\sigma(2b_n) = \sqrt{\sum_n \Big[y_n\Big]^2 - \left(\sum_n y_n\right)^2}, \quad \text{with } y_n = 2b_{n+1} - 2b_n. \tag{4.35}$$

We focus on the variances of $\{a_n, 2b_n\}$ because, for a random initial state undergoing evolution under a random matrix Hamiltonian, these variances are expected to be equal [306, 307]. (Note that these definitions differ from those used in [84, 91].) Figure 4.11 clearly demonstrates that integrable triangles exhibit the highest variance in their Lanczos coefficients. Following them, isosceles triangles show intermediate variance, with right triangles next, and finally generic pseudo-integrable and non-integrable triangles displaying the lowest variances. Intriguingly, the Lanczos variances are found to be anticorrelated with the average LSR: higher average LSR values (indicative of stronger level repulsion) are associated with lower variance in the Lanczos coefficients.

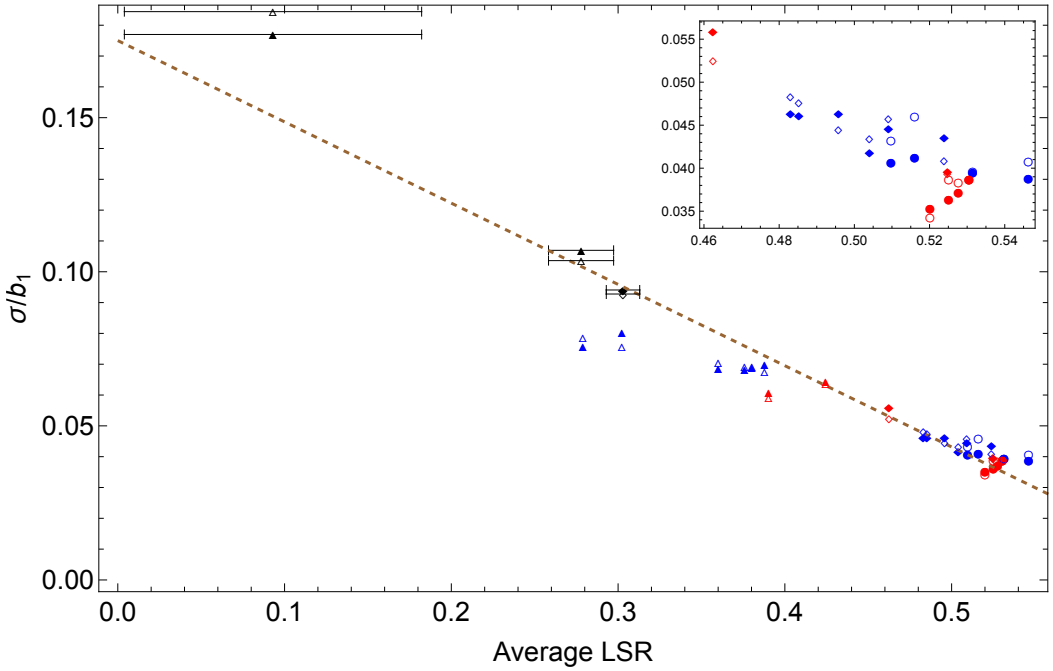

Figure 4.11: Standard deviations (normalised by b_1) of the Lanczos coefficients $\{a_n, 2b_n\}$ plotted against the average LSR for all 27 triangular billiards. For integrable triangles, the error bars represent the range between the upper and lower average LSR values (obtained by substituting ill-defined $0/0$ ratios with 0 or 1). A clear anticorrelation is observed: lower average LSR values correspond to higher Lanczos variances. The dashed brown line is a linear fit with a slope of -0.262 and a positive intercept of 0.174. The inset emphasizes the behaviour for non-isosceles, pseudo-integrable, and non-integrable triangles. Figure taken from [65].

Localisation of Energy Eigenstates in Krylov Space

Another key diagnostic is the degree to which energy eigenstates are localised in the Krylov basis. This is quantified by examining the overlap $|\langle O_n|E_j\rangle|$ between the energy eigenstates and the Krylov basis vectors. In practice, one finds that this overlap is negligible for eigenstates with energies satisfying $|E_j| > 2b_n$ [136]. As shown in Eq. 39 of [307], one has

$$\sum_{E'\in[E,E+dE]} \left|\langle O_m|E'\rangle\right|^2 \approx \frac{\Theta\left(4b_m^2-(E-a_m)^2\right)}{\pi\sqrt{4b_m^2-(E-a_m)^2}}\,dE, \tag{4.36}$$

where Θ is the Heaviside function, and since the average values of a_m vanish while b_m decreases with m, it follows that high-energy (as well as very low-energy) eigenstates tend to reside predominantly on Krylov vectors with small index n. This phenomenon is illustrated in Fig. 4.12.

For integrable triangles, the overlaps $|\langle O_n|E_j\rangle|$ for a given j tend to concentrate around a

particular n. Such behaviour, which is reminiscent of Anderson localisation in disordered systems, is attributed to the disorder in the Lanczos coefficients [91, 304, 329].

To further quantify this localisation, we calculate the inverse participation ratio (IPR) for each energy eigenstate in the Krylov basis:

$$\mathrm{IPR}_j = \sum_{n=1}^{K} \left| \langle O_n | E_j \rangle \right|^4. \tag{4.37}$$

A completely localised eigenstate (i.e., $|E_j\rangle = |O_n\rangle$ for some n) has $\mathrm{IPR}_j = 1$, whereas an eigenstate uniformly spread over all K Krylov vectors has $\mathrm{IPR}_j = 1/K$. The overall localisation for the system is then quantified as

$$\mathrm{IPR} = \sum_{j=1}^{D} \mathrm{IPR}_j = \sum_{j=1}^{D} \sum_{n=1}^{K} \left| \langle O_n | E_j \rangle \right|^4. \tag{4.38}$$

Figure 4.13 reveals a clear hierarchy: integrable triangles exhibit the strongest localisation (highest IPR), followed by isosceles triangles, then right-angled triangles, and finally generic pseudo-integrable and non-integrable triangles.

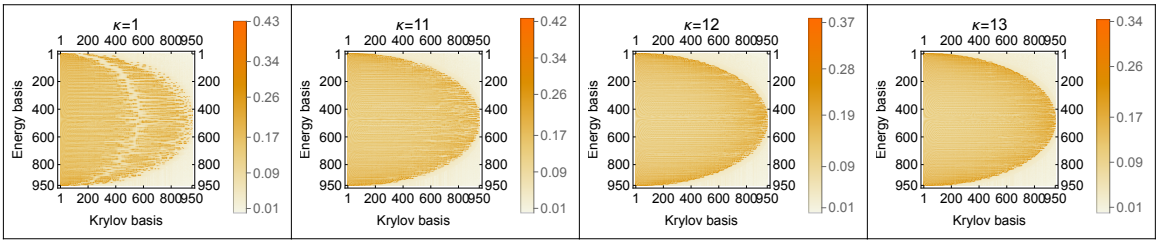

Figure 4.12: Overlap matrices $|\langle E_j | O_n \rangle|$ for four representative triangles: $\kappa = 1$ (integrable, equilateral), $\kappa = 11$ (pseudo-integrable, isosceles), $\kappa = 12$ (pseudo-integrable, right), and $\kappa = 13$ (pseudo-integrable, general). Energy eigenstates with extreme eigenvalues tend to localize on Krylov basis vectors with small n, and the highest degree of localisation is observed for integrable triangles. Figure taken from [65].

Spread Complexity

We now turn to the computation of spread complexity for our set of triangular billiards, as illustrated in Figs. 4.14a and 4.14b. Notably, integrable triangles behave markedly differently from the pseudo-integrable and non-integrable ones. In the integrable case, the spread complexity initially rises to a plateau, exhibits oscillatory behaviour, and then falls sharply to zero at periodic intervals. These features signal the occurrence of Poincaré recurrences: in a finite-dimensional Hilbert space of dimension K, recurrences are expected on a timescale proportional to K for integrable systems, whereas for non-integrable (chaotic) systems the

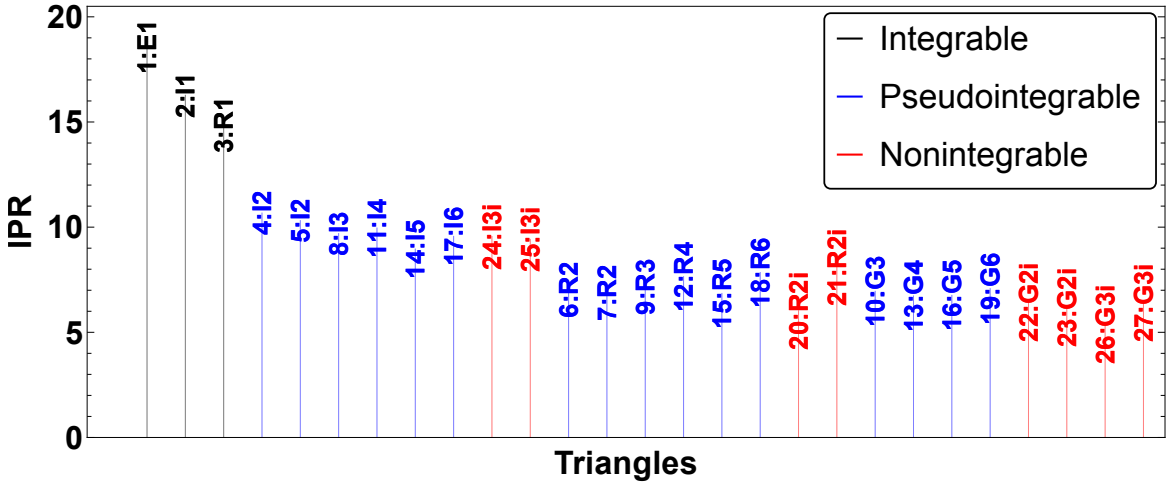

Figure 4.13: Inverse participation ratio (IPR) for all 27 triangular billiards. Data points are labeled as $\kappa : Tg$, where κ denotes the triangle index from Table 4.1, T indicates the type of triangle (E for equilateral, I for isosceles, R for right, and G for general), and g represents the genus of the triangle's translation surface. For irrational triangles (with infinite genus), g is replaced by $2i$ or $3i$, corresponding to triangles with two and three irrational angles, respectively. The highest IPR values are observed for integrable triangles, followed in decreasing order by isosceles, right, and generic triangles. Figure taken from [65].

recurrence time typically scales as e^K [332]. Indeed, the periodic vanishing of the spread complexity in integrable triangle billiards indicates that the system returns to its initial state at these quantum recurrence times [332]. The observed recurrences derive from the commensurability in the spectra of integrable triangles [84, 273, 333–335], while the reduced plateau height is linked to the larger variance in the Lanczos coefficients in these systems [91].

In contrast, both pseudo-integrable and non-integrable (general) triangles display spread complexity characteristic of chaotic behaviour. Their spread complexity curves feature an initial ascent to a well-defined peak followed by a gradual decline to a plateau, as predicted in [55, 307].

A similar comparison across triangle types, but focusing on triangles with genus-six translation surfaces, is shown in Figs. 4.15a and 4.15b. Here, the peak height of the spread complexity is noticeably suppressed in triangles with symmetry. In particular, isosceles triangles display a reduction in the complexity peak, which becomes even more pronounced when examining higher moments of the complexity distribution.

Symmetry also impacts the complexity when one resolves the dynamics into symmetry sectors. As illustrated in Fig. 4.16, the spread complexity computed separately for the symmetric and antisymmetric sectors of isosceles triangles shows a clear peak followed by a plateau, typical of chaotic evolution. However, when the full spectrum is combined, these

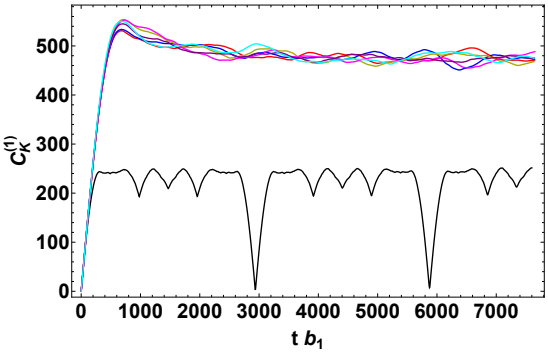

(a) Spread complexity (first moment, $\alpha = 1$, as per Eq. (2.74)) for triangular billiards of different genera.

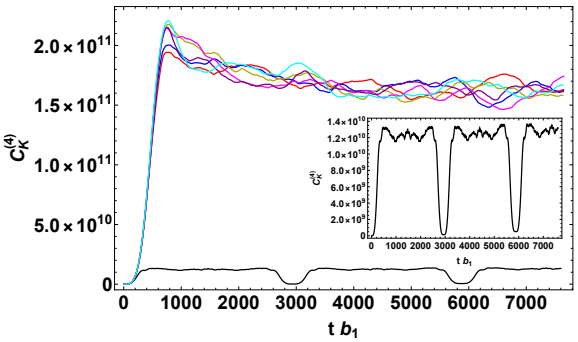

(b) Fourth moment of spread complexity (i.e. $\alpha = 4$ in Eq. (2.74)) for triangular billiards of varying genus.

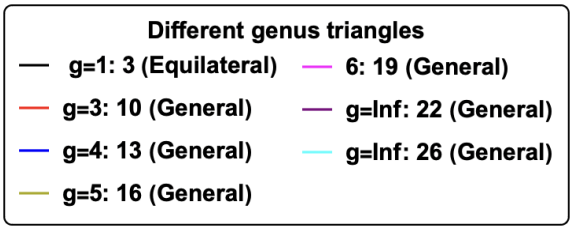

(c) Label for Figs. 4.14a and 4.14b.

Figure 4.14: Spread complexity and its fourth moment for several triangular billiards: $\kappa = 1$ (integrable, equilateral), $\kappa = 10$ (general, genus three), $\kappa = 13$ (general, genus four), $\kappa = 16$ (general, genus five), and $\kappa = 19$ (general, genus six). The integrable (genus one) triangle exhibits oscillations and periodic drops to zero, in sharp contrast to the monotonically saturating behaviour observed in pseudo-integrable and non-integrable (chaotic) cases. Figure taken from [65].

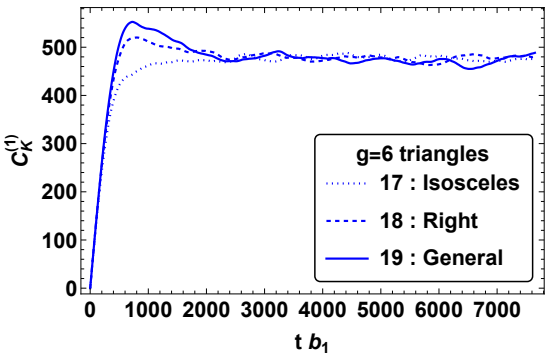

(a) Spread complexity ($\alpha = 1$) for different types of genus-six triangular billiards.

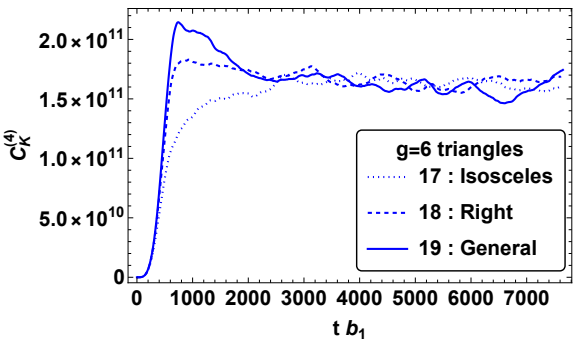

(b) Fourth moment of spread complexity ($\alpha = 4$) for triangles with genus six.

Figure 4.15: Comparison of spread complexity for genus-six triangles of different symmetry classes: $\kappa = 17$ (isosceles), $\kappa = 18$ (right-angled), and $\kappa = 19$ (general). The presence of symmetry is associated with a reduced peak in the spread complexity, a difference that becomes even more prominent for the fourth moment. Figure taken from [65].

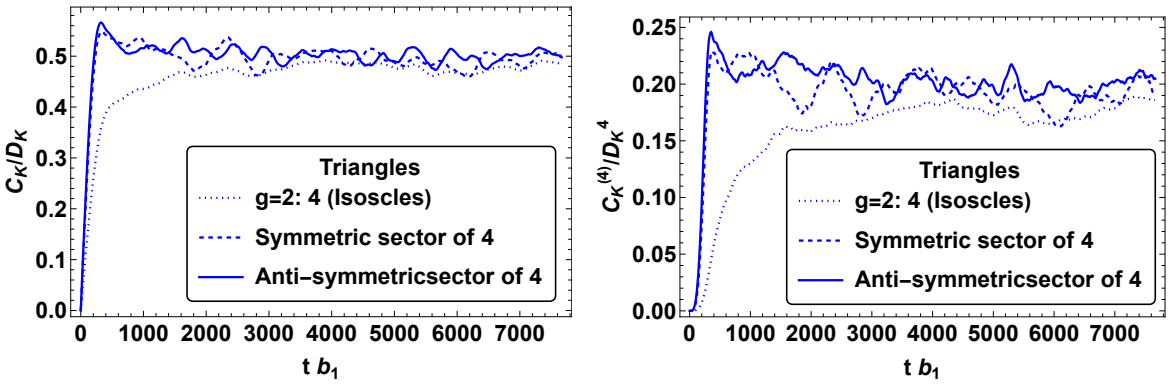

(a) Spread complexity ($\alpha = 1$) for the symmetric and antisymmetric sectors of an isosceles triangular billiard.

(b) Fourth moment of spread complexity for the symmetric and antisymmetric sectors of the same isosceles triangle.

Figure 4.16: The symmetric and antisymmetric sectors of an isosceles triangle (with a genus-two translation surface, $\kappa = 4$) both exhibit the characteristic peak and plateau of chaotic dynamics, even though the combined dynamics do not display this feature prominently. Figure taken from [65].

features are diluted and the overall complexity lacks the pronounced peak.

We further illustrate the advantages of the Krylov space analysis by comparing the evolution of the wave function in real space with its evolution in Krylov space. For numerical convenience, we restrict the study to a subset of energy eigenstates ranging from the 51st to the 150th level. Figure 4.17a shows snapshots of the amplitude of the wave function in real space, $\left|\langle x, y|\psi(t)\rangle\right|$, at various times, while Fig. 4.17b presents corresponding snapshots of the amplitudes in Krylov space, $\{|\phi_n(t)|^2\}$, along with the time evolution of the spread complexity $C_K^{(1)}(t)$. Although the real-space profile remains relatively uniform over time, the Krylov-space representation reveals clear changes, with the wave function fragmenting into localised packets that traverse the Krylov chain. This contrast underscores the sensitivity of the Krylov approach to temporal sequencing and its ability to capture subtle aspects of wave function evolution that may be obscured in real space.

4.1.5 Discussion

In this Section, we have explored the quantum dynamics of twenty-seven triangular billiards, which exhibit a wide range of behaviours—integrable, pseudointegrable, and non-integrable determined by the triangles' internal angles. We characterised each system using a combination of spectral probes (average level spacing ratios and spectral complexity) and dynamical measures (variance of the Lanczos coefficients, localisation of energy eigenstates in the Krylov basis, and the time evolution of spread complexity). Our results can be summarised as follows:

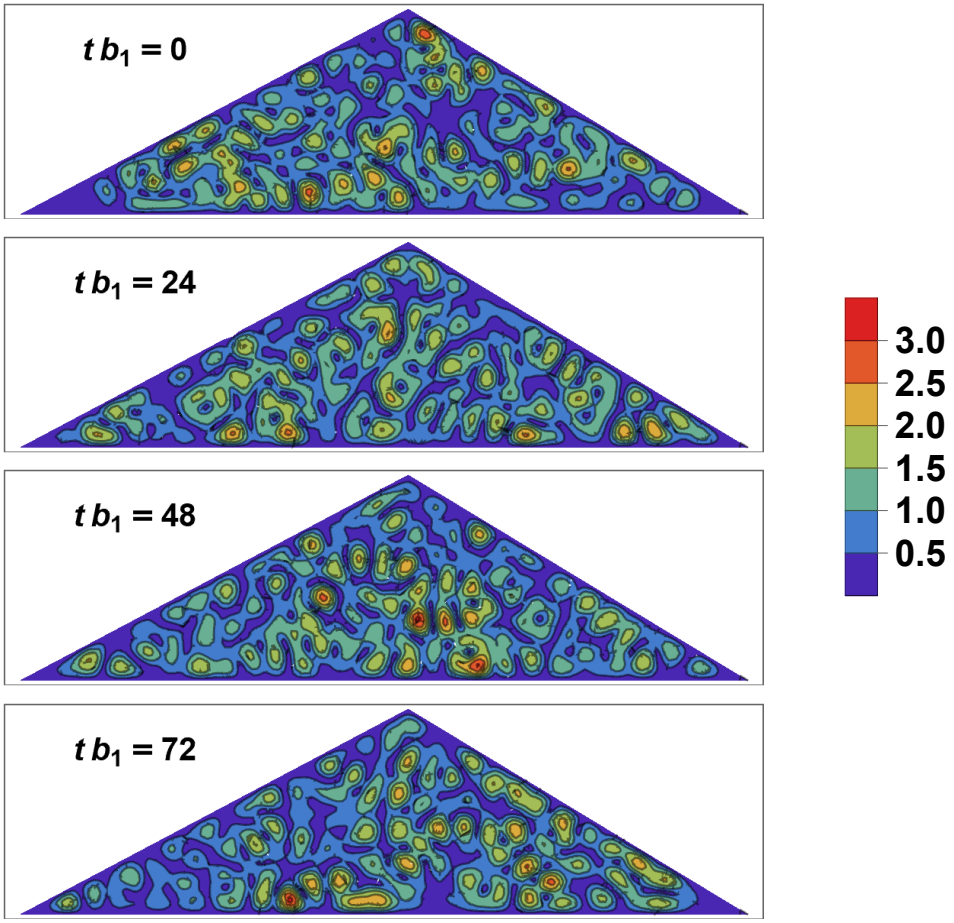

(a) Snapshots of the real-space amplitude $|\langle x, y|\psi(t)\rangle|$ at dimensionless times $t\,b_1 = 0,\ 24,\ 48,\ 72$.

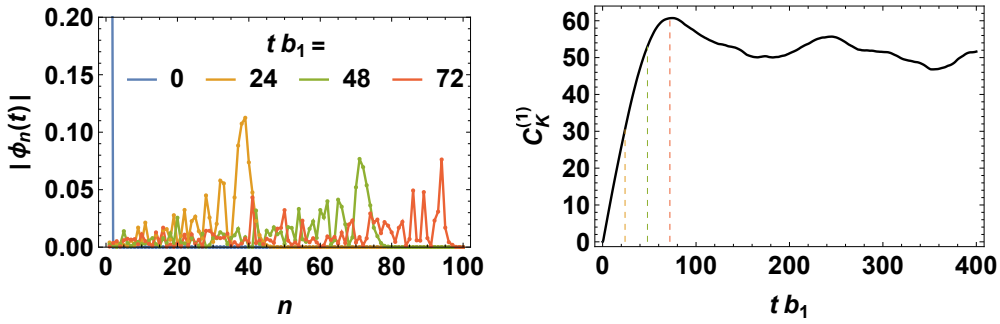

(b) Left panel: Snapshots of the Krylov-space amplitudes $\{|\phi_n(t)|^2\}$. Right panel: The evolution of the spread complexity $C_K^{(1)}(t)$ with dashed lines indicating times $t\,b_1 = 24,\ 48,\ 72$.

Figure 4.17: Comparison between the evolution in real space and in Krylov space for a general irrational triangle with truncation $D = 100$. The Krylov space evolution, as captured by spread complexity, encodes temporal sequence information not evident in the relatively featureless real-space profile. Figure taken from [65].

- **Integrable triangles:** These systems show the lowest average level spacing ratios, indicating the highest fluctuations in level spacings. The spectral degeneracies inherent in integrable triangles lead to a quadratic growth of spectral complexity at late times—faster than the linear growth expected from Poisson distributions. In addition, the Lanczos coefficients in these cases exhibit the largest variance, and the energy eigenstates are strongly localised in the Krylov basis. Consequently, the spread complexity of integrable billiards lacks the pronounced peak observed in chaotic systems and instead displays marked Poincaré recurrences, reflecting the commensurate nature of their spectra [84, 91, 273, 333–335].

- **Isosceles triangles:** Whether belonging to the pseudointegrable or non-integrable classes, isosceles triangles display average level spacing ratios and spread complexity growth that are close to those expected for Poisson spectra. Their Lanczos coefficient variances are intermediate—smaller than those in integrable systems yet considerably larger than in triangles without symmetry—resulting in energy eigenstate localisation that is less extreme than in integrable cases but more pronounced than in generic triangles. Although the overall spread complexity does not exhibit the stark recurrences seen in integrable systems, it also lacks the characteristic complexity peak typical of chaotic dynamics.

- **Symmetry sectors in isosceles triangles:** When the Hilbert space is decomposed into symmetric and antisymmetric sectors, both components yield average level spacing ratios close to the Gaussian Orthogonal Ensemble (GOE) value. Nonetheless, their spectral complexity exhibits significant oscillations before converging to the GOE behaviour. Individually, each symmetry sector shows a clear complexity peak followed by a descent to a plateau, even though these features are suppressed in the total, symmetry-mixed dynamics.

- **Right triangles:** For right triangles in both the pseudointegrable and non-integrable categories, the spectral features are somewhat intermediate. On average, their level spacing ratios are slightly lower than the GOE prediction (yet still well above the Poisson benchmark), and their spectral complexity grows marginally faster. Additionally, right triangles display a slightly higher variance in their Lanczos coefficients and a modestly greater degree of localisation in the Krylov basis compared to generic triangles. The evolution of their spread complexity, however, is essentially indistinguishable from that of generic triangles at our current numerical resolution.

- **Generic pseudointegrable triangles:** These systems have average level spacing ratios and spectral complexity growth that align well with the expectations of GOE random

matrix theories. Their Lanczos coefficient variances are low, albeit marginally higher than those in generic non-integrable systems. The energy eigenstates of these billiards are relatively delocalised in the Krylov basis (though slightly more localised than in general non-integrable triangles), and their overall spread complexity evolution closely mimics that anticipated for chaotic dynamics.

- **Generic non-integrable triangles:** These billiards exhibit average level spacing ratios and spectral complexity growth in excellent agreement with the GOE predictions. They are distinguished by the lowest variances in their Lanczos coefficients and the most delocalised energy eigenstates in the Krylov basis. Their spread complexity evolution is precisely as expected for chaotic systems.

It would be advantageous to perform higher-precision numerical simulations to further resolve the subtle differences between pseudointegrable and non-integrable systems. Although all the triangular billiards studied possess vanishing classical Lyapunov exponents, the emergence of chaotic behaviour is rooted in the way trajectories split at the corners and in the topology of the translation surface. Notably, the finite-genus translation surfaces characterising pseudointegrable triangles differ dramatically from the infinite-genus surfaces of non-integrable ones. Understanding how this topological distinction influences quantum dynamics may benefit from a path-integral treatment that explicitly accounts for trajectories traversing distinct handles of the surface.

4.2 Spread Complexity in Non-Hermitian Systems and Purification

Building on the insights gained from our study of unitary quantum dynamics in triangular billiards, we now turn our attention to non-unitary evolution. In this section, we examine how Krylov spread complexity behaves when the quantum state undergoes non-unitary dynamics—specifically, we explore the combined effects of measurement-induced non-unitarity and PT symmetry, and demonstrate how these processes can ultimately be mapped back to an effective unitary evolution via purification. In principle, the methods we have developed are versatile and applicable to any non-unitary dynamics; however, for definiteness we focus on the quantum first passage problem (QFPP) [336–341]. Within the QFPP framework, repeated projective measurements—intrinsically non-unitary operations according to quantum mechanics—induce dynamics that are governed by an effective non-Hermitian Hamiltonian, with the time interval between successive measurements serving as a perturbative parameter.

Previously, Krylov complexity has been explored for the unitary evolution of isolated systems [54, 91] and for the non-unitary evolution of operators in open systems, where the dynamics are generated by the Liouvillian superoperator $\mathscr{L} = [H, \cdot]$ rather than by the Hamiltonian H itself [62, 68–70, 342]. In our work, we extend these approaches by incorporating additional non-unitary effects arising from PT symmetry and by employing purification techniques to recast the non-unitary dynamics as an effective unitary evolution. This extension not only broadens the scope of our framework but also yields valuable insight into the manifestation of measurement-induced non-Hermitian effects in the time evolution of quantum states.

4.2.1 Measurement-Induced Dynamics and the Zeno Effect

We begin our analysis with the tight-binding Hamiltonian [337, 338], which serves as the foundation for investigating the quantum first passage problem (QFPP)[1]. By applying a perturbative treatment to account for non-unitary evolution under periodic projective measurements, an effective non-Hermitian Hamiltonian emerges. This operator is then used to evolve position eigenstates, allowing us to extract the non-Hermitian total probability, spread complexity, and spread entropy—key indicators that differentiate measurement-induced non-unitarity from standard unitary evolution.

Building on the previous use of the bi-Lanczos algorithm for non-unitary operator complexity in [69], we extend the method to assess state complexity when a quantum system is subjected to regular projective measurements. Our work pursues a dual objective: first, to adapt the bi-Lanczos approach for evaluating spread complexity, and second, to probe the behaviour of measurement-induced quantum channels. In this context, we introduce a novel complex symmetric Lanczos algorithm—tailored for complex symmetric matrices—that significantly reduces computational workload and memory usage by operating within a single Krylov space, unlike the separate bra–ket treatment required by bi-Lanczos.

We apply these techniques to the QFPP and analyze spread complexity as well as spread entropy in the Krylov basis under both open and periodic boundary conditions. In all cases, the evolution is characterised by an initial increase in complexity, followed by a prolonged decay phase that eventually leads to saturation. This extended decay, which contrasts with the rapid equilibration seen under unitary dynamics, signifies a distinct measurement-induced effect. Moreover, we find that variations in the choice of the initial state result in markedly different dynamics and saturation values for both complexity and entropy.

In a further exploration, a quench scenario is considered in which the non-Hermitian

[1]The quantum first passage problem (QFPP) considers a quantum state evolving under a lattice Hamiltonian subject to local projective measurements performed on particular lattice sites [338].

perturbation parameter is gradually increased from zero. This effectively enlarges the time interval between measurements. By selecting eigenstates of the Hermitian tight-binding Hamiltonian as initial conditions, we examine the evolution governed by the quenched, effective non-Hermitian Hamiltonian. For the single-particle ground state, the dynamics transition from oscillatory behaviour to a regime featuring rapid initial growth, followed by decay and eventual saturation. In contrast, when the first excited state is used as the initial state, the onset of complexity growth is delayed as the measurement interval shortens. Such behaviour suggests a transition in complexity dynamics contingent on measurement frequency—a phenomenon reminiscent of a measurement-induced phase transition [343–347]. In the limit of extremely frequent measurements, the system's initial state remains essentially unaltered in the Hilbert space, a signature manifestation of the quantum Zeno effect [348–350].

Finally, because our effective non-Hermitian Hamiltonian is a complex symmetric matrix, it enables a direct comparison between the conventional bi-Lanczos algorithm [351–353] and our newly implemented complex symmetric Lanczos method. The latter demonstrates superior efficiency, as it circumvents the need to separately treat the bra and ket vectors by using a unified Krylov space. Notably, our numerical experiments confirm that both algorithms yield exactly equivalent results, validating the effectiveness of the complex symmetric Lanczos approach in handling non-Hermitian dynamics.

4.2.2 Non-Unitary Evolution and Modified Lanczos Methods

Quantum evolution is inherently unitary because the Hamiltonian H is Hermitian; the corresponding evolution operator $U = e^{-iHt}$ preserves probability. However, in many practical situations—such as open system dynamics or the act of measurement—the effective evolution deviates from unitarity. In these cases, one often models the dynamics with an effective non-Hermitian Hamiltonian. For instance, if $H = H_1 + iH_2$ (with $H \neq H^\dagger$ and $H_1,\ H_2$ Hermitian), the state evolves as

$$|\psi(t)\rangle_{nh} = e^{-iHt}|\psi(0)\rangle_{nh} = e^{H_2 t - iH_1 t}|\psi(0)\rangle_{nh}. \tag{4.39}$$

Here the imaginary contribution from H_2 alters the norm of the state, necessitating a continuous re-normalisation.

Revised Normalisation and Definitions of Probability, Complexity, and Entropy

To maintain a consistent probabilistic interpretation during non-unitary evolution, we introduce a modified normalisation procedure in the Krylov basis. When a system is initialised

with the density matrix

$$\rho_{nh}(0) = |\psi(0)\rangle_{nh}\langle\psi(0)|_{nh},$$

its evolution is dictated by [354]

$$\rho_{nh}(t) = \frac{e^{-iHt}\rho_{nh}(0)e^{iH^\dagger t}}{\mathrm{Tr}\left[e^{-iHt}\rho_{nh}(0)e^{iH^\dagger t}\right]}. \tag{4.40}$$

This prescription guarantees that the state remains properly normalised at all times.

In the Krylov basis, we start with the initial matrix wave function

$$|\Phi_{nh}(0)\rangle_K = \begin{pmatrix} 1 \\ 0 \\ 0 \\ 0 \\ \vdots \\ 0 \end{pmatrix}_K, \tag{4.41}$$

which is equivalent to setting $\psi_n(0) = \delta_{n,0}$ as per (2.74) (with the first element identified as $\psi_0(0)$). We then define the corresponding Krylov-space density matrix as

$$(\rho_{nh})_K(0) = |\Phi_{nh}(0)\rangle_K\langle\Phi_{nh}(0)|_K = \begin{pmatrix} 1 & 0 & \cdots & 0 \\ 0 & 0 & \cdots & 0 \\ \vdots & \vdots & \ddots & \vdots \\ 0 & 0 & \cdots & 0 \end{pmatrix}_{K\times K}. \tag{4.42}$$

The evolution is then generated by the non-Hermitian tridiagonal form L (obtained via an appropriate Lanczos algorithm) so that the time-dependent state in the Krylov basis is re-normalised at each instant

$$|\widetilde{\Phi}(t)\rangle_K = \frac{e^{-iLt}|\Phi_{nh}(0)\rangle_K}{\sqrt{\mathrm{Tr}\left[e^{-iLt}(\rho_{nh})_K(0)e^{iL^\dagger t}\right]}} = \begin{pmatrix} \widetilde{\phi}_0(t) \\ \widetilde{\phi}_1(t) \\ \widetilde{\phi}_2(t) \\ \vdots \\ \widetilde{\phi}_{K-1}(t) \end{pmatrix}_K, \quad P(t) = {}_K\langle\widetilde{\Phi}(t)|\widetilde{\Phi}(t)\rangle_K = 1. \tag{4.43}$$

In what follows, this dynamically normalised state permits definitions of spread entropy and

complexity that closely mirror their unitary counterparts

$$C_S(t) = \frac{\sum_n n\,|\widetilde{\phi}_n(t)|^2}{P(t)}, \qquad S_S(t) = -\frac{\sum_n |\widetilde{\phi}_n(t)|^2 \ln |\widetilde{\phi}_n(t)|^2}{P(t)}. \tag{4.44}$$

[2]

Constructing the Krylov Basis for Non-Hermitian Systems

In the Hermitian case, the Lanczos algorithm produces a tridiagonal form of the Hamiltonian. For non-Hermitian matrices, however, a straightforward extension (the Arnoldi method) yields an upper Hessenberg matrix—its extra off-diagonals complicate the standard evaluation of Krylov complexity [69]. To overcome this obstacle, we employ modified Lanczos methods tailored to non-unitary evolution.

Bi-Lanczos Algorithm The bi-Lanczos algorithm circumvents the limitations imposed by non-Hermiticity by simultaneously evolving two sets of basis vectors. In this approach, one propagates an initial normalised ket $|q_1\rangle$ and its conjugate bra $\langle p_1| = \langle q_1|$ using the operators A and $A^\dagger$ respectively. These two sets, $\{|q_j\rangle\}$ and $\{\langle p_j|\}$, form bi-orthogonal bases that span their respective Krylov subspaces

$$\mathscr{K}^j(A, |q_1\rangle) \equiv \{A|q_1\rangle, A^2|q_1\rangle, \dots\}, \quad \mathscr{K}^j(\langle p_1|, A) \equiv \{\langle p_1|A, \langle p_1|A^2, \dots\}.$$

They satisfy the bi-orthogonality condition

$$\langle p_i|q_j\rangle = \delta_{ij}. \tag{4.45}$$

Since the initial state is chosen as $|\psi(0)\rangle = |p_1\rangle = |q_1\rangle$, one automatically has $\langle p_1|q_1\rangle = 1$.

The non-Hermitian operator A does not act identically on bra and ket vectors, and therefore its action requires two three-term recurrence relations

$$c_{j+1}\,|q_{j+1}\rangle = A\,|q_j\rangle - a_j\,|q_j\rangle - b_j\,|q_{j-1}\rangle, \tag{4.46}$$

$$b^*_{j+1}\,|p_{j+1}\rangle = A^\dagger\,|p_j\rangle - a^*_j\,|p_j\rangle - c^*_j\,|p_{j-1}\rangle. \tag{4.47}$$

These recursions lead to a tridiagonal representation T_j of the matrix A in the bi-orthogonal

[2] Note that the square root over the trace in the denominator of Eq. (4.43) equals unity when the revised normalisation is fully enforced. In this way, the denominator in Eq. (4.43) effectively reproduces that in Eq. (4.40).

basis

$$T_j = \begin{pmatrix} a_1 & b_2 & 0 & \dots & 0 \\ c_2 & a_2 & b_3 & \ddots & \vdots \\ 0 & \ddots & \ddots & \ddots & 0 \\ \vdots & \ddots & c_{j-1} & a_{j-1} & b_j \\ 0 & \dots & 0 & c_j & a_j \end{pmatrix}. \tag{4.48}$$

The bi-Lanczos method is implemented as follows:

1. **Initialisation:** Choose two normalised vectors $|p_1\rangle = |q_1\rangle = |\psi(0)\rangle$ so that $\langle p_1|q_1\rangle = 1$. Initialize the Lanczos coefficients by setting

$$b_1 = c_1 = 0, \quad a_1 = \langle p_1|A|q_1\rangle = \langle q_1|A|q_1\rangle.$$

2. **Recursive Construction (for $j \geq 1$):** For each iteration, perform the following steps:

   a) *Generate Intermediate Vectors:* Compute

$$|r_j'\rangle = A\,|q_j\rangle, \qquad |s_j'\rangle = A^\dagger\,|p_j\rangle.$$

   b) *Subtract Previous Contributions:* Form the residual vectors by removing the components along the previous two basis vectors

$$|r_j\rangle = |r_j'\rangle - a_j\,|q_j\rangle - b_j\,|q_{j-1}\rangle, \qquad |s_j\rangle = |s_j'\rangle - a_j^*\,|p_j\rangle - c_j^*\,|p_{j-1}\rangle. \tag{4.49}$$

   c) *Determine Next Coefficients:* Evaluate the inner product $\omega_j = \langle r_j|s_j\rangle$ and define

$$c_{j+1} = \sqrt{|\omega_j|}, \qquad b_{j+1} = \frac{\omega_j^*}{c_{j+1}}. \tag{4.50}$$

   d) *Normalize New Basis Vectors:* Construct the next basis elements as

$$|q_{j+1}\rangle = \frac{|r_j\rangle}{c_{j+1}}, \qquad |p_{j+1}\rangle = \frac{|s_j\rangle}{b_{j+1}^*}.$$

   e) *Enforce Full Bi-Orthogonalisation:* Due to potential numerical instabilities (which arise because only the immediate two preceding vectors are subtracted), one may lose full orthogonality. To remedy this, apply a complete Gram–Schmidt

procedure:

$$|q_j\rangle \to |q_j\rangle - \sum_{l=1}^{j-1} \langle p_l|q_j\rangle\, |q_l\rangle, \qquad |p_j\rangle \to |p_j\rangle - \sum_{l=1}^{j-1} \langle q_l|p_j\rangle\, |p_l\rangle.$$

f) *Update Diagonal Coefficient:* Finally, determine the new diagonal element by

$$a_{j+1} = \langle p_{j+1}|A|q_{j+1}\rangle. \tag{4.51}$$

3. **Termination:** When the inner product ω_j becomes zero at $j = \mathscr{K}$, no further linearly independent basis vectors can be generated. In that case, for an $N \times N$ matrix A, one obtains two $N \times \mathscr{K}$ matrices

$$P_{\mathscr{K}} \equiv \Big[p_1, p_2, \ldots, p_{\mathscr{K}}\Big], \quad Q_{\mathscr{K}} \equiv \Big[q_1, q_2, \ldots, q_{\mathscr{K}}\Big],$$

such that

$$P_{\mathscr{K}}^{\dagger} A\, Q_{\mathscr{K}} = T_{\mathscr{K}},$$

with $T_{\mathscr{K}}$ given by Eq. (4.48).

This procedure yields the full sets of bi-orthogonal basis vectors $\{|q_j\rangle\}$ and $\{|p_j\rangle\}$ along with the Lanczos coefficients a_j [Eq. (4.51)], b_j and c_j [Eq. (4.50)]. Note that the coefficients c_j are real by definition since $c_j = \sqrt{|\omega_{j-1}|}$, while the b_j may be complex (though in magnitude $|c_j| = |b_j|$) [69].

The wave function $|\psi(t)\rangle$ can be expanded in both Krylov bases as

$$|\psi(t)\rangle = \sum_{j=1}^{\mathscr{K}} \Phi_j^q(t)\, |q_j\rangle = \sum_{j=1}^{\mathscr{K}} \Phi_j^p(t)\, |p_j\rangle. \tag{4.52}$$

Using the normalisation of Eq. (4.42), one defines the total probability in the bi-orthogonal basis by

$$P^{(bl)}(t) = \sum_n \Big|\tilde{\Phi}_n^{p*}(t)\, \tilde{\Phi}_n^q(t)\Big|,$$

where the superscript (bl) denotes quantities derived via the bi-Lanczos algorithm and the tildes indicate that the coefficients have been normalised so that $P^{(bl)}(t) = 1$ at all times. The associated measures of spread complexity and entropy are then given by

$$C_S^{(bl)}(t) = \sum_n n \Big|\tilde{\Phi}_n^{p*}(t)\, \tilde{\Phi}_n^q(t)\Big|, \tag{4.53}$$

$$S_S^{(bl)}(t) = -\sum_n \Big(\Big|\tilde{\Phi}_n^{p*}(t)\, \tilde{\Phi}_n^q(t)\Big|\Big) \ln\Big[\Big|\tilde{\Phi}_n^{p*}(t)\, \tilde{\Phi}_n^q(t)\Big|\Big]. \tag{4.54}$$

While the bi-Lanczos algorithm furnishes a robust framework for studying spread complexity in non-Hermitian systems, its computational memory demands can become significant for large Hilbert space dimensions. For cases involving complex symmetric Hamiltonians, we therefore introduce an alternative approach (discussed below) that is both more efficient and less memory intensive.

Complex Symmetric Lanczos Algorithm

In this section we introduce a cost-efficient algorithm specifically designed for complex symmetric matrices. This approach will be employed in Section 4.2.3 when addressing a complex symmetric Hamiltonian H_{eff} that obeys $H_{\text{eff}}^T = H_{\text{eff}}$, but $H_{\text{eff}}^\dagger \neq H_{\text{eff}}$, demonstrating its practical utility.

The concept of complex symmetry is purely algebraic and does not affect the spectral properties of a matrix. In fact, for any given set of n numbers there exists a complex symmetric $n \times n$ matrix A whose eigenvalues exactly match these numbers, even though such matrices are not necessarily diagonalizable. Despite this, the special algebraic structure of complex symmetric matrices permits significant reductions in both computational cost and memory requirements compared to the general non-Hermitian bi-Lanczos method.

A matrix A is diagonalizable in the complex symmetric case if its eigenvector matrix Z can be chosen so that $Z^T A Z = \text{diag}(\lambda_1, \lambda_2, \ldots, \lambda_n)$, with the additional property that $Z^T Z = I_n$, implying that Z is complex orthogonal. This complex orthogonality is crucial as it allows one to construct a Krylov basis efficiently. To achieve this, we modify the conventional Lanczos algorithm to ensure that the resulting basis vectors retain complex orthogonality even when they are themselves complex.

Using these ideas, the complex symmetric Lanczos algorithm [352] reexpresses the matrix A in a tridiagonal form. One begins with a normalised initial vector $|q_1\rangle = |\psi(0)\rangle$, and constructs the Krylov space $\mathscr{K}^j\big(A, |q_1\rangle\big) \equiv \{A|q_1\rangle, A^2|q_1\rangle, \ldots\}$. Due to the complex orthogonality condition—where we define the bra associated with $|q_j\rangle$ as its transpose, i.e. $\langle q_j| = (|q_j\rangle)^T$—each basis vector satisfies $\langle q_j|q_j\rangle = 1$. The Krylov basis is then generated via the three-term recurrence relation

$$\beta_{j+1}|q_{j+1}\rangle = A|q_j\rangle - \alpha_j|q_j\rangle - \beta_j|q_{j-1}\rangle, \tag{4.55}$$

which leads to the tridiagonal matrix representation

$$\tilde{T}_j = \begin{pmatrix} \alpha_1 & \beta_2 & 0 & \dots & 0 \\ \beta_2 & \alpha_2 & \beta_3 & \ddots & \vdots \\ 0 & \ddots & \ddots & \ddots & 0 \\ \vdots & \ddots & \beta_{j-1} & \alpha_{j-1} & \beta_j \\ 0 & \dots & 0 & \beta_j & \alpha_j \end{pmatrix}. \tag{4.56}$$

Implementing the standard Lanczos procedure under the constraint of complex orthogonality produces the Krylov basis matrix $Q = [\hat{q}_1\ \hat{q}_2\ \dots\ \hat{q}_n]$, which satisfies $Q^T Q = I_n$ and results in the similarity transformation $\tilde{T}_j = Q_j^T A\, Q_j$.

It is instructive to compare the tridiagonal matrices T_j and $\tilde{T}_j$ obtained via the bi-Lanczos and the complex symmetric Lanczos methods (see Eqs. (4.48) and (4.56), respectively). The clear advantage of the complex symmetric Lanczos algorithm is that it requires only a single set of Krylov basis vectors (as generated in Eq. (4.55)). Consequently, the off-diagonal elements of $\tilde{T}_j$ are identical, so that the tridiagonal matrix is symmetric. In contrast, the bi-Lanczos algorithm produces a tridiagonal matrix T_j that is generally not symmetric. Although the diagonal entries agree ($a_j = \alpha_j$), the off-diagonal elements differ in that $b_j \neq \beta_j$ and $c_j \neq \beta_j$; however, their magnitudes coincide: $|\beta_j| = |b_j| = |c_j|$. Thus, in terms of absolute values, the matrices satisfy $|T_j| = |\tilde{T}_j|$.

This efficient algorithm for complex symmetric matrices will be utilised in Section 4.2.3 for the analysis of Hamiltonians exhibiting complex symmetric structure, particularly in the study of the quantum first passage problem.

4.2.3 Complexity and Entropy under Projective Measurements

To illustrate features of non-unitary evolution, we focus on a concrete case known as the quantum first passage problem (QFPP). While the methods presented in the previous section are general and applicable to any non-unitary dynamics, the discussion here is tailored to the QFPP, emphasising the sensitivity of Krylov basis measures to its specific characteristics. In Section 4.2.3 we review the QFPP, and in Section 4.2.3 we present our numerical results.

First Passage Problem

The QFPP in quantum mechanics addresses the probability that a particle, initially located at a given site, reaches a designated target site for the first time within a fixed time interval [355]. This problem is significant not only in quantum physics but also in areas such as chemical reaction dynamics, electron transport in materials, and even biological processes.

As shown in [337, 338], the time evolution of a quantum system subject to periodic projective measurements can be recast as a non-Hermitian process exhibiting non-unitary evolution. In our study we adopt the framework of [337, 338], where a quantum particle on a lattice evolves under a tight-binding Hamiltonian while its position is repeatedly measured at predefined sites. Between detections, the system evolves unitarily; however, the projective operations representing measurements introduce non-unitarity.

Let us consider a Hamiltonian of the form

$$H = \underbrace{\sum_{l,m} H_{l,m}\,|l\rangle\langle m|}_{H_S} + \underbrace{\sum_{\alpha,\beta} H_{\alpha,\beta}\,|\alpha\rangle\langle\beta|}_{H_M} + \underbrace{\sum_{\alpha,l}\Big(V_{\alpha,l}\,|\alpha\rangle\langle l| + V_{l,\alpha}\,|l\rangle\langle\alpha|\Big)}_{V}, \tag{4.57}$$

where each state $|l\rangle$ denotes a lattice site. The lattice sites are split into those belonging to the system (indexed by Roman letters l and m) and those where measurements are performed (indexed by Greek letters α and β), following the notation in [338]. Under unitary evolution, the state evolves as $|\psi(t)\rangle = U_t|\psi(0)\rangle$, with $U_t = e^{-iHt}$.

To incorporate projective measurements, we define the projection operator $A = \sum_{\alpha\in D}|\alpha\rangle\langle\alpha|$, where D denotes the set of detection sites. Its complement $B = 1 - A$, projects onto the system subspace. When the state is measured, the detection probability is $p = \langle\psi|A|\psi\rangle$, while the survival probability (i.e. the probability that no detection occurs) is $P = \langle\psi|B|\psi\rangle = 1 - p$. A positive detection collapses the state to $A|\psi\rangle$, whereas failure to detect forces a collapse to $B|\psi\rangle$. This process is repeated until a detection takes place.

Between successive measurements, the effective time evolution operator is given by $\tilde{U}_\tau = B\,e^{-iH\tau}\,B = B\,U_\tau\,B$, where τ is the interval between measurements. After $M+1$ measurements, the overall evolution is

$$\mathscr{U}_{M+1} = \left(\tilde{U}_\tau\right)^M = B\,U_\tau\,B\,U_\tau\,\cdots\,\underbrace{B\,U_\tau}_{M\text{ times}}\,B, \tag{4.58}$$

using the identity $B^2 = B$. Since B is non-unitary, a second-order perturbative expansion for small τ leads to an effective non-Hermitian Hamiltonian. Specifically,

$$\tilde{U}_\tau = e^{-iH_{\text{eff}}\tau} + \mathscr{O}(\tau^3) \quad\Longrightarrow\quad \mathscr{U}_{M+1} \approx e^{-iH_{\text{eff}}t}, \quad t = M\tau, \tag{4.59}$$

$$\text{where}\quad H_{\text{eff}} = H_S - \frac{i\tau}{2}\sum_{l,m}\sum_{\alpha} V_{l,\alpha}\,V_{\alpha,m}\,|l\rangle\langle m|. \tag{4.60}$$

Thus, H_{eff} is composed of a Hermitian part H_S and a non-Hermitian correction that determines the complex portion of the eigenspectrum. Note that H_{eff} acts on all lattice sites except

the detector sites.[3] It is important to emphasize that taking the limit $\tau \to 0$ in the perturbative expansion (representing nearly continuous measurements) is not equivalent to setting $\tau = 0$, which would restore the original Hermitian Hamiltonian. Similarly, interpreting $\tau \to \infty$ as the unitary limit is not accurate because the perturbative treatment fails for large τ.

We now consider two one-dimensional models: (i) a model with open boundary conditions and (ii) a model with periodic boundary conditions. Starting from the tight-binding Hamiltonian for N sites,

$$H_{\text{TB}} = -\sum_{l=1}^{N-1} \Big(|l+1\rangle\langle l| + |l\rangle\langle l+1| \Big), \tag{4.61}$$

we place a detector at the Nth site. In this case, the projection operator is $A = |N\rangle\langle N|$ and the complementary projector is

$$B = \sum_{l=1}^{N-1} |l\rangle\langle l|.$$

Then, to first order in τ, the effective Hamiltonian for the open chain is

$$H_{\text{eff}} = -\sum_{l=1}^{N-2} \Big(|l+1\rangle\langle l| + |l\rangle\langle l+1| \Big) - \frac{i\tau}{2} \, |N-1\rangle\langle N-1|. \tag{4.62}$$

Here the non-Hermitian term (denoted by V_{eff}) is localised at site $N-1$.

For periodic boundary conditions where $|N+1\rangle = |1\rangle$, the operators A and B remain unchanged, but the effective Hamiltonian becomes

$$H_{\text{eff}} = -\sum_{l=1}^{N-2} \Big(|l+1\rangle\langle l| + |l\rangle\langle l+1| \Big) - \frac{i\tau}{2} \Big(|N-1\rangle\langle N-1| + |1\rangle\langle 1| + |1\rangle\langle N-1| + |N-1\rangle\langle 1| \Big). \tag{4.63}$$

In the periodic case the Hamiltonian possesses $(N-2)/2$ eigenvalues that are two-fold degenerate. As described in [338], half of the eigenstates remain unaffected by the measurement process. Moreover, for periodic boundary conditions the survival probability does not decay to zero at long times unless the initial state is localised at the $(N/2)$th site for even N, whereas in the open boundary case the survival probability inevitably decays to zero.

Results for Krylov State Complexity and Entropy

In our analysis we use the normalised definitions for spread complexity and spread entropy as given in Eq. (4.44), noting that the total Krylov probability defined in Section 4.2.2 remains constant even under non-unitary evolution.

[3] From now on the system is defined as the chain excluding the detector sites.

We now detail the numerical findings for the spread complexity and entropy in the context of the quantum first passage problem (QFPP). Our presentation is organised into three parts. First, we examine the spread complexity of the non-Hermitian tight-binding chain under both open (Section 4.2.3) and periodic boundary conditions (Section 4.2.3). In these studies, we vary both the non-Hermiticity perturbation parameter τ and the position as well as the spatial spread of the initial state. Next, we focus on a quench scenario (Section 4.2.3) in which the system is initialised in eigenstates of the Hermitian tight-binding Hamiltonian and evolved using the effective non-Hermitian Hamiltonian. In addition, we analyze the behaviour of both the Krylov entropy and total probability across these cases to elucidate the universal characteristics imposed by the non-Hermitian dynamics.

Open Boundary Conditions We begin with a tight-binding chain subject to repeated projective measurements, such that its effective time evolution is governed by the non-Hermitian Hamiltonian given in Eq. (4.62). In what follows, we first describe the evolution of the wave function towards a steady state, and then discuss the corresponding time evolution of the spread complexity and entropy.

Steady State For the QFPP with open boundary conditions, the steady state is defined as the state that remains invariant, aside from small fluctuations, under the action of the Hamiltonian. These states for non-equilibrium systems play a role similar to that of thermal states in the unitary case. As the initial state evolves according to Eq. (4.40), it eventually explores the entire Krylov space and settles into a steady state, leading to the saturation of both spread complexity and entropy. In our simulations for open boundary conditions the steady-state profile (illustrated in Figure 4.18) is centered at the lth site of a chain with total sites $N = 2l$. Importantly, the steady state does not depend on the choice of the initial state or on the time interval τ between measurements. Moreover, if the initial state already exhibits a spatial spread similar to that of the steady state, the resulting spread complexity attains a low saturation value. In contrast, an initial state with a narrower spread that gradually explores more sites results in a more pronounced evolution of complexity.

Spread Complexity Figure 4.19 displays the time evolution of the Krylov spread complexity (as defined in Eq. (4.44)) for the tight-binding chain. In Figure 4.19a, the dependence on the non-Hermiticity parameter τ is illustrated, while Figure 4.19b shows the effect of varying the initial state's spread. In all cases, the spread complexity initially grows, undergoes prolonged oscillations, and finally saturates to a constant value significantly lower than the peak value. The oscillatory behaviour originates partly from the integrable nature of the underlying system and partly from the interplay between the repeated projective measure-

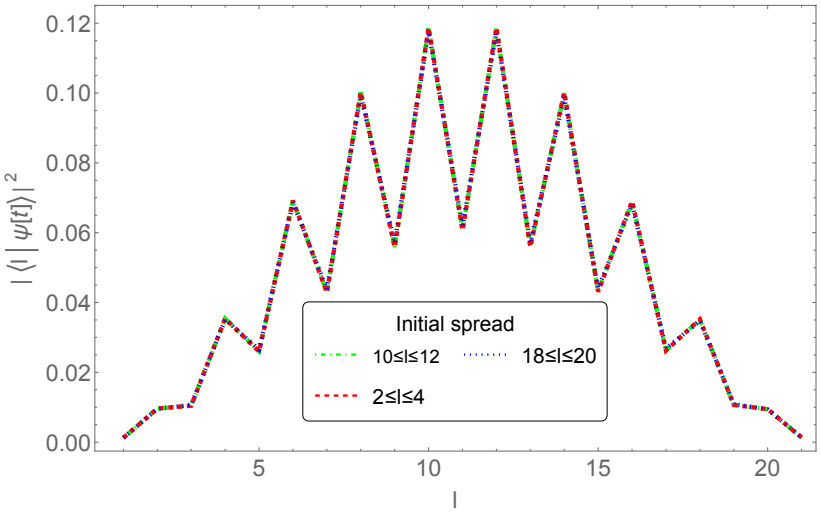

Figure 4.18: Spread of the steady state at late times $t = 30000$ for different initial state spreads, for open boundary conditions with total number of sites $N = 22$ and non-Hermiticity parameter $\tau = 0.1$. The final state is independent of the initial state. Figure taken from [63].

ments and the finite chain length. As observed in the inset of Figure 4.19a, modifying the measurement frequency alters the oscillation period. The eventual saturation signals the system's approach to the steady state, as discussed above.

For a fixed initial state covering sites $18 \leq l \leq 22$ and total sites $N = 42$, Figure 4.19a shows that increasing τ (from $\tau = 0.1$ in green to $\tau = 0.2$ in red and $\tau = 0.5$ in blue) leads to a more rapid decay of the oscillations, hence an earlier saturation. This result indicates that a longer time between measurements allows the effect of the interaction to propagate more widely throughout the system, expediting the approach to the universal steady state. Nonetheless, the saturation value of the spread complexity remains unchanged with varying τ, in agreement with previous findings on non-unitary operator complexity in open systems [69].

The saturation value and the rate at which saturation is achieved also depend sensitively on the initial state's spread. As shown in Figure 4.19b, an initial state with a narrower spread (e.g. over $9 \leq l \leq 13$) takes longer to saturate and reaches a lower complexity compared to a state with a broader spread (e.g. over $10 \leq l \leq 12$). Furthermore, initial states localised closer to the chain's center saturate faster and at lower complexity values than those that are farther removed from the center. This symmetry is evidenced by the overlapping complexity curves for states initially spanning $2 \leq l \leq 4$ (orange) and $18 \leq l \leq 20$ (dashed cyan), as well as for states with spreads $2 \leq l \leq 6$ (pink) and $16 \leq l \leq 20$ (dashed blue). Such symmetry in the complexity dynamics reflects the analogous symmetry in the survival probability $S(t) = \langle\psi(0)|\psi(t)\rangle$ [338].

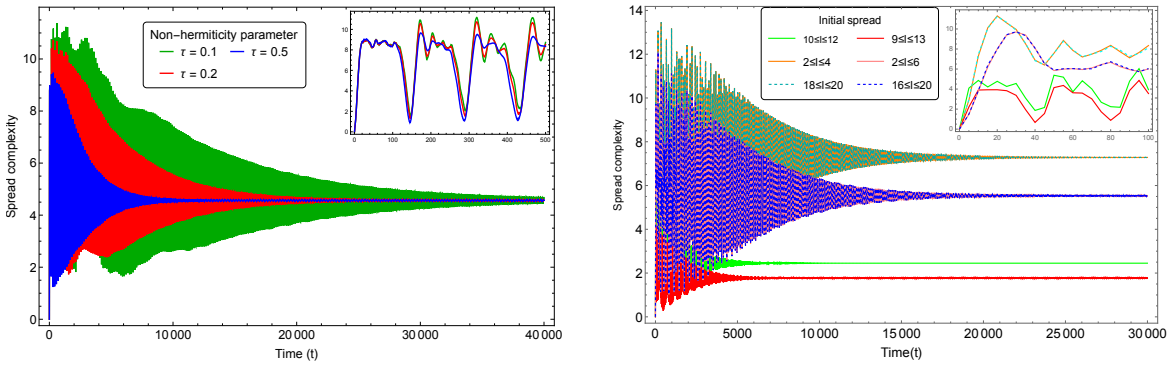

(a) Time variation of spread complexity for different values of τ.

(b) Time variation of spread complexity for different initial state spreads.

Figure 4.19: (a) Time dependence of spread complexity for non-Hermiticity parameters $\tau = 0.1$ (green), 0.2 (red), and 0.5 (blue) with fixed total sites $N = 42$ and initial state spanning $18 \leq l \leq 22$. (b) Time variation of spread complexity for initial states with spreads $9 \leq l \leq 13$ (red), $10 \leq l \leq 12$ (green), $2 \leq l \leq 6$ (pink), $2 \leq l \leq 4$ (orange), $16 \leq l \leq 20$ (dashed blue), and $18 \leq l \leq 20$ (dashed cyan) with fixed $N = 22$ and $\tau = 0.1$. Insets display early-time behaviour. Figure taken from [63].

Spread Entropy We now turn to the temporal evolution of the spread entropy, as defined in Eq. (4.44). Figure 4.20 shows that the spread entropy initially increases rapidly, then exhibits oscillations of diminishing amplitude before finally saturating. Figure 4.20a illustrates the spread entropy for different values of τ ($\tau = 0.1$ in green, 0.2 in red, and 0.5 in blue). The dependence on τ is qualitatively similar to that seen for spread complexity: larger τ values lead to a faster suppression of oscillations and quicker saturation, while the final saturation value remains the same. This reinforces our previous conclusion regarding the universality of the steady state for a given initial state.

Figure 4.20b further demonstrates that the saturation value and the rate of saturation of spread entropy depend on the initial state's position and spread. Specifically, initial states centered near the middle of the chain (e.g. spanning $9 \leq l \leq 13$ or $10 \leq l \leq 12$ in a chain of $N = 22$ sites) saturate more quickly and attain lower entropy values than those farther from the center (e.g. spanning $2 \leq l \leq 4$ or $18 \leq l \leq 20$). This behaviour is analogous to what is observed for the spread complexity. In fact, previous studies [55] have conjectured that the spread complexity may be approximated by the exponential of the spread entropy, and our results suggest that this relation holds even under non-Hermitian evolution.

Periodic Boundary Condition

We now turn to the QFPP under periodic boundary conditions, where the effective non-Hermitian Hamiltonian is given in Eq. (4.63). In this case, we first examine the time evolution of the wave function and the corresponding steady state profile in the position basis.

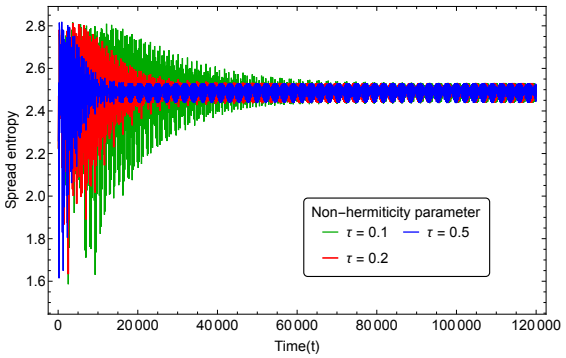

(a) Time variation of spread entropy for different values of τ.

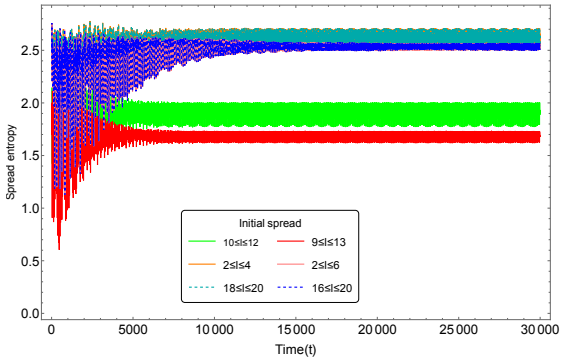

(b) Time variation of spread entropy for different initial state spreads.

Figure 4.20: (a) Temporal behaviour of spread entropy for non-Hermiticity parameters $\tau = 0.1$ (green), 0.2 (red), and 0.5 (blue) with fixed total sites $N = 42$ and initial state spanning $18 \leq l \leq 22$. (b) Time evolution of spread entropy for initial state spreads $9 \leq l \leq 13$ (red), $10 \leq l \leq 12$ (green), $2 \leq l \leq 6$ (pink), $2 \leq l \leq 4$ (orange), $16 \leq l \leq 20$ (dashed blue), and $18 \leq l \leq 20$ (dashed cyan) with $N = 22$ and $\tau = 0.1$. Figure taken from [63].

Next, we analyze the time dependence of both spread complexity and spread entropy using the non-Hermitian normalisation from Eq. (4.43) and the definitions in Eq. (4.44). (For the dependence on τ, the behaviour is similar to that in open boundary conditions.) Notably, the response to different initial states in periodic systems yields distinct physical outcomes.

Steady States For periodic boundary conditions, the nature of the steady state varies with the initial state. Figure 4.21 shows the steady-state spread profiles for different initial conditions. A localised steady state is observed only when the initial state is centered around the middle of the chain (specifically, when $18 \leq l \leq 24$ for a chain of length $N = 42$). In essence, if the initial state's position is around the central site (i.e. the l-th site of a lattice chain of length $2l$), the steady state localizes at the center. Conversely, if the initial state is concentrated near the detector (for example, for $2 \leq l \leq 7$ or $35 \leq l \leq 40$ in a chain with $N = 42$), the non-unitary evolution does not drive the system toward a localised state. Instead, the wave function becomes distributed with varying probabilities across different sites and, at late times, oscillates about this extended distribution.

Spread Complexity Figure 4.22a presents the time evolution of spread complexity, as defined in Eq. (4.44), for several initial state spreads with fixed $N = 42$ and $\tau = 0.1$. When the initial state includes the central site (e.g. for an initial spread of $18 \leq l \leq 24$, shown in green), the complexity exhibits growth, decay, and saturation behaviour similar to that observed under open boundary conditions. In this scenario, the saturation value is notably

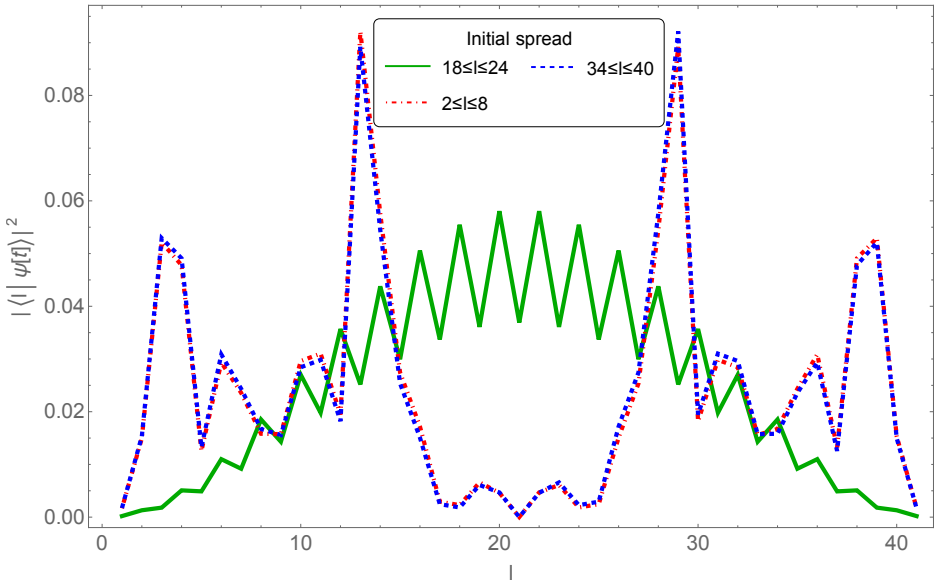

Figure 4.21: Spread of the steady state at late times ($t = 50000$) for different initial state spreads under periodic boundary conditions with $N = 42$ and non-Hermiticity parameter $\tau = 0.1$. Unlike the open boundary case (Figure 4.18), here the steady state profile depends on the initial state. Figure taken from [63].

suppressed. This suppression is attributed to the reduced effective dimension of the Krylov space—when the initial state is centered, the Krylov space becomes approximately half the total dimension, thereby expediting the steady state and lowering the saturation value. On the other hand, if the initial state is distributed away from the center, the time-evolved state does not settle into a localised steady state (as seen in Figure 4.21); it oscillates around a distribution with support over all sites. This results in red and blue curves in Figures 4.22a and 4.22b that display more pronounced oscillatory saturation.

For initial states that do not encompass the central region, the late-time evolution of complexity resembles that of an effectively unitary system: the decay phase is brief and followed by extended oscillations with an amplitude that grows with the spatial spread of the initial state. Moreover, the associated time-dependent Krylov probability, defined in Eq. (2.74), also reaches a constant value at an early time. This behaviour explains why off-center initial states display a higher saturation value in spread complexity compared to those centered on the chain.

Spread Entropy Figure 4.22b displays the evolution of spread entropy for different initial state configurations. Its temporal behaviour closely follows that of spread complexity. When the initial state is centered around the middle of the chain, the spread entropy undergoes significant oscillations that decrease in amplitude over time, eventually saturating at a fixed value. In contrast, if the initial state is located near the detector, the spread entropy grows

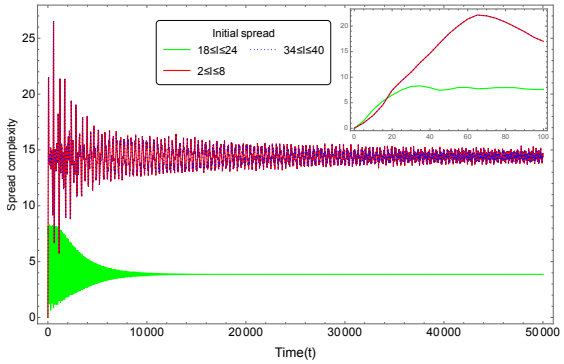

(a) Time evolution of spread complexity for various initial state spreads.

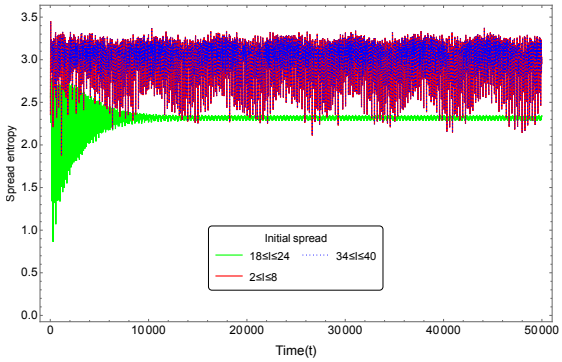

(b) Time evolution of spread entropy for various initial state spreads.

Figure 4.22: (a) Spread complexity and (b) spread entropy for initial state spreads $18 \leq l \leq 24$ (green), $2 \leq l \leq 8$ (red), and $34 \leq l \leq 40$ (dotted blue), with fixed total sites $N = 42$ and $\tau = 0.1$ under periodic boundary conditions. For states centered around the middle (green), the oscillations decay rapidly, whereas for off-center states (red, dotted blue), the oscillatory saturation phase is more evident. Figure taken from [63].

and oscillates about a saturation value without a pronounced decay phase. The symmetry observed in the red and blue curves of Figures 4.22b and 4.22a corroborates earlier findings regarding the steady state and spread complexity. In particular, for off-center initial states, the spread entropy exhibits behaviour characteristic of effective unitarity.

Quenching Eigenstates of the Hermitian Hamiltonian

Next, we investigate the dynamics of the Krylov spread complexity under a quench from a Hermitian to a non-Hermitian Hamiltonian. In our protocol, the system (assumed to have open boundary conditions, as in Section 4.2.3) is initially prepared in an eigenstate of the Hermitian tight-binding Hamiltonian H_{TB}, given in Eq. (4.61). Since an eigenstate of H_{TB} evolves trivially (up to an overall phase) for all times $t < 0$, no nontrivial complexity develops until the quench occurs at $t = 0$. At this point, the Hamiltonian is suddenly changed from H_{TB} to the effective non-Hermitian Hamiltonian H_{eff} of Eq. (4.62). The quench Hamiltonian, H_q, is therefore defined as

$$H_q = \begin{cases} H_{\text{TB}} = H_{\text{TB}}^{\dagger}, & -\infty \leq t < 0, \\ H_{\text{eff}} \neq H_{\text{eff}}^{\dagger}, & t \geq 0. \end{cases} \tag{4.64}$$

After $t = 0$, the system evolves under the complex symmetric non-Hermitian Hamiltonian, which builds the corresponding Hilbert space as a result of the measurement dynamics. In previous sections the initial states were chosen as position eigenstates distributed over a few lattice sites. Such states are not eigenstates of either H_{TB} or H_{eff}, so they exhibit nontrivial

spreading under both unitary and non-unitary evolution. By contrast, in the quench scenario the initial state is already an eigenstate of H_{TB}, and the nontrivial evolution arises solely from the measurement-induced dynamics that occur in intervals of τ after the quench.

For our study, we choose two types of initial states:

(i) The single-particle ground state, denoted by $|\psi_{\text{GS}}\rangle$.

(ii) The single-particle first excited state, denoted by $|\psi_{\text{FES}}\rangle$.

Quenching the Single-Particle Ground State We first consider the quench where the system is prepared in the ground state,

$$|\psi(t=0)\rangle = |\psi_{\text{GS}}\rangle.$$

Figure 4.23a illustrates that $|\psi_{\text{GS}}\rangle$ displays maximum support at the central site of the chain, with a distribution similar to the steady state observed for open boundary conditions (cf. Figure 4.18). Once the quench occurs, the effective non-Hermitian Hamiltonian H_{eff} governs the subsequent dynamics. In Figure 4.23b we see that if the time gap τ between consecutive measurements is large, an appreciable initial growth in the spread complexity appears, followed by a decay and eventual saturation similar to the open boundary case. In contrast, for smaller τ, the initial rise in complexity is largely suppressed, such that the complexity oscillates around a nearly constant value. This dependence on τ—which sets the measurement frequency—demonstrates that more frequent measurements (small τ) restrict the state from significantly spreading in the Hilbert space, consistent with the quantum Zeno effect [348–350].

A transition in the complexity behaviour is evident as τ varies. As τ increases from values on the order of 10^{-2} to those on the order of 10^{-1}, a pronounced initial growth in complexity is observed, followed by a long decay period and a higher saturation level (see Figure 4.23b). For very small τ, the measurements occur so frequently that the state does not have sufficient time to evolve appreciably, hence the spread complexity remains nearly constant—an unmistakable signature of the quantum Zeno effect.

Since the ground state $|\psi_{\text{GS}}\rangle$ (Figure 4.23a) already exhibits a spatial profile similar to the steady state (Figure 4.18), the overall saturation value of the spread complexity is suppressed. In order to observe a more pronounced effect of the quantum Zeno mechanism, it is instructive to examine the evolution starting from the first excited state.

Quenching the Single-Particle First Excited State Now, let the system be prepared in the first excited state,

$$|\psi(t=0)\rangle = |\psi_{\text{FES}}\rangle,$$

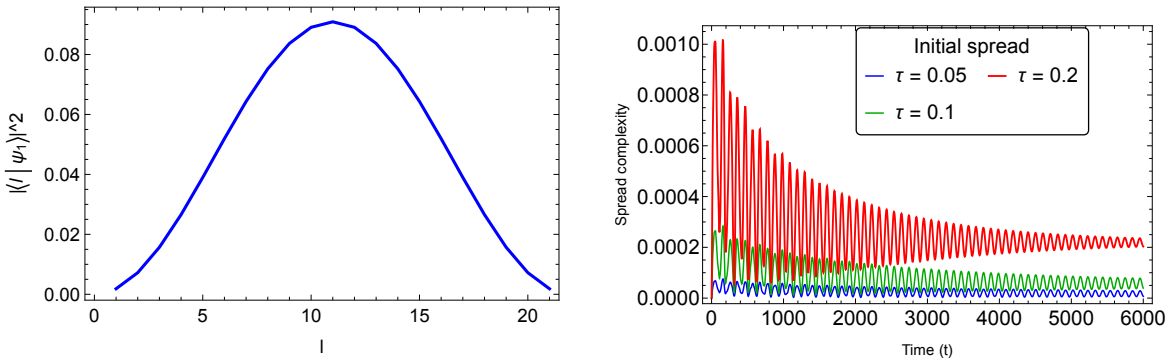

(a) (b)

Figure 4.23: (a) The single-particle ground state of the Hermitian tight-binding Hamiltonian for $N = 22$. (b) Spread complexity evolution for $N = 22$ and different measurement intervals $\tau = 0.05$ (blue), 0.1 (green), and 0.2 (red) when the initial state is $|\psi_{\text{GS}}\rangle$. For more frequent measurements (smaller τ), the initial growth is suppressed and the complexity oscillates around a fixed value. Figure taken from [63].

which is shown in Figure 4.24a. Because this state has a minimum at the central site, its initial distribution differs markedly from the steady state of the non-Hermitian evolution. Figure 4.24b displays the spread complexity for the first excited state under different τ. Here, we observe that, for larger τ, the spread complexity begins to grow earlier (e.g. the red curve corresponding to $\tau = 0.2$), while for smaller τ the growth is delayed. This delayed onset of complexity for small τ is a clear manifestation of the quantum Zeno effect, whereby continuous projective measurements impede the evolution of the state. Notably, despite the different time scales, the final saturation values of the spread complexity are identical for different τ, which confirms that the system eventually relaxes into the same steady state.

In summary, this quench protocol highlights a measurement-induced phase transition in the complexity dynamics. When the system is quenched from the Hermitian to the non-Hermitian regime, the subsequent evolution of the spread complexity is strongly influenced by the measurement interval τ and the nature of the initial state. The single-particle ground state, being already similar to the steady state, exhibits suppressed complexity growth, while the first excited state shows a clear delay in the onset of complexity for small τ, in perfect agreement with the expectations from the quantum Zeno effect [348–350].

4.2.4 PT-Symmetric Quantum Systems

In this subsection, we employ Krylov state complexity [55] as a tool to probe the wave function spreading and localisation dynamics in $\mathscr{P}\mathscr{T}$-symmetric systems. To illustrate these

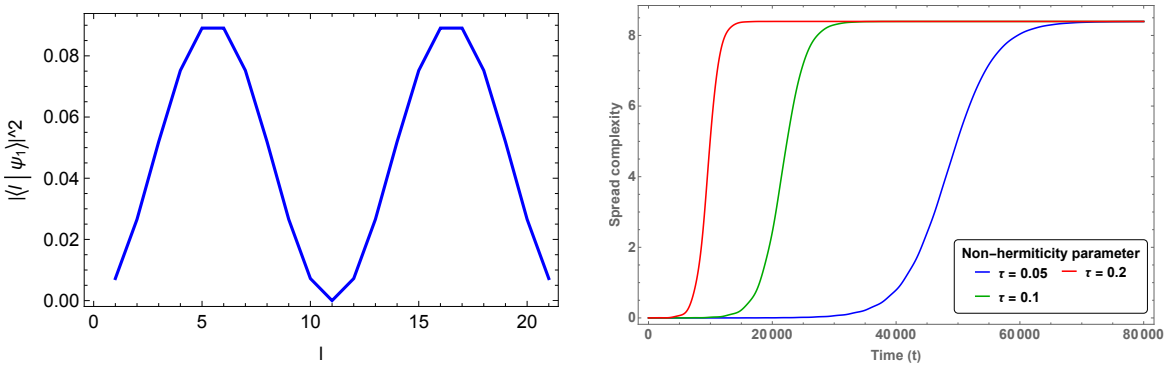

(a) (b)

Figure 4.24: (a) The single-particle first excited state of the Hermitian tight-binding Hamiltonian for $N = 22$. (b) Spread complexity evolution for $N = 22$ and measurement intervals $\tau = 0.05$ (blue), 0.1 (green), and 0.2 (red) when the initial state is $|\psi_{\text{FES}}\rangle$. For smaller τ, the complexity starts growing later, indicating a stronger quantum Zeno effect. Figure taken from [63].

ideas, we consider a $\mathscr{P}\mathscr{T}$-symmetric tight-binding model [356] defined by

$$H = -J \sum_{l=1}^{N-1} \left(a_l^\dagger a_{l+1} + \text{h.c.} \right) + i\gamma \left(a_1^\dagger a_1 - a_N^\dagger a_N \right), \tag{4.65}$$

where the creation and annihilation operators $a_i^\dagger$ and a_i (which may be bosonic or fermionic) act on the i-th site. The model exhibits two distinct phases: in the $\mathscr{P}\mathscr{T}$-unbroken phase all eigenvalues are real, while in the $\mathscr{P}\mathscr{T}$-broken phase two eigenvalues become purely imaginary. These phases are separated by a critical point at which a two-fold degeneracy at zero eigenvalue occurs [356].

In the $\mathscr{P}\mathscr{T}$-broken regime the emergence of a pair of imaginary eigenvalues induces localisation of the wave function at the lattice boundary; this phenomenon is widely known as the non-Hermitian skin effect [357–363]. Under time evolution, the state

$$|\psi(t)\rangle = e^{-iHt} |\psi(0)\rangle$$

tends to concentrate near the left-most site of the chain. This localisation is not only manifest in the original lattice basis but can be mapped to a dual tight-binding chain constructed in Krylov space via the Lanczos coefficients, as described in [55]. In this dual representation the localisation implies that the evolved state occupies only a limited number of Krylov basis vectors, which results in a suppression of the spread complexity.

By contrast, in the $\mathscr{P}\mathscr{T}$-unbroken phase the time-evolved single-particle state spreads over the entire lattice and oscillates between sites. On the corresponding dual Krylov chain,

the spread complexity initially increases and later saturates with large oscillations, reflecting the effective unitary behaviour and finite-size effects of the system [364]. The different behaviour of spread complexity in the two phases provides a distinctive signature of the $\mathscr{P}\mathscr{T}$-phase transition.

To quantitatively assess the degree of localisation in Krylov space, we introduce a dynamic measure termed the Krylov inverse participation ratio (KIPR). Inspired by the conventional inverse participation ratio (IPR) used in studies of Anderson localisation [327, 328], KIPR is defined such that higher values indicate stronger localisation. Unlike its Hermitian counterpart, the KIPR for non-Hermitian dynamics must account for the fact that eigenstates do not form an orthogonal basis. By using a Lanczos algorithm adapted to complex symmetric Hamiltonians [63], we are able to construct a complex orthogonal Krylov basis suited to $\mathscr{P}\mathscr{T}$-symmetric systems. We also note that Krylov operator complexity has been employed previously to investigate $\mathscr{P}\mathscr{T}$-phase transitions [365].

Our analysis reveals that the model described by Eq. (4.65) undergoes a localisation-delocalisation transition coinciding with the $\mathscr{P}\mathscr{T}$-phase transition. In the $\mathscr{P}\mathscr{T}$-broken phase, the evolved wave function localizes at the left boundary, which is reflected by a marked suppression in the saturation values of both the spread entropy and the entropic complexity; these suppressions are quantitatively related to the localisation strength as measured by the KIPR. Notably, while the spread complexity in the broken phase does not reliably signal changes in localisation strength—unlike in the unitary scenario [91]—the entropic complexity remains a sensitive probe. It effectively captures the reduction in the number of Krylov basis vectors needed to represent the state by measuring the effective Hilbert space dimension that stores the entropy distribution.

$\mathscr{P}\mathscr{T}$ Phase Transition and Localisation.—

We now investigate the phase transition properties of the system governed by the $\mathscr{P}\mathscr{T}$-symmetric tight-binding Hamiltonian of Eq. (4.65) and introduce our measures of spread complexity. This Hamiltonian features uniform nearest-neighbor hopping and two on-site potentials of equal magnitude but opposite sign, namely $\pm i\gamma$, with the tunnelling strength fixed at $J = 1$. The parity operator $\mathscr{P}$ and the time-reversal operator $\mathscr{T}$ act as $\mathscr{P}a_l^\dagger\mathscr{P} = a_{N+1-l}^\dagger$ and $\mathscr{T}i\mathscr{T} = -i$, respectively, ensuring that $[H, \mathscr{P}\mathscr{T}] = 0$. In the $\mathscr{P}\mathscr{T}$-unbroken phase all eigenstates are eigenstates of $\mathscr{P}\mathscr{T}$ and all eigenvalues are real, so that evolution is unitary. By contrast, in the $\mathscr{P}\mathscr{T}$-broken phase $N-2$ eigenvalues remain real while two eigenvalues form a complex-conjugate pair [356]:

$$E_{\kappa\pm} = \pm i\, 2J \sinh(\kappa).$$

Here, the parameter κ is determined by the relations

$$\gamma^2 = \begin{cases} J^2 \dfrac{\sinh\Big(\kappa(N+1)\Big)}{\sinh\Big(\kappa(N-1)\Big)} & \text{for } N = 2n+1, \\ J^2 \dfrac{\cosh\Big(\kappa(N+1)\Big)}{\cosh\Big(\kappa(N-1)\Big)} & \text{for } N = 2n. \end{cases}$$

The eigenvectors corresponding to the complex eigenvalues, denoted $|E_+\rangle$ and $|E_-\rangle$, are localised on opposite edges of the lattice (see Fig. 4.25). These states are not eigenstates of the $\mathscr{P}\mathscr{T}$ operator, thereby breaking the $\mathscr{P}\mathscr{T}$ symmetry. The resulting accumulation of amplitude at one boundary is known as the non-Hermitian skin effect.

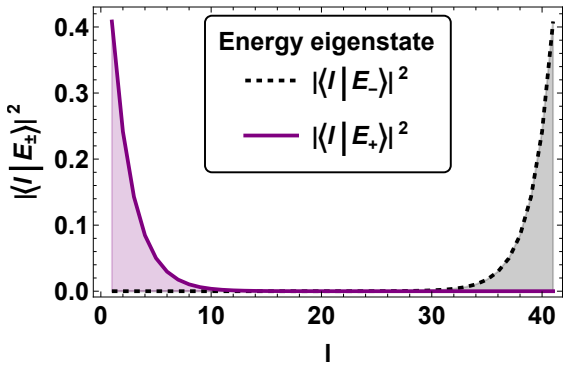

Figure 4.25: Right (black dashed) and left (purple) edge states in the $\mathscr{P}\mathscr{T}$-broken phase with $N = 40$, $J = 1$, and $\gamma = 1.3$. The energy eigenvalues are $E_{\kappa-} = -0.530769i$ and $E_{\kappa+} = 0.530769i$, respectively, illustrating that $|E_+\rangle$ and $|E_-\rangle$ are localised at the left and right edges of the lattice. Figure taken from [64].

As detailed in [356, 366], the transition between the $\mathscr{P}\mathscr{T}$-symmetric and broken phases occurs at critical values of γ. These are given by

$$\gamma = \begin{cases} J\sqrt{\dfrac{n+1}{n}} & \text{for } N = 2n+1, \\ J & \text{for } N = 2n. \end{cases} \tag{4.66}$$

At this transition point (see Eq. (4.66)), two eigenvalues coalesce at zero, forming an exceptional point [356, 366].

We now apply Krylov state complexity [55] to probe the system. In addition to spread complexity, an alternative entropic measure of complexity is given by

$$C_S(t) = e^{S(t)}, \tag{4.67}$$

which quantifies the minimal Hilbert space dimension required to encode the Krylov weight distribution.

To dynamically assess wave function localisation in Krylov space, we introduce the Krylov inverse participation ratio (KIPR):

$$\text{KIPR}(t) = \sum_{n=0}^{D-1} |\langle K_n|\psi(t)\rangle|^4 = \sum_{n=0}^{D-1} |\tilde{\psi}_n(t)|^4. \tag{4.68}$$

A KIPR value of one indicates complete localisation on a single Krylov vector, whereas if the state is equally spread over a D-dimensional Krylov space then $\text{KIPR}(t) = \frac{1}{D}$.

Localisation in the $\mathscr{P}\mathscr{T}$-Broken Phase.— In the $\mathscr{P}\mathscr{T}$-broken phase the amplitude of the eigenstate $|E_+\rangle$, corresponding to the eigenvalue $E_{\kappa+} = i\,2J\sinh(\kappa)$, grows as

$$|E_+(t)\rangle = e^{-iHt}|E_+(0)\rangle = e^{2J\sinh(\kappa)t}|E_+(0)\rangle.$$

Thus, at long times the state $|E_+\rangle$ dominates the time evolution, and since it is principally localised at the first lattice site (see Fig. 4.25), a generic state eventually becomes localised at that edge.

The localisation-delocalisation transition is equally evident in Krylov space. In Fig. 4.26 we show the time evolution of spread complexity (top panel), entropic complexity (middle panel), and KIPR (bottom panel) for an initial state uniformly spread over the 12^{th} to 18^{th} sites of a chain with $N = 40$ and $J = 1$. In the $\mathscr{P}\mathscr{T}$-symmetric phase ($\gamma < 1$) the spread complexity exhibits initial growth followed by large oscillations due to the real energy spectrum and finite-size effects. In contrast, in the $\mathscr{P}\mathscr{T}$-broken phase ($\gamma > 1$) the complexity saturates quickly, after a smaller yet more rapid initial rise. At the critical point $\gamma = 1$, the initial growth is subdued and the saturation value is higher than in the broken phase, with reduced fluctuations as the system transitions to a localised regime.

The spread complexity $C(t)$ quantifies the extent to which the state spreads over the Krylov basis. In a finite system the exploration of the full Krylov space eventually leads to saturation or oscillatory behaviour. In the $\mathscr{P}\mathscr{T}$-symmetric phase the state remains delocalised, yielding a larger effective support, whereas in the $\mathscr{P}\mathscr{T}$-broken phase the state becomes localised, resulting in a lower saturation value of $C(t)$. Correspondingly, the entropic complexity $C_S(t)$ also drops in the broken phase, reflecting a reduction in the effective Hilbert space dimension. Furthermore, the KIPR defined in Eq. (4.68) serves as a direct measure of localisation. At $t = 0$, when the state is completely localised on $|K_0\rangle$, the KIPR equals one. In the symmetric phase, as the state delocalizes, the KIPR decays and oscillates around zero; in the broken phase it decays, then rises to a constant value indicating persistent localisation.

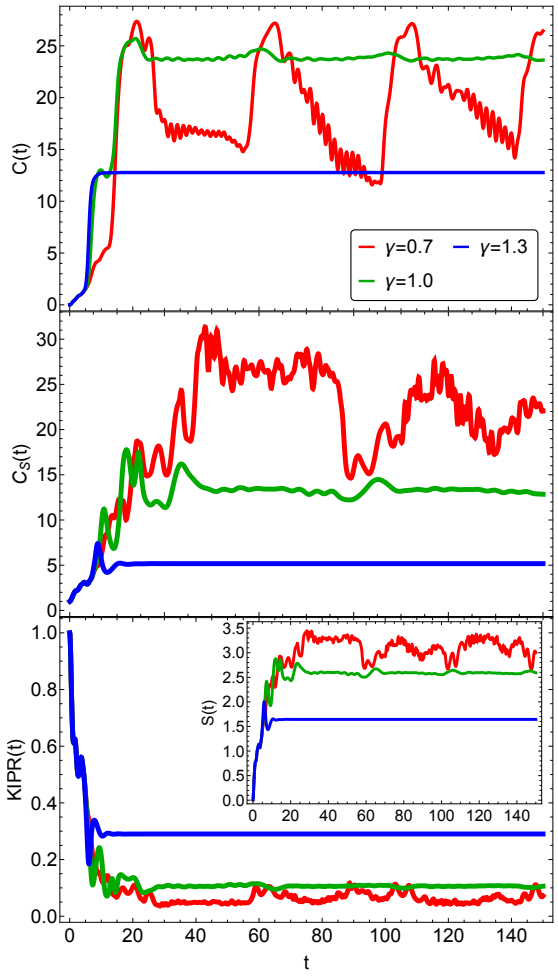

Figure 4.26: Time evolution of spread complexity (top), entropic complexity (middle), and KIPR (bottom) for an initial state uniformly spread over the 12^{th}–18^{th} sites of a chain with $N = 40$ and $J = 1$. The inset shows the evolution of spread entropy. In the $\mathscr{P}\mathscr{T}$-broken phase, both spread complexity and entropy are suppressed relative to the symmetric phase, while the KIPR indicates stronger localisation. Figure taken from [64].

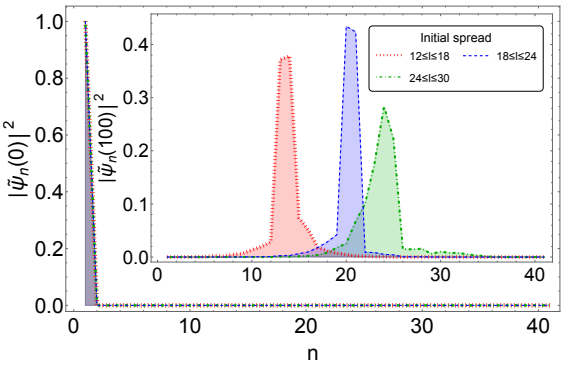

Figure 4.27: Localisation of time-evolved initial states in Krylov space. The main plot shows $|\tilde{\psi}_n(0)|^2$ at $t = 0$, where the state is entirely localised on $|K_0\rangle$, while the inset shows the distribution $|\tilde{\psi}_n(t)|^2$ at $t = 100$ for initial states with different spreads. Here $N = 40$, $J = 1$, and $\gamma = 1.3$. Figure taken from [64].

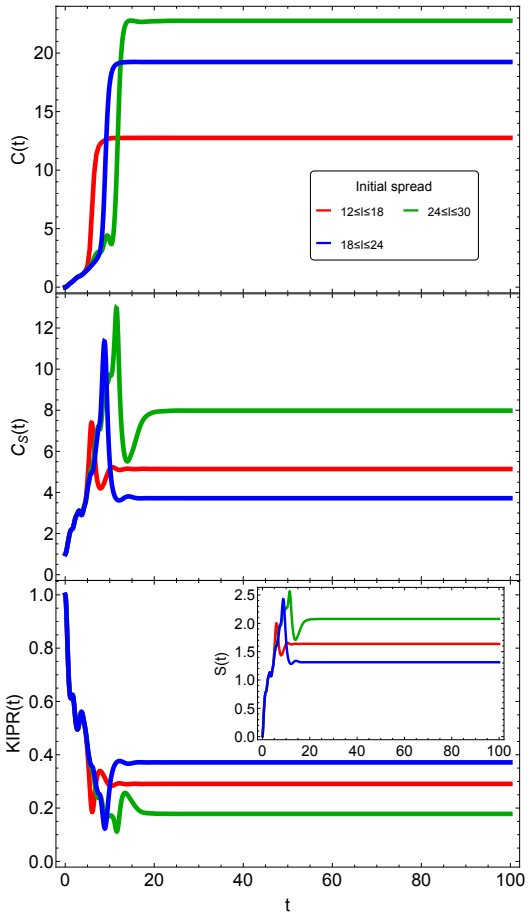

Figure 4.28: Saturation behaviour of spread complexity (top), entropic complexity (middle), and KIPR (bottom), with spread entropy shown in the inset, for various initial states in the broken phase. Parameters are $N = 40$, $J = 1$, and $\gamma = 1.3$. The saturation value of spread entropy decreases with increased localisation, while the hierarchy of saturation values in spread complexity does not directly follow localisation strength. Figure taken from [64].

The intermediate saturation of KIPR at the critical point $\gamma = 1$ supports the picture that the $\mathscr{P}\mathscr{T}$-symmetry breaking and the localisation-delocalisation transition occur concurrently, culminating in the non-Hermitian skin effect.

The location in Krylov space where localisation is observed depends on the spread of the initial state. Figure 4.27 shows the amplitude $|\tilde{\psi}_n(t)|^2$ of the Krylov wave function for different initial states at $t = 0$ (main plot) and at late times (inset). Initially, all the weight is concentrated in $|K_0\rangle$, but for an initial state uniformly spread over lattice sites l_1 to l_2, the evolved state becomes localised on Krylov vectors $|K_n\rangle$ with $l_1 \leq n \leq l_2$. Notably, if the initial state includes the central site, the overlap amplitude in Krylov space is higher compared to cases without the central region.

Our further findings (see Fig. 4.28) indicate that the saturation values of spread complexity, entropic complexity, and KIPR vary markedly with the precise positioning of the initial state.

For example, an initial state uniformly covering the central region yields an intermediate saturation value for $C(t)$ (blue curve in Fig. 4.28), even when localisation is strong. In contrast, both spread entropy and $C_S(t)$ consistently decrease as localisation becomes more pronounced. This discrepancy arises because the definition of $C(t)$ weights higher-index Krylov vectors more heavily; if localisation occurs at a later Krylov step, $C(t)$ remains elevated even under strong localisation. Thus, entropic measures (spread entropy and entropic complexity) serve as more reliable indicators of localisation strength.

In summary, these results demonstrate that the spread complexity, entropic complexity, and KIPR in Krylov space effectively capture the $\mathscr{P}\mathscr{T}$ phase transition and the corresponding localisation-delocalisation phenomenon. In the $\mathscr{P}\mathscr{T}$-broken phase, stronger localisation leads to a reduced effective Hilbert space dimension, which is most clearly reflected in the entropic measures.

4.2.5 Krylov Complexity of Purification

In many-body systems, the complexity of states and operators is central to understanding thermalisation, chaos, and environmental effects. Within the holographic framework, complexity has also become a focal point for studies of black holes—the interior growth of a black hole has been linked to the increase in complexity over time, prompting proposals for gravitational duals of complexity [39–49]. These developments are essential for addressing enduring puzzles about black hole interiors and the information paradox [40–43].

In this subsection, we introduce a novel framework to study the Krylov operator complexity of mixed states by examining both the spread state complexity and the corresponding Krylov operator complexity obtained via a purification procedure. Unlike previous studies [367] which embed the density matrix into a doubled Hilbert space, our method maps a mixed state to a pure state in an enlarged Hilbert space by incorporating an environment, ensuring overall unitary evolution. This approach, known as purification [368–370], has been used to investigate mixed-state measures such as the entanglement of purification [371] and the circuit complexities of purification (CoPs) [372–388]. Our framework provides a quantitatively unified approach to understanding complexity growth in both pure and mixed states and bridges existing gaps in current methodologies. In contrast to circuit CoPs and similar entanglement of purification measures—which rely on minimising over all possible purifications—we exploit the freedom inherent in isometries within the purification process to relate mixed-state Krylov complexity to both operator and state complexities of purification. Although purification-based measures often differ from original mixed-state complexities [389], we demonstrate that for a specific choice of isometry the CoP recovers the same dynamical behaviour as the standard complexity.

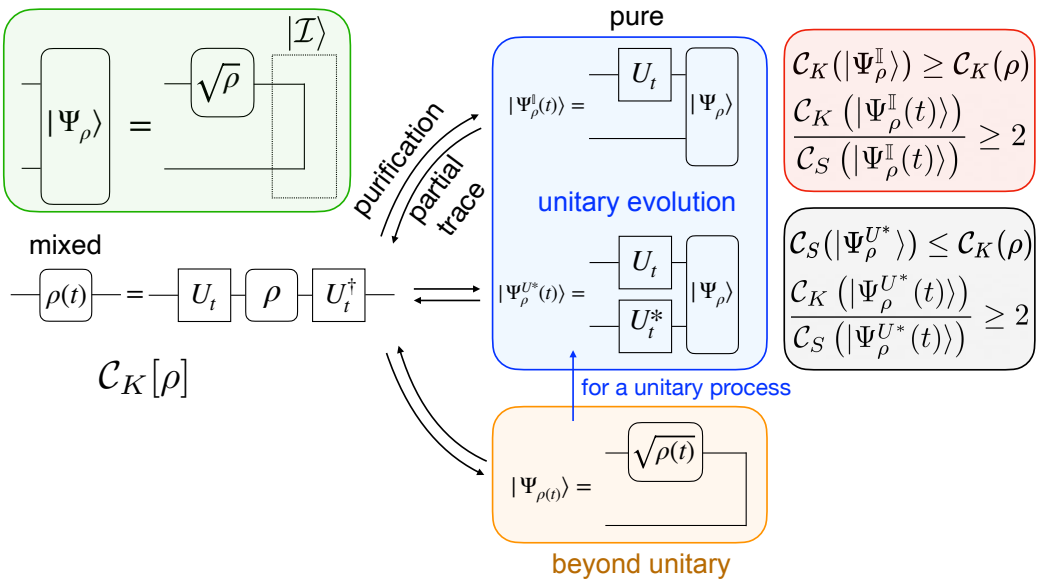

Figure 4.29: Graphical visualisation of the purification schemes illustrated via circuit diagrams. The upper left panel shows the purified state $|\psi_\rho\rangle$ corresponding to the mixed density matrix ρ. The central blue and orange panels depict how the time evolution of $\rho(t)$ is embedded into the pure state through different purification choices, while the rightmost panels summarize the bounds for mixed and purification complexities. Figure taken from [66].

We explore three distinct purification schemes—time-independent, time-dependent, and instantaneous purifications. These schemes induce different temporal evolutions on the ancilla, leading to various growth patterns in complexity even though, after tracing out the ancilla, the underlying mixed-state evolution remains the same.

A central result of our work is the derivation of inequalities linking mixed-state complexities and CoPs. We verify these inequalities using unitarily evolving arbitrary one-qubit mixed states as well as two-qubit Werner states. Moreover, we observe that our conjectured relations also hold for a non-unitarily evolving infinite-dimensional Gibbs state with increasing temperature. A consistent quasiparticle picture emerges when we identify the state with the Minkowski vacuum in a Rindler frame. Importantly, we demonstrate that the spread CoP for a thermal state is bounded above by certain thermodynamic quantities, in accordance with the Lloyd bound [390]. Finally, we introduce a new quantity, termed *mutual Krylov complexity*, and show that for the thermofield double (TFD) state, the Krylov complexity is subadditive—a result that contrasts with holographic complexity proposals such as the complexity=volume (CV) and CV2.0 conjectures [39, 44–49].

Definitions.— To evaluate the circuit complexities of purification (CoPs), we begin by introducing three distinct purification schemes. Prior to purification, only operator complexity

is defined for mixed states, but once a mixed state is mapped to a pure state via purification, both state and operator complexities become accessible. The detailed definitions of state and operator complexities, collectively denoted by $C_{S,K}$, can be found in Sec. 2.3.

Given a density matrix ρ on a system S, a generic purification is written as

$$\left|\Psi_\rho^V\right\rangle_{SA} = (\rho^{1/2} \otimes V_{R\to A}) \left|\mathscr{I}\right\rangle_{SR},$$

where V is an isometry from an auxiliary space R to the ancillary space A satisfying $V^\dagger V = \mathbf{1}_R$, and

$$\left|\mathscr{I}\right\rangle_{SR} = \sum_{n=1}^{\operatorname{rank}\rho} |n\rangle_S \otimes |n\rangle_R$$

is an unnormalised maximally entangled (EPR) state [368–370]. If ρ evolves under the unitary operator $U_t = e^{-iHt}$, then the purified state evolves as

$$\left|\Psi_\rho^V(t)\right\rangle = (U_t\rho^{1/2} \otimes V(t)) \left|\mathscr{I}\right\rangle = (U_t \otimes V(t)) \left|\Psi_\rho\right\rangle,$$

where we have defined $|\Psi_\rho\rangle := \left|\Psi_\rho^{\mathbb{I}}\right\rangle$, the initial purification with minimal dimension. (Note that unless ρ is full-rank, this differs from the canonical purification [391].) Crucially, any choice of $V(t)$ will yield the same evolution $\rho \mapsto \rho(t) = U_t\rho U_t^\dagger$ for the system.

One natural option is to choose a time-independent isometry, $V(t) = \mathbb{I}$, leading to the *time-independent purification* (TIP):

$$\left|\Psi_\rho^{\mathbb{I}}(t)\right\rangle = (U_t \otimes \mathbb{I}) \left|\Psi_\rho\right\rangle. \tag{4.69}$$

Alternatively, by selecting $V(t) = U_t^*$, we obtain the *time-dependent purification* (TDP) defined by

$$\left|\Psi_\rho^{U^*}(t)\right\rangle = (U_t\rho^{1/2}U_t^\dagger \otimes \mathbb{I}) \left|\mathscr{I}\right\rangle = (U_t \otimes U_t^*) \left|\Psi_\rho\right\rangle, \tag{4.70}$$

which is motivated by the requirement that the purification remain static when $\rho \propto \mathbb{I}$. Lastly, the *instantaneous purification* is given by taking the purification of the instantaneous density matrix:

$$\left|\Psi_{\rho(t)}\right\rangle = (\rho(t)^{1/2} \otimes \mathbb{I}) \left|\mathscr{I}\right\rangle. \tag{4.71}$$

This latter prescription is applicable even when ρ evolves non-unitarily—i.e., when a pure state might become mixed—and it coincides with the time-dependent purification in the case of unitary evolution. Although numerous purification choices exist, the three schemes above are optimal for studying Krylov CoPs under reasonable assumptions.

These purification schemes allow us to define two types of complexities for the purified state: (i) the Krylov complexity (defined via Eq. (2.90)) when the state is expressed in its

density matrix form, and (ii) the spread complexity (defined via Eq. (2.74)) when working with the state vector representation. (Notice that our normalisation differs from that in [392], where, due to the use of the Choi-Jamiołkowski isomorphism, an additional normalisation by $\mathrm{Tr}\,\rho^2$ is required. In our approach, since we assume $\mathrm{Tr}\,\rho = 1$, no further normalisation is necessary.)

Our approach avoids the need for minimisation over purifications, unlike earlier circuit CoP proposals, while still yielding an optimal definition under certain conditions. For instance, if one employs a time-independent isometry, then the Krylov and spread complexities remain unaffected because any isometry dependence cancels out in the autocorrelation function. In contrast, for a time-dependent isometry the Hilbert space dimension can be held constant over time by preparing a sufficiently large ancilla. Consequently, the isometry may be factorised as $V(t) = W(t)V_0$, where V_0 is time-independent and $W(t)$ is a unitary that depends on time. To ensure that the CoP accurately approximates the original complexity, it must vanish when there is no evolution; that is, when the original complexity is zero. This condition implies that we require $W(t)V_0 = W_0U_t^*$, where W_0 is an arbitrary time-independent isometry. Since the upper bound of complexity increases with the dimension of the Hilbert space [303], the minimal complexity is achieved by the smallest possible purification. By choosing $V_0 = W_0 = \mathbb{I}$, we recover the time-dependent purification as defined in Eq. (4.70). A parallel argument similarly leads to the instantaneous purification given in Eq. (4.71).

Inequalities among Complexities.— Employing the three purification schemes described above, we now conjecture certain inequalities relating mixed-state complexities and the CoPs, supported by both analytical and numerical evidence presented in the subsequent section[4]. Specifically, we propose that:

1. The Krylov operator complexity of a mixed state is bounded from above by that of its time-independent purification and from below by the state complexity of its time-dependent purification:

$$\mathscr{C}_K\Big(\big|\Psi_\rho^{\mathbb{I}}(t)\big\rangle\Big) \geq \mathscr{C}_K\Big(\rho(t)\Big) \geq \mathscr{C}_S\Big(\big|\Psi_\rho^{U^*}(t)\big\rangle\Big), \tag{4.72}$$

   with equality in the limit where ρ is pure.

2. The ratio $\mathscr{C}_S\Big(\big|\Psi_\rho^{U^*}(t)\big\rangle\Big)/\mathscr{C}_K\Big(\rho(t)\Big)$ remains approximately constant over time, with its exact value dependent on the purity of ρ.

[4] For pure states, our definitions of CoPs naturally reduce to the established notions of complexity.

3. Within a fixed purification scheme, the CoPs satisfy the inequality

$$\mathscr{C}_K\Big(\big|\Psi_\rho^{U^*,\mathbb{I}}(t)\big\rangle\Big) \geq 2\,\mathscr{C}_S\Big(\big|\Psi_\rho^{U^*,\mathbb{I}}(t)\big\rangle\Big).$$

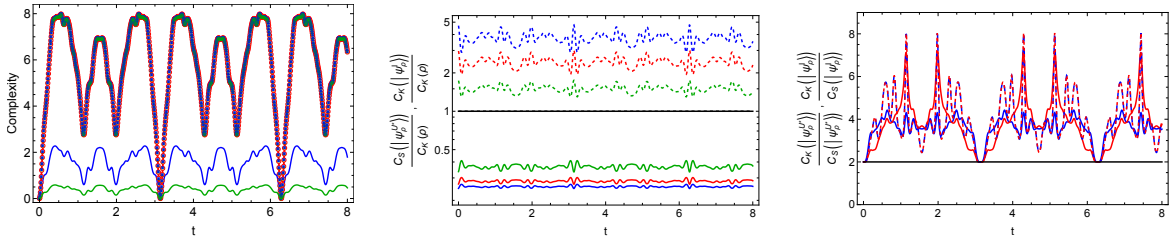

(a) (b) (c)

Figure 4.30: Time evolution of the complexities for the Werner states defined in Eq. (4.96) with $r = 4$ and $q = 15$ in the Hamiltonian of Eq. (4.98) is presented. Panel (a) shows the evolution of $\mathscr{C}_K(|\Psi_\rho^{\mathbb{I}}(t)\rangle)$ (red), $\mathscr{C}_K(\rho(t))$ (blue), and $\mathscr{C}_S(|\Psi_\rho^{U^*}(t)\rangle)$ (green) for two cases: when $p = 1/4$ (solid curve) and as $p \to 1$ (dotted points). It is observed that all complexity measures coincide in the limit $p \to 1$, and additionally, $\mathscr{C}_K(|\Psi_\rho^{\mathbb{I}}(t)\rangle)$ remains nearly identical for different values of p. Panel (b) plots the ratios between the operator complexity and the CoPs, namely, $\mathscr{C}_K(|\Psi_\rho^{\mathbb{I}}(t)\rangle)/\mathscr{C}_K(\rho(t))$ (dashed curve) and $\mathscr{C}_S(|\Psi_\rho^{U^*}(t)\rangle)/\mathscr{C}_K(\rho(t))$ (solid curve), for several choices of p: $p = 1/4$ (blue), $p = 1/3$ (red), $p = 1/2$ (green), and $p \to 1$ (black), with the data displayed on a logarithmic scale. Panel (c) displays the ratio $\mathscr{C}_K/\mathscr{C}_S$ comparing the state and operator CoPs for the time-independent purification (dashed curve) and the time-dependent purification (solid curve), for $p = 1/4$ (blue) and $p \to 1$ (red), along with a reference line fixed at 2 (black). Figure taken from [66].

One-Qubit Mixed States In this part we discuss the *complexity of purification* (CoP) for arbitrary one-qubit mixed states under a generic unitary evolution and illustrate the proposed bounds. We also provide supporting evidence for the inequality between the Krylov complexity and the spread complexity for pure one-qubit states, and the two-qubit Werner state case.

In this section we compute the spread and Krylov complexities of purification for generic one-qubit mixed states and verify our conjectures. A general one-qubit density matrix can be obtained by applying a rotation to a diagonal mixed state. In particular, we write $\rho = V\,\rho_0\,V^\dagger$, with $\rho_0 = \mathrm{diag}(p_1, p_2)$, where the probabilities satisfy $0 < p_1 = 1 - p_2 < 1$, and the unitary operator V is given by

$$V = \begin{pmatrix} \cos\frac{\theta}{2} & -e^{i\lambda}\sin\frac{\theta}{2} \\ e^{-i\phi}\sin\frac{\theta}{2} & e^{i(\lambda-\phi)}\cos\frac{\theta}{2} \end{pmatrix}. \tag{4.73}$$

Here the global phase of V has been removed as it does not affect ρ. Choosing the energy

eigenbasis, the Hamiltonian is taken to be diagonal, $H = \mathrm{diag}(E_1, E_2), \quad \text{with} \quad E_1 \leq E_2$. We introduce the energy spacing as $\Delta E = E_2 - E_1$ and define the dimensionless time variable $\tau = t\,\Delta E$. Under time evolution, the state transforms as $\rho(t) = U_t\,\rho\,U_t^\dagger$ with $U_t = e^{-iHt}$.

Following the moment method as employed in [59], we express the operator complexities associated with purification in terms of a common function

$$C[\mu] = \mu\Big(\sin^2\tau + 8(1-\mu)\sin^4\frac{\tau}{2}\Big). \tag{4.74}$$

More precisely, we have

$$C_K^{\mathbb{I}} = C[\mu^{\mathbb{I}}], \quad C_K = C[\mu_*], \quad C_S^{U^*} = C[\mu^{U^*}], \tag{4.75}$$

where the parameters are defined as

$$\mu^{\mathbb{I}} = \frac{1-(\Delta p)^2\cos^2\theta}{2}, \quad \mu_* = \frac{(\Delta p)^2\sin^2\theta}{1+(\Delta p)^2}, \quad \mu^{U^*} = \frac{(\Delta\sqrt{p})^2\sin^2\theta}{2}. \tag{4.76}$$

Here, we use the shorthand notations $\Delta p = p_1 - p_2$ and $\Delta\sqrt{p} = \sqrt{p_1} - \sqrt{p_2}$. With these analytical forms, our conjecture (4.72) is confirmed for arbitrary one-qubit mixed states and their evolution. Furthermore, one finds that $C_K \geq 2C_S$, and the ratio $\frac{\mathscr{C}_S\left(\left|\Psi_\rho^{U^*}(t)\right\rangle\right)}{\mathscr{C}_K\left(\rho(t)\right)}$ remains approximately constant over time, its mean value depending on the purity of ρ. It is also noteworthy that $C_K^{\mathbb{I}}$ loses its purity dependence when $\theta = \pi/2$, which indicates that the time evolution basis is orthogonal to the diagonalising basis of the initial state. In contrast, C_K and $C_S^{U^*}$ become independent of the purity only in the absence of time evolution (i.e. when $\theta = 0$ or π).

We now describe the calculation of the autocorrelation functions that serve as the starting point for both Krylov and spread complexities of purification. In our framework the following unnormalised autocorrelation functions are defined as

$$\begin{aligned}
G_S^{\mathbb{I}}(t) &= \langle\Psi_\rho^{\mathbb{I}}(t)|\Psi_\rho^{\mathbb{I}}(0)\rangle = \mathrm{Tr}\Big(\rho\,U_t^\dagger\Big),\\
G_K^{\mathbb{I}}(t) &= \mathrm{Tr}\Big[\Big|\Psi_\rho^{\mathbb{I}}(t)\Big\rangle\Big\langle\Psi_\rho^{\mathbb{I}}(t)\Big|\,\Big|\Psi_\rho^{\mathbb{I}}(0)\Big\rangle\Big\langle\Psi_\rho^{\mathbb{I}}(0)\Big|\Big] = \Big|\mathrm{Tr}\Big(\rho\,U_t^\dagger\Big)\Big|^2,\\
G_K(t) &= \mathrm{Tr}\Big[\rho(t)\,\rho\Big],\\
G_S^{U^*}(t) &= \langle\Psi_\rho^{U^*}(t)|\Psi_\rho^{U^*}(0)\rangle = \mathrm{Tr}\Big[\rho^{1/2}(t)\,\rho^{1/2}\Big],\\
G_K^{U^*}(t) &= \mathrm{Tr}\Big[\Big|\Psi_\rho^{U^*}(t)\Big\rangle\Big\langle\Psi_\rho^{U^*}(t)\Big|\,\Big|\Psi_\rho^{U^*}(0)\Big\rangle\Big\langle\Psi_\rho^{U^*}(0)\Big|\Big] = \Big|\mathrm{Tr}\Big(\rho^{1/2}(t)\,\rho^{1/2}\Big)\Big|^2,
\end{aligned} \tag{4.77}$$

where $\rho^{1/2}(t) = U_t\, V\, \rho_0^{1/2}\, V^\dagger\, U_t^\dagger$. Using the notation in (4.73), the autocorrelation functions and return amplitudes of (4.77) can be explicitly computed via the moment recursion method as discussed in (2.79). The following are the analytical forms of the autocorrelation and return amplitudes for the expressions mentioned in (4.77),

$$G_S^{\mathbb{I}}(t) = \left(p_1 \cos^2\frac{\theta}{2} + p_2 \sin^2\frac{\theta}{2}\right)e^{iE_1 t} + \left(p_1 \sin^2\frac{\theta}{2} + p_2 \cos^2\frac{\theta}{2}\right)e^{iE_2 t}, \tag{4.78}$$

$$G_K^{\mathbb{I}}(t) = 1 - \left(1 - (\Delta p)^2 \cos^2\theta\right)\sin^2\frac{\tau}{2}, \tag{4.79}$$

$$G_K(t) = p_1^2 + p_2^2 - (\Delta p)^2 \sin^2\theta\, \sin^2\frac{\tau}{2}, \tag{4.80}$$

$$G_S^{U^*}(t) = 1 - (\Delta\sqrt{p})^2 \sin^2\theta\, \sin^2\frac{\tau}{2}, \tag{4.81}$$

$$G_K^{U^*}(t) = \left[1 - (\Delta\sqrt{p})^2 \sin^2\theta\, \sin^2\frac{\tau}{2}\right]^2. \tag{4.82}$$

It is clear from these expressions that all autocorrelation functions depend only on the angle θ and the parameters p_1 and p_2, while ϕ and λ do not enter.

Using the moment method in the Krylov formalism (see (2.79)), the resulting complexities of purification for the generic one-qubit system are found to be

$$C_K^{\mathbb{I}}(t) = 2\sin^2\frac{\tau}{2}\left(1 - (\Delta p)^2\cos^2\theta\right)\left(1 + \sin^2\frac{\tau}{2}(\Delta p)^2\cos^2\theta\right) \tag{4.83}$$

$$C_S^{\mathbb{I}}(t) = \sin^2\frac{\tau}{2}\left(1 - (\Delta p)^2\cos^2\theta\right) \tag{4.84}$$

$$C_K(t) = \frac{(\Delta p)^2\sin^2\theta}{1 + (\Delta p)^2}\left(\sin^2\tau + 8\left(1 - \frac{(\Delta p)^2\sin^2\theta}{1 + (\Delta p)^2}\right)\sin^4\frac{\tau}{2}\right) \tag{4.85}$$

$$C_S^{U^*}(t) = \frac{(\Delta\sqrt{p})^2\sin^2\theta}{2}\left(\sin^2\tau + 8\left(1 - \frac{(\Delta\sqrt{p})^2\sin^2\theta}{2}\right)\sin^4\frac{\tau}{2}\right) \tag{4.86}$$

$$\begin{aligned} C_K^{U^*}(t) = b_1^2\Bigg[&\left(1 - b_1^2\sin^2\tfrac{\tau}{2}\right)^2\sin^2\tau + 8\sin^4\tfrac{\tau}{2}\left(b_2^2 - b_1^2 b_2^2\sin^2\tfrac{\tau}{2}\right. \\ &\left. + b_1^2\sin^4\tfrac{\tau}{2}\left(\frac{(b_1^2-1)\left(2 + (2-b_2^2)^2\right)}{b_2^2} + b_4^2(2-b_2^2)\right)\right)\Bigg]. \end{aligned} \tag{4.87}$$

with the more involved Lanczos coefficients entering the expression for $C_K^{U^*}(t)$ being defined by

$$\begin{aligned} b_1 &= \left|\Delta\sqrt{p}\,\sin\theta\right|, \quad b_2 = \sqrt{1 + \frac{1}{2}(\Delta\sqrt{p})^2\sin^2\theta}, \\ b_4 &= \sqrt{-14 + 3(\Delta\sqrt{p})^2\sin^2\theta + \frac{36}{2 + (\Delta\sqrt{p})^2\sin\theta}}\,. \end{aligned} \tag{4.88}$$

A straightforward calculation shows that

$$\frac{C_K^{\mathbb{I}}(t)}{2\,C_S^{\mathbb{I}}(t)} = 1 + \sin^2\frac{\tau}{2}(\Delta p)^2\cos^2\theta \geq 1, \tag{4.89}$$

and it can be further verified that $C_K^{U^*}(t) \geq 2\,C_S^{U^*}(t)$ holds analytically, although the derivation is less trivial. Figure 4.31c illustrates that the ratio C_K/C_S is indeed greater than or equal to 2 over time for two sets of parameters (e.g. $\Delta p = 0.4,\ \theta = \pi/3$ for the solid curve and $\Delta p = 0.98,\ \theta = \pi/4$ for the dashed curve).

Moreover, it is noteworthy that $C_K^{\mathbb{I}}$, C_K, and $C_S^{U^*}$ share the same Krylov structure. In all cases only two nonvanishing Lanczos coefficients appear, yielding the common functional form

$$C[\mu] = \mu\left(\sin^2\tau + 8(1-\mu)\sin^4\frac{\tau}{2}\right), \tag{4.90}$$

with the parameters specified as

$$\mu^{\mathbb{I}} = \frac{1-(\Delta p)^2\cos^2\theta}{2}, \quad \mu_* = \frac{(\Delta p)^2\sin^2\theta}{1+(\Delta p)^2}, \quad \mu^{U^*} = \frac{(\Delta\sqrt{p})^2\sin^2\theta}{2}. \tag{4.91}$$

It is then apparent that the time dependence of these complexities is similar, differing only by their coefficients. Analysing the allowed range $0 \leq p(1-p) \leq 1/4$, one can show that the coefficients of $\sin^2\tau$ and $\sin^4(\tau/2)$ in $C_K^{\mathbb{I}} - C_K$ and in $C_K - C_S^{U^*}$ are non-negative. This proves our conjecture that

$$C_K^{\mathbb{I}} \geq C_K \geq C_S^{U^*}, \tag{4.92}$$

for generic unitarily evolving one-qubit mixed states. We also observe that the temporal fluctuations of the ratio $C_S^{U^*}(t)/C_K(t)$ are comparatively smaller than its mean value, as shown in Fig. 4.31b.

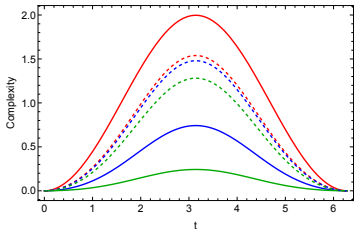

(a) Complexities $\mathscr{C}_K^{\mathbb{I}}(t)$ (red), $\mathscr{C}_K(t)$ (blue), and $\mathscr{C}_S^{U^*}(t)$ (green).

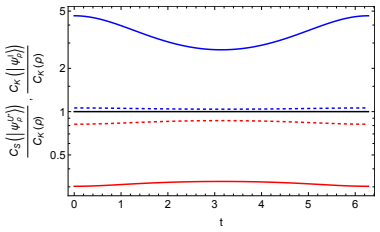

(b) Logarithmic plot of the ratios $\mathscr{C}_K^{\mathbb{I}}(t)/\mathscr{C}_K(t)$ (blue) and $\mathscr{C}_S^{U^*}(t)/\mathscr{C}_K(t)$ (red).

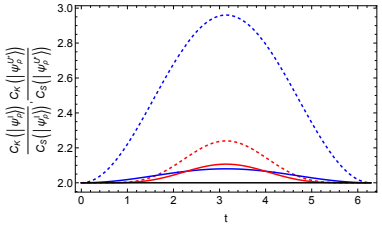

(c) $\mathscr{C}_K/\mathscr{C}_S$ for TIP (blue) and TDP (red), with the reference line at 2 (black).

Figure 4.31: Time dependence of the complexities of generic one-qubit mixed states (4.73) for different parameters: $\Delta p = 0.4,\ \theta = \pi/3$ (solid curve) and $\Delta p = 0.98,\ \theta = \pi/4$ (dashed curve). Figure taken from [66].

To further support the conjecture $C_K \geq 2C_S$, consider next a pure one-qubit state undergoing an arbitrary unitary evolution. As discussed in [59], the Krylov operator complexity of a pure state density matrix $\rho = |\psi\rangle\langle\psi|$ with $|\psi\rangle = \cos\theta\ |E_1\rangle + \sin\theta\, e^{i\phi}\ |E_2\rangle$, evolving under the Hamiltonian $H = E_1\ |E_1\rangle\langle E_1| + E_2\ |E_2\rangle\langle E_2|$, is given by

$$\mathscr{C}_K(|\psi(t)\rangle) = \frac{1}{2}\sin^2(2\theta)\Big(\sin^2\tau + 2\Big(3+\cos(4\theta)\Big)\sin^4\frac{\tau}{2}\Big). \tag{4.93}$$

We also find corresponding spread complexity for this evolution from the return amplitude. The spread complexity is given by

$$\mathscr{C}_S(|\psi(t)\rangle) = \sin^2(2\theta)\sin^2\frac{\tau}{2}. \tag{4.94}$$

With (4.93) and (4.94) in hand, we evaluate their ratio and find that it satisfies

$$\frac{\mathscr{C}_K(|\psi(t)\rangle)}{2\mathscr{C}_S(|\psi(t)\rangle)} = 1 + \cos^2(2\theta)\sin^2\frac{\tau}{2} \geq 1. \tag{4.95}$$

This confirms our conjectured inequality $\mathscr{C}_K \geq 2\,\mathscr{C}_S$ for any one-qubit pure state under generic unitary evolution.

Two-Qubit Werner States The two-qubit Werner state is defined as

$$\rho = \frac{p}{2}\Big(|01\rangle - |10\rangle\Big)\Big(\langle 01| - \langle 10|\Big) + \frac{1-p}{4}\mathbb{I}_{4\times 4}. \tag{4.96}$$

Here, the parameter p interpolates between the maximally mixed state ($\rho \propto \mathbb{I}$ at $p = 0$) and the pure, maximally entangled state

$$|Y\rangle \equiv \frac{|01\rangle - |10\rangle}{\sqrt{2}}, \tag{4.97}$$

at $p = 1$. In addition, the state is separable for $p \leq \frac{1}{3}$ and becomes entangled for larger p.

Because the Werner state commutes with the Pauli matrices $\sigma_i \otimes \sigma_i$ for any $i = x, y, z$, a Hamiltonian inducing nontrivial time evolution is considered:

$$H = \boldsymbol{\sigma}_x \otimes \boldsymbol{\sigma}_y + r\,\boldsymbol{\sigma}_y \otimes \boldsymbol{\sigma}_z + q\,\boldsymbol{\sigma}_z \otimes \boldsymbol{\sigma}_x, \tag{4.98}$$

where r and q are free parameters. For the time-independent purification, the evolution is governed by $H \otimes \mathbb{I}$, while the time-dependent purification follows $H \otimes \mathbb{I} - \mathbb{I} \otimes H^*$. To avoid additional symmetries, the coefficients in (4.98) are chosen to be distinct. In Fig. 4.30 the parameters $r = 4$ and $q = 15$ were selected.

Since we focus on the mixed-state complexity (i.e. $p < 1$), and given that the Werner state is full-rank, the initial state for the CoPs is taken as the canonical purification

$$|\Psi_\rho\rangle = \sqrt{\frac{1+p}{4}}\,|YY\rangle + \sqrt{\frac{1-p}{4}}\Big(|II\rangle + |XX\rangle + |ZZ\rangle\Big), \tag{4.99}$$

where $|I\rangle$, $|X\rangle$, $|Y\rangle$, and $|Z\rangle$ form the Bell basis [370].

Figure 4.30a demonstrates that operator complexity of the original mixed state, $\mathscr{C}_K(\rho(t))$ (blue curve), is bounded by the CoPs. Two initial state purities are considered: one with $p = 1/4$ (solid line) and another with $p \to 1$ (dotted line). The recurrence time is common to all cases [65, 84]. In this figure, the operator complexity of the time-independent purification, $\mathscr{C}_K(\left|\psi^{\mathbb{I}}_\rho(t)\right\rangle)$ (red curve), serves as an upper bound, while the state complexity of the time-dependent purification, $\mathscr{C}_S(\left|\psi^{U^*}_\rho(t)\right\rangle)$ (green curve), provides a lower bound. In the limit $p \to 1$, the inequalities (4.72) become saturated, reflecting the doubled Hilbert space structure inherent in the purification process[5]. Furthermore, Fig. 4.30a shows that when the Hamilto-

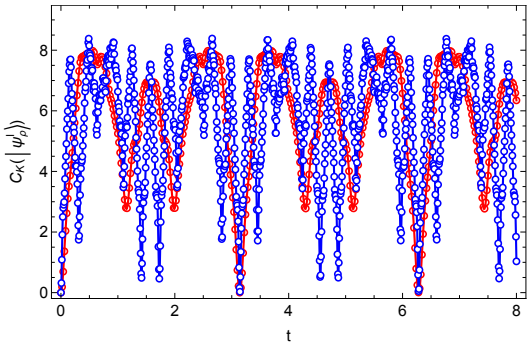

(a) Krylov complexity of time-independent purification

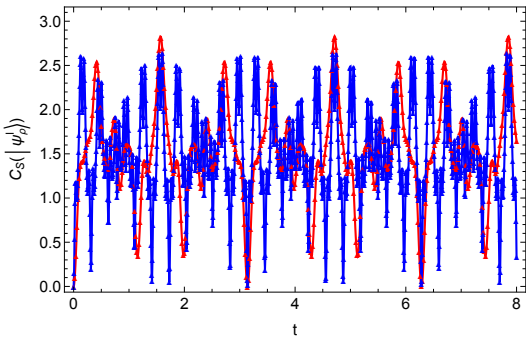

(b) Spread complexity of time-independent purification

Figure 4.32: In both panels the red curves correspond to Hamiltonian parameters of (8) with $r = 4$ and $q = 15$, while the blue curves correspond to $r = 10$ and $q = 50$. In panel (a), empty circles (both red and blue) denote the purified state with $p \to 1$, and solid lines correspond to $p = 1/4$ for the initial state (7). Panel (b) uses solid triangles for the purified state with $p \to 1$ and solid lines for $p = 1/4$. In summary, for both the operator and state complexities the curves overlap for different initial state purities provided the Hamiltonian is fixed, but differ when the Hamiltonian parameters change. Figure taken from [66].

nian is fixed, initial states with different purities yield the same complexity $\mathscr{C}_{S,K}(\left|\Psi^{\mathbb{I}}_{\rho(t)}\right\rangle)$, suggesting that the complexity derived from the time-independent purification is a robust indicator of the system's evolution. Figure 4.30b displays the time dependence of the ratio $\mathscr{C}_K(\rho(t))$, revealing an approximately proportional relationship to the state complexity of

[5]The equality between $\mathscr{C}_K(\rho(t))$ and $\mathscr{C}_K(\left|\Psi^{\mathbb{I}}_\rho(t)\right\rangle)$ for pure states is evident from the matching autocorrelation functions.

the time-dependent purification with a purity-dependent proportionality constant. Finally, Fig. 4.30c confirms that, for a consistent purification of the Werner state, the inequality

$$\mathscr{C}_K(t) \geq 2\mathscr{C}_S(t) \tag{4.100}$$

holds regardless of the initial state. This observation extends the pure state result $\mathscr{C}_K = 2\mathscr{C}_S$ reported in [59] and supports the conjecture that $\mathscr{C}_K \geq 2\mathscr{C}_S$ is a general property, verifiable analytically for an arbitrary qubit under any time evolution.

We observe that the complexity of time-independent purification, denoted by

$$\mathscr{C}_{S,K}\left(\left|\psi_\rho^{\mathbb{I}}(t)\right\rangle\right), \tag{4.101}$$

is almost insensitive to the purity of the initial state for Werner states. As can be seen in Fig. 4.32, the complexities for different initial state purities overlap in practice, making the time-independent purification a robust probe for the dynamical properties of the Hamiltonian. In other words, while the state and operator complexity associated with time-independent purification vary with Hamiltonian parameters, they remain nearly constant when the initial state changes. We suggest that, in future studies, the complexity of time-independent purification could serve as a diagnostic tool for the time evolution — for example, indicating the transition from integrable to chaotic behaviour in Hamiltonian systems. In addition, we

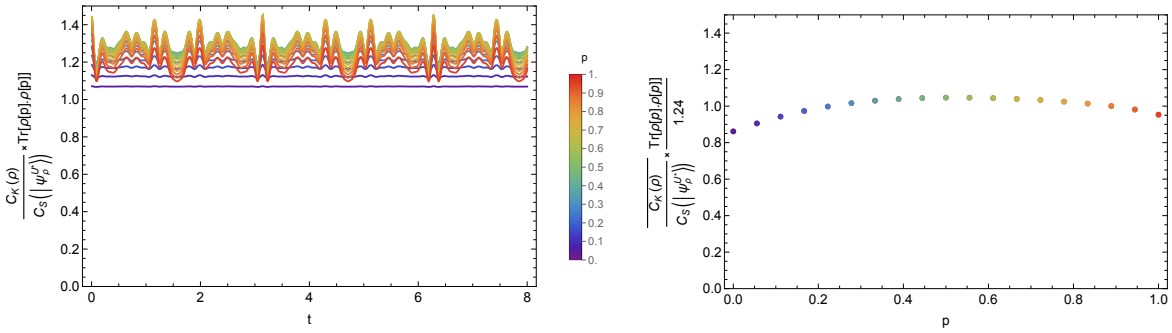

(a) (b)

Figure 4.33: The central legend (common to both panels) indicates different values of the parameter p. Results are generated using Hamiltonian (8) with $r = 4$ and $q = 15$. (a) Time evolution of $R\left(\rho(t)\right)$ for various initial state purities. The narrow range of $R\left(\rho(t)\right)$ demonstrates that $\mathscr{C}_K\left(\rho(t)\right)/\mathscr{C}_S\left(\left|\Psi_\rho^{U^*}(t)\right\rangle\right)$ is, up to fluctuations, inversely proportional to the initial purity. (b) The time average of the ratio multiplied by the purity, $\overline{\mathscr{C}_K\left(\rho(t)\right)/\mathscr{C}_S\left(\left|\Psi_\rho^{U^*}(t)\right\rangle\right)} \times \mathrm{Tr}\left(\rho^2\right)$, over the recurrence time. Figure taken from [66].

examine the ratio between the operator complexity of the original mixed state and the state

complexity of its instantaneous purification. Define the quantity

$$R\Big(\rho(t)\Big) = \frac{\mathscr{C}_K\Big(\rho(t)\Big)}{\mathscr{C}_S\Big(\Big|\Psi_\rho^{U^*}(t)\Big\rangle\Big)} \times \mathrm{Tr}\Big(\rho^2\Big). \tag{4.102}$$

Figure 4.33(a) shows the time evolution of $R\Big(\rho(t)\Big)$ for different values of the initial state purity of the density matrix given in (7) under the Hamiltonian (8) with $r = 4$ and $q = 15$. The data indicate that $R\Big(\rho(t)\Big)$ is concentrated within a narrow range, suggesting that the ratio $\mathscr{C}_K\Big(\rho(t)\Big)/\mathscr{C}_S\Big(\Big|\Psi_\rho^{U^*}(t)\Big\rangle\Big)$ is, up to small fluctuations, inversely proportional to the purity. This behaviour is further confirmed by the time-average of this quantity over the recurrence time [65, 84], as displayed in Fig. 4.33(b).

Finally, Table 4.2 summarizes various measures of the fluctuations in $\mathscr{C}_K(\rho)/\mathscr{C}_S\Big(\Big|\Psi_\rho^{U^*}\Big\rangle\Big)$ for different values of the parameter p in the Werner state (5). The column labeled "Mean Ratio" represents the time average of $\mathscr{C}_K(\rho)/\mathscr{C}_S\Big(\Big|\Psi_\rho^{U^*}\Big\rangle\Big)$ over one recurrence period. Our numerical analysis shows that the coefficient of variation (the standard deviation divided by the average) is below 5%, indicating strong concentration around a constant value.

According to (4), the operator complexity $\mathscr{C}_K(\rho)$ is bounded from below by the state complexity of the instantaneous purification $\mathscr{C}_S\Big(\Big|\Psi_\rho^{U^*}\Big\rangle\Big)$, and their time evolutions are quite similar. In this section, we show that the dependence of the ratio $\frac{\mathscr{C}_K(\rho)}{\mathscr{C}_S\Big(\Big|\Psi_\rho^{U^*}\Big\rangle\Big)}$ on the initial state is essentially determined by the purity, $\mathrm{Tr}(\rho^2)$, of the density matrix (note that the purity is preserved under unitary evolution). (It is worth mentioning that the ratio considered here is the inverse of the one plotted in Fig. 2c.) In Fig. 4.33a, we plot

$$R\Big(\rho(t)\Big) = \frac{\mathscr{C}_K\Big(\rho(t)\Big)}{\mathscr{C}_S\Big(\Big|\Psi_\rho^{U^*}(t)\Big\rangle\Big)} \times \mathrm{Tr}\Big(\rho^2\Big) \tag{4.103}$$

as a function of time. Our findings show that $R\Big(\rho(t)\Big)$ is inversely proportional to the initial state purity, aside from small fluctuations. This behaviour is further confirmed by the temporal average of $R\Big(\rho(t)\Big)$ taken over one recurrence period [65, 84], as presented in Fig. 4.33b.

These results provide quantitative evidence that the operator complexity of the original mixed state and the state complexity of its instantaneous purification not only evolve similarly but also that their ratio is predominantly governed by the purity of the initial state.

Table 4.2: Fluctuations in the ratio $\mathscr{C}_K(\rho)/\mathscr{C}_S\left(\left|\Psi_\rho^{U^*}\right\rangle\right)$. The "Mean Ratio" (MR) column denotes the time-average of the ratio over a recurrence period. Abbreviations: p – purity of the state; MR – Mean Ratio; MF – Max Fluctuation; $\frac{\text{MF}}{\text{Mean}}$ – relative error bound (max-fluctuation–to–mean ratio); SD – Standard Deviation; CV – Coefficient of Variation.

p	MR	MF	$\frac{\text{MF}}{\text{Mean}}$	SD	CV
0.05	4.15293	0.00749117	0.00180383	0.0024406	0.000587681
0.10	4.21076	0.0300677	0.0071407	0.0098186	0.00233179
0.15	4.17875	0.0653824	0.0156464	0.0214341	0.00512932
0.20	4.06963	0.108645	0.0266966	0.035815	0.00880055
0.25	3.90057	0.154135	0.039516	0.0511794	0.013121
0.30	3.68988	0.196617	0.0532855	0.0658721	0.0178521
0.35	3.45453	0.232235	0.0672263	0.0786423	0.022765
0.40	3.20857	0.258787	0.080655	0.0887352	0.0276557
0.45	2.96264	0.275544	0.0930062	0.0958452	0.0323513
0.50	2.72414	0.282851	0.103831	0.0999993	0.0367086
0.55	2.49770	0.281694	0.112781	0.101429	0.0406089
0.60	2.28586	0.273334	0.119576	0.100459	0.0439482
0.65	2.08957	0.260618	0.124723	0.0974282	0.0466261
0.70	1.90872	0.247372	0.129601	0.092631	0.0485304
0.75	1.74247	0.229515	0.131718	0.0862786	0.0495151
0.80	1.58940	0.207308	0.130432	0.0784558	0.049362
0.85	1.44755	0.180514	0.124703	0.0690446	0.0476974
0.90	1.31405	0.147889	0.112544	0.0575134	0.043768
0.95	1.18309	0.105116	0.0888489	0.04205	0.0355424
1.00	1.00000	2.54323×10^{-8}	2.54323×10^{-8}	1.01514×10^{-8}	1.01514×10^{-8}

Non-Unitary Evolution in Infinite-Dimensional Systems Next we apply our framework to an infinite-dimensional diagonal mixed state undergoing a non-unitary evolution and discuss its instantaneous purification, complexity measures, and quasiparticle interpretation. In our example the mixed state evolves from a pure state at $t = 0$ to a maximally mixed state as $t \to \infty$, and the evolution is generated by a completely positive, trace-preserving map rather than a unitary operator.

Consider the mixed state

$$\rho(t) = \frac{1}{\cosh^2(\alpha t)} \sum_{n=0}^{\infty} \tanh^{2n} r \ |n\rangle\langle n| \,, \tag{4.104}$$

which interpolates between a pure state at $t = 0$ and a maximally mixed state at $t \to \infty$. Its instantaneous purification is given by a two-mode squeesed vacuum (TMSV)

$$\left|\Psi_{\rho(t)}\right\rangle = \frac{1}{\cosh r} \sum_{n=0}^{\infty} (-i)^n \tanh^n(\alpha t) \ |n\rangle \, |n\rangle \,, \tag{4.105}$$

which is valid for $t > 0$ (i.e. as long as $\rho(t)$ is mixed). This purified state may be viewed as starting from $|0\rangle\,|0\rangle$ and then being driven by a two-mode squeesing Hamiltonian

$$H = \alpha\Big(a\,b + a^\dagger\,b^\dagger\Big), \tag{4.106}$$

acting on the enlarged Hilbert space (with a and $a^\dagger$ the annihilation and creation operators for the system and b, $b^\dagger$ those for the ancilla) [376, 393, 394]. Importantly, the time evolution for the mixed state $\rho(t)$ with $r = \alpha t$ is not generated by H; rather, it arises from tracing out the ancilla after a unitary evolution on the full system.

Since the evolution is non-unitary, we can study both the operator complexity of the original mixed state and the operator or state complexity of its instantaneous purification. In our framework the autocorrelation function for $\mathscr{C}_K(\rho(t))$ is given by $\mathrm{Tr}(\rho(t)\rho(0))$, while for $\mathscr{C}_K(\big|\Psi_{\rho(t)}\big\rangle)$ it is given by $\Big[\mathrm{Tr}\Big(\rho^{1/2}(t)\rho^{1/2}(0)\Big)\Big]^2$. In our example both expressions evaluate to $\mathrm{sech}^2(\alpha t)$, and thus the corresponding Krylov complexities coincide. In fact, one obtains [54, 79]

$$\mathscr{C}_K(\rho(t)) = \mathscr{C}_K\Big(\big|\Psi_{\rho(t)}\big\rangle\Big) = 2\sinh^2(\alpha t). \tag{4.107}$$

Furthermore, the spread complexity of the instantaneous purification can be computed from the Gaussian nature of the TMSV state. Since the Krylov basis in this case is the number basis, we have

$$\mathscr{C}_S\Big(\big|\Psi_{\rho(t)}\big\rangle\Big) = \langle n\rangle = \sinh^2(\alpha t). \tag{4.108}$$

Thus, both $\mathscr{C}_K(\rho(t))$ and $\mathscr{C}_S\Big(\big|\Psi_{\rho(t)}\big\rangle\Big)$ exhibit exponential growth with the same exponent, up to a factor of two. These results illustrate that the complexity of purification (CoP) captures key features of the Krylov complexity in non-unitary evolution and supports our conjectures that

$$\mathscr{C}_K\Big(|\Psi\rangle\Big) \geq 2\,\mathscr{C}_S\Big(|\Psi\rangle\Big) \quad \text{and} \quad \mathscr{C}_S\Big(|\Psi\rangle\Big) \leq \mathscr{C}_K(\rho).$$

It is also worth noting that, by using the translational invariance of the spread complexity [395], one can show that the spread CoP for the mixed state at a reference time $t = t_0$ is given by $\sinh^2\Big[\alpha(t - t_0)\Big]$, which provides a computational advantage over the operator complexity when no closed analytical form is available.

Thermal Interpretation and Quasiparticle Picture The mixed state (4.104) and its purification (4.105) can be identified with a Gibbs state and a thermofield double (TFD) state

of a harmonic oscillator, respectively[6]. Here the time parameter t is related to the inverse temperature β via

$$\tanh^2(\alpha t) = e^{-\beta(t)\Delta E}, \tag{4.109}$$

where ΔE is the energy spacing of the harmonic oscillator. In other words, after time t one may recast the mixed state and its purification as

$$\rho(t) \propto e^{-\beta(t)H_{\rm HO}}, \quad \left|\Psi_{\rho(t)}\right\rangle \propto \sum_{n=0}^{\infty} e^{-\beta(t)E_n^{\rm HO}/2} \, |n\rangle \, |n\rangle \,, \tag{4.110}$$

with $H_{\rm HO} = \sum_n E_n \, |n\rangle\langle n|$ and $E_n^{\rm HO} = (n+1/2)\Delta E$. We emphasize that although the mixed state is the Gibbs state and the purification is the TFD state with respect to $H_{\rm HO}$, the purification is driven by the two-mode squeesing Hamiltonian H, not by $H_{\rm HO}$.

Based on the identification between the TMSV and the TFD state, one may give a quasiparticle interpretation to the spread complexity (4.108). In this picture the complexity $\mathscr{C}_S\Big(\left|\Psi_{\rho(t)}\right\rangle\Big)$ grows by the exchange of Rindler particles between two Rindler wedges, so that the growth rate is naturally given by the average number of exchanged quasiparticles. The same argument applies to a perturbation falling into a black hole[7]. Exchanging one Hawking quantum between the exterior and its interior partner leads to thermalisation and an increase of one unit in the spread complexity. Moreover, the factor of 2 in (4.107) is explained by the fact that, since the original mixed state only "sees" one Rindler wedge, both absorption and emission occur simultaneously, thereby doubling the complexity growth per unit time.

Subsystem Complexity and Thermodynamic Bounds Following [392], one can also define a subsystem complexity. Let the spread operator for the subsystem L be given by

$$K_L = {\rm Tr}_R \sum_n n \, |n_L \, n_R\rangle\langle n_L \, n_R| = \sum_n n \, |n\rangle\langle n|_L \,. \tag{4.111}$$

Then the subsystem spread complexity is defined as

$$\mathscr{C}_S^L(\rho(t)) = {\rm Tr}\Big(K_L \, \rho_L(t)\Big). \tag{4.112}$$

For the state (4.104), one finds $\mathscr{C}_S^L(\rho(t)) = \sinh^2(\alpha t)$. In the quasiparticle picture the spread operator, defined on a single subsystem, only captures the effect of outgoing quanta, hence

[6] This identification follows from the fact that the two-mode squeesing operation is equivalent to the Bogoliubov transformation relating the Rindler and Minkowski vacua.

[7] Note that the mapping $\tanh^2(\alpha t) = \exp(-\beta(t)\Delta E)$ agrees with the late-time behaviour observed in perturbations [54, 79].

the subsystem complexity grows solely by the contribution from outgoing particles.

We now highlight a relation between the spread complexity and thermodynamic quantities. The time derivative of the spread complexity (4.108) together with the energy $E = \langle H_{\rm HO}\rangle$ and the von Neumann entropy S (evaluated at the inverse temperature $\beta(t) = -(\Delta E)^{-1}\log\tanh^2(\alpha t)$) satisfy

$$\dot{\mathscr{C}}_S := \frac{d\mathscr{C}_S\Big(\big|\Psi_{\rho(t)}\big\rangle\Big)}{dt} \leq \frac{\alpha}{\Delta E}\,2E, \quad \dot{\mathscr{C}}_S \leq \frac{\alpha}{\Delta E}\,TS. \tag{4.113}$$

This inequality is reminiscent of the Lloyd bound [390] on complexity growth. In a situation where no characteristic scales other than ΔE are present, one may take $\alpha \sim \Delta E$, so that (4.113) reduces to $\dot{\mathscr{C}}_S \lesssim E$ and $\dot{\mathscr{C}}_S \lesssim TS$, in agreement with holographic complexity bounds arising from the CV proposal [39, 44–48, 387]. Notably, the first bound in (4.113) saturates at late times as observed for black hole dynamics. The similarity of (4.113) with quantum speed limits on Krylov complexity growth [60, 71, 396] further suggests that the Lloyd bound may serve as a speed limit for spread complexity.

Finally, we define the mutual Krylov complexity for a bipartite state ρ_{AB} by

$$\Delta\mathscr{C}(A:B) = \mathscr{C}\Big(\rho_A(t)\Big) + \mathscr{C}\Big(\rho_B(t)\Big) - \mathscr{C}\Big(\rho_{AB}(t)\Big), \tag{4.114}$$

where $\mathscr{C}$ can denote the Krylov operator complexity, the subsystem complexity, or the operator/state CoP. In the TFD case one has $\Delta\mathscr{C}(L:R) = 2\mathscr{C}\Big(\rho(t)\Big) - \mathscr{C}\Big(\big|\Psi_{\rho(t)}\big\rangle\Big)$. Using (4.107), (4.108), and (4.112), one finds that $\Delta\mathscr{C}(L:R)$ equals $2\sinh^2(\alpha t)$ when $\mathscr{C} = \mathscr{C}_K$ and equals $\sinh^2(\alpha t)$ when $\mathscr{C} = \mathscr{C}_S$. In all cases the operator complexity and the state/operator CoPs exhibit subadditivity, $\Delta\mathscr{C}(L:R) \geq 0$, in contrast to the superadditivity of holographic complexity observed in the CV and CV2.0 proposals [380, 381, 395, 397]. Since the present calculation is based on a free-field spectrum with $E_n \propto n$, further analysis in holographic conformal field theory is necessary to clarify the discrepancy between the mutual Krylov and holographic complexities.

4.2.6 Discussion

In this Section we have established a comprehensive framework for studying mixed-state complexity through purifications in the Krylov formalism and have demonstrated the efficacy of complexity measures in the Krylov space in characterising non-unitary dynamics induced by periodic measurements as well as $\mathscr{PT}$-phase transitions in tight-binding systems. Our numerical and analytical investigations reveal that the spread complexity and spread entropy, defined in the Krylov basis, serve as robust probes of information spreading for non-unitary

evolution. For example, in the quantum first passage problem, the system is repeatedly measured to determine whether it has reached a detector site, thereby inducing effective non-unitary dynamics. In this scenario, the total probability in the Krylov basis is maintained at unity through a time-dependent normalisation, and both spread complexity and entropy initially grow, then undergo an extended decay period, and finally saturate to a steady state; the saturation level is largely suppressed relative to the peak due to contributions from the imaginary parts of the diagonal coefficients of the effective tridiagonal matrix. Interestingly, although the non-unitary evolution exhibits distinct behaviour such as the quantum Zeno effect when the measurement interval τ is very short, for larger τ the system equilibrates more rapidly, resulting in a faster decay and earlier saturation.

Our study of tight-binding Hamiltonians with complex on-site potentials reveals that within the $\mathscr{P}\mathscr{T}$-symmetric phase the wave functions remain delocalised and exhibit oscillatory behaviour at late times, while in the $\mathscr{P}\mathscr{T}$-broken phase the emergence of a non-Hermitian skin effect leads to localisation at the edge; this localisation–delocalisation transition is simultaneously reflected in the behaviour of spread complexity, spread entropy, entropic complexity, and the Krylov inverse participation ratio (KIPR) as reliable indicators of the $\mathscr{P}\mathscr{T}$-phase transition. In the $\mathscr{P}\mathscr{T}$-broken phase, the saturation values of spread entropy and entropic complexity are markedly suppressed, in agreement with the notion that localised quantum states are less complex [91]. Moreover, our results for the non-unitary dynamics generalise naturally to mixed states undergoing unitary evolution via purification: we have established bounds on the original mixed-state complexity in terms of the Krylov complexity of purification (CoP) and demonstrated that such bounds are robust even in infinite-dimensional setups, where a consistent quasiparticle picture emerges from the Rindler frame.

Taken together, these findings underscore that the Krylov-based spread measures not only capture the intricate interplay between non-unitarity, measurement-induced perturbations, and effective unitarity under periodic boundary conditions but also provide insight into the unitary-to-non-unitary transition following a quench. Our approach further bridges the gap between complexity growth and thermodynamic bounds, as the spread complexity obeys the Lloyd bound and connects to the quantum speed limit, while the newly defined mutual Krylov complexity may play an important role in identifying potential gravity duals in holographic theories. Looking ahead, the bounds and methods developed here could be tested in many-body systems and may impose new restrictions on the spread of wave functions, similar in spirit to the Lieb-Robinson bound [398]. These results also offer promising applications in electron transport and nanostructure physics, where effective non-Hermitian Hamiltonians constructed from measured diagonal and hopping amplitudes can be rigorously analysed using Krylov-based complexity measures [399, 400].

4.3 Complexity in String Theory and Holography

The concept of complexity has attracted increasing interest in high-energy theory. Originally introduced to characterize the growth of the Einstein-Rosen bridge for AdS black holes [39], it now stands as a promising probe into the dynamics of quantum systems. A natural progression is to investigate its role within superstring theory, especially in the context of the AdS/CFT correspondence, which demands that both bosonic and fermionic contributions are taken into account.

One central quantity is spread complexity, first defined in [55], which measures how a state disperses under Schrödinger time evolution. Frequently, the challenge lies in the numerical implementation of the Lanczos algorithm—a key step for extracting spread complexity in various quantum systems. However, as highlighted in [79], for particular classes of states such as coherent states, spread complexity can be computed entirely analytically. In that work, by identifying the Hamiltonian with the generator of the coherent state evolution, the Krylov basis was recognised to coincide with states in a highest weight representation.

Coherent states, renowned as the most "classical" of quantum states, are widely employed in the analysis of semiclassical regimes. In string theory and holography, they play a pivotal role by capturing phenomena ranging from D-brane dynamics to Lin-Lunin-Maldacena (LLM) geometries [401, 402], as well as the dynamics of strings endowed with large quantum charges—a subject addressed in detail later. Yet, in its present form, the spread complexity framework remains too restrictive to encompass many of these rich holographic scenarios because, in the semiclassical limit, the Hilbert space is usually well represented by a basis of coherent states.

Here we generalise the notion of spread complexity by considering the coherent state itself as the initial state, driven by the corresponding semiclassical expectation value of the Hamiltonian. Notably, this Hamiltonian is typically nonlinear in the algebra generators. Extending the formulation to extract the complexity associated with a given operator thus requires significant modifications. Although spread complexity is well understood for coherent states pertaining to rank-one Lie algebras, a comprehensive treatment of holography also demands the incorporation of fermionic generators and the study of coherent states tied to semisimple Lie groups. Our objective is to derive spread complexity for superstring states and their duals in the semiclassical regime of planar holography.

The AdS/CFT correspondence provides a unique laboratory for examining gauge and gravity theories concurrently. In the planar limit [403], where $N \to \infty$, both sides of the correspondence become integrable. Under these conditions, planar Feynman diagrams dominate, corresponding to single-trace operators in the gauge theory. A seminal observation in [404] was that, when the analysis is restricted to scalar operators, the one-loop planar

dilatation operator is equivalent to an integrable spin chain. This identification greatly simplifies the task of computing anomalous dimensions through integrability techniques such as the Bethe ansatz. In many instances, additional reliance on supersymmetry, either via BPS states or in the Berenstein-Maldacena-Nastase (BMN) limit [405], becomes necessary to perform explicit computations and to explore the implications of the correspondence.

Further simplification emerges when an extra semiclassical limit is taken, as shown in [406]. This limit establishes a precise correspondence between strings propagating in $AdS_5 \times S^5$ and the anomalous dimensions of the corresponding Super Yang-Mills (SYM) operators, a relation that is strikingly confirmed in [108, 407, 408]. In the near-BPS sector, the phase space dynamics of point-like "fast" string states directly correspond to the coherent state representation of the spin chain in SYM. Such a duality not only links states on both sides of the correspondence but also aligns the non-linear sigma-model actions describing their dynamics. Consequently, the energies of a broad class of string solutions match the anomalous dimensions of gauge theory operators without resorting to individual calculations. Reviews such as [409–411] provide an extensive bibliography on these developments.

A significant challenge in this context is to define a measure of complexity that resonates with holographic principles. Although various definitions have been proposed recently on both field theory and gravity sides [39, 44–49, 66, 74, 75, 94, 98, 412–418], many of these proposals remain under active scrutiny concerning their mutual compatibility across the duality. By focusing on a specific sector of the holographic correspondence, we compute spread complexity for strings in $AdS_5 \times S^5$ and for their dual states, which appear as ferromagnetic excitations of the spin chain. In doing so, we extend the spread complexity framework to the semiclassical limit of planar holography, enabling, for the first time, access to the spread complexity of string states.

Our exploration begins with an analysis of purely fermionic coherent states, illustrating how the underlying statistics can markedly alter the conventional picture of spread complexity. For instance, the fermionic Heisenberg-Weyl coherent state naturally leads to a finite, as opposed to a semi-infinite, chain—a fact that turns out to be foundational when interpreting spread complexity in more intricate contexts. After examining the simplest case of a single fermion, we extend our discussion to multi-fermion coherent states, which are essential for understanding purely fermionic string states.

Complexity gains additional layers when both fermions and bosons are present. In such scenarios, the traditional Krylov chain picture [54] requires refinement. We argue that the Krylov chain should be viewed as a path navigating through a higher-dimensional lattice that includes both bosonic and fermionic axes. Although the bosonic directions extend semi-infinitely, the fermionic components remain finite. Furthermore, the directionality of the Krylov path is dictated by an emergent dynamical rank-one algebra—a feature noted

in [74, 75], which until now lacked a complete explanation. To clarify this mechanism, we analyze two cases: one where a coherent state is generated from a free boson and a free fermion, and another involving a supercoherent state governed by the supergroup $OSp(2|1)$, whose bosonic subgroup, $SL(2)$, has been extensively studied [79].

An intriguing aspect of the $OSp(2|1)$ example is that it introduces a spread driven by a fermionic operator without leading to a finite-dimensional Krylov space—a result contrary to naive expectations based solely on free fermion modes. We demonstrate that when evolution is driven by a supercharge, the Krylov space becomes infinite-dimensional. This outcome is deeply rooted in the fact that supercharges, when squared, generate translations.

Armed with these conceptual tools, we finally turn our attention to computing spread complexity within the planar sector of the holographic correspondence under the semiclassical limit. In this limit, the dynamics on both the string and gauge theory sides coalesce, allowing a single computation to yield a complexity measure applicable to both. A crucial insight is that spread complexity is most naturally formulated from the gauge theory perspective, where the Hilbert space is naturally described in terms of coherent states. Unlike the standard situation where one starts with a unique lowest-weight state, here the initial state is a product state comprising many coherent states. Remarkably, string states propagating on distinct submanifolds of $AdS_5 \times S^5$ give rise to Lanczos coefficients that correspond to effective $SL(2)$ or $SU(2)$ coherent states. This observation, initially surprising, aligns with our earlier analysis whereby a Krylov path is traced through a higher-dimensional space.

Furthermore, given that the Hamiltonian in this context is that of a spin chain, the evolution of coherent states proceeds along a modified one-dimensional trajectory, resulting in a distinct temporal dependence. In the continuum limit, the spin chain acquires an additional spatial coordinate, meaning that spread complexity now exhibits dependence on both space and time. This variation reflects the worldsheet dynamics of string states. Consistent with the string picture, the spread complexity remains bounded due to the restriction of the string's motion to a compact submanifold, even as it is embedded within the non-compact space of $AdS_5 \times S^5$.

4.3.1 (Super-)Coherent States and Semiclassics

The holographic correspondence between string theory on $AdS_5 \times \text{CFT}_4$ and gauge theory is underpinned by the supergroup $PSU(2,2|4)$. To compute the spread complexity of string states in the planar sector, it is essential to understand the Hilbert space constructed from coherent states associated with this supergroup and its subgroups. In extending spread complexity to these semiclassical string states, one must address two key issues:

i. The displacement operators now belong to Lie groups whose rank exceeds one.

ii. These operators must take values in a *super* Lie group.

In what follows, we review the construction of the relevant coherent states and the corresponding Hilbert spaces, while highlighting the crucial components for calculating their spread complexity.

Coherent States for Lie Groups

The construction of coherent states for a Lie group was established by Perelomov and Gilmore [419–421]. Let G be a Lie group with a unitary, irreducible representation ρ acting on a Hilbert space $\mathscr{H}$. Choosing a reference state $|\psi_0\rangle$, the coherent states are defined by

$$|\psi\rangle = \rho(g)\,|\psi_0\rangle\,, \quad g \in G.$$

When considering connected and simply connected Lie groups, these coherent states can be written as

$$|\psi(\xi)\rangle = \exp\Big(i\sum_{\mu}\xi_\mu T_\mu\Big)|\psi_0\rangle, \tag{4.115}$$

where $\{T_\mu\}$ are the generators of the Lie algebra $\mathfrak{g}$ and the ξ_μ are complex parameters. Restricting to real ξ_μ ensures that the displacement operator

$$D(\xi) = \exp\Big(i\sum_{\mu}\xi_\mu T_\mu\Big)$$

is unitary. The subgroup $G_{\psi_0} \subset G$ that leaves $|\psi_0\rangle$ invariant up to a phase, i.e. $\rho(g)\,|\psi_0\rangle = e^{i\phi}\,|\psi_0\rangle$ with $\phi \in [0, 2\pi)$, is known as the stabilizer subgroup, and the set of coherent states is naturally associated with the coset G/G_{ψ_0}.

A notable example arises when the exponent in the displacement operator is identified with the system's Hamiltonian, thereby equating the parameter ξ with the time variable t. This case has been studied in [55, 77, 79, 422] in the context of spread complexity. In many situations, however, the displacement operator is not directly generated by the Hamiltonian. Moreover, until now the algebra generators $\{T_\mu\}$ have predominantly been taken from bosonic Lie algebras of rank one. Generalising this framework to include higher-rank algebras and superalgebras necessitates a reformulation of the current Krylov complexity formalism.

Assume that the Lie algebra is semisimple so that its generators can be partitioned into ladder operators E_α and mutually commuting elements H_i. Given a semisimple Lie algebra $\mathfrak{g}$ and a highest weight representation ρ_Λ, one selects the corresponding lowest weight state $|\Lambda\rangle$—which is annihilated by all lowering operators—as the reference state $|\psi_0\rangle$. The

corresponding Lie group-valued coherent state is then constructed as

$$|\Lambda(\xi)\rangle = \exp\Big(i\sum_{\alpha}\xi_\alpha E_\alpha + i\sum_i \xi_i H_i\Big)|\Lambda\rangle, \tag{4.116}$$

with the normalisation condition $|\Lambda(0)\rangle = |\Lambda\rangle$. In this expression, the descendant states created by successive applications of the raising operators assemble to build the full coherent state, effectively "climbing" the weight lattice of ρ_Λ.

To illustrate how spread complexity is evaluated, we now review two well-known examples: the Heisenberg-Weyl (HW) coherent state and the $\mathfrak{sl}(2)$ coherent state. These examples serve as the foundational "atomic components" for the spread complexity associated with more general Lie groups and, in particular, the string states.

Heisenberg-Weyl Coherent State

The spread complexity of HW coherent states was computed in [79]. Here, one starts with the standard bosonic creation and annihilation operators, $a_B^\dagger$ and a_B, which satisfy the commutation relation $[a_B, a_B^\dagger] = \mathbb{1}$. The number operator is defined as $N_B = a_B^\dagger a_B$, acting on the Fock states $|n\rangle$ as $N_B\,|n\rangle = n|n\rangle$.

The action of the ladder operators on the number states is given by

$$a_B^\dagger|n\rangle = \sqrt{n+1}\,|n+1\rangle, \tag{4.117}$$

$$a_B|n\rangle = \sqrt{n}\,|n-1\rangle. \tag{4.118}$$

A bosonic coherent state $|\xi\rangle$ is defined as an eigenstate of a_B, constructed by applying the displacement operator

$$D(\xi) = \exp\Big(\xi a_B^\dagger - \bar{\xi} a_B\Big) \tag{4.119}$$

to the vacuum state. In explicit form, the coherent state is written as

$$|\xi\rangle = D(\xi)|0\rangle = e^{-|\alpha t|^2/2}\sum_{n=0}^{\infty}\frac{(i\alpha t)^n}{\sqrt{n!}}|n\rangle, \tag{4.120}$$

where the time dependence is fixed by setting $\xi = i\alpha t$ according to the semiclassical equations of motion. The probability of occupying the n^{th} Krylov state is

$$p_n = |\langle n|\xi\rangle|^2 = e^{-|\xi|^2}\frac{|\xi|^{2n}}{n!}. \tag{4.121}$$

Identifying the number operator N_B as the spread complexity operator, the complexity is

given by

$$\mathscr{C}(t) = \langle \xi | N_B | \xi \rangle = |\xi|^2 = \alpha^2 t^2. \tag{4.122}$$

The complexity grows quadratically with time, where the square of the displacement parameter determines the proportionality constant.

$\mathfrak{sl}(2)$ Coherent State

While the HW coherent state is particularly appealing for its simplicity, many of the algebras encountered in our applications are semisimple and decompose in the Chevalley basis into several $\mathfrak{sl}(2)$ copies linked by their root structures. The spread complexity for the $\mathfrak{sl}(2)$ coherent state was first derived in [55]. The $\mathfrak{sl}(2)$ algebra is spanned by three generators satisfying the commutation relations

$$[L_0, L_{\pm 1}] = \mp L_{\pm 1}, \tag{4.123}$$

$$[L_1, L_{-1}] = 2L_0. \tag{4.124}$$

Choosing the displacement operator for the coherent state as

$$D(\alpha, \gamma) = \exp\left[i\Big(\alpha(L_{-1} + L_1) + \gamma L_0\Big)t\right], \tag{4.125}$$

and interpreting its exponent as the Hamiltonian, one considers a highest-weight irreducible representation labelled by h. The Krylov basis is then constructed as

$$|K_m\rangle = |h, h+m\rangle = \frac{L_{-1}^m |h\rangle}{\|L_{-1}^m |h\rangle\|}, \qquad \|L_{-1}^m |h\rangle\|^2 = m! \frac{\Gamma(2h+m)}{\Gamma(2h)}, \tag{4.126}$$

where the norm is defined by $\| \, |v\rangle \, \| = \sqrt{\langle v|v\rangle}$. The probability for the coherent state to reside in the m^{th} Krylov state is given by [423]

$$p_m(t) = \frac{\Gamma(2h+m)}{m!\,\Gamma(2h)} \frac{\left(\dfrac{\sinh^2\left(\alpha t \sqrt{1-\frac{\gamma^2}{4\alpha^2}}\right)}{\cosh^2\left(\alpha t \sqrt{1-\frac{\gamma^2}{4\alpha^2}}\right) - \frac{\gamma^2}{4\alpha^2}}\right)^m}{\left(\dfrac{\cosh^2\left(\alpha t \sqrt{1-\frac{\gamma^2}{4\alpha^2}}\right) - \frac{\gamma^2}{4\alpha^2}}{1-\frac{\gamma^2}{4\alpha^2}}\right)^{2h}}. \tag{4.127}$$

The spread complexity for the $\mathfrak{sl}(2)$ coherent state is computed as

$$\mathscr{C}(t) = \langle \alpha, \gamma, h | L_0 - h | \alpha, \gamma, h \rangle = \frac{2h}{1 - \frac{\gamma^2}{4\alpha^2}} \sinh^2\left(\alpha t \sqrt{1 - \frac{\gamma^2}{4\alpha^2}}\right). \tag{4.128}$$

It is important to note that the complexity expressed in Eq. (4.128) may exhibit either periodic or exponential behaviour depending on the values of the parameters α and γ. At this stage, the specific time dependence of these parameters may seem arbitrary; this issue is discussed in detail in Subsection 4.3.1.

In summary, the study of coherent states associated with both bosonic and semisimple Lie algebras lays the groundwork for extending the spread complexity framework to more complicated setups, including those involving super Lie groups and higher-rank algebras. Such generalisations are essential for exploring the semiclassical aspects of string states in holography while maintaining consistency in notation and approach across the various components.

Super Lie Group-Valued Coherent States and Their Complexity

In many areas of physics—ranging from particle physics and string theory to condensed matter—fermionic degrees of freedom are essential. Their inclusion naturally brings superalgebra symmetries into play. Before exploring how these fermionic aspects influence spread complexity, we briefly review superalgebras and the construction of their coherent states.

Super Lie algebras extend ordinary Lie algebras by incorporating a $\mathbb{Z}_2$-gradation (Grassmann parity). This grading distinguishes the bosonic (even) generators from the fermionic (odd) ones. Correspondingly, the Hilbert space decomposes as

$$\mathscr{H} = \mathscr{H}_{\text{even}} \oplus \mathscr{H}_{\text{odd}} \,. \tag{4.129}$$

Even generators close under the commutator, while odd generators anticommute to yield even elements; the commutator between an even and an odd generator remains odd. In the semiclassical regime, one may introduce an analogue of the Cartan basis for superalgebras (see, e.g., [424] for a pedagogical discussion), so that many aspects of the standard theory carry over with important modifications discussed below.

We now consider coherent states defined by a displacement operator that takes values in a super Lie algebra. Acting on a ground state $|\Lambda\rangle$ of definite Grassmann parity, one introduces

$$|\Lambda(\xi, \zeta)\rangle = \exp\left(i \sum_{\alpha} \xi_\alpha E_\alpha + i \sum_{A} \zeta_A G_A + i \sum_{i} \xi_i H_i\right) |\Lambda\rangle \,, \tag{4.130}$$

where E_α and H_i are bosonic generators and the G_A denote the fermionic (odd) generators. The coefficients ζ_A are Grassmann-valued, ensuring that the entire displacement operator is Grassmann even. Consequently, the state $|\Lambda(\xi,\zeta)\rangle$ inherits the Grassmann parity of $|\Lambda\rangle$.

When computing physical quantities such as probabilities and spread complexity, it is necessary to extract bosonic numbers from expressions that may contain Grassmann numbers. For instance, if one has a general Grassmann element

$$A = z + y\,\zeta_0 + x\,\bar{\zeta}_0 + w\,\bar{\zeta}_0\zeta_0\,, \tag{4.131}$$

with $z, y, x, w \in \mathbb{C}$, and ζ_0 a Grassmann odd unit along with its complex conjugate $\bar{\zeta}_0$, one employs Grassmann integration to define a semiclassical average. Specifically,

$$\langle A\rangle_{\rm cl} = \int d\zeta_0\, d\bar{\zeta}_0\, e^{\bar{\zeta}_0\zeta_0}\, A = z + w\,, \tag{4.132}$$

which effectively projects out the fermionic degrees of freedom. This averaging procedure obeys the properties

$$\begin{aligned} &\langle z\rangle_{\rm cl} = z, \quad \langle\bar{\zeta}_0\zeta_0\rangle_{\rm cl} = -\langle\zeta_0\bar{\zeta}_0\rangle_{\rm cl} = 1,\\ &\langle\zeta_0\rangle_{\rm cl} = \langle\bar{\zeta}_0\rangle_{\rm cl} = 0\,. \end{aligned} \tag{4.133}$$

A similar prescription is used in the free fermion analysis to extract physical probabilities and spread complexities. In this context, the spread complexity is defined by

$$\mathscr{C}(\xi,\chi,\Lambda) = \int d\zeta_0\, d\bar{\zeta}_0\, e^{\bar{\zeta}_0\zeta_0}\langle\Lambda(\xi,\chi)|K|\Lambda(\xi,\chi)\rangle\,, \tag{4.134}$$

where χ is a fermionic label and K is the Krylov operator.

Coherent State Path Integral and Semiclassical Approximation

A central issue in evaluating spread complexity is to determine the time-dependence arising from the Hamiltonian evolution of the coherent state. This evolution is characterised by the phase-space trajectory of the state. The coherent-state path integral formalism, introduced by Klauder [425–427], provides a natural way to address this problem.

In this formalism, the transition amplitude between an initial state $|\Psi(\xi_1)\rangle$ at time t_i and a final state $|\Psi(\xi_2)\rangle$ at time t_f, governed by the Hamiltonian H, is written as

$$\mathscr{T} = \int \mathscr{D}\Psi\, \exp\Big(iS(\Psi)\Big)\,, \tag{4.135}$$

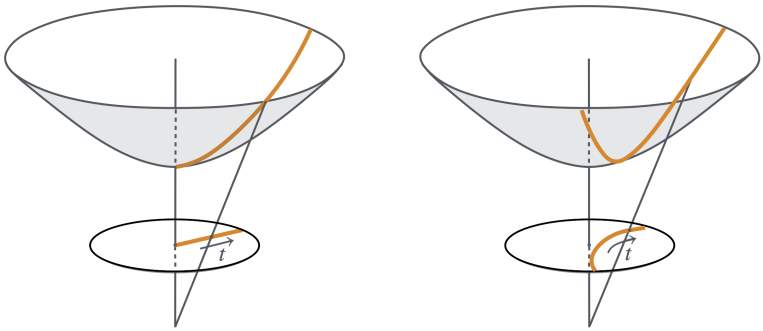

Figure 4.34: The phase-space trajectory of the coherent state is determined by solving the semiclassical equations of motion. The left panel shows the trajectory for a linear $SL(2,\mathbb{R})$ Hamiltonian, while the right panel illustrates a different path in phase space corresponding to an alternative Hamiltonian. Although the set of coherent states is the same, the resulting complexities differ due to the distinct time evolutions. Figure taken from [67].

with the action

$$S = \int_{t_i}^{t_f} dt\, L = \int_{t_i}^{t_f} dt \left(\langle \Psi | \partial_t | \Psi \rangle - \langle \Psi | H | \Psi \rangle \right). \tag{4.136}$$

Expanding the action around the classical trajectory in phase space leads to the semiclassical equations of motion. Averaging the quantum Hamiltonian over the coherent state,

$$\mathsf{H} \equiv \langle \Psi | H | \Psi \rangle \,, \tag{4.137}$$

defines a Hamilton function whose equations of motion determine the time evolution $\xi = \xi(t)$ appearing in Eq. (4.116).

As an illustrative example, consider the $SL(2)$-coherent state discussed in subsection 4.3.1. The parameter ξ for the coherent state of $SL(2)$ is a complex number representing a point on the hyperbolic disk, as the coset $SL(2)/U(1)$ is isomorphic to a hyperbolic space. Parameterize ξ as $\xi = \tanh\left(\rho/2\right) e^{i\phi}$, with $\rho \in \mathbb{R}_+$ and $\phi \in [0, 2\pi)$. For a linear Hamiltonian of the form

$$H_{SL(2,\mathbb{R})} = \xi \left(L_1 + L_{-1} \right), \tag{4.138}$$

the semiclassical equations yield the solution $\phi = \pi/2$ and $\rho = 2\alpha t$. This corresponds to a trajectory along a fixed great circle in the hyperbolic disk (see Fig. 4.34). Other, more complicated Hamiltonians—such as those arising in spin chain models—will lead to alternative paths $\xi = \xi(t)$, and, consequently, to different spread complexities.

4.3.2 Spread Complexity with Fermions

We now turn to the computation of spread complexity in systems with fermionic degrees of freedom. This serves as a preliminary step toward understanding the spread complexity of

superstring states in the planar limit.

4.3.3 Fermionic Heisenberg-Weyl Algebra

To introduce fermionic coherent states, consider oscillators whose creation and annihilation operators satisfy the anticommutation relations

$$\{a_F, a_F^\dagger\} = 1, \quad \{a_F, a_F\} = \{a_F^\dagger, a_F^\dagger\} = 0\,. \tag{4.139}$$

Because the fermionic number operator $N_F = a_F^\dagger a_F$ has eigenvalues 0 and 1, the state space is two-dimensional. In contrast, for bosons an n-particle state is given by

$$|n_B\rangle = \frac{1}{\sqrt{n!}}(a_B^\dagger)^n|0\rangle\,,$$

whereas for fermions an n-particle state is constructed as

$$|n_F\rangle = (a_F^\dagger)_1(a_F^\dagger)_2\cdots(a_F^\dagger)_n|0\rangle\,.$$

The coherent state for the fermionic oscillator is generated by the displacement operator

$$|\xi\rangle = D(\xi)|0\rangle = \exp\Big(\xi\, a_F^\dagger - a_F\,\bar{\xi}\Big)|0\rangle = \sum_n \frac{(\xi\, a_F^\dagger - a_F\,\bar{\xi})^n}{n!}|0\rangle\,, \tag{4.140}$$

where ξ may be either Grassmann even or odd. We now consider these two cases in turn.

Case I: Grassmann Even Parameter

When ξ is Grassmann even, the nilpotency of the fermionic operators enables an exact summation of the series in Eq. (4.140). In fact, one obtains

$$D(\xi) = \cos|\xi| + \sin|\xi|\Big(e^{i\phi}a_F^\dagger - e^{-i\phi}a_F\Big)\,, \tag{4.141}$$

with $|\xi| = \sqrt{\xi\bar{\xi}}$ and $\xi = |\xi|e^{i\phi}$. Hence, the fermionic coherent state becomes

$$|\xi\rangle_F = D(\xi)|0\rangle = \cos|\xi||0\rangle + e^{i\phi}\sin|\xi||1\rangle\,. \tag{4.142}$$

Because only two states appear, the Krylov space here is finite-dimensional, spanned solely by $|0\rangle$ and $|1\rangle$. In contrast to the infinite-dimensional (or semi-infinite) chain encountered for bosonic coherent states (e.g., the $\mathfrak{sl}(2,\mathbb{R})$ case in [79]), the fermionic system yields a chain of only two nodes (see Fig. 4.35).

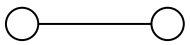

Figure 4.35: For bosonic coherent states (e.g., those of $\mathfrak{sl}(2,\mathbb{R})$) the Krylov chain is semi-infinite. In contrast, fermionic coherent states, owing to their nilpotency, yield a chain with only two nodes.

Accordingly, one may identify $\xi = i\alpha t$, where t denotes time and α is a constant. The state can then be expressed as a finite linear combination

$$|\psi(t)\rangle = \varphi_0(t)|0\rangle + \varphi_1(t)|1\rangle\,, \tag{4.143}$$

and the spread complexity is given by

$$\mathscr{C}(t) = \langle\psi(t)|N_F|\psi(t)\rangle = \sum_{m=0}^{1} m\,|\varphi_m(t)|^2 = \sin^2(\alpha t)\,. \tag{4.144}$$

Alternatively, choosing $|1\rangle$ as the ground state would yield $\mathscr{C}(t) = \cos^2(\alpha t)$. In any case, the finite-dimensionality of the Hilbert space leads to a periodic spread complexity.

Case II: Grassmann Odd Parameter

Next, consider the displacement operator with a Grassmann odd parameter, which we denote by ζ. In this case, the corresponding displacement operator is given by

$$|\zeta\rangle = D(\zeta)|0\rangle = \exp\Big(a_F^\dagger\zeta - \bar{\zeta}\,a_F\Big)|0\rangle = \Big(1 - \tfrac{1}{2}\bar{\zeta}\zeta\Big)|0\rangle + \zeta\,|1\rangle\,. \tag{4.145}$$

It is straightforward to verify that $D(\zeta)^\dagger = D(\zeta)^{-1} = D(-\zeta)$. The corresponding wave functions are

$$\varphi_0 = \langle 0|\zeta\rangle = 1 - \tfrac{1}{2}\bar{\zeta}\zeta, \quad \varphi_1 = \langle 1|\zeta\rangle = \zeta\,. \tag{4.146}$$

In this formulation the absolute squares $|\varphi_i|^2$ depend explicitly on the Grassmann variables. It can be shown that one may set $\zeta = i\alpha\,\zeta_0\,t$, where ζ_0 is a unit Grassmann vector and $\alpha \in \mathbb{R}$ [67]. To obtain physical (bosonic) probabilities, one performs an averaging over the Grassmann parameters as prescribed in Eq. (4.132). Thus, the probabilities are defined by

$$p_i = \int d\zeta_0\, d\bar{\zeta}_0\, e^{\bar{\zeta}_0\zeta_0}|\varphi_i|^2 = \begin{cases} 1 - \alpha^2 t^2\,, & \text{for } i = 0\,, \\ \alpha^2 t^2\,, & \text{for } i = 1\,. \end{cases} \tag{4.147}$$

These bosonic probabilities sum to one, although note that the evolution is meaningful only for $|\alpha t| \leq 1$.

The spread complexity is similarly defined by averaging,

$$\mathscr{C}(t) = \int d\zeta_0\, d\bar{\zeta}_0\, e^{\bar{\zeta}_0\zeta_0} \langle\zeta|N_F|\zeta\rangle = \alpha^2 t^2\,, \tag{4.148}$$

where we have used the relation $\langle\bar{\zeta}_0\zeta_0\rangle_{\rm cl} = 1$. This result is identical to the bosonic case in Eq. (4.122), but with the crucial restriction $|\alpha t| \leq 1$, ensuring that the evolution finishes once the state has fully transitioned from $|0\rangle$ to $|1\rangle$. Consequently, the spread complexity remains bounded—a behaviour also noted in bosonic systems with finite-dimensional Krylov subspaces.

Superposition of Fermionic Heisenberg-Weyl Algebras

To advance our investigation of complexity from single-fermionic coherent states to more intricate systems, we now consider multi-fermionic coherent states. This development enables us to study how expanding the Hilbert space with additional fermionic modes affects complexity. Such multi-mode coherent states also appear naturally in the path-integral formulation of fermionic field theories. For instance, in a fermionic system with chiral fermions confined in a finite interval $[-L/2, L/2]$, the momentum k becomes quantised according to [428]

$$k = \frac{2\pi n}{L} \quad \text{for} \quad n \in \mathbb{Z}\,. \tag{4.149}$$

For a single fermion, one writes the mode expansion as

$$\begin{aligned} \psi(x) &= \left(\frac{2\pi}{L}\right)^{\frac{1}{2}} \sum_{n=-\infty}^{\infty} e^{-i\frac{2\pi n}{L}x}\,(a_F)_n\,, \\ (a_F)_n &= (2\pi L)^{-\frac{1}{2}} \int_{-L/2}^{L/2} dx\, e^{i\frac{2\pi n}{L}x}\,\psi(x)\,. \end{aligned} \tag{4.150}$$

The fermionic creation and annihilation operators $(a_F)_k^\dagger$ and $(a_F)_k$ for each momentum mode satisfy

$$\{(a_F)_k,\, (a_F)_l^\dagger\} = \delta_{kl}\,. \tag{4.151}$$

Grassmann Even Parameters

A family of coherent states for an N-mode fermionic system is defined in terms of these operators [429] by

$$|\{\xi_k\}\rangle = \bigotimes_{k=1}^{N} \left(\cos|\xi_k|\,|0\rangle_k + e^{i\phi_k}\sin|\xi_k|\,|1\rangle_k\right), \tag{4.152}$$

where each parameter ξ_k is a complex number of Grassmann even type. In this formulation the complete displacement operator is given as the product of the N individual fermionic displacement operators (see Eq. (4.141)) for every momentum mode.

To promote the displacement operators to time evolution operators, we set

$$\xi_k = i\alpha_k\, t\,, \tag{4.153}$$

with α_k a mode-dependent constant. Starting from the vacuum state $|0\rangle$, the time-evolved state becomes

$$\begin{aligned} |\{\alpha_k\}, t\rangle &= \bigotimes_k \cos(|\alpha_k t|)\left(|0\rangle_k + e^{i\phi_k}\tan(|\alpha_k t|)\,|1\rangle_k\right) \\ &= \bigotimes_k \lambda_k\left(|0\rangle_k + \eta_k\,|1\rangle_k\right), \end{aligned} \tag{4.154}$$

where, for notational simplicity, we have defined

$$\lambda_k = \cos(|\alpha_k t|) \quad \text{and} \quad \eta_k = e^{i\phi_k}\tan(|\alpha_k t|)\,. \tag{4.155}$$

In this multi-mode framework the Krylov basis is constructed by successively applying fermion creation operators to the all-mode vacuum state. The number of fermions in a given Krylov vector indicates the "distance" from the initial state. For example, states like $|100\ldots\rangle$ and $|010\ldots\rangle$ are one step away, while $|101\ldots\rangle$ or $|011\ldots\rangle$ correspond to configurations with two or more fermions, respectively. In the simplest instance when $\xi_i = \xi$ for all modes, the Krylov basis yields a uniform superposition over fermion number states. In more general circumstances, the superposition becomes non-uniform and the explicit determination of the basis is technically more involved.

Even so, one can still compute the complexity associated with the spreading of the time-dependent state in the Fock basis. This is achieved by weighting the probability of each state by its total fermion number. (Note that, in general, the Fock basis is larger than the Krylov basis; in fact, the spread complexity computed in the Fock basis serves as an upper bound for the true spread complexity [55].) For a configuration with occupation numbers $\{n_k\}$, we

label a Krylov vector as $|\{n_k\}, N\rangle$ where $N = \sum_k n_k$ is the total number of fermions.

For the single-mode case, the multi-fermion coherent state of Eq. (4.154) reduces to the result of the single fermion (cf. Eq. (4.142)), and one finds a complexity given by

$$\mathscr{C} = \lambda^2 |\eta|^2 = \sin^2(\alpha t)\,. \tag{4.156}$$

For a two-mode system the state is

$$|\alpha_1, \alpha_2, t\rangle = (\lambda_1\lambda_2)\Big(|00\rangle + \eta_1\,|1_1 0\rangle + \eta_2\,|0_1 1\rangle + \eta_1\eta_2\,|1_1 1_2\rangle\Big)\,. \tag{4.157}$$

More generally, for a configuration in which exactly ℓ out of N fermions are excited, the normalised wave function can be written as

$$\varphi_{\ell,\{\epsilon\}}(t) = \left(\prod_{i=1}^{\ell}\lambda_i\right)\eta_1^{\varepsilon_{1,\ell}}\cdots\eta_N^{\varepsilon_{N,\ell}}\,, \tag{4.158}$$

where the occupancy of each mode is indicated by $\{\epsilon\} \equiv \{\varepsilon_{1,\ell}, \varepsilon_{2,\ell}, \ldots, \varepsilon_{N,\ell}\}$ with $\varepsilon_{i,\ell} \in \{0,1\}$ and $\sum_i \varepsilon_{i,\ell} = \ell$. Consequently, the probability to find the state in a Fock basis configuration is

$$p_{\ell,\{\epsilon\}}(t) = \left(\prod_{i=1}^{\ell}\lambda_i^2\right)\eta_1^{2\varepsilon_{1,\ell}}\cdots\eta_N^{2\varepsilon_{N,\ell}}\,. \tag{4.159}$$

For example, when $\ell = 2$, one obtains an expression for the complexity in the Fock basis

$$\begin{aligned}\mathscr{C}_F(t) &= (\lambda_1\lambda_2)^2\Big(|\eta_1|^2 + |\eta_2|^2 + 2|\eta_1\eta_2|^2\Big)\\ &= 1 - \cos\Big[(\alpha_1-\alpha_2)t\Big]\cos\Big[(\alpha_1+\alpha_2)t\Big]\,.\end{aligned} \tag{4.160}$$

This expression displays oscillatory behaviour, with the precise form depending on the values of α_1 and α_2.

For an N-mode fermionic coherent state, the total spreading complexity in the Fock basis can be expressed as the sum of contributions from sectors with fixed particle number

$$\begin{aligned}\mathscr{C}_F(t) &= \left(\sum_{i=1}^{N}|\eta_i|^2 + \sum_{\substack{i,j=1\\(i>j)}}^{N} 2|\eta_i\eta_j|^2 + \cdots + \sum_{\substack{i_1,i_2,\ldots,i_N=1\\(i_1>i_2>\cdots>i_N)}}^{N}\left|\prod_{j=1}^{N}\eta_{i_j}\right|^2\right)\left(\prod_{i=1}^{N}\lambda_i^2\right)\\ &= c_1(t) + c_2(t) + \cdots + c_N(t)\,.\end{aligned} \tag{4.161}$$

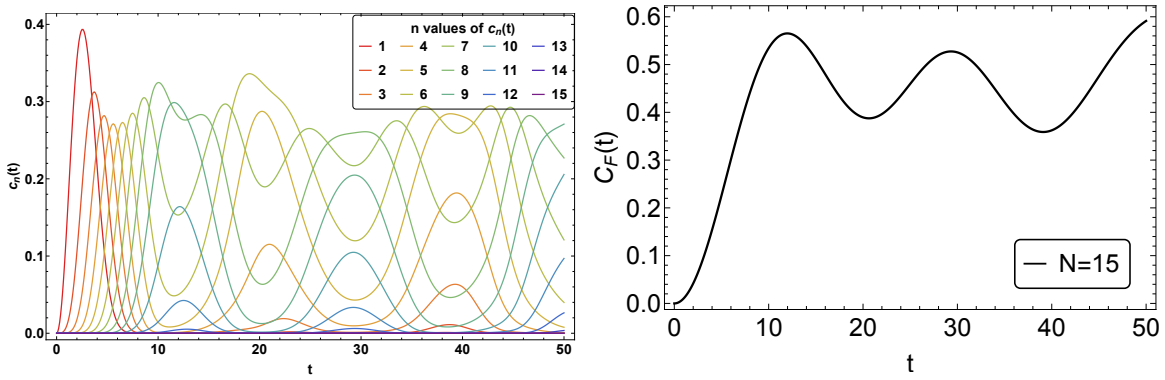

Figure 4.36: Left: Complexity contributions in the Fock basis for fixed total fermion number states normalised by the Hilbert space dimension. Warmer colors correspond to contributions from states with lower fermion numbers, whereas cooler tones represent those from states with higher fermion numbers. Early in time, low-fermion-number states dominate; later on, contributions from higher fermion numbers become more important. Right: The total normalised complexity for a 15-mode fermionic coherent state with randomly chosen $\{\alpha_k\}$ in the interval [0, 1]. The plot illustrates how the overall spread complexity arises from the cumulative contributions of individual fermion-number sectors. Figure taken from [67].

Here, the contribution from states with exactly m fermions is defined as

$$c_m(t) = \sum_{\substack{i_1,i_2,\ldots,i_m=1 \\ (i_1>\cdots>i_m)}}^{N} m \left| \prod_{l=1}^{m} \tan(|\alpha_l t|) \right|^2 \left(\prod_{i=1}^{N} \cos^2(|\alpha_i t|) \right) . \tag{4.162}$$

In the general case, expression (4.161) does not simplify further. However, if all displacement parameters are identical, namely $\alpha_k = \alpha$ for all k, the complexity reduces to

$$\mathscr{C}_F(t) = 2^{N-2} N^2 (N+1) \sin^2(\alpha t) . \tag{4.163}$$

In this special situation the contributions from each mode oscillate in unison, and the overall complexity is equivalent to that obtained from a uniform superposition of fermionic number states up to a constant factor

$$\mathscr{C}_F(t) = \frac{1}{6} N^2 (N+1)(2N+1) \sin^2(t) . \tag{4.164}$$

A more general scenario arises when the parameters $\{\alpha_k\}$ differ, being randomly selected from a given range. In that case each momentum mode is displaced differently from the vacuum. The normalised spread complexity computed in the Fock basis is illustrated in Fig. 4.36. Although the total complexity does not follow a simple oscillatory pattern, the contributions from sectors with fixed fermion number still oscillate and peak at different time scales. At early times, configurations with few fermions dominate, while at later times

states with higher fermion numbers provide the largest contributions. According to [55], the spread complexity computed in the Fock basis constitutes an upper bound on the true spread complexity since the Fock basis is typically much larger than the Krylov basis.

Grassmann Odd Parameters

For displacement operators built from Grassmann odd parameters, consider the product

$$D(\vec{\zeta})|0\rangle = \prod_{k=1}^{N} \exp\Big((a_F)_k^\dagger \, \zeta_k - \bar{\zeta}_k \, (a_F)_k \Big) |0\rangle \,, \tag{4.165}$$

where the anticommutation relations $\{(a_F)_k,\, (a_F)_l^\dagger\} = \delta_{kl}$ hold. In this case the Grassmann oddness of the ζ_k implies that the individual displacement operators commute with each other. If we define the total fermion number operator by $N_F = \sum_{k=1}^{N} (N_F)_k$, then the total spread complexity is given by

$$\mathscr{C} = \sum_{k=1}^{N} C_k(t) \,, \tag{4.166}$$

with each mode contributing

$$C_k(t) = \alpha_k^2 t^2 \,, \tag{4.167}$$

in complete analogy with Eq. (4.148).

4.3.4 Spread Complexity with Bosons and Fermions

In this section we extend the notion of spread complexity to superalgebras. We start with the supersymmetric harmonic oscillator (see Subsection 4.3.5), which already exhibits the essential features that emerge when both bosonic and fermionic generators come into play. Later on, we shall see even more pronounced novelties in the context of the superalgebra $\mathfrak{osp}(2|1)$ (see Subsection 4.3.6). The new features we encounter are as follows:

- The initial state $|\psi_0\rangle$ is free to spread through a higher-dimensional lattice (the weight lattice of the Hilbert space $\mathscr{H}$ of a superalgebra representation) rather than a simple chain. In this section the lattice is composed of several semi-infinite ladders so that its dimension (the rank r of the algebra) is two.

- Under Hamiltonian evolution, the state $|\psi_0\rangle$ follows its Krylov chain. Viewed within the lattice, this chain becomes a one-dimensional *Krylov path* (or *spread path*) obtained via the embedding $\mathscr{K} \hookrightarrow \mathscr{H}$. Although the chain explores the full Hilbert space, the path itself is always one-dimensional (see Fig. 4.37).

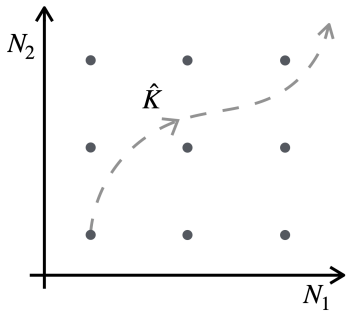

Figure 4.37: The lattice points represent the basis of the Hilbert space $\mathscr{H}$. A point in this lattice is determined by the position operators $\vec{X}$. An initial state $|\psi_0\rangle$, chosen for instance as the lower left basis vector, evolves under a displacement operator D so that its Krylov path (dashed line) is read off as the sequence of lattice points it passes through. Figure taken from [67].

- The Krylov subspace $\mathscr{K} \subseteq \mathscr{H}$ is generated by a single creation operator—typically a linear combination of several superalgebra generators—which naturally singles out an annihilator and a spread complexity operator. These three operators together form a rank-one dynamical algebra that governs the spread of $|\psi_0\rangle$ through $\mathscr{K}$.

In this new setup it is interesting to ask how $|\psi_0\rangle$ disperses in the lattice, thereby revealing the nature of the embedding $\mathscr{K} \hookrightarrow \mathscr{H}$. By analogy with spread complexity on a chain, where the Krylov operator plays the role of a position operator, we define position operators

$$\vec{X} = (X_1, \ldots, X_r)$$

on the lattice. Their expectation values measure the average position of the coherent state's Krylov path along the lattice directions. This motivates defining *lattice complexities* by

$$\vec{\mathscr{C}}^{\mathrm{L}}(\xi, \chi, \Lambda) = \left| \int d\zeta_0 \, d\bar{\zeta}_0 \, e^{\bar{\zeta}_0 \zeta_0} \langle \Lambda(\xi, \chi) | \vec{X} | \Lambda(\xi, \chi) \rangle \right| , \tag{4.168}$$

which is an r-dimensional vector. The absolute value ensures that any sign ambiguity arising from the lattice orientation is removed. For simplicity we assume that the position operators commute, that is, $[X_i, X_j] = 0$, and we choose them so that $\vec{X}|\Lambda\rangle = 0$, thereby placing the initial state $|\Lambda\rangle$ at the origin.

4.3.5 Super-Heisenberg–Weyl Algebra

We now consider the supersymmetric extension of the Heisenberg–Weyl algebra. The fundamental operators are the bosonic annihilation and creation operators a_B, $a_B^\dagger$ and the

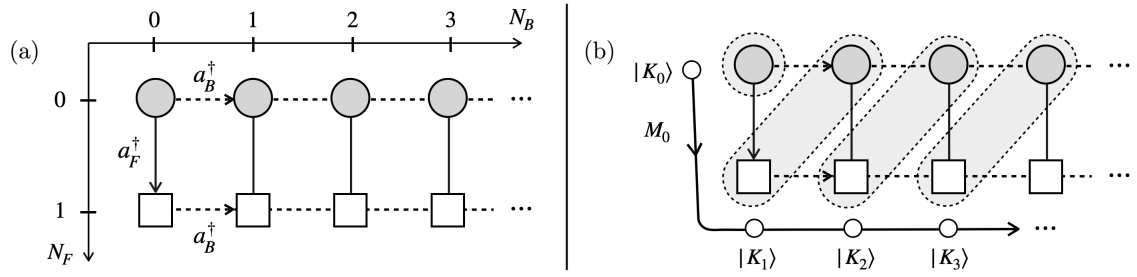

Figure 4.38: Left: The Hilbert space $\mathscr{H}$ is organised as a lattice labeled by basis vectors $|n,\nu\rangle$, with bosonic states drawn as circles and fermionic states as squares. Right: Taking $|\psi_0\rangle = |0,0\rangle$, the Krylov basis generated by the displacement operator in Eq. (4.173) forms a bosonic Fock space. Each Krylov vector is a linear combination of bosonic and fermionic lattice points; specifically, the n^{th} Krylov vector is a superposition of the n^{th} fermionic and $(n+1)^{\text{st}}$ bosonic sites. Figure taken from [67].

fermionic ones a_F, $a_F^\dagger$, which satisfy the (anti-)commutation relations

$$[a_B, a_B^\dagger] = \mathbb{1} \quad \text{and} \quad \{a_F, a_F^\dagger\} = \mathbb{1}\,. \tag{4.169}$$

These operators act on the product super Hilbert space

$$\mathscr{H} = \mathscr{H}_B \otimes \mathscr{H}_F\,,$$

with basis elements labeled by

$$|n,\nu\rangle \equiv |n\rangle \otimes |\nu\rangle\,,$$

where the first entry represents bosonic occupancy, $n = 0, 1, 2, \ldots$, and the second entry denotes the fermionic occupancy, $\nu = 0, 1$. An orthonormal basis for $\mathscr{H}$ is spanned by

$$|n,\nu\rangle = \frac{(a_B^\dagger)^n (a_F^\dagger)^\nu}{\sqrt{n!}}|0,0\rangle\,, \tag{4.170}$$

which forms the lattice shown in the left panel of Fig. 4.38. Here the states with $\nu = 0$ are called bosonic, while those with $\nu = 1$ are fermionic. The ladder operations act as follows

$$a_B|n,\nu\rangle = \sqrt{n}\,|n-1,\nu\rangle\,, \quad a_B^\dagger|n,\nu\rangle = \sqrt{n+1}\,|n+1,\nu\rangle\,, \tag{4.171}$$

$$a_F|n,\nu\rangle = \delta_{\nu,1}\,|n,0\rangle\,, \quad a_F^\dagger|n,\nu\rangle = \delta_{\nu,0}\,|n,1\rangle\,. \tag{4.172}$$

The state $|0,0\rangle$ is the ground state of the super Hilbert space.

A coherent state for a unitary representation of the supergroup is obtained by acting with

the displacement operator

$$D(\xi,\zeta)=\exp\left(\xi\, a_B^\dagger-\bar{\xi}\, a_B+\zeta\, a_F^\dagger+\bar{\zeta}\, a_F\right) \tag{4.173}$$

on the ground state. Note that thanks to the (anti-)commutation relations this operator factorises into a product of bosonic and fermionic displacement operators. Following the standard procedure (see, e.g., [79] and Subsection 4.3.3), we expand the coherent state in the lattice basis

$$|\xi,\zeta\rangle=D(\xi,\zeta)|0,0\rangle=e^{-|\xi|^2/2}\sum_{n=0}^{\infty}\frac{\xi^n}{\sqrt{n!}}\left[\left(1-\frac{1}{2}\bar{\zeta}\zeta\right)|n,0\rangle+\zeta\,|n,1\rangle\right]. \tag{4.174}$$

Setting $\zeta=0$ one recovers the bosonic HW coherent state (cf. Eq. (4.120)), while $\xi=0$ yields the fermionic coherent state (cf. Eq. (4.145)).

It is important to stress that the lattice basis $\{|n,\nu\rangle\}$ is not in general identical to the Krylov basis. For instance, a first Lanczos iteration yields a vector proportional to $(\xi\, a_B^\dagger+\zeta\, a_F^\dagger)|0,0\rangle$, which is a linear combination of several lattice points (see Fig. 4.38). Nevertheless, examining the expansion in Eq. (4.174) allows us to understand how the Krylov chain is embedded in the lattice.

By reading off the wavefunctions,

$$\varphi_n^{\nu=0}(\xi,\zeta)=\langle n,0|\xi,\zeta\rangle=\frac{\xi^n e^{-|\xi|^2/2}}{\sqrt{n!}}\left(1-\frac{1}{2}\bar{\zeta}\zeta\right), \tag{4.175}$$

$$\varphi_n^{\nu=1}(\xi,\zeta)=\langle n,1|\xi,\zeta\rangle=\frac{\xi^n e^{-|\xi|^2/2}}{\sqrt{n!}}\,\zeta\,, \tag{4.176}$$

one may then proceed by setting $\xi=\xi(t)$ and $\zeta=f(t)\zeta_0$, where ζ_0 is a unit Grassmann odd element and $f(t)$ is a complex function. After performing the necessary semiclassical averaging over the Grassmann variables (see Subsection 4.3.1), the probabilities that the state occupies a given lattice point become

$$p_n^\nu(t)=\begin{cases}\dfrac{|\xi(t)|^{2n}}{n!}e^{-|\xi(t)|^2}\left(1-|f(t)|^2\right), & \text{for } \nu=0\,,\\[2ex] \dfrac{|\xi(t)|^{2n}}{n!}e^{-|\xi(t)|^2}|f(t)|^2, & \text{for } \nu=1\,.\end{cases} \tag{4.177}$$

In geometric terms, these probabilities indicate the likelihood that the Krylov path passes through the lattice point $|n,\nu\rangle$ at time t.

The position operator along the horizontal axis in Fig. 4.38 is given by N_B, and the vertical

one by N_F. Their corresponding lattice complexities,

$$\mathscr{C}_i^L(t) = \int d\zeta_0\, d\bar{\zeta}_0\, e^{\bar{\zeta}_0\zeta_0} \langle \xi, \theta | N_i | \xi, \theta \rangle, \quad \text{with } i = B, F\,, \tag{4.178}$$

yield

$$\mathscr{C}_B^L(t) = |\xi(t)|^2 \quad \text{and} \quad \mathscr{C}_F^L(t) = |f(t)|^2\,. \tag{4.179}$$

These operators here do not measure the spread along the Krylov chain but rather quantify how the chain is embedded within the overall lattice.

The Krylov Basis and Its Complexity

To obtain the Krylov basis we first define the following bosonic Heisenberg–Weyl operators

$$A = \frac{\xi\, a_B^\dagger + \zeta\, a_F^\dagger}{\sqrt{\bar{\xi}\xi + \bar{\zeta}\zeta}}\,, \quad A^\dagger = \frac{\bar{\xi}\, a_B - \bar{\zeta}\, a_F}{\sqrt{\bar{\xi}\xi + \bar{\zeta}\zeta}}\,, \quad [A, A^\dagger] = \mathbb{1}\,. \tag{4.180}$$

In these terms the displacement operator in Eq. (4.173) can be recast as

$$D(\xi, \zeta) = \exp\left[\sqrt{\bar{\xi}\xi + \bar{\zeta}\zeta}\,(A^\dagger - A)\right]. \tag{4.181}$$

This is recognised as the standard bosonic HW displacement operator with effective parameter $\sqrt{\bar{\xi}\xi + \bar{\zeta}\zeta}$. Consequently, the Krylov basis $\{|K_k\rangle\}$ for the super-Heisenberg–Weyl coherent states is precisely the Fock space generated by $A^\dagger$. Each Krylov vector is a linear superposition of the lattice states $\{|n, \nu\rangle\}$; in other words, the Krylov chain traces a one-dimensional path through the two-dimensional lattice (see Fig. 4.38).

With this mapping, all aspects of spread complexity follow as in the purely bosonic case. The probabilities associated with the Krylov states are

$$p_k = \langle e^{-(\bar{\xi}\xi+\bar{\zeta}\zeta)} \frac{(\bar{\xi}\xi + \bar{\zeta}\zeta)^k}{k!} \rangle_{\text{cl}} = e^{-|\xi(t)|^2} \frac{|\xi(t)|^{2k}}{k!} \left(1 + |f(t)|^2 \left(\frac{k}{|\xi(t)|^2} - 1\right)\right). \tag{4.182}$$

Therefore, the spread complexity is given by

$$\mathscr{C}_{\text{HW}}(t) = \langle \bar{\xi}\xi + \bar{\zeta}\zeta \rangle_{\text{cl}} = |\xi(t)|^2 + |f(t)|^2 = (\alpha t)^2\,, \tag{4.183}$$

with $|f(t)|^2 \leq 1$ and $\alpha \in \mathbb{R}$. The functions $\xi(t)$ and $f(t)$ must vanish at $t = 0$ to ensure that $\mathscr{C}_{\text{HW}}(0) = 0$. For example, one may choose $|\xi(t)|^2 = (\alpha t)^2 - \sin^2(\alpha t)$ and $|f(t)|^2 = \sin^2(\alpha t)$.

In summary, the evolution under the displacement operator in Eq. (4.173) that involves both bosonic and fermionic degrees of freedom can be mapped onto an effective bosonic HW

system. In this picture the Krylov chain is embedded as a one-dimensional path within the lattice formed by the basis vectors of $\mathscr{H} = \mathscr{H}_B \otimes \mathscr{H}_F$. We now turn our attention to a more intricate example.

4.3.6 OSp$(2|1)$ or $\mathscr{N} = 1$ SL(2)

The simplest supersymmetric extension of $\mathfrak{sl}(2)$ is the $\mathfrak{osp}(2|1)$ algebra. Besides the $\mathfrak{sl}(2)$ generators L_0 and $L_{\pm1}$, it includes two fermionic generators $G_{\pm\frac{1}{2}}$ obeying the graded commutation relations

$$[L_{+1}, L_{-1}] = 2L_0, \quad [L_{\pm1}, L_0] = \pm L_{\pm1}\,, \tag{4.184}$$

$$[L_{\pm1}, G_{\mp\frac{1}{2}}] = \pm G_{\pm\frac{1}{2}}, \quad \{G_{\frac{1}{2}}, G_{-\frac{1}{2}}\} = 2L_0\,, \tag{4.185}$$

$$\{G_{\pm\frac{1}{2}}, G_{\pm\frac{1}{2}}\} = 2L_{\pm1}, \quad [L_0, G_{\pm\frac{1}{2}}] = \mp\frac{1}{2}\, G_{\pm\frac{1}{2}}\,. \tag{4.186}$$

An additional generator J, which plays the role of a fermion number operator, is introduced to count the number of supercharge applications. It satisfies

$$[L_0, J] = 0, \quad [L_{\pm1}, J] = 0, \quad [J, G_{\pm\frac{1}{2}}] = -G_{\pm\frac{1}{2}}\,. \tag{4.187}$$

A rigorous justification arises by viewing $\mathfrak{osp}(2|1)$ as a subalgebra of the extended superalgebra $\mathfrak{osp}(2|2)$, within which the operator J naturally appears as the generator of a $U(1)$ R-symmetry. A more precise understanding of its role emerges by embedding the symmetry algebra into the larger superalgebra $\mathfrak{osp}(2|2) \supset \mathfrak{osp}(2|1)$, which is generated by the eight operators $(L_0, L_{\pm1}, J, G^a_r)$, where $a = \pm$ and $r = \pm\frac{1}{2}$. The Cartan subalgebra is two-dimensional, generated by the commuting bosonic operators (L_0, J). Here, L_0 is the familiar $\mathfrak{sl}(2)$ Cartan element, while J generates a $U(1)$ R-symmetry. The fermionic operators G^a_r then serve to link distinct $\mathfrak{sl}(2)$ modules.

In general, representations of $\mathfrak{osp}(2|2)$ are larger than those of $\mathfrak{osp}(2|1)$, such as the one described in eq. (4.190). For any highest-weight representation, the ground state is annihilated by L_1 and both $G^{\pm}_{1/2}$. However, there exists a special class known as *atypical* or *(anti-)chiral* representations, where the ground state is also annihilated by either $G^{+}_{-1/2}$ (in the chiral case) or $G^{-}_{-1/2}$ (in the anti-chiral case). As a result, only one fermionic generator—namely $G^{-}_{-1/2}$ or $G^{+}_{-1/2}$—acts non-trivially on the ground state.

In the chiral case, the structure of the representation precisely matches the graded ladder structure in eq. (4.190), with only $L_0, L_{\pm1}, G^{-}_{\pm1/2}$, and J acting non-trivially. Identifying $G^{-}_{\pm1/2} \mapsto G_{\pm1/2}$, one recovers the same algebraic dynamics studied earlier in this section, but now augmented with an explicit $U(1)$ R-charge J.

Importantly, J commutes with the $\mathfrak{sl}(2)$ subalgebra and counts the action of the super-

charges with one negative unit (in the chiral case)[8]

$$[L_0, J] = 0, \quad [L_{\pm 1}, J] = 0, \quad [J, G_{\pm 1/2}] = -\, G_{\pm 1/2}. \tag{4.188}$$

As such, J is blind to horizontal transitions within the $\mathfrak{sl}(2)$ weight lattice, but it detects vertical spreading corresponding to fermionic ladder operations, as depicted in Figure 4.39. On the highest-weight ground state, its action is given by

$$J\,|h\rangle = 2h\;|h\rangle\,. \tag{4.189}$$

Because $G^2_{\pm\frac{1}{2}} = L_{\pm 1}$, the operator J has only two distinct eigenvalues.

Since $\mathfrak{sl}(2)$ is a subalgebra of $\mathfrak{osp}(2|1)$, the representations of $\mathfrak{osp}(2|1)$ are built by uniting two $\mathfrak{sl}(2)$ representations into a supermultiplet. In our case the fermionic generators $G_{\pm\frac{1}{2}}$ connect two $\mathfrak{sl}(2)$ subspaces, leading to the graded Hilbert space

$$\mathscr{H}_h^{\mathfrak{osp}(2|1)} = \mathscr{H}_h^{\mathfrak{sl}(2)} \oplus \mathscr{H}_{h+\frac{1}{2}}^{\mathfrak{sl}(2)}\,. \tag{4.190}$$

Here $\mathscr{H}_h^{\mathfrak{sl}(2)}$ is generated from a lowest weight state $|h\rangle$ satisfying

$$L_1|h\rangle = 0, \quad G_{\frac{1}{2}}|h\rangle = 0, \quad L_0|h\rangle = h|h\rangle, \quad J|h\rangle = 2h|h\rangle\,. \tag{4.191}$$

The state $G_{-\frac{1}{2}}|h\rangle = \sqrt{2h}\,|h+\frac{1}{2}\rangle$ (up to normalisation) belongs to the second $\mathfrak{sl}(2)$ representation and has opposite Grassmann parity relative to $|h\rangle$. Note that under the usual $\mathfrak{sl}(2)$ evolution (e.g., generated by the operator in Eq. (4.125)), these two subspaces do not mix; the mixing is solely driven by the supercharges $G_{\pm\frac{1}{2}}$.

The commuting operators L_0 and J naturally organize the multiplet (4.190) into a lattice, as depicted in Fig. 4.39. In this lattice the horizontal direction is measured by L_0, while the vertical direction, which reflects fermion number, is measured by J.

Unitary OSp$(2|1)$ Supercoherent State

In this subsection, we analyze displacement operators for $OSp(1|2)$—as presented, for example, in [430]—and adopt the following unitary form:

$$D(\xi,\chi) = \exp\!\left[\xi\, L_{-1} - \bar{\xi}\, L_1 + \chi\, G_{-\frac{1}{2}} + \bar{\chi}\, G_{\frac{1}{2}}\right], \tag{4.192}$$

where the parameters χ and $\bar{\chi}$ are Grassmann odd. In contrast to Subsection 4.3.5, here we begin by isolating the dynamical algebra that yields both the Krylov basis and its associated

[8] For anti-chiral representations, the R-charge assigns a positive unit to the supercharge.

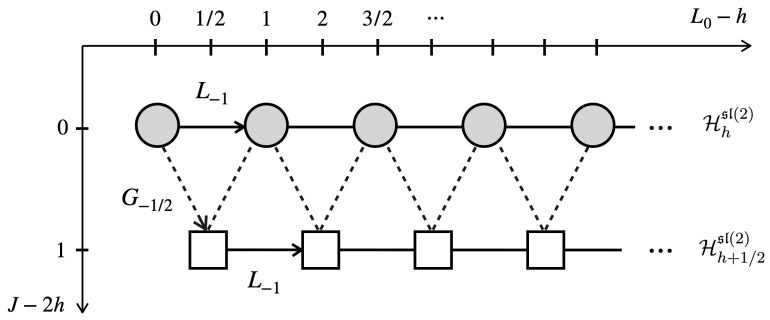

Figure 4.39: A highest weight representation of $OSp(1|2)$ couples two $SL(2,\mathbb{R})$ representations via the action of the fermionic generators. Horizontal movement corresponds to progression in the $\mathfrak{sl}(2)$ multiplet, whereas vertical movement tracks fermion number. Note that $G^2_{\pm\frac{1}{2}} = L_{\pm 1}$, so the fermionic action is not nilpotent. Figure taken from [67].

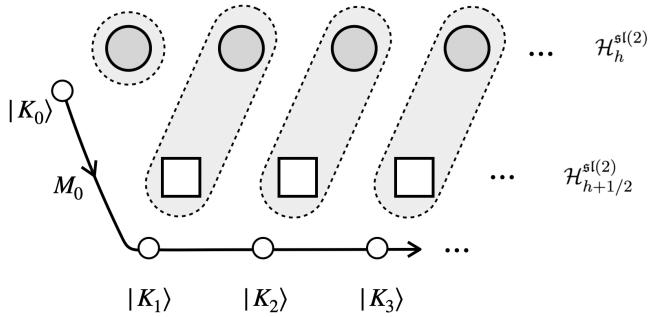

Figure 4.40: Each n^{th} Krylov vector $|K_n\rangle$ is built by pairing the n^{th} state of $\mathscr{H}_h^{\mathfrak{sl}(2)}$ (represented as a circle) with the $(n-1)^{\text{th}}$ state of $\mathscr{H}_{h+\frac{1}{2}}^{\mathfrak{sl}(2)}$ (represented as a square). The starting vector $|K_0\rangle$ appears on its own, without a partner. Clearly, this means that the Krylov subspace $\mathscr{K}$ lies within $\mathscr{H}_h^{\mathfrak{osp}(2|1)}$. Moreover, the particular linear combinations generated by the operator M_{-1}^n, which mix these circle and square states, delineate a *Krylov path* traversing the weight lattice of $\mathscr{H}_h^{\mathfrak{osp}(2|1)}$. Figure taken from [67].

operator; details on the lattice complexities will follow later.

A key step is to rewrite the exponent in Eq. (4.192) so as to identify a dynamical spread algebra. To that end, we define

$$M_1 = i\,\frac{\bar{\xi}\,L_1 - \bar{\chi}\,G_{\frac{1}{2}}}{\sqrt{|\xi|^2 + \bar{\chi}\,\chi}}\,, \tag{4.193}$$

$$M_{-1} = -\,i\,\frac{\xi\,L_{-1} + \bar{\chi}\,G_{\frac{1}{2}}}{\sqrt{|\xi|^2 + \bar{\chi}\,\chi}}\,, \tag{4.194}$$

$$M_0 = L_0 + \frac{\bar{\xi}\,\chi}{2|b|^2}\,G_{\frac{1}{2}} - \frac{\xi\,\bar{\chi}}{2|b|^2}\,G_{-\frac{1}{2}}\,, \tag{4.195}$$

which obey the $\mathfrak{sl}(2)$ commutation relations

$$[M_0, M_{\pm 1}] = \mp M_{\pm 1}\,, \qquad [M_1, M_{-1}] = 2\,M_0\,. \tag{4.196}$$

In these variables the displacement operator in Eq. (4.192) assumes the same form as the standard $\mathfrak{sl}(2)$ displacement operator (cf. Eq. (4.125)), with the identifications $\alpha\, t \to \sqrt{|\xi|^2 + \bar{\chi}\,\chi}$ and $\gamma \to 0$.

Starting from the lowest weight state $|h\rangle$, the Krylov basis is constructed as

$$|K_n\rangle = \frac{M_{-1}^n |h\rangle}{\|M_{-1}^n |h\rangle\|} \quad \text{with} \quad \|M_{-1}^n |h\rangle\|^2 = n! \frac{\Gamma(2h+n)}{\Gamma(2h)}\,. \tag{4.197}$$

A short calculation shows that the basis element $|K_n\rangle$ is a linear combination of the n^{th} state in $\mathscr{H}_h^{\mathfrak{sl}(2)}$ and the $(n-1)^{\text{th}}$ state in $\mathscr{H}_{h+\frac{1}{2}}^{\mathfrak{sl}(2)}$, as illustrated in Figure 4.40. In this way the Krylov basis selects a one-dimensional path (the *Krylov path*) through the full weight lattice of the $OSp(2|1)$ representation, i.e. $\mathscr{K} \subset \mathscr{H}^{\mathfrak{osp}(2|1)}$.

The evolution along the Krylov basis is determined analogously to the $\mathfrak{sl}(2)$ case (see Eq. (4.128)), but with the additional feature that semiclassical averaging over the Grassmann parameters must be performed (cf. Eq. (4.134)). Thus, we define the spread complexity associated with M_0 by

$$\mathscr{C}^{(M_0)}_{\mathfrak{osp}(2|1)} = \Big\langle \langle \xi, \chi, h| \Big(M_0 - h \Big) |\xi, \chi, h\rangle \Big\rangle_{\text{cl}} = \Big\langle 2h\, \sinh^2\Big(\sqrt{|\xi|^2 + \bar{\chi}\,\chi} \Big) \Big\rangle_{\text{cl}}\,, \tag{4.198}$$

which upon evaluation yields

$$\mathscr{C}^{(M_0)}_{\mathfrak{osp}(2|1)} = 2h\, \sinh^2\Big(|\xi(t)|\Big) + h\,|\xi(t)|\, \sinh\Big(2|\xi(t)|\Big)\, |f(t)|^2\,. \tag{4.199}$$

By comparing the intermediate expression in Eq. (4.198) with the corresponding $\mathfrak{sl}(2)$ result (see Eq. (4.128)), one deduces that the temporal dependence must satisfy

$$\Big\langle |\xi|^2 + \bar{\chi}\,\chi \Big\rangle_{\text{cl}} = |\xi|^2 + |f|^2 = (\alpha\, t)^2 \quad (\alpha \in \mathbb{R})\,. \tag{4.200}$$

In particular, one finds that $\mathscr{C}^{(M_0)}_{\mathfrak{osp}(2|1)} \geq \mathscr{C}_{\mathfrak{sl}(2)}$, with equality only if either $f = 0$ or $\xi = 0$, thereby constraining the choice of the function $f(t)$.

Lattice Complexities: We now measure the progression through the Krylov basis with respect to the underlying weight lattice. Recall that the lattice of the highest weight representation is labeled by the commuting operators (L_0, J); hence, these naturally serve as position operators. To fix the origin at the initial state $|h\rangle$, we define the effective position operators

by

$$\vec{X} = (L_0 - h,\ J - 2h)\,. \tag{4.201}$$

The lattice complexity is then defined as

$$\vec{\mathscr{C}}^{L}(\xi,\chi,h) = \left| \int d\zeta_0\, d\bar{\zeta}_0\, e^{\bar{\zeta}_0\,\zeta_0}\, \langle \xi,\chi,h|\vec{X}|\xi,\chi,h\rangle \right|. \tag{4.202}$$

The horizontal spread (along L_0) becomes

$$\mathscr{C}^{(h)}_{\mathrm{osp}(1|2)}(\xi,\chi) = \left| 2h\,\sinh^2\Big(|\xi|\Big) + \frac{2h}{|\xi|^2}\Big(\cosh\Big(|\xi|\Big) - \cosh\Big(2|\xi|\Big) + |\xi|\,\sinh\Big(2|\xi|\Big)\Big)|f(t)|^2 \right|. \tag{4.203}$$

If one sets $\chi = 0$, this expression reduces to the pure $SL(2,\mathbb{R})$ result, namely $\mathscr{C}^{(h)}_{\mathrm{SL}(2,\mathbb{R})}(\xi) = 2h\,\sinh^2(|\xi|)$. Meanwhile, the vertical spread (as measured by the J operator) is given by

$$\mathscr{C}^{J}_{\mathfrak{osp}(2|1)} = \left| \int d\zeta_0\, d\bar{\zeta}_0\, e^{\bar{\zeta}_0\,\zeta_0}\, \langle \xi,\chi,h|(J-2h)|\xi,\chi,h\rangle \right| = P^{(h+\frac{1}{2})} = 4h\,\frac{\cosh(|\xi|)-1}{|\xi|^2}\,|f(t)|^2\,, \tag{4.204}$$

where $P^{(h+\frac{1}{2})}$ denotes the probability of being in the sector $\mathscr{H}^{\mathfrak{sl}(2)}_{h+\frac{1}{2}}$. Since $P^{(h+\frac{1}{2})}$ is constrained between 0 and 1, this in turn imposes the bound

$$0 \le |f|^2 \le \frac{|\xi|^2}{4h\Big(\cosh(|\xi|)-1\Big)}\,. \tag{4.205}$$

A Remark on the Purely Grassmann Case: It is instructive to consider the limit in which we set $\xi = 0$ in Eq. (4.192). Then the evolution under the displacement operator reduces to

$$|h\rangle \to |\chi,h\rangle \equiv |0,\chi,h\rangle = e^{\chi\,G_{-\frac{1}{2}} + \bar{\chi}\,G_{\frac{1}{2}}}|h\rangle = (1 - h\,\bar{\chi}\,\chi)|h\rangle + \chi\,G_{-\frac{1}{2}}|h\rangle\,. \tag{4.206}$$

Due to the Grassmann odd nature of χ, this evolution involves only two Krylov steps. One then finds

$$\mathscr{C}^{(h)}_{\mathrm{osp}(1|2)}(0,f(t)\zeta_0) = \int d\zeta_0\, d\bar{\zeta}_0\, e^{\bar{\zeta}_0\,\zeta_0}\, \langle \chi,h|(L_0-h)|\chi,h\rangle = h\,|f(t)|^2\,, \tag{4.207}$$

$$\mathscr{C}^{J}_{\mathrm{osp}(1|2)}(0,f(t)\zeta_0) = \left| \int d\zeta_0\, d\bar{\zeta}_0\, e^{\bar{\zeta}_0\,\zeta_0}\, \langle \chi,h|(J-2h)|\chi,h\rangle \right| = 2h\,|f(t)|^2\,. \tag{4.208}$$

This behaviour closely mirrors that found in Subsection 4.3.3 and demonstrates that a purely Grassmann-odd evolution saturates after only two Krylov steps. It is therefore natural to explore the scenario when the supercharge is accompanied by a Grassmann even parameter, which we discuss next.

Supercharge Induced Spread

The distinctive feature of the $\mathfrak{osp}(2|1)$ algebra is the presence of the supercharges $G_{\pm\frac{1}{2}}$. In order to isolate and study the spread induced solely by these operators, we consider the Hermitian combination

$$\mathscr{L} = \alpha\left(G_{-\frac{1}{2}} + G_{\frac{1}{2}}\right), \tag{4.209}$$

where the parameter $\alpha \in \mathbb{R}$ is taken to be Grassmann even. Note that as $\mathscr{L}$ is now an overall Grassmann odd operator, its exponential $e^{\mathscr{L}}$ does not belong to the supergroup $OSp(2|1)$ in the standard sense. Consequently, the coherent state method does not directly apply; instead, we study this evolution via the Lanczos algorithm. As in the simpler case discussed in Subsection 4.3.3, the resulting Krylov basis will alternate between Grassmann even and odd states.

We now carry out the Lanczos procedure for the fermionic operator in eq. (4.209). Consider an initial state $|K_0\rangle = |h\rangle$ on which the evolution will be performed. We adopt the notation $||\,|v\rangle\,|| = \sqrt{\langle v|v\rangle}$ for the norm of a state $|v\rangle$ in Hilbert space. Note also that $G^{\dagger}_{\pm 1/2} = G_{\mp 1/2}$. The initial step of the Lanczos algorithm yields

$$|A_1\rangle = \mathscr{L}\,|h\rangle \;=\; \alpha\, G_{-1/2}\,|h\rangle\;, \tag{4.210}$$

$$b_1^2 = \alpha^2 \left\| G_{-1/2}\,|h\rangle \right\|^2 \;=\; 2\,\alpha^2\, h\,, \tag{4.211}$$

$$|K_1\rangle = \frac{1}{b_1}\, G_{-1/2}\,|h\rangle \;=\; \frac{G_{-1/2}\,|h\rangle}{\left\| G_{-1/2}\,|h\rangle \right\|}\,. \tag{4.212}$$

We continue by computing

$$|A_2\rangle = \frac{\alpha}{\left\| G_{-1/2}\,|h\rangle \right\|}\, G^2_{-1/2}\,|h\rangle\;, \tag{4.213}$$

$$b_2^2 = \alpha^2\, \frac{\left\| G^2_{-1/2}\,|h\rangle \right\|^2}{\left\| G_{-1/2}\,|h\rangle \right\|^2} \;=\; 2\,\alpha^2\, h\,, \tag{4.214}$$

$$|K_2\rangle = \frac{1}{b_2}\, G^2_{-1/2}\,|h\rangle \;=\; \frac{1}{\left\| L_{-1}\,|h\rangle \right\|}\, L_{-1}\,|h\rangle\;, \tag{4.215}$$

where $G^2_{-1/2} = L_{-1}$ has been employed. Repeating these steps reveals a recognizable pattern

for the Krylov basis:

$$|K_n\rangle \;=\; \frac{G^n_{-1/2}\,|h\rangle}{\left\|G^n_{-1/2}\,|h\rangle\right\|}, \qquad b_n \;=\; \alpha\,\frac{\left\|G^n_{-1/2}\,|h\rangle\right\|}{\left\|G^{n-1}_{-1/2}\,|h\rangle\right\|}. \tag{4.216}$$

Because each of these states resides in a distinct energy eigenspace, they are mutually orthogonal, and the Lanczos coefficients b_n convert the normalisation of $|K_{n-1}\rangle$ into the normalisation of $|K_n\rangle$, as expected. In order to determine the Lanczos coefficients (4.216) more explicitly, we must compute $\left\|G^n_{-1/2}\,|h\rangle\right\|^2 = \langle h|\,G^n_{1/2}G^n_{-1/2}\,|h\rangle$. For even $n = 2k$, we exploit the identity $G^2_{-1/2} = L_{-1}$, giving

$$\left\|G^{2k}_{-1/2}\,|h\rangle\right\|^2 \;=\; \left\|L^k_{-1}\,|h\rangle\right\|^2 \;=\; k!\,\frac{\Gamma(2h+k)}{\Gamma(2h)}\,. \tag{4.217}$$

For odd $n = 2k+1$, note that

$$G_{-1/2}\,|h\rangle \;=\; \sqrt{2h}\;\,|h+1/2\rangle\,, \tag{4.218}$$

since $|h+1/2\rangle$ is normalised to unity, just like $|h\rangle$. Consequently,

$$\left\|G^{2k+1}_{-1/2}\,|h\rangle\right\|^2 \;=\; 2h\left\|L^k_{-1}\,|h+1/2\rangle\right\|^2 \;=\; k!\,\frac{\Gamma(2h+k+1)}{\Gamma(2h)}\,. \tag{4.219}$$

Putting it all together, for n even ($n = 2k$) and odd ($n = 2k+1$) respectively, the Lanczos coefficients read

$$b_{2k} \;=\; \alpha\,\frac{\left\|G^{2k}_{-1/2}\,|h\rangle\right\|}{\left\|G^{2k-1}_{-1/2}\,|h\rangle\right\|} \;=\; \alpha\,\sqrt{k}\,, \qquad b_{2k+1} \;=\; \alpha\,\frac{\left\|G^{2k+1}_{-1/2}\,|h\rangle\right\|}{\left\|G^{2k}_{-1/2}\,|h\rangle\right\|} \;=\; \alpha\,\sqrt{2h+k}\,. \tag{4.220}$$

Since consecutive Krylov vectors belong to distinct eigenspaces (separated by half-integer shifts), they are orthogonal. In fact, for even n the vector $|K_n\rangle$ shares the Grassmann parity of $|h\rangle$ and resides in $\mathscr{H}_h^{\mathfrak{sl}(2)}$, whereas for odd n it belongs to $\mathscr{H}_{h+\frac{1}{2}}^{\mathfrak{sl}(2)}$. This $\mathbb{Z}_2$ alternation is reflected in the Lanczos coefficients, which, are given by

$$b_{2k} = \alpha\,\sqrt{k} \quad \text{and} \quad b_{2k+1} = \alpha\,\sqrt{2h+k}\,. \tag{4.221}$$

These coefficients have previously appeared in the context of Laguerre polynomial-associated Krylov complexity [431]. In fact, by matching the parameters of the complexity computed in

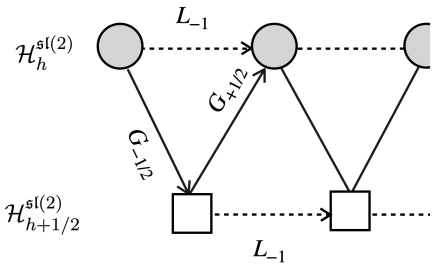

Figure 4.41: The evolution under the supercharge $\mathscr{L}$ produces a zig-zag Krylov path that alternates between Grassmann even and odd states. In this case the Krylov space exhausts the full weight lattice, i.e. $\mathscr{K} = \mathscr{H}_h^{\mathfrak{osp}(2|1)}$. Figure taken from [67].

[431] with Eq. (4.221), one obtains the spread complexity

$$\mathscr{C}_S(t) = \frac{(\alpha t)^2}{2} + \frac{4h-1}{4(2h-1)}\left[1 - e^{-(\alpha t)^2}\ {}_2F_2\left(\frac{3}{2} - 2h; \frac{1}{2}; (\alpha t)^2\right)\right], \tag{4.222}$$

$$\mathscr{C}_S(t) \overset{t\to\infty}{=} \frac{(\alpha t)^2}{2} + \frac{4h-1}{4(2h-1)}\left[1 - \frac{\sqrt{\pi}}{\Gamma\left(\frac{3}{2} - 2h\right)}\,(\alpha t)^{2-4h}\right], \tag{4.223}$$

where ${}_2F_2$ denotes a generalised hypergeometric function. As detailed in [431], the complexity exhibits oscillatory behaviour at early times and eventually approaches a quadratic scaling at late times. In comparison with the purely fermionic HW coherent state (cf. Subsection 4.3.3), where a Grassmann even parameter induced oscillations and a Grassmann odd parameter gave t^2 growth, the spread complexity in Eq. (4.222) represents a hybrid behaviour.

Finally, note that squaring the operator in Eq. (4.209) yields

$$\mathscr{L}^2 = \alpha^2\Big(L_{-1} + L_1\Big) + 2\alpha^2\, L_0\,, \tag{4.224}$$

which is purely bosonic and matches the form used in the standard $\mathfrak{sl}(2)$ displacement operator (cf. Eq. (4.125)). For the corresponding spread complexity, this implies that an initially exponential growth is truncated to quadratic growth. Specifically, evolving the ground states in $\mathscr{H}_h^{\mathfrak{sl}(2)}$ and $\mathscr{H}_{h+\frac{1}{2}}^{\mathfrak{sl}(2)}$ under $\mathscr{L}^2$ produces

$$\mathscr{C}_h^{\mathscr{L}^2}(t) = 2h\,\alpha^4 t^2 \quad \text{and} \quad \mathscr{C}_{h+\frac{1}{2}}^{\mathscr{L}^2}(t) = 2\Big(h + \tfrac{1}{2}\Big)\alpha^4 t^2\,. \tag{4.225}$$

Thus, for unitary representations with $h > 0$, both approaches yield the same late-time quadratic scaling as in Eq. (4.223)[9].

[9] For non-unitary representations, the scaling in Eq. (4.223) may differ.

4.3.7 Spread Complexity in Semiclassical String Settings of $AdS_5 \times S^5$

We next examine our main objective: computing spread complexity in the semiclassical regime of string theory on $AdS_5 \times S^5$ and its holographic dual in the planar limit of the AdS_5/CFT$_4$ correspondence.

The first part of this section reviews how coherent states arise on both the gauge side and the string side, focusing on their role in the effective spin-chain descriptions. We then evaluate the spread complexity of rotating string configurations embedded in different subspaces of $AdS_5 \times S^5$. (See also [87] for related discussions of operator Krylov complexity in similar spin-chain systems. Here, however, we approach the problem using the *semiclassical* continuum limit of such spin chains, which correspond to large angular momentum string states in the bulk.)

Throughout, our strategy is as follows. From the relevant spin-chain Hamiltonian in the continuum limit, we reconstruct the phase-space trajectories by solving the classical equations of motion. Once the time and (when relevant) spatial dependencies in the coherent state are obtained, we compute the corresponding return amplitude and employ the moment recursion method to extract the Lanczos coefficients. The ensuing spread complexity effectively traces out a one-dimensional trajectory in Krylov space, mirroring the general patterns discussed in Section 4.3.4.

Defining Spread Complexity for Semiclassical Spin Chains

Before delving into explicit examples, let us emphasize a few important distinctions that arise when adapting spread complexity to this semiclassical sector:

- **Initial coherent state versus vacuum:** Unlike in subsections 4.3.2 and 4.3.4, where the starting point was often a vacuum or a lowest-weight configuration, the initial state is now a coherent state at each site of the spin chain, i.e. a product of L coherent states (see eq. (2.29) for a schematic example).

- **Hamiltonian evolution rather than exponential displacements:** Whereas earlier models used time evolution generated by displacement operators, here the relevant evolution is governed by the spin-chain Hamiltonian. This Hamiltonian is quadratic in the symmetry generators, typically yielding second-order differential equations in the semiclassical regime. For instance, eq. (2.25) features nearest-neighbor couplings that raise in one site while lowering at the adjacent site.

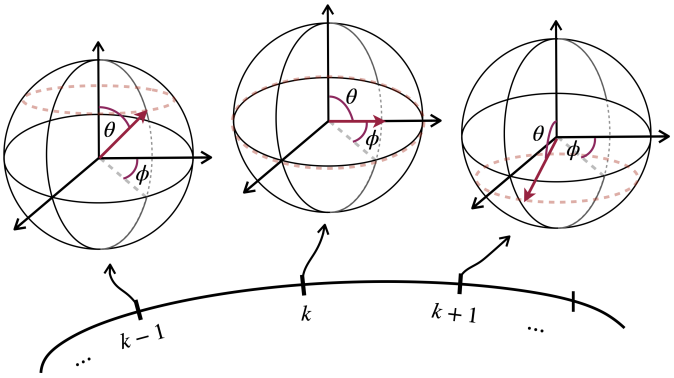

Figure 4.42: Schematic depiction of coherent-state configurations along a spin chain. Each site is approximated by a coherent state in the semiclassical limit. Transitioning to the continuum turns the discrete sites into a spatial coordinate σ. The figure only highlights the coherent states at discrete points, but in reality one has a continuum of sites along the chain. Figure taken from [67].

- **Nontrivial spatial dependence:** A single spin chain generally features L sites with interactions between neighboring sites. Taking the continuum limit means passing to a spatial coordinate σ, so that the coherent-state parameters become σ-dependent as well as time-dependent. The resulting complexity often acquires both temporal and spatial structure (see Fig. 4.42). In specific cases, one may even find a time-*independent* but spatially nontrivial spread complexity.

These novel features expand the range of solutions compared to simpler toy models, offering multiple possible trajectories in phase space for the coherent states at each site (cf. Fig. 4.34). In the following subsections, we study how such richer dynamics affect spread complexity in specific examples of rotating semiclassical strings.

Spread Complexity for Rotating String States

In the semiclassical regime of the planar holographic correspondence, an important class of solutions is given by the so-called rotating strings. These are nearly point-like strings that spin with high momentum within a specific submanifold of $AdS_5 \times S^5$, and they are associated with distinct subgroups of the supergroup $PSU(2,2|4)$. In this section, we determine the spread complexity by computing the relevant survival amplitude for various (super) string states. Equivalently, this analysis applies to long single-trace operators, which are captured by spin chains in different closed subsectors of the symmetry algebra $\mathfrak{psu}(2,2|4)$ of the $AdS_5 \times S^5$ correspondence.

It is remarkable that, despite the nuances outlined in Section 4.3.7 relative to previous studies, the spread complexity still organizes itself in terms of an effective $\mathfrak{sl}(2)$ or $\mathfrak{su}(2)$

structure. In fact, the Lanczos coefficients we extract for rotating strings are characteristic of both the compact and non-compact subsectors of the $\mathfrak{psu}(2,2|4)$ symmetry algebra. Crucially, this does not mean that the resulting spread complexity immediately coincides with the known complexity of standard $SL(2)$ or $SU(2)$ coherent states as discussed in [79]. Rather, due to the evolution driven by the spin chain Hamiltonian, the time dependence of the complexity traces an entirely new path through the coherent state phase space. In other words, while the functional form resembles an $\mathfrak{sl}(2)$ or $\mathfrak{su}(2)$ complexity — an *atomic pattern* — its time evolution differs from that found in [79].

A similar picture emerges when we extend our discussion to a fermionic sector: the spread complexity again exhibits an atomic pattern, this time echoing the results obtained for multi-fermion states in Section 4.3.2. Moreover, across all the cases considered, the process of taking the continuum limit of the spin chain naturally introduces a spatial profile along the worldsheet, so that the spread complexity becomes a function of both time and the spatial coordinate.

$SU(2)$ Subsector

We first consider the simplest closed subsector corresponding to the $SU(2)$ (Heisenberg XXX) spin chain. The one-loop dilatation operator, which acts as the Hamiltonian of the spin chain in the scalar $SU(2)$ sector, is given by (2.24). In this scenario, the string states are localised near the center of AdS_5 and rotate on S^5 within two out of three available planes; in the notation of [106], one has $S_1, S_2 = 0$, $J_3 = 0$, with nonzero J_1, J_2. For completeness, the $SU(2)$ coherent state is expressed as

$$\begin{aligned} |z,j\rangle &= (1+|z|^2)^{-j} \sum_{n=0}^{2j} z^n \sqrt{\frac{\Gamma(2j+1)}{n!\,\Gamma(2j-n+1)}}\,|j,-j+n\rangle \\ &= \cos\!\big(\theta/2\big)^{2j} \sum_{n=0}^{2j} e^{i\,n\,\phi}\,\tan\!\big(\theta/2\big)^{n} \sqrt{\frac{\Gamma(2j+1)}{n!\,\Gamma(2j-n+1)}}\,|j,-j+n\rangle, \end{aligned} \tag{4.226}$$

after reparameterising via $z = e^{i\phi}\tan(\theta/2)$. The full spin chain state is then the L-fold tensor product

$$\Big|\{(z_k,j_k)\}_{k=1}^{L}\Big\rangle = \bigotimes_{k=1}^{L} |z_k,j_k\rangle.$$

To identify an appropriate phase-space trajectory for these states, we examine the contin-

uum equations of motion derived in [108]

$$\begin{aligned} \sin(\theta)\,\partial_t\theta \;+\; \tilde{\lambda}\,j\,\partial_\sigma\Big[\sin^2\theta\,\partial_\sigma\phi\Big] &= 0, \\ \sin(\theta)\,\partial_t\phi \;+\; \tilde{\lambda}\,j\,\partial_\sigma^2\theta \;-\; \tilde{\lambda}\,j\,\sin\theta\cos\theta\,(\partial_\sigma\phi)^2 &= 0, \end{aligned} \tag{4.227}$$

with $\tilde{\lambda} = \lambda/(4\pi^2)$, and subject to the periodic boundary conditions $\phi(\sigma = J, t) = \phi(\sigma = 0, t)$ and $\theta(\sigma = J, t) = \theta(\sigma = 0, t)$.

Adopting the Ansatz $\partial_\sigma\phi = 0$ leads to rotating string solutions that satisfy the zero-momentum constraint imposed by trace cyclicity in eq. (2.21). In this case, one finds $\partial_t\theta = 0$ and, from $\partial_t^2\phi = \omega$, it follows that $\partial_t\phi = \omega$. The spatial variation is then determined by

$$\partial_\sigma^2\theta \;=\; -\frac{\omega}{\lambda\,j}\,\sin\theta, \tag{4.228}$$

which integrates to yield $\partial_\sigma\theta = \pm\sqrt{a + b\cos\theta}$, where a is an integration constant and $b = 2\omega/\lambda$. Depending on the relation between a and $|b|$, one obtains either circular or folded rotating strings; for example, if $b > |a|$, a point-like string oscillates between $-\theta_0$ and θ_0, with $\theta_0 = \arccos(-a/b)$.

Choosing $\phi = \omega t$ and setting $\theta(\sigma) = \theta_i(\sigma)$ to retain a nontrivial σ-profile, the coherent state for the $j = \frac{1}{2}$ representation becomes

$$|(z, 1/2), t\rangle \;=\; \frac{1}{\cos\Big(\theta(\sigma)/2\Big)}\sum_{n=0}^{1} e^{i\,n\,\omega t}\,\tan\Big(\theta(\sigma)/2\Big)^n\,|1/2, -1/2 + n\rangle. \tag{4.229}$$

The time-evolved spin chain state for L sites is thus the tensor product of L copies of eq. (4.229). To capture the complexity generated during this time evolution, we compute the autocorrelation function

$$S(t) = \Big\langle \{(z_k, j_k)\}_{k=1}^{L}, t \;\Big|\; \{(z_k, j_k)\}_{k=1}^{L}, 0 \Big\rangle,$$

and use the moment recursion method to obtain the Lanczos coefficients

$$a_n = \omega\Big[1 - 2\cos^2\Big(\theta(\sigma)/2\Big)\Big]\,(n - L/2) - \frac{L\omega}{2}, \qquad b_n = \frac{\omega\,\sin\Big(\theta(\sigma)\Big)}{2}\sqrt{n\,(n + L - 1)}. \tag{4.230}$$

These coefficients can be reparameterised by defining $\alpha = \omega\,\sin\Big(\theta_i(\sigma)\Big)/2$, $j_{\mathfrak{su}(2)} = \frac{L}{2}$, $\gamma = \omega\Big[1 - 2\cos^2\Big(\theta_i(\sigma)/2\Big)\Big]$, and $\delta = -\frac{L\omega}{2}$, so that they take the standard form

$$a_n = \gamma\,(-j_{\mathfrak{su}(2)} + n) + \delta, \quad b_n = \alpha\sqrt{n\,\Big(2j_{\mathfrak{su}(2)} + 1 - n\Big)}. \tag{4.231}$$

Accordingly, the spread complexity is given by

$$\mathscr{C}(t,\sigma) = \frac{2j}{1+\frac{\gamma^2}{4\alpha^2}} \sin^2\left(\alpha t\sqrt{1+\frac{\gamma^2}{4\alpha^2}}\right) = \frac{L}{\csc^2\big(\theta(\sigma)\big)} \sin^2\Big(\frac{\omega\, t}{2}\Big)\,, \tag{4.232}$$

where we have used the relation $\sqrt{1+\frac{\gamma^2}{4\alpha^2}} = \csc\big(\theta_i(\sigma)\big)$ appropriate for the coefficients in eq. (4.230). Notably, this result shows that the spread complexity of the string state has both time and spatial dependence; its oscillatory behaviour in time is controlled by the initial value of $\theta_i(\sigma)$. In the continuum limit, with L large but finite, this formula accurately characterizes the complexity for string states propagating in $S^3 \subset S^5$ as well as for the corresponding single-trace operators (see eq. (2.21)), up to corrections of order $1/L$.

$SU(3)$ Subsector

Beyond the $SU(2)$ sector, we next examine the subalgebra $\mathfrak{su}(3)$ within $\mathfrak{psu}(2,2|4)$ [106, 432], which on the gauge side corresponds to single-trace operators constructed from all three complex scalars. In the $SU(3)$ sector the one-loop dilatation operator can be expressed in terms of the 3×3 Gell-Mann matrices, the generators $SU(3)$ algebra, λ^r, $r = 1,\ldots,8$ [106]. The exact form of the Hamiltonian is given by

$$\mathscr{D}_{SU(3)} = \frac{\lambda}{(4\pi)^2}\sum_{l=1}^{L}\left(\frac{4}{3} - \sum_{r=1}^{8}\lambda_l^r\lambda_{l+1}^r\right)\,. \tag{4.233}$$

Restricting to the case $j=\frac{1}{2}$, the corresponding coherent state is given by

$$|n\rangle = \cos\theta\, e^{i\varphi}\,|1\rangle \;+\; \cos\psi\,\sin\theta\, e^{-i\varphi}\,|2\rangle \;+\; \sin\psi\,\sin\theta\, e^{i\phi}\,|3\rangle\,. \tag{4.234}$$

Rotating string solutions in this sector are described by the Ansatz presented in [432]:

$$\theta=\theta_0,\quad \psi=\psi_0,\quad \partial_\sigma\varphi = q,\quad \partial_\sigma\phi = \ell\,, \tag{4.235}$$

with integer parameters q and ℓ. The equations of motion then determine the angular velocities through

$$\dot\varphi = -\frac{\lambda}{J^2}\left[\ell\Big(\frac{J_1}{J}-\frac{J_2}{J}\Big)+q\,\frac{J_3}{J}\right] \equiv \omega_\varphi\,, \tag{4.236}$$

$$\dot\phi = \frac{\lambda}{2J^2}\left[(q^2-\ell^2-2q)\Big(\frac{J_1}{J}-\frac{J_2}{J}\Big)+q\,\frac{J_3}{J}\right] \equiv \omega_\phi\,, \tag{4.237}$$

while the fixed angles are related to the conserved charges by

$$\frac{J_1 - J_2}{J_1 + J_2} = \cos(2\psi_0), \quad \frac{J_3}{J} = \sin^2\theta_0 \,. \tag{4.238}$$

Thus, the coherent state representing a rotating string in the $SU(3)$ subsector takes the form

$$|z\rangle = \cos\theta_0\, e^{i(q\sigma+\omega_\varphi t)}\,|1\rangle + \cos\psi_0\,\sin\theta_0\, e^{-i(q\sigma+\omega_\varphi t)}\,|2\rangle + \sin\psi_0\,\sin\theta_0\, e^{i(\ell\sigma+\omega_\phi t)}\,|3\rangle \,. \tag{4.239}$$

To measure the complexity associated with the evolution of the state in eq. (4.239), we compute the autocorrelation function $S(t) = \langle n(t)|n(0)\rangle$, and extract the Lanczos coefficients via the moment recursion method. They are found to be

$$a_n = 2\omega\, f(\theta,\psi)\left(n - \frac{L}{2}\right), \quad b_n = \omega\sqrt{n\,(L-n+1)\,g(\theta,\psi)}\,, \tag{4.240}$$

with the functions $g(\theta,\psi) = \sin^2\theta\,\cos^2\psi\left(-2\sin^2\theta\cos(2\psi) + \cos(2\theta) + 3\right)$, and $f(\theta,\psi) = \cos^2\theta - \sin^2\theta\cos(2\psi)$. It is noteworthy that the return amplitude $S(t) = \langle n(t)|n(0)\rangle$ is independent of σ, and hence so is the complexity. Using the reparameterisation $\alpha = \omega\sqrt{g(\theta,\psi)}$, $j_{\mathfrak{su}(2)} = \frac{L}{2}$, $\gamma = 2\omega f(\theta,\psi)$, $\delta = 0$, the Lanczos coefficients become

$$a_n = \gamma\left(-j_{\mathfrak{su}(2)} + n\right), \quad b_n = \alpha\sqrt{n\left(2j_{\mathfrak{su}(2)} + 1 - n\right)}\,. \tag{4.241}$$

Thus, the spread complexity is given by

$$\mathscr{C}(t) = \frac{2j}{1+\frac{\gamma^2}{4\alpha^2}}\,\sin^2\!\left(\alpha t\sqrt{1+\frac{\gamma^2}{4\alpha^2}}\right) = \frac{L}{1+\frac{f(\theta,\psi)^2}{g(\theta,\psi)}}\,\sin^2\!\left(\omega t\sqrt{g(\theta,\psi)+f(\theta,\psi)^2}\right). \tag{4.242}$$

Here, the oscillatory nature of $\mathscr{C}(t)$ is controlled by the ratio $f(\theta,\psi)^2/g(\theta,\psi)$, and the finite chain length L (serving as the total spin) sets the dimension of the Krylov subspace (which truncates at $L+1$).

$SU(1,1)$ or $SL(2)$ Subsector

In the non-compact $SL(2)$ subsector, the dilatation operator is equivalent to the Hamiltonian of a Heisenberg spin chain with states in $\mathfrak{sl}(2)$. On the gauge theory side, this sector comprises single-trace operators involving a single scalar field with derivatives; on the string side, it corresponds to excitations along the AdS_5 directions [106, 433, 434]. The coherent state for

this representation is given by

$$|\vec{n}\rangle = \sum_{m=0}^{\infty} \frac{1}{\cosh\left(\frac{\rho}{2}\right)^{2j}} \sqrt{\frac{\Gamma(m+2j)}{m!\,\Gamma(2j)}}\, e^{im\phi} \tanh\left(\frac{\rho}{2}\right)^{m} |j, j+m\rangle\,. \tag{4.243}$$

Here, the states are parametrised by a two-dimensional hyperboloid and we fix $j = \frac{1}{2}$ so that the representation is infinite-dimensional.

Proceeding to the continuum limit, the equations of motion transform into their analytically continued form [433]

$$\begin{aligned} \sinh\rho\,\partial_t\rho - \frac{\tilde{\lambda}}{L^2}\,\partial_\sigma\Big(\partial_\sigma\phi\,\sinh^2\rho\Big) &= 0, \\ \sinh\rho\,\partial_t\phi + \frac{\tilde{\lambda}}{L^2}\left[\partial_\sigma^2\rho - \frac{1}{2}\sinh(2\rho)\left(\partial_\sigma\phi\right)^2\right] &= 0\,, \end{aligned} \tag{4.244}$$

with $\tilde{\lambda} = \lambda/(4\pi^2)$. These equations describe a fast-spinning string propagating on a torus $S^1_\phi \times S^1_\varphi$, with one circle located in AdS_5 and the other in S^5.

A particularly simple solution [433] is obtained by choosing $\partial_\sigma\phi = 0$, which forces $\partial_t\rho = 0$ and $\partial_t\phi = \omega$, so that $\rho = \rho(\sigma)$ satisfies

$$\omega\,\sinh\rho + \frac{\tilde{\lambda}}{L^2}\,\partial_\sigma^2\rho = 0\,. \tag{4.245}$$

Integrating this equation once yields

$$\partial_\sigma\rho = \pm\sqrt{q - b\,\cosh\rho}\,, \quad \text{with} \quad b = \frac{2L^2\omega}{\tilde{\lambda}}, \tag{4.246}$$

where the integration constant q is chosen so that $q > b$. This solution characterizes a string with profile $\rho(\sigma)$ rotating at constant angular velocity along an S^1 in AdS_5.

The corresponding coherent state, incorporating the time evolution with frequency ω, is

$$|\vec{n}\rangle = \sum_{m=0}^{\infty} \frac{1}{\cosh\left(\frac{\rho(\sigma)}{2}\right)^{2j}} \sqrt{\frac{\Gamma(m+2j)}{m!\,\Gamma(2j)}}\, e^{im\omega\tau} \tanh\left(\frac{\rho(\sigma)}{2}\right)^{m} |j, j+m\rangle\,. \tag{4.247}$$

Evaluating the autocorrelation function for the state in eq. (4.247), the Lanczos coefficients are determined to be

$$a_n = -\omega\,\cosh\Big(\rho(\sigma)\Big)\left(n + \frac{L}{2}\right) + \frac{k\,\omega}{2}, \quad b_n = \frac{\omega\,\sinh\Big(\rho(\sigma)\Big)}{2}\sqrt{n\,(n+L-1)}\,, \tag{4.248}$$

with k denoting an additional constant. By defining $\alpha = \omega \sinh\Big(\rho(\sigma)\Big)/2, h = \frac{L}{2}$, $\gamma = -\omega \cosh\Big(\rho(\sigma)\Big)$, $\delta = \frac{k\omega}{2}$, the coefficients assume the standard form

$$a_n = \gamma\,(h+n) + \delta, \quad b_n = \alpha\,\sqrt{n(n+2h-1)}\,. \tag{4.249}$$

Following the methodology of [55], the spread complexity is then given by

$$\mathscr{C}(t,\sigma) = \frac{2h}{1-\frac{\gamma^2}{4\alpha^2}}\,\sinh^2\!\Big(\alpha\,t\,\sqrt{1-\frac{\gamma^2}{4\alpha^2}}\Big) = \frac{L}{\operatorname{csch}\Big(\rho(\sigma)\Big)^2}\,\sin^2\!\Big(\omega\,t\Big)\,, \tag{4.250}$$

where we have used the relation $\sqrt{1-\frac{\gamma^2}{4\alpha^2}} = i\,\operatorname{csch}\Big(\rho(\sigma)\Big)$. Although the underlying representation is infinite-dimensional, the spread complexity still displays oscillatory behaviour in time, with the period determined by $\operatorname{csch}\Big(\rho(\sigma)\Big)$ and an amplitude that scales with the chain length L. This oscillatory feature reflects the fact that the string dynamics is effectively confined to a compact subspace (namely, $S^1 \times S^1$) within the non-compact geometry of $AdS_5 \times S^5$.

$PSU(1|1)$ Subsector

Next, we turn to a case that incorporates fermionic degrees of freedom and captures the anomalous dimensions of operators such as those in eq. (2.22). The simplest all-loop closed subsector is given by

$$PSU(1|1) \subset SU(2|3) \subset PSU(2,2|1)$$

as discussed in [104, 435]. This sector describes operators built from a single scalar and a single fermionic component, e.g. $\operatorname{tr}(X^I \psi^K)$, which is a special case within the $SU(2|3)$ single-trace operators of eq. (2.22). The relevant equations of motion, obtained via the semiclassical approximation and subsequent continuum limit, were derived and analysed in [436] and [437].

In this subsector the coherent state is defined as

$$|n\rangle = \Big(1 - \frac{1}{2}\,\zeta^*\,\zeta\Big)|0\rangle + \zeta\,|1\rangle\,, \tag{4.251}$$

where $|0\rangle$ denotes the bosonic vacuum state and $|1\rangle$ denotes the state with a single fermionic excitation.

Proceeding to the continuum limit, the semiclassical action takes the form

$$S = -\int dt\,\Big[i\Big\langle n\,\Big|\,\frac{d}{dt}\Big|n\Big\rangle + \langle n|H|n\rangle\Big]$$

$$= -\frac{L}{2\pi}\int dt\, d\sigma \left[i\,\zeta^*\,\partial_t\zeta + \frac{\lambda}{2L^2}\,\partial_\sigma\zeta^*\,\partial_\sigma\zeta \right] . \tag{4.252}$$

This action describes a nonrelativistic fermion in $(1+1)$ dimensions. Its equation of motion is given by

$$i\,\partial_t\zeta = -\frac{L^2}{\lambda}\,\partial_\sigma^2\zeta\,. \tag{4.253}$$

Because the underlying spin chain is periodic, we impose the boundary condition

$$\zeta(2\pi,t) = \pm\zeta(0,t),$$

which leads to the general solution

$$\zeta(\sigma,t) = \zeta_0 \sum_n \Big(A_n\, e^{-i\,k_n^2\,t}\cos\big(\kappa_n\sigma\big) + B_n\, e^{-i\,k_n^2\,t}\sin\big(\kappa_n\sigma\big)\Big)\,, \tag{4.254}$$

where $\kappa_n = n$ for periodic boundary conditions (or $n+\frac{1}{2}$ for anti-periodic ones), with $k_n^2 = \frac{L^2\kappa_n^2}{\lambda}$, and ζ_0 is a unit Grassmann-odd parameter. By choosing, without loss of generality, that the coherent state at time $t=0$ and at $\sigma=0$ lies entirely in the bosonic ground state, we fix $A_n = 0$ for all n. Thus, one may write

$$\zeta(\sigma,t) = \zeta_0 \sum_{n=0}^{\infty} e^{-i\,k_n^2\,t}\sin\big(\kappa_n\sigma\big)\,. \tag{4.255}$$

In order to construct the Krylov basis, we observe that the Hamiltonian in the action (4.252) is Grassmann even, so it preserves the grading of the states. Since the coherent state in eq. (4.251) for a single lattice site is defined in a two-dimensional space, the initial state naturally serves as the first Krylov basis vector. There is then only one other basis vector with the same grading, given (up to normalisation) by the unique vector orthogonal to the initial state. Consequently, under Hamiltonian evolution, the single-site Hilbert space remains two-dimensional, and the normalised Krylov basis vectors can be written as

$$\begin{aligned} |K_0\rangle &= \Big(1 - \frac{1}{2}\,\bar\zeta\,\zeta\Big)|b\rangle + \zeta\,|f\rangle\,, \\ |K_1\rangle &= \frac{1}{\langle\bar\zeta\zeta\rangle}\Big(\bar\zeta\,\zeta\,|b\rangle - \zeta\,|f\rangle\Big)\,, \end{aligned} \tag{4.256}$$

where $|b\rangle$ and $|f\rangle$ denote the bosonic and fermionic states, respectively, and $\langle\cdot\rangle$ indicates the semiclassical averaging over fermionic degrees of freedom as defined in eq. (4.132).

Returning to the solution (4.255), we note that while the infinite series may not converge

for either periodic or anti-periodic boundary conditions, each individual term in the sum is a valid solution of eq. (4.253). Hence, it is natural to truncate the series to a finite number of terms. Choosing a single summand,

$$\zeta(\sigma,t) = \zeta_0 e^{-i\,k_n^2\,t}\sin\Big(\kappa_n\sigma\Big),$$

renders the quantity $\bar{\zeta}(\sigma,t)\zeta(\sigma,t)$ time independent; consequently, the coherent state does not develop a nontrivial Krylov subspace under evolution. The simplest nontrivial truncation is to retain two summands, so that

$$\zeta(\sigma,t) = \zeta_0 \sum_{n=1}^{2} e^{-i\,k_n^2\,t}\sin\Big(\kappa_n\sigma\Big)\,. \tag{4.257}$$

This choice generates two distinct Krylov basis vectors

$$\begin{aligned} |K_0\rangle &= \left(1 - \frac{\bar{\zeta}_0\zeta_0}{2}\left[\sum_{j=1}^{2}\sin\Big(\kappa_{n_j}\sigma\Big)\right]^2\right)|b\rangle + \zeta_0\left[\sum_{j=1}^{2}\sin\Big(\kappa_{n_j}\sigma\Big)\right]|f\rangle\,, \\ |K_1\rangle &= \bar{\zeta}_0\zeta_0\left[\sum_{j=1}^{2}\sin\Big(\kappa_{n_j}\sigma\Big)\right]|b\rangle - \zeta_0|f\rangle\,. \end{aligned} \tag{4.258}$$

For the time-evolved initial coherent state from eq. (4.251), one can then define the spread complexity as

$$\mathscr{C}(t) = \langle\, |\langle K_1|n(t)\rangle|^2\,\rangle\,, \tag{4.259}$$

which, for the two-summand solution, evaluates to

$$\mathscr{C}(t) = \left[\sum_{j=1}^{2}\sin\Big(\kappa_{n_j}\sigma\Big)\right]\left[\sum_{l=1}^{2}\sin\Big(\kappa_{n_l}\sigma\Big)\Big(1-2\cos\Big(k_{n_l}^2\,t\Big)\Big)\right]. \tag{4.260}$$

This expression can be generalised to a spin chain with L lattice sites. In practice, as discussed in Section 4.3.3, determining the Krylov basis for arbitrary displacement parameters is analytically challenging. A useful simplification arises when all sites share the same displacement parameter, in which case the Krylov basis for the full chain is constructed as the uniform linear combination of all permutations with k copies of $|K_1\rangle$ and $L-k$ copies of $|K_0\rangle$ forming the k^{th} Krylov vector. The overall spread complexity then takes the form

$$\mathscr{C}(t) = \sum_{k=0}^{L} k\left|\phi_0^{L-k}\,\phi_1^{k}\right|^2, \tag{4.261}$$

with the definitions

$$\phi_0(t) = \langle K_0|n(t)\rangle, \qquad \phi_1(t) = \langle K_1|n(t)\rangle\,. \tag{4.262}$$

While the computations here bear similarities to those for single- and multi-fermion cases in Section 4.3.2, several key distinctions—highlighted in Section 4.3.7—are noteworthy. In all these instances, however, the pattern remains consistent: the spread complexity condenses into an atomic Krylov trajectory, now governed by the multi-fermionic Heisenberg–Weyl coherent state framework discussed in Section 4.3.3.

4.3.8 Discussion

In this Section, we have developed a generalised framework for spread complexity that incorporates fermionic and supercoherent states, extending previous studies focused on bosonic systems. The principal motivation stems from the desire to formulate spread complexity within the context of supersymmetric systems, particularly those appearing in the AdS/CFT correspondence. By restricting our analysis to a semiclassical sector of holography where analytic control is available, we have been able to compute spread complexity explicitly through coherent state techniques.

Semiclassical systems are often amenable to a path integral description in terms of coherent states. Exploiting the group-theoretic structures underlying such systems, we analytically evaluated the spread complexity in a wide class of models governed by (super-)algebras. A key insight that emerged is the necessity to reinterpret the Krylov chain as a *Krylov path*—a trajectory through the weight lattice associated with a highest weight representation of a Lie or super-Lie algebra. This reformulation naturally explains the emergence of effective dynamical $\mathfrak{sl}(2)$ structures, as previously noted in [74]. Our results establish these structures concretely within coherent-state-based semiclassical evolutions.

Within our approach, the spread complexity is determined by the time-evolved trajectory of a coherent state in phase space under the action of a Hamiltonian. While multiple systems may exhibit $\mathfrak{sl}(2)$ or $\mathfrak{su}(2)$ algebraic patterns, the specific Hamiltonian dictates distinct phase space dynamics, and consequently, different time dependencies in complexity. This feature is particularly evident in our computation of spread complexity for rotating string configurations, detailed in Section 4.3.7.

We extended the formalism to include both single- and multi-fermion coherent states [429, 438]. Single fermionic systems, due to their intrinsically finite-dimensional Hilbert spaces, give rise to bounded and periodic spread complexities. In contrast, multifermion systems possess a richer internal structure, reflecting the enlarged Hilbert space formed by different

fermion number sectors. In these cases, the Krylov basis construction becomes analytically intractable for generic displacement parameters. We thus analysed a simplified situation where all displacement operators share a common parametrisation, leading to an oscillatory complexity profile. For more general configurations, we established an upper bound on the spread complexity via averaging over randomly chosen displacement parameters in the Fock basis. The resulting ensemble behaviour illustrates a non-oscillatory growth pattern governed by aggregated fermionic mode contributions.

We then turned to systems governed by superalgebras, focusing on the super Heisenberg–Weyl and $\mathfrak{osp}(2|1)$ algebras. In these cases, Krylov basis vectors form paths through lattices defined by both bosonic and fermionic weight directions. The evolution is driven by displacement operators constructed from combinations of bosonic and fermionic ladder elements. We identified two distinct perspectives on spread:

(1) The standard notion of spread complexity $\mathscr{C}$, measures how a state disperses over the Krylov basis. This basis—and its companion Krylov operator—originates from the dynamical algebra of the displacement operator that drives the time evolution.

(2) Interpreting the Krylov chain as a trajectory on the lattice, we quantify its spread by decomposing it into the lattice's own basis vectors.

The particular case of a Grassmann-even displacement operator admits an interpretation consistent with known constructions of supergroup coherent states. Additionally, we investigated evolution driven by a Grassmann-odd Hamiltonian, namely a supercharge. Remarkably, we were able to connect the resulting spread complexity to known Laguerre polynomial structures previously derived in [431], thereby offering a physical realisation in a supersymmetric context.

Building on these insights, we explored spread complexity in the semiclassical limit of the planar AdS/CFT correspondence. In this regime, the dynamics of long single-trace operators and their dual string states are equivalent. Consequently, complexities computed on either side of the duality are physically meaningful and holographically consistent. By taking the continuum limit of integrable spin chains and assigning a coherent state to each site, we captured the space-time dependent evolution of spread complexity in various symmetry subsectors of $PSU(2,2|4)$. These correspond to classical string configurations propagating on specific submanifolds of $AdS_5 \times S^5$.

Even though these holographic systems appear structurally distinct from those in earlier sections, the resulting complexities once again exhibit the characteristic "atomic" $\mathfrak{sl}(2)$ or $\mathfrak{su}(2)$ behaviour. Crucially, however, the spin chain Hamiltonians induce different coherent state trajectories in phase space, thereby imprinting distinct temporal and spatial signatures on the complexity.

Taken together, our results suggest that spread complexity is sensitive to the geometry traversed by the evolving state. In the context of strings propagating on compact subspaces of $AdS_5 \times S^5$, boundedness in complexity emerges as a direct reflection of the compactness of the underlying geometry, despite being embedded within a non-compact target space.

5 Conclusion and Outlook

This dissertation has examined a range of questions at the intersection of quantum information, many-body physics, and holography, with a particular focus on how notions of complexity and correlation structure behave in both discrete and continuum settings. While the individual chapters address distinct problems—from the structure of aperiodic spin chains to the behaviour of Krylov complexity in chaotic and non-unitary systems—they are connected by a broader interest in how information-theoretic tools can offer new perspectives on established topics in theoretical physics.

Instead of pursuing an all-encompassing framework, this thesis adopts a bottom-up strategy: it examines representative systems in depth, using well-defined computational tools motivated by clear physical insights. In doing so, the work contributes to several active areas of research: the development of discrete models inspired by holography, the refinement of complexity measures in quantum dynamics, and the application of quantum information concepts such as geometric quantum discord to problems in gravity and field theory.

The results obtained provide both conceptual insights and technical methods that may be useful in future investigations. In the remainder of this section, we summarize the main contributions from each part of the thesis and suggest a number of directions in which these ideas could be further developed.

Aperiodic Spin Chains, Discrete Holography, and Entanglement (Section 3.1)

We initiated our inquiry by examining infinite spin chains endowed with couplings that are aperiodically modulated by sequences associated with regular hyperbolic tilings of the Poincaré disk. These models, proposed in [157], serve as a stepping stone toward a discrete holographic duality wherein the bulk geometry is tessellated by a hyperbolic tiling and the boundary is realised by an aperiodic spin chain. We established a general framework for analysing aperiodic singlet phases (ASPs) at strong-disorder renormalisation group (SDRG) fixed-points by imposing four conditions—criticality, gaplessness, cyclicity under SDRG transformations, and the existence of an ASP—that in turn yield direct access to correlation functions, entanglement entropy, and mutual information. This allowed us to generalise results from known CFT-inspired approaches and to adapt continuum AdS/CFT geodesic arguments to these discrete setups. Novel outcomes include analytic formulae for the mutual information of consecutive spin-block subsystems in aperiodic chains, where a piecewise linear structure emerges, controlled by the interplay of the modulation pattern and the nature

of the SDRG cycle.

Motivated by discrete holography, we then investigated two classes of aperiodic spin-chain Hamiltonians, one possessing dihedral-group symmetries and another with a global $SO(N)$ symmetry. In both cases, we found that the effective central charge grows either linearly or logarithmically, depending on the specifics of the spin representation or large-N limit. Although the models studied here lack a strong-coupling limit or gauge symmetry essential to standard AdS/CFT, they constitute a promising step in systematically introducing new ingredients—such as SYK-like interactions and finite-temperature tilings—to probe black hole analogs and dynamical bulk degrees of freedom in the discrete holography framework.

Geometric Quantum Discord and the Factorisation Puzzle (Section 3.2)

Next, we presented a novel procedure to characterigeneralise boundary non-factorisation via the geometric quantum discord (GQD). For generic pure states and the Thermo-Field Double (TFD) state, we showed that GQD signals the breakdown of factorisation in a modular or thermal partition function, respectively, and is thus intrinsically related to wormhole geometries in the bulk. We identified a Thermo-Mixed Double (TMD) state that minimises the TFD's GQD, representing its "closest classical approximation." This new viewpoint clarifies the factorisation puzzle from a quantum-information perspective, offering a tractable measure that complements entanglement-based probes.

In addition, we proved that two distinct geometric measures of quantum correlations coincide for pure states, reinforcing the robustness of GQD. We speculated on its extension to mixed states, as well as on potential holographic calculations of GQD in field theories, possibly involving cosmic branes in the bulk. These developments set the stage for broader explorations into non-perturbative features of wormholes, new TMD states, and the complex interplay of decoherence, replica wormholes, and Schatten norms.

Chaos, Integrability, and Complexity in Quantum Triangular Billiards (Section 4.1)

Shifting our focus to quantum billiards, we investigated twenty-seven triangular domains with internal angles supporting integrable, pseudo-integrable, or non-integrable classical dynamics. By examining their spectra through average level spacing ratios (LSRs), we discovered a continuous spectrum of behaviours ranging from Poisson-like (typical of integrable systems) to Wigner-Dyson-like (characteristic of chaotic theories). Spectral complexity and various aspects of Krylov complexity (the variances of Lanczos coefficients, eigenstate localisation in the Krylov basis, and time evolution of spread complexity) allowed us to map out clear distinctions among these triangles:

- **Integrable triangles** manifest degeneracies in their energy spectra, leading to faster-than-linear spectral complexity growth, pronounced Poincaré recurrences, and strongly

localised energy eigenstates.

- **Isosceles triangles** exhibit traits intermediate between full integrability and chaos, lacking large recurrences and displaying spectral features near Poisson distributions once symmetry sectors are combined.

- **Right and generic triangles** approach chaotic behaviour most closely, with level statistics matching Gaussian Orthogonal Ensemble (GOE) predictions, delocalised eigenstates in the Krylov basis, and spread complexity that rises to a peak followed by a plateau.

These results emphasise how geometric parameters and boundary reflections collectively induce chaotic or integrable patterns in quantum billiards. Future work could leverage path integral methods on corresponding translation surfaces, possibly revealing how scarring phenomena or high-genus topologies encode the difference between pseudo-integrable and non-integrable billiards. Extensions to quantum field theories dual to gravity remain an especially compelling direction.

Non-Hermitian Evolution, Measurement-Induced Complexity, and the Quantum Zeno Regime (Section 4.2)

We next investigated non-unitary dynamics generated by repeated projective measurements on a one-dimensional tight-binding chain. Extending the Krylov machinery to this setting, we employed both the bi-Lanczos construction and a complex-symmetric Lanczos algorithm that halves the required memory. Within this framework, spread complexity (and its companion, spread entropy) affords a sharp diagnostic of measurement-induced evolution, leading to the following picture:

- For any fixed monitoring interval τ, complexity grows at early times, then enters a prolonged decay before saturating at a plateau.

- Raising the measurement rate $1/\tau$ delays the onset of growth and in the $\tau \to 0$ limit the rise is postponed indefinitely, signalling the quantum-Zeno freeze-out.

- The asymptotic value is sensitive to the initial state, establishing a clear hierarchy among quenches that begin from ground, excited, or generic states.

We then extended our analysis to tight-binding Hamiltonians with complex on-site potentials localised at the boundaries, allowing us to explore systems exhibiting $\mathscr{P}\mathscr{T}$ symmetry. In the unbroken phase, wave functions remain delocalised and oscillatory, while in the broken phase, edge-localised states emerge—a manifestation of the non-Hermitian skin effect. This transition is marked by a shift from extended to localised eigenstates, and we showed

that all Krylov-space probes—spread complexity, spread entropy, entropic complexity, and KIPR—are sensitive to this transition. In the broken phase, the saturation values of all complexity measures decrease due to the localisation of the state, in line with the broader observation that localised states tend to exhibit lower complexity [91]. Interestingly, while spread entropy and entropic complexity decrease monotonically with increasing localisation strength, spread complexity saturation value changes incoherently to localisation strength due to its inherent dependence on the monotonically increasing weight factor. The KIPR, in contrast, offers a direct quantitative measure of localisation in Krylov space, and its behaviour across the $\mathscr{PT}$-transition provides a useful benchmark for future studies of non-Hermitian systems.

We also introduced a framework for analysing mixed-state complexity within the Krylov formalism, based on different schemes of purification. By defining the Krylov complexity of purification (CoP), we established conjectural inequalities relating CoP to the complexity of the original mixed state. These bounds were tested in concrete examples including one-qubit and two-qubit states under unitary evolution, and further extended to infinite-dimensional thermal states undergoing non-unitary dynamics. A consistent quasiparticle interpretation of these results was found within the Rindler frame. Notably, while spread complexity adheres to the Lloyd bound, the Krylov-based complexities in this framework differ from holographic expectations derived from CV and CV2.0 conjectures of holographic complexity, primarily due to the subadditivity of Krylov complexity.

In addition, we proposed a new diagnostic—mutual Krylov complexity—as a tool to study correlations in mixed states. This quantity may help distinguish whether a given complexity has a geometric dual, particularly in holographic setups. Looking ahead, these results suggest a number of promising directions. The inequalities for CoPs could be tested in many-body systems, possibly constraining the spread of information as bounded by Lieb–Robinson-type relations [398]. Further work is needed to understand the behaviour of superadditivity and subadditivity in Krylov complexity for holographic field theories, especially in light of existing conjectures relating complexity to geometry.

Together, these studies deepen our understanding of how complexity and localisation interact in non-unitary quantum systems, and they point toward a broader, more flexible framework for analysing quantum dynamics beyond the unitary paradigm. The Krylov basis, with its algebraic structure and interpretive clarity, continues to prove itself a powerful lens through which to study both equilibrium and out-of-equilibrium behaviour in modern quantum theory.

Fermionic and Supercoherent State Complexity, and Perspectives for Holography (Section 4.3)

Lastly, we broadened the Krylov-based spread complexity program to encompass fermionic coherent states, multifermionic systems, superalgebras, and supercoherent states. By mapping the dynamics onto higher-dimensional "Krylov paths" defined by the weight lattice of the pertinent Lie or super-Lie algebras, we demonstrated how canonical $\mathfrak{sl}(2)$ or $\mathfrak{su}(2)$ structures reemerge in the complexity analysis, even though the underlying Hamiltonians are considerably more involved. This allowed for explicit evaluations of spread complexity in settings as diverse as supersymmetric quantum mechanics, supercharges generating oscillatory time evolution, and coherent-state approximations to rotating strings in AdS/CFT.

Our results for single-fermion systems revealed periodic bounded complexities reflecting finite-dimensional Krylov spaces, while multifermion setups yielded richer dynamics driven by cross-coupled fermionic modes. Extending these methods to superstring states, we highlighted how boundedness in the Krylov chain can encode the compactness of the target-space submanifold in $AdS_5 \times S^5$. Future explorations will likely push these ideas further, for example into Lin–Lunin–Maldacena geometries, higher-rank algebras, or anyonic systems with fractional statistics. Such generalisations promise to deepen our grasp of how supersymmetry, topology, and large-N expansions intertwine within the holographic framework.

Outlook and Open Directions

Taken together, these studies underscore the breadth of physical phenomena that can be understood via robust quantum-information diagnostics such as geometric quantum discord, spread complexity, and operator growth analyses. They also highlight the many subtleties that arise when one endeavours to discretise holographic spacetimes, incorporate measurement-induced non-unitarity, or expand coherent-state methods to supersymmetric frameworks. In this final section, we briefly outline several future directions that naturally extend the results obtained here.

Spread Complexity in Extended String Configurations In the semiclassical regime of AdS/CFT, we have thus far focused on rotating string configurations. However, the coherent state–string correspondence applies more broadly to various classical string solutions, including pulsating strings, spiky strings, and giant magnons. Many of these persist under integrable and non-integrable deformations of the target space or the underlying dynamics. Computing spread complexity in these more general settings could offer new insights into the interplay between integrability and chaos in string theory. In particular, comparing transitions observed in Krylov complexity with integrable-to-chaotic crossovers in spin chains models corresponding to higher-loop dilatation operators could shed new light on chaotic string

dynamics using condensed matter models.

Topology and Complexity in LLM Geometries Another direction involves extending the framework of spread complexity to probe the topology of smooth gravitational backgrounds. Lin–Lunin–Maldacena (LLM) geometries, which are semiclassically dual to coherent states in half-BPS sectors of $\mathcal{N} = 4$ SYM, present an especially tractable class of solutions. Here, one may study the evolution of graviton coherent states propagating through different LLM geometries and use the resulting spread complexity to extract topological features of the underlying spacetime. Perturbing a fixed LLM geometry with a localised coherent wavepacket effectively introduces a dynamical time parameter, with respect to which complexity can be defined and studied. This approach could provide a concrete way to relate gravitational topology with observable complexity growth, potentially uncovering new structure in the gravitational phase space.

Measurement-Induced Transitions and Holography Measurement-induced phase transitions (MIPTs), wherein the entanglement properties of a system are drastically altered by the rate and nature of measurements, represent a rich area for future investigation. When the measurement rate exceeds a critical threshold, entanglement transitions from a volume-law to an area-law scaling. In holographic contexts, these transitions have been linked to modifications in quantum teleportation protocols and the emergence of traversable wormholes in the dual geometry. Extending the Krylov-based methods developed here to study MIPTs in both spin-chain and holographic models could shed light on how measurement dynamics manifest in the bulk and whether complexity diagnostics can capture the critical structure of such transitions. Open questions remain regarding how the choice of measurement basis, frequency, and locality affect the dual gravitational interpretation and whether a coherent notion of complexity persists across the transition.

Quantum Ergodic Hierarchy and Algebraic Classification Finally, a longer-term direction concerns the algebraic and geometric classification of quantum chaos using tools from operator algebras and phase space topology. In holographic systems, quantum states tend to exhibit strong ergodicity, suggesting that they may occupy higher rungs of the ergodic hierarchy. One natural question is whether this can be made precise by examining the von Neumann algebras associated with various classes of quantum systems. In lattice models, one might systematically break integrability and track the resulting evolution of observables and ground states, potentially mapping different ergodic regimes to different algebraic structures. Building on earlier work in this thesis, we also propose using the Wigner function to relate classical phase space topology—integrable, pseudo-integrable, or chaotic—with

flow structures in quantum mechanics. Since every smooth foliation of a classical manifold generates a von Neumann algebra, this connection may serve as a unifying language for understanding dynamical complexity across classical and quantum domains.

Taken together, these directions represent a natural continuation of the ideas developed in this dissertation. They also reflect the growing convergence of quantum information, condensed matter, and high-energy theory in addressing foundational questions in quantum dynamics. Whether through novel model-building approaches, gravitational dualities, or algebraic reformulations, the tools of complexity and correlation are likely to remain central to the theoretical landscape in the years ahead.

Bibliography

[1] I. Kant, *Kritik der Urteilskraft*, tredition, 2012.

[2] S. Carnot, *Réflexions sur la puissance motrice du feu et sur les machines propres à développer cette puissance*, *Annales scientifiques de l'École Normale Supérieure* **2e série, 1** (1872) 393–457.

[3] R. Clausius, *Ueber die bewegende kraft der wärme und die gesetze, welche sich daraus für die wärmelehre selbst ableiten lassen*, *Annalen der Physik* **155** (Jan., 1850) 368–397.

[4] W. Thomson, *Xv.—on the dynamical theory of heat, with numerical results deduced from mr joule's equivalent of a thermal unit, and m. regnault's observations on steam*, *Transactions of the Royal Society of Edinburgh* **20** (1853) 261–288.

[5] W. Nernst, *Ueber die berechnung chemischer gleichgewichte aus thermischen messungen*, *Nachrichten von der Gesellschaft der Wissenschaften zu Göttingen, Mathematisch-Physikalische Klasse* **1906** (1906) 1–40.

[6] W. Nernst, *Experimental and Theoretical Applications of Thermodynamics to Chemistry*, Mrs. H.E. Silliman mem. lects, C. Scribner's sons, 1907.

[7] R. Clausius, *Ueber verschiedene für die anwendung bequeme formen der hauptgleichungen der mechanischen wärmetheorie*, *Annalen der Physik* **201** (Jan., 1865) 353–400.

[8] L. Boltzmann, *Weitere Studien über das Wärmegleichgewicht unter Gasmolekülen*, p. 115–225, Vieweg+Teubner Verlag, 1970, 10.1007/978-3-322-84986-1_3.

[9] L. Boltzmann, *Über die beziehung zwischen dem zweiten hauptsatze der mechanischen wärmetheorie und der wahrscheinlichkeitsrechnung resp. den sätzen über das wärmegleichgewicht*, in *Wissenschaftliche Abhandlungen* (F. Hasenöhrl, ed.), Cambridge Library Collection – Physical Sciences, pp. 164–223, Cambridge University Press, Cambridge, 2012.

[10] C. E. Shannon, *A mathematical theory of communication*, *Bell System Technical Journal* **27** (July, 1948) 379–423.

[11] C. E. Shannon and W. Weaver, *The mathematical theory of communication*, University of Illinois Press, Baltimore, MD, Dec., 1949.

[12] T. M. Cover and J. A. Thomas, *Elements of Information Theory*, Wiley, Oct., 2001, 10.1002/0471200611.

[13] D. Huffman, *A method for the construction of minimum-redundancy codes*, *Proceedings of the IRE* **40** (Sept., 1952) 1098–1101.

[14] R. W. Hamming, *Error detecting and error correcting codes*, *Bell System Technical Journal* **29** (Apr., 1950) 147–160.

[15] R. Gallager, *Low-density parity-check codes*, *IEEE Transactions on Information Theory* **8** (Jan., 1962) 21–28.

[16] D. MacKay, *Good error-correcting codes based on very sparse matrices*, *IEEE Transactions on Information Theory* **45** (Mar., 1999) 399–431.

[17] T. Richardson and R. Urbanke, *The capacity of low-density parity-check codes under message-passing decoding*, *IEEE Transactions on Information Theory* **47** (2001) 599–618.

[18] J. G. Proakis, *Digital Communication*, McGraw Hill Higher Education, Maidenhead, England, 4 ed., Aug., 2000.

[19] J. v. Neumann, *Thermodynamik quantenmechanischer gesamtheiten*, *Nachrichten von der Gesellschaft der Wissenschaften zu Göttingen, Mathematisch-Physikalische Klasse* **1927** (1927) 273–291.

[20] J. VonNeumann, *Mathematische Grundlagen der Quantenmechanik*, Springer, 1932.

[21] J. M. Maldacena, *The Large N limit of superconformal field theories and supergravity*, *Adv. Theor. Math. Phys.* **2** (1998) 231–252, [hep-th/9711200].

[22] E. Witten, *Anti-de Sitter space and holography*, *Adv. Theor. Math. Phys.* **2** (1998) 253–291, [hep-th/9802150].

[23] S. S. Gubser, I. R. Klebanov and A. M. Polyakov, *Gauge theory correlators from noncritical string theory*, *Phys. Lett. B* **428** (1998) 105–114, [hep-th/9802109].

[24] G. 't Hooft, *Dimensional reduction in quantum gravity*, *Conf. Proc. C* **930308** (1993) 284–296, [gr-qc/9310026].

[25] L. Susskind, *The World as a hologram*, *J. Math. Phys.* **36** (1995) 6377–6396, [hep-th/9409089].

[26] O. Aharony, S. S. Gubser, J. M. Maldacena, H. Ooguri and Y. Oz, *Large N field theories, string theory and gravity*, *Phys. Rept.* **323** (2000) 183–386, [hep-th/9905111].

[27] R. Bousso, *The Holographic principle*, *Rev. Mod. Phys.* **74** (2002) 825–874, [hep-th/0203101].

[28] J. D. Bekenstein, *Black holes and entropy*, *Phys. Rev. D* **7** (1973) 2333–2346.

[29] S. W. Hawking, *Particle Creation by Black Holes*, *Commun. Math. Phys.* **43** (1975) 199–220.

[30] J. M. Bardeen, B. Carter and S. W. Hawking, *The Four laws of black hole mechanics*, *Commun. Math. Phys.* **31** (1973) 161–170.

[31] A. Strominger and C. Vafa, *Microscopic origin of the Bekenstein-Hawking entropy*, *Phys. Lett. B* **379** (1996) 99–104, [hep-th/9601029].

[32] S. Ryu and T. Takayanagi, *Holographic derivation of entanglement entropy from AdS/CFT*, *Phys. Rev. Lett.* **96** (2006) 181602, [hep-th/0603001].

[33] S. Ryu and T. Takayanagi, *Aspects of Holographic Entanglement Entropy*, *JHEP* **08** (2006) 045, [hep-th/0605073].

[34] D. V. Fursaev, *Proof of the holographic formula for entanglement entropy*, *JHEP* **09** (2006) 018, [hep-th/0606184].

[35] V. E. Hubeny, M. Rangamani and T. Takayanagi, *A Covariant holographic entanglement entropy proposal*, *JHEP* **07** (2007) 062, [0705.0016].

[36] A. Lewkowycz and J. Maldacena, *Generalized gravitational entropy*, *JHEP* **08** (2013) 090, [1304.4926].

[37] T. Faulkner, A. Lewkowycz and J. Maldacena, *Quantum corrections to holographic entanglement entropy*, *JHEP* **11** (2013) 074, [1307.2892].

[38] D. Stanford and L. Susskind, *Complexity and Shock Wave Geometries*, *Phys. Rev. D* **90** (2014) 126007, [1406.2678].

[39] L. Susskind, *Computational Complexity and Black Hole Horizons*, *Fortsch. Phys.* **64** (2016) 24–43, [1403.5695].

[40] L. Susskind, *Entanglement is not enough*, *Fortsch. Phys.* **64** (2016) 49–71, [1411.0690].

[41] A. R. Brown and L. Susskind, *Second law of quantum complexity*, *Phys. Rev. D* **97** (2018) 086015, [1701.01107].

[42] D. Stanford and L. Susskind, *Complexity and shock wave geometries*, *Phys. Rev. D* **90** (2014) 126007, [1406.2678].

[43] L. Susskind and Y. Zhao, *Switchbacks and the bridge to nowhere*, 1408.2823.

[44] A. R. Brown, D. A. Roberts, L. Susskind, B. Swingle and Y. Zhao, *Complexity, action, and black holes*, *Phys. Rev. D* **93** (2016) 086006, [1512.04993].

[45] D. Carmi, S. Chapman, H. Marrochio, R. C. Myers and S. Sugishita, *On the Time Dependence of Holographic Complexity*, *JHEP* **11** (2017) 188, [1709.10184].

[46] L. Susskind, *Three Lectures on Complexity and Black Holes*, SpringerBriefs in Physics, Springer, 10, 2018, 10.1007/978-3-030-45109-7, [1810.11563].

[47] R.-Q. Yang, *Upper bound on cross sections inside black holes and complexity growth rate*, *Phys. Rev. D* **102** (2020) 106001, [1911.12561].

[48] N. Engelhardt and r. Folkestad, *General bounds on holographic complexity*, *JHEP* **01** (2022) 040, [2109.06883].

[49] J. Couch, W. Fischler and P. H. Nguyen, *Noether charge, black hole volume, and complexity*, *JHEP* **03** (2017) 119, [1610.02038].

[50] M. Alishahiha, *Holographic Complexity*, *Phys. Rev. D* **92** (2015) 126009, [1509.06614].

[51] D. Carmi, R. C. Myers and P. Rath, *Comments on Holographic Complexity*, *JHEP* **03** (2017) 118, [1612.00433].

[52] O. Ben-Ami and D. Carmi, *On Volumes of Subregions in Holography and Complexity*, *JHEP* **11** (2016) 129, [1609.02514].

[53] S. Chapman, H. Marrochio and R. C. Myers, *Complexity of Formation in Holography*, *JHEP* **01** (2017) 062, [1610.08063].

[54] D. E. Parker, X. Cao, A. Avdoshkin, T. Scaffidi and E. Altman, *A Universal Operator Growth Hypothesis*, *Phys. Rev. X* **9** (2019) 041017, [1812.08657].

[55] V. Balasubramanian, P. Caputa, J. M. Magan and Q. Wu, *Quantum chaos and the complexity of spread of states*, *Phys. Rev. D* **106** (2022) 046007, [2202.06957].

[56] D. A. Turkington, *Generalized Vectorization, Cross-Products, and Matrix Calculus*, Cambridge University Press, Feb., 2013, 10.1017/cbo9781139424400.

[57] B. N. Parlett, *The Symmetric Eigenvalue Problem*, Society for Industrial and Applied Mathematics, 1998, 10.1137/1.9781611971163, [https://epubs.siam.org/doi/pdf/10.1137/1.9781611971163].

[58] C. Lanczos, *An iteration method for the solution of the eigenvalue problem of linear differential and integral operators*, *J. Res. Natl. Bur. Stand. B* **45** (1950) 255–282.

[59] P. Caputa, H.-S. Jeong, S. Liu, J. F. Pedraza and L.-C. Qu, *Krylov complexity of density matrix operators*, *JHEP* **05** (2024) 337, [2402.09522].

[60] N. Hörnedal, N. Carabba, A. S. Matsoukas-Roubeas and A. del Campo, *Ultimate speed limits to the growth of operator complexity*, *Commun. Phys.* **5** (2022) 207, [2202.05006].

[61] P. Nandy, A. S. Matsoukas-Roubeas, P. Martínez-Azcona, A. Dymarsky and A. del Campo, *Quantum Dynamics in Krylov Space: Methods and Applications*, 5, 2024.

[62] A. Bhattacharya, P. Nandy, P. P. Nath and H. Sahu, *Operator growth and krylov construction in dissipative open quantum systems*, *JHEP* **12** (2022) 081, [2207.05347].

[63] A. Bhattacharya, R. N. Das, B. Dey and J. Erdmenger, *Spread complexity for measurement-induced non-unitary dynamics and Zeno effect*, *JHEP* **03** (2024) 179, [2312.11635].

[64] A. Bhattacharya, R. N. Das, B. Dey and J. Erdmenger, *Spread complexity and localization in $\mathscr{P}\mathscr{T}$-symmetric systems*, 2406.03524.

[65] V. Balasubramanian, R. N. Das, J. Erdmenger and Z.-Y. Xian, *Chaos and integrability in triangular billiards*, 2407.11114.

[66] R. N. Das and T. Mori, *Krylov complexity of purification*, 2408.00826.

[67] R. N. Das, S. Demulder, J. Erdmenger and C. Northe, *Spread complexity for the planar limit of holography*, 2412.09673.

[68] B. Bhattacharjee, X. Cao, P. Nandy and T. Pathak, *Operator growth in open quantum systems: lessons from the dissipative SYK*, *JHEP* **03** (2023) 054, [2212.06180].

[69] A. Bhattacharya, P. Nandy, P. P. Nath and H. Sahu, *On Krylov complexity in open systems: an approach via bi-Lanczos algorithm*, *JHEP* **12** (2023) 066, [2303.04175].

[70] B. Bhattacharjee, P. Nandy and T. Pathak, *Operator dynamics in Lindbladian SYK: a Krylov complexity perspective*, *JHEP* **01** (2024) 094, [2311.00753].

[71] A. Bhattacharya, P. P. Nath and H. Sahu, *Speed limits to the growth of Krylov complexity in open quantum systems*, *Phys. Rev. D* **109** (2024) L121902, [2403.03584].

[72] P. Nandy, T. Pathak and M. Tezuka, *Probing quantum chaos through singular-value correlations in sparse non-Hermitian SYK model*, 2406.11969.

[73] S. Chapman, S. Demulder, D. A. Galante, S. U. Sheorey and O. Shoval, *Krylov complexity and chaos in deformed Sachdev-Ye-Kitaev models*, *Phys. Rev. B* **111** (2025) 035141, [2407.09604].

[74] P. Caputa, B. Chen, R. W. McDonald, J. Simón and B. Strittmatter, *Spread Complexity Rate as Proper Momentum*, 2410.23334.

[75] Z.-Y. Fan, *Momentum-Krylov complexity correspondence*, 2411.04492.

[76] P. Caputa and S. Datta, *Operator growth in 2d cft*, *JHEP* **12** (2021) 188, [2110.10519].

[77] S. S. Haque, J. Murugan, M. Tladi and H. J. R. Van Zyl, *Krylov complexity for jacobi coherent states*, 2212.13758.

[78] D. Patramanis and W. Sybesma, *Krylov complexity in a natural basis for the Schrödinger algebra*, *SciPost Phys. Core* **7** (2024) 037, [2306.03133].

[79] P. Caputa, J. M. Magan and D. Patramanis, *Geometry of krylov complexity*, *Phys. Rev. Res.* **4** (2022) 013041, [2109.03824].

[80] B. Craps, O. Evnin and G. Pascuzzi, *Multiseed Krylov Complexity*, *Phys. Rev. Lett.* **134** (2025) 050402, [2409.15666].

[81] B. Craps, O. Evnin and G. Pascuzzi, *A relation between Krylov and Nielsen complexity*, 2311.18401.

[82] S. Baiguera, V. Balasubramanian, P. Caputa, S. Chapman, J. Haferkamp, M. P. Heller et al., *Quantum complexity in gravity, quantum field theory, and quantum information science*, 2503.10753.

[83] H. A. Camargo, V. Jahnke, H.-S. Jeong, K.-Y. Kim and M. Nishida, *Spectral and Krylov complexity in billiard systems*, *Phys. Rev. D* **109** (2024) 046017, [2306.11632].

[84] K. Hashimoto, K. Murata, N. Tanahashi and R. Watanabe, *Krylov complexity and chaos in quantum mechanics*, *JHEP* **11** (2023) 040, [2305.16669].

[85] E. Rabinovici, A. Sánchez-Garrido, R. Shir and J. Sonner, *Operator complexity: a journey to the edge of Krylov space*, *JHEP* **06** (2021) 062, [2009.01862].

[86] A. Bhattacharya, P. P. Nath and H. Sahu, *Krylov complexity for nonlocal spin chains*, *Phys. Rev. D* **109** (2024) 066010, [2312.11677].

[87] E. Rabinovici, A. Sánchez-Garrido, R. Shir and J. Sonner, *Krylov complexity from integrability to chaos*, *JHEP* **07** (2022) 151, [2207.07701].

[88] F. B. Trigueros and C.-J. Lin, *Krylov complexity of many-body localization: Operator localization in krylov basis*, *SciPost Phys.* **13** (2022) 037, [2112.04722].

[89] K. Cohen, Y. Oz and D.-l. Zhong, *Complexity measure diagnostics of ergodic to many-body localization transition*, *Phys. Rev. B* **110** (2024) L180101, [2404.15940].

[90] M. Ganguli and A. Jana, *State Dependent Spread Complexity Dynamics in Many-Body Localization Transition*, 2409.02186.

[91] E. Rabinovici, A. Sánchez-Garrido, R. Shir and J. Sonner, *Krylov localization and suppression of complexity*, *JHEP* **03** (2022) 211, [2112.12128].

[92] P. Caputa and S. Liu, *Quantum complexity and topological phases of matter*, *Phys. Rev. B* **106** (2022) 195125, [2205.05688].

[93] P. Caputa, N. Gupta, S. S. Haque, S. Liu, J. Murugan and H. J. R. Van Zyl, *Spread complexity and topological transitions in the kitaev chain*, *JHEP* **01** (2023) 120, [2208.06311].

[94] E. Rabinovici, A. Sánchez-Garrido, R. Shir and J. Sonner, *A bulk manifestation of Krylov complexity*, *JHEP* **08** (2023) 213, [2305.04355].

[95] M. Ambrosini, E. Rabinovici, A. Sánchez-Garrido, R. Shir and J. Sonner, *Operator K-complexity in DSSYK: Krylov complexity equals bulk length*, 2412.15318.

[96] M. P. Heller, J. Papalini and T. Schuhmann, *Krylov spread complexity as holographic complexity beyond JT gravity*, 2412.17785.

[97] P. Caputa and G. Di Giulio, *Local Quenches from a Krylov Perspective*, 2502.19485.

[98] P.-Z. He, *Revisit the relationship between spread complexity rate and radial momentum*, 2411.19172.

[99] P. Basteiro, R. N. Das, G. Di Giulio and J. Erdmenger, *Aperiodic spin chains at the boundary of hyperbolic tilings*, *SciPost Phys.* **15** (2023) 218, [2212.11292].

[100] S. Banerjee, P. Basteiro, R. N. Das and M. Dorband, *Geometric quantum discord signals non-factorization*, *JHEP* **08** (2023) 104, [2305.04952].

[101] J. Martín García, *Quantum Complexity and Holography*. PhD thesis, U. Autonoma, Madrid (main), 2020. 2209.04632.

[102] N. Beisert et al., *Review of AdS/CFT Integrability: An Overview*, *Lett. Math. Phys.* **99** (2012) 3–32, [1012.3982].

[103] G. Arutyunov and S. Frolov, *Foundations of the $AdS_5 \times S^5$ Superstring. Part I*, *J. Phys. A* **42** (2009) 254003, [0901.4937].

[104] N. Beisert, *The su(2|3) dynamic spin chain*, *Nucl. Phys. B* **682** (2004) 487–520, [hep-th/0310252].

[105] M. Staudacher, *The Factorized S-matrix of CFT/AdS*, *JHEP* **05** (2005) 054, [hep-th/0412188].

[106] B. Stefanski, Jr. and A. A. Tseytlin, *Large spin limits of AdS/CFT and generalized Landau-Lifshitz equations*, *JHEP* **05** (2004) 042, [hep-th/0404133].

[107] J. A. Minahan and K. Zarembo, *The Bethe ansatz for N=4 superYang-Mills*, *JHEP* **03** (2003) 013, [hep-th/0212208].

[108] M. Kruczenski, *Spin chains and string theory*, *Phys. Rev. Lett.* **93** (2004) 161602, [hep-th/0311203].

[109] E. Schrodinger, *Die gegenwartige Situation in der Quantenmechanik*, *Naturwiss.* **23** (1935) 807–812.

[110] A. Einstein, B. Podolsky and N. Rosen, *Can quantum mechanical description of physical reality be considered complete?*, *Phys. Rev.* **47** (1935) 777–780.

[111] J. S. Bell, *On the Problem of Hidden Variables in Quantum Mechanics*, *Rev. Mod. Phys.* **38** (1966) 447–452.

[112] M. A. Nielsen and I. L. Chuang, *Quantum Computation and Quantum Information*, Cambridge University Press, 6, 2012, 10.1017/cbo9780511976667.

[113] A. Kitaev and J. Preskill, *Topological entanglement entropy*, *Phys. Rev. Lett.* **96** (2006) 110404, [hep-th/0510092].

[114] B. Swingle, *Entanglement Renormalization and Holography*, *Phys. Rev. D* **86** (2012) 065007, [0905.1317].

[115] M. Van Raamsdonk, *Comments on quantum gravity and entanglement*, 0907.2939.

[116] M. Van Raamsdonk, *Building up spacetime with quantum entanglement*, *Gen. Rel. Grav.* **42** (2010) 2323–2329, [1005.3035].

[117] J. Maldacena and L. Susskind, *Cool horizons for entangled black holes*, *Fortsch. Phys.* **61** (2013) 781–811, [1306.0533].

[118] P. Basteiro, *Discrete Holography: Through the Quantum Information Looking-Glass*. PhD thesis, Wurzburg U., 2024. 10.25972/OPUS-37565.

[119] W. Zurek, *Einselection and decoherence from an information theory perspective*, *Annalen der Physik* **512** (Nov., 2000) 855–864.

[120] H. Ollivier and W. H. Zurek, *Quantum discord: A measure of the quantumness of correlations*, *Physical Review Letters* **88** (Dec., 2001) .

[121] L. Henderson and V. Vedral, *Classical, quantum and total correlations*, *Journal of Physics A: Mathematical and General* **34** (Aug., 2001) 6899–6905.

[122] R. Horodecki, P. Horodecki, M. Horodecki and K. Horodecki, *Quantum entanglement*, *Rev. Mod. Phys.* **81** (2009) 865–942, [quant-ph/0702225].

[123] G. Adesso, T. R. Bromley and M. Cianciaruso, *Measures and applications of quantum correlations*, *J. Phys. A* **49** (2016) 473001, [1605.00806].

[124] K. Modi, A. Brodutch, H. Cable, T. Paterek and V. Vedral, *The classical-quantum boundary for correlations: Discord and related measures*, *Rev. Mod. Phys.* **84** (2012) 1655.

[125] C. E. Shannon, *A mathematical theory of communication*, *Bell Syst. Tech. J.* **27** (1948) 379–423.

[126] C. Lanczos, *An iteration method for the solution of the eigenvalue problem of linear differential and integral operators*, *Journal of Research of the National Bureau of Standards* **45** (1950) 255–282.

[127] V. Viswanath, G. Muller and G. Mueller, *The recursion method (lecture notes in physics monographs)*, .

[128] J. Liesen and Z. Strakos, *Krylov Subspace Methods: Principles and Analysis*, Oxford University Press, 10, 2012, 10.1093/acprof:oso/9780199655410.001.0001.

[129] L. D'Alessio, Y. Kafri, A. Polkovnikov and M. Rigol, *From quantum chaos and eigenstate thermalization to statistical mechanics and thermodynamics*, *Adv. Phys.* **65** (2016) 239–362, [1509.06411].

[130] T. Mori, T. N. Ikeda, E. Kaminishi and M. Ueda, *Thermalization and prethermalization in isolated quantum systems: a theoretical overview*, *Journal of Physics B: Atomic, Molecular and Optical Physics* **51** (May, 2018) 112001.

[131] F. Haake, *Quantum Signatures of Chaos*, Springer Series in Synergetics, Springer, Berlin, 2010, 10.1007/978-3-642-05428-0.

[132] H. Mori, *A continued-fraction representation of the time-correlation functions*, *Progress of Theoretical Physics* **34** (1965) 399–416.

[133] F. Cyrot-Lackmann, *On the electronic structure of liquid transitional metals*, *Advances in Physics* **16** (1967) 393–400.

[134] R. Haydock, *The recursive solution of the schrodinger equation*, in *Solid state physics*, vol. 35, pp. 215–294, Elsevier, 1980.

[135] D. E. Parker, X. Cao, A. Avdoshkin, T. Scaffidi and E. Altman, *A universal operator growth hypothesis*, *Phys. Rev. X* **9** (2019) 041017, [1812.08657].

[136] J. Erdmenger, S.-K. Jian and Z.-Y. Xian, *Universal chaotic dynamics from Krylov space*, *JHEP* **08** (2023) 176, [2303.12151].

[137] M. Headrick, *Entanglement Renyi entropies in holographic theories*, *Phys. Rev. D* **82** (2010) 126010, [1006.0047].

[138] D. D. Blanco, H. Casini, L.-Y. Hung and R. C. Myers, *Relative Entropy and Holography*, *JHEP* **08** (2013) 060, [1305.3182].

[139] T. Hartman, *Entanglement Entropy at Large Central Charge*, (3, 2013) , [1303.6955].

[140] T. Faulkner, *The Entanglement Renyi Entropies of Disjoint Intervals in AdS/CFT*, (3, 2013) , [1303.7221].

[141] A. J. Kollár, M. Fitzpatrick and A. A. Houck, *Hyperbolic lattices in circuit quantum electrodynamics*, *Nature* **571** (Jul, 2019) 45–50.

[142] P. M. Lenggenhager, A. Stegmaier, L. K. Upreti, T. Hofmann, T. Helbig, A. Vollhardt et al., *Simulating hyperbolic space on a circuit board*, *Nature Communications* **13** (July, 2022) .

[143] A. Chen, H. Brand, T. Helbig, T. Hofmann, S. Imhof, A. Fritzsche et al., *Hyperbolic matter in electrical circuits with tunable complex phases*, 2022. 10.48550/ARXIV.2205.05106.

[144] G. Policastro, D. T. Son and A. O. Starinets, *The Shear viscosity of strongly coupled N=4 supersymmetric Yang-Mills plasma*, *Phys. Rev. Lett.* **87** (2001) 081601, [hep-th/0104066].

[145] P. Kovtun, D. T. Son and A. O. Starinets, *Holography and hydrodynamics: Diffusion on stretched horizons*, *JHEP* **10** (2003) 064, [hep-th/0309213].

[146] P. Kovtun, D. T. Son and A. O. Starinets, *Viscosity in strongly interacting quantum field theories from black hole physics*, *Phys. Rev. Lett.* **94** (2005) 111601, [hep-th/0405231].

[147] U. W. Heinz and M. Jacob, *Evidence for a new state of matter: An Assessment of the results from the CERN lead beam program*, nucl-th/0002042.

[148] M. Axenides, E. G. Floratos and S. Nicolis, *Modular discretization of the AdS_2/CFT_1 holography*, *JHEP* **02** (2014) 109, [1306.5670].

[149] M. Axenides, E. Floratos and S. Nicolis, *The arithmetic geometry of AdS_2 and its continuum limit*, *SIGMA* **17** (2021) 004, [1908.06641].

[150] M. Axenides, E. Floratos and S. Nicolis, *The continuum limit of the modular discretization of AdS_2*, in *21st Hellenic School and Workshops on Elementary Particle Physics and Gravity*, 5, 2022, [2205.03637].

[151] M. Asaduzzaman, S. Catterall, J. Hubisz, R. Nelson and J. Unmuth-Yockey, *Holography on tessellations of hyperbolic space*, *Phys. Rev. D* **102** (Aug, 2020) 034511.

[152] R. C. Brower, C. V. Cogburn, A. L. Fitzpatrick, D. Howarth and C.-I. Tan, *Lattice setup for quantum field theory in* ads_2, *Phys. Rev. D* **103** (May, 2021) 094507.

[153] M. Asaduzzaman, S. Catterall, J. Hubisz, R. Nelson and J. Unmuth-Yockey, "Holography for Ising spins on the hyperbolic plane." 11, 2021.

[154] R. C. Brower, C. V. Cogburn and E. Owen, "Hyperbolic Lattice for Scalar Field Theory in AdS_3." 2, 2022.

[155] E. Gesteau, M. Marcolli and S. Parikh, "Holographic tensor networks from hyperbolic buildings." 2, 2022.

[156] P. Basteiro, F. Dusel, J. Erdmenger, D. Herdt, H. Hinrichsen, R. Meyer et al., *Breitenlohner-Freedman bound on hyperbolic tilings*, (5, 2022) , [2205.05081].

[157] P. Basteiro, G. Di Giulio, J. Erdmenger, J. Karl, R. Meyer and Z.-Y. Xian, *Towards Explicit Discrete Holography: Aperiodic Spin Chains from Hyperbolic Tilings*, *SciPost Phys.* **13** (2022) 103, [2205.05693].

[158] H. Yan, *Hyperbolic fracton model, subsystem symmetry, and holography*, *Phys. Rev. B* **99** (2019) 155126, [1807.05942].

[159] H. Yan, *Hyperbolic Fracton Model, Subsystem Symmetry, and Holography II: The Dual Eight-Vertex Model*, *Phys. Rev. B* **100** (2019) 245138, [1906.02305].

[160] W. Magnus, *Noneuclidean Tesselations and Their Groups*, Academic Press, Amsterdam, Boston, 1 ed., 1974.

[161] H. S. M. Coxeter and W. O. J. Moser, *Generators and Relations for Discrete Groups*, Springer Berlin Heidelberg, 1980, 10.1007/978-3-662-21943-0.

[162] H. S. M. Coxeter, *The trigonometry of hyperbolic tessellations*, *Canadian Mathematical Bulletin* **40** (1997) 158–168.

[163] L. Boyle, M. Dickens and F. Flicker, *Conformal Quasicrystals and Holography*, *Phys. Rev. X* **10** (2020) 011009, [1805.02665].

[164] S.-k. Ma, C. Dasgupta and C.-k. Hu, *Random Antiferromagnetic Chain*, *Phys. Rev. Lett.* **43** (1979) 1434–1437.

[165] C. Dasgupta and S.-k. Ma, *Low-temperature properties of the random Heisenberg antiferromagnetic chain*, *Phys. Rev. B* **22** (1980) 1305–1319.

[166] C. Holzhey, F. Larsen and F. Wilczek, *Geometric and renormalized entropy in conformal field theory*, *Nucl. Phys. B* **424** (1994) 443–467, [hep-th/9403108].

[167] G. Vidal, J. I. Latorre, E. Rico and A. Kitaev, *Entanglement in quantum critical phenomena*, *Phys. Rev. Lett.* **90** (2003) 227902, [quant-ph/0211074].

[168] A. Jahn, Z. Zimborás and J. Eisert, *Central charges of aperiodic holographic tensor network models*, *Phys. Rev. A* **102** (2020) 042407, [1911.03485].

[169] W. Zhang, H. Yuan, N. Sun, H. Sun and X. Zhang, *Observation of novel topological states in hyperbolic lattices*, *Nature Communications* **13** (May, 2022) .

[170] J. Maciejko and S. Rayan, *Hyperbolic band theory*, *Sci. Adv.* **7** (2021) abe9170, [2008.05489].

[171] J. Maciejko and S. Rayan, *Automorphic Bloch theorems for hyperbolic lattices*, *Proc. Nat. Acad. Sci.* **119** (2022) e2116869119, [2108.09314].

[172] T. Bzdušek and J. Maciejko, *Flat bands and band-touching from real-space topology in hyperbolic lattices*, *Phys. Rev. B* **106** (2022) 155146, [2205.11571].

[173] I. Boettcher, A. V. Gorshkov, A. J. Kollár, J. Maciejko, S. Rayan and R. Thomale, *Crystallography of hyperbolic lattices*, *Phys. Rev. B* **105** (2022) 125118, [2105.01087].

[174] N. Cheng, F. Serafin, J. McInerney, Z. Rocklin, K. Sun and X. Mao, *Band theory and boundary modes of high-dimensional representations of infinite hyperbolic lattices*, *Phys. Rev. Lett.* **129** (Aug, 2022) 088002.

[175] F. D. M. Haldane, *Continuum dynamics of the 1-D Heisenberg antiferromagnetic identification with the O(3) nonlinear sigma model*, *Phys. Lett. A* **93** (1983) 464–468.

[176] F. D. M. Haldane, *Nonlinear field theory of large spin Heisenberg antiferromagnets. Semiclassically quantized solitons of the one-dimensional easy Axis Neel state*, *Phys. Rev. Lett.* **50** (1983) 1153–1156.

[177] J. Erdmenger, C. Hoyos, A. O'Bannon and J. Wu, *A Holographic Model of the Kondo Effect*, *JHEP* **12** (2013) 086, [1310.3271].

[178] J. Erdmenger, M. Flory, C. Hoyos, M.-N. Newrzella, A. O'Bannon and J. Wu, *Holographic impurities and Kondo effect*, *Fortsch. Phys.* **64** (2016) 322–329, [1511.09362].

[179] J. Erdmenger, *Holographic Kondo Models*, *Springer Proc. Phys.* **239** (2020) 155–194.

[180] M. Ammon and J. Erdmenger, *Gauge/gravity duality: Foundations and applications*, Cambridge University Press, Cambridge, 4, 2015.

[181] S. Sachdev and J. Ye, *Gapless spin-fluid ground state in a random quantum heisenberg magnet*, *Phys. Rev. Lett.* **70** (May, 1993) 3339–3342.

[182] A. Kitaev, *A simple model of quantum holography*, Talks at KITP, April 7, 2015 and May 27, 2015.

[183] S. Sachdev, *Bekenstein-Hawking Entropy and Strange Metals*, *Phys. Rev. X* **5** (2015) 041025, [1506.05111].

[184] A. P. Vieira, *Aperiodic quantum XXZ chains: Renormalization-group results*, *Phys. Rev. B* **71** (Apr, 2005) 134408.

[185] P. Calabrese, J. Cardy and E. Tonni, *Entanglement entropy of two disjoint intervals in conformal field theory*, *J. Stat. Mech.* **0911** (2009) P11001, [0905.2069].

[186] H. S. M. Coxeter and W. O. J. Moser, *Generators and Relations for Discrete Groups*, Springer Berlin Heidelberg, 1957, 10.1007/978-3-662-25739-5.

[187] A. L. Edmonds, J. H. Ewing and R. S. Kulkarni, *Torsion free subgroups of fuchsian groups and tessellations of surfaces*, *Inventiones Mathematicae* **69** (Oct., 1982) 331–346.

[188] S. Katok, *Fuchsian Groups*, Chicago Lectures in Mathematics, University of Chicago Press, 1992.

[189] F. Sausset and G. Tarjus, *Periodic boundary conditions on the pseudosphere*, *Journal of Physics A: Mathematical and Theoretical* **40** (oct, 2007) 12873.

[190] E. Kienzle and S. Rayan, *Hyperbolic band theory through Higgs bundles*, *Adv. Math.* **409** (2022) 108664, [2201.12689].

[191] K. Ikeda, S. Aoki and Y. Matsuki, *Hyperbolic band theory under magnetic field and Dirac cones on a higher genus surface*, *J. Phys. Condens. Matter* **33** (2021) 485602, [2104.13314].

[192] A. Attar and I. Boettcher, *Selberg trace formula in hyperbolic band theory*, *Phys. Rev. E* **106** (2022) 034114, [2201.06587].

[193] G. Shankar and J. Maciejko, *Hyperbolic Lattices and Two-Dimensional Yang-Mills Theory*, *Phys. Rev. Lett.* **133** (2024) 146601, [2309.03857].

[194] H. S. M. Coxeter, *Regular honeycombs in hyperbolic space*, 1956.

[195] N. L. Balazs and A. Voros, *Chaos on the pseudosphere*, *Phys. Rept.* **143** (1986) 109–240.

[196] N. I. Lobachevskii, *Geometrische Untersuchungen zur Theorie der Parallellinien*, Mayer & Mueller, 1887, 10.5479/sil.344583.39088005689559.

[197] R. Greene and S. Krantz, *Function Theory of One Complex Variable*, Graduate studies in mathematics, American Mathematical Society, 2002.

[198] S. G. Krantz, *Handbook of Complex Variables*, Birkhäuser Boston, 1999, 10.1007/978-1-4612-1588-2.

[199] R. Keown, *An Introduction to Group Representation Theory*, Academic Press, 1975.

[200] D. Dummit and R. Foote, *Abstract algebra*, John Wiley & Sons, 2004.

[201] R. Juhász and Z. Zimborás, *Entanglement entropy in aperiodic singlet phases*, *J. Stat. Mech* **2007** (2007) P04004–P04004, [cond-mat/0703527].

[202] F. Iglói, R. Juhász and Z. Zimborás, *Entanglement entropy of aperiodic quantum spin chains*, *EPL* **79** (2007) 37001, [cond-mat/0701527].

[203] A. P. Vieira, *Low-Energy Properties of Aperiodic Quantum Spin Chains*, *Phys. Rev. Lett.* **94** (2005) 077201, [cond-mat/0403635].

[204] K. Hida, *New Universality Class in Spin-One-Half Fibonacci Heisenberg Chains*, *Phys. Rev. Lett.* **93** (2004) 037205, [cond-mat/0403602].

[205] J. Hermisson, *Aperiodic and correlated disorder in XY chains: exact results*, *J. Phys. A* **33** (1999) 57–59, [cond-mat/9808238].

[206] G. Refael and J. E. Moore, *Entanglement Entropy of Random Quantum Critical Points in One Dimension*, *Phys. Rev. Lett.* **93** (2004) 260602, [cond-mat/0406737].

[207] P. Calabrese and J. L. Cardy, *Entanglement entropy and quantum field theory*, *J. Stat. Mech.* **0406** (2004) P06002, [hep-th/0405152].

[208] V. Balasubramanian and S. F. Ross, *Holographic particle detection*, *Phys. Rev. D* **61** (2000) 044007, [hep-th/9906226].

[209] J. Erdmenger and N. Miekley, *Non-local observables at finite temperature in AdS/CFT*, *JHEP* **03** (2018) 034, [1709.07016].

[210] P. Ruggiero, V. Alba and P. Calabrese, *Entanglement negativity in random spin chains*, *Phys. Rev. B* **94** (Jul, 2016) 035152.

[211] G. Refael and J. E. Moore, *Entanglement entropy of random quantum critical points in one dimension*, *Phys. Rev. Lett.* **93** (Dec, 2004) 260602.

[212] H. Casini, C. D. Fosco and M. Huerta, *Entanglement and alpha entropies for a massive Dirac field in two dimensions*, *J. Stat. Mech.* **0507** (2005) P07007, [cond-mat/0505563].

[213] S. Furukawa, V. Pasquier and J. Shiraishi, *Mutual Information and Compactification Radius in a c=1 Critical Phase in One Dimension*, *Phys. Rev. Lett.* **102** (2009) 170602, [0809.5113].

[214] M. Caraglio and F. Gliozzi, *Entanglement Entropy and Twist Fields*, *JHEP* **11** (2008) 076, [0808.4094].

[215] V. L. Quito, P. L. S. Lopes, J. A. Hoyos and E. Miranda, *Highly symmetric random one-dimensional spin models*, *Phys. Rev. B* **100** (Dec, 2019) 224407.

[216] H. Georgi, *Lie Algebras In Particle Physics: from Isospin To Unified Theories*, Frontiers in Physics, Taylor and Francis, 1999.

[217] H.-H. Tu, G.-M. Zhang and T. Xiang, *Class of exactly solvable $so(n)$ symmetric spin chains with matrix product ground states*, *Phys. Rev. B* **78** (Sep, 2008) 094404.

[218] P. Hayden, S. Nezami, X.-L. Qi, N. Thomas, M. Walter and Z. Yang, *Holographic duality from random tensor networks*, *JHEP* **11** (2016) 009, [1601.01694].

[219] D. Ben-Zion and J. McGreevy, *Strange metal from local quantum chaos*, *Phys. Rev. B* **97** (2018) 155117, [1711.02686].

[220] J. Maldacena and D. Stanford, *Remarks on the Sachdev-Ye-Kitaev model*, *Phys. Rev. D* **94** (2016) 106002, [1604.07818].

[221] J. Polchinski and V. Rosenhaus, *The Spectrum in the Sachdev-Ye-Kitaev Model*, *JHEP* **04** (2016) 001, [1601.06768].

[222] R. Jackiw, *Lower dimensional gravity*, *Nuclear Physics B* **252** (1985) 343–356.

[223] C. Teitelboim, *Gravitation and hamiltonian structure in two spacetime dimensions*, *Physics Letters B* **126** (1983) 41–45.

[224] S. S. Gubser, M. Heydeman, C. Jepsen, M. Marcolli, S. Parikh, I. Saberi et al., *Edge length dynamics on graphs with applications to p-adic AdS/CFT*, *JHEP* **06** (2017) 157, [1612.09580].

[225] S. S. Gubser, J. Knaute, S. Parikh, A. Samberg and P. Witaszczyk, *p-adic AdS/CFT*, *Commun. Math. Phys.* **352** (2017) 1019–1059, [1605.01061].

[226] M. Heydeman, M. Marcolli, I. Saberi and B. Stoica, *Tensor networks, p-adic fields, and algebraic curves: arithmetic and the AdS_3/CFT_2 correspondence*, *Adv. Theor. Math. Phys.* **22** (2018) 93–176, [1605.07639].

[227] M. Heydeman, M. Marcolli, S. Parikh and I. Saberi, *Nonarchimedean holographic entropy from networks of perfect tensors*, *Adv. Theor. Math. Phys.* **25** (2021) 591–721, [1812.04057].

[228] L.-Y. Hung, W. Li and C. M. Melby-Thompson, *p-adic CFT is a holographic tensor network*, *JHEP* **04** (2019) 170, [1902.01411].

[229] L. Susskind and E. Witten, *The Holographic bound in anti-de Sitter space*, hep-th/9805114.

[230] J. M. Maldacena, *Eternal black holes in anti-de Sitter*, *JHEP* **04** (2003) 021, [hep-th/0106112].

[231] E. Verlinde and H. Verlinde, *A Conversation on ER = EPR*, 2212.09389.

[232] H. Verlinde, *ER = EPR revisited: On the Entropy of an Einstein-Rosen Bridge*, 2003.13117.

[233] W. Zurek, *Einselection and decoherence from an information theory perspective*, *Annalen der Physik* **9** (2000) 855–864.

[234] H. Ollivier and W. H. Zurek, *Quantum discord: A measure of the quantumness of correlations*, *Phys. Rev. Lett.* **88** (Dec, 2001) 017901.

[235] L. Henderson and V. Vedral, *Classical, quantum and total correlations*, *Journal of physics A: mathematical and general* **34** (2001) 6899.

[236] J. Dajka, M. Mierzejewski, J. Luczka, R. Blattmann and P. Hänggi, *Negativity and quantum discord in davies environments*, *Journal of Physics A: Mathematical and Theoretical* **45** (nov, 2012) 485306.

[237] M. Poxleitner and H. Hinrichsen, *Gaussian continuous-variable isotropic state*, *Phys. Rev. A* **104** (Sep, 2021) 032423.

[238] Y. Huang, *Computing quantum discord is NP-complete*, *New Journal of Physics* **16** (mar, 2014) 033027.

[239] B. Dakić, V. Vedral and Č. Brukner, *Necessary and sufficient condition for nonzero quantum discord*, *Physical Review Letters* **105** (nov, 2010) .

[240] A. Bera, T. Das, D. Sadhukhan, S. S. Roy, A. Sen(De) and U. Sen, *Quantum discord and its allies: a review of recent progress*, *Reports on Progress in Physics* **81** (dec, 2017) 024001.

[241] D. Girolami and G. Adesso, *Interplay between computable measures of entanglement and other quantum correlations*, *Phys. Rev. A* **84** (Nov, 2011) 052110.

[242] W.-z. Guo, *Correlations in geometric states*, *JHEP* **08** (2020) 125, [2003.03933].

[243] H. Verlinde, *Wormholes in Quantum Mechanics*, 2105.02129.

[244] S. Antonini, B. Grado-White, S.-K. Jian and B. Swingle, *Holographic measurement and quantum teleportation in the SYK thermofield double*, *JHEP* **02** (2023) 095, [2211.07658].

[245] S. Antonini, B. Grado-White, S.-K. Jian and B. Swingle, *Holographic measurement in CFT thermofield doubles*, 2304.06743.

[246] K. Papadodimas and S. Raju, *Remarks on the necessity and implications of state-dependence in the black hole interior*, *Phys. Rev. D* **93** (2016) 084049, [1503.08825].

[247] H. Verlinde, *Deconstructing the Wormhole: Factorization, Entanglement and Decoherence*, 2105.02142.

[248] S. Banerjee, J.-W. Bryan, K. Papadodimas and S. Raju, *A toy model of black hole complementarity*, *JHEP* **05** (2016) 004, [1603.02812].

[249] X. Dong, *The Gravity Dual of Renyi Entropy*, *Nature Commun.* **7** (2016) 12472, [1601.06788].

[250] V. Balasubramanian, A. Lawrence, J. M. Magan and M. Sasieta, *Microscopic origin of the entropy of black holes in general relativity*, 2212.02447.

[251] V. Balasubramanian, A. Lawrence, J. M. Magan and M. Sasieta, *Microscopic origin of the entropy of astrophysical black holes*, 2212.08623.

[252] J. Chakravarty, *Overcounting of interior excitations: A resolution to the bags of gold paradox in AdS*, *JHEP* **02** (2021) 027, [2010.03575].

[253] B. Freivogel, D. Nikolakopoulou and A. F. Rotundo, *Wormholes from Averaging over States*, *SciPost Phys.* **14** (2023) 026, [2105.12771].

[254] K. Goto, Y. Kusuki, K. Tamaoka and T. Ugajin, *Product of random states and spatial (half-)wormholes*, *JHEP* **10** (2021) 205, [2108.08308].

[255] P. Chaturvedi, V. Malvimat and G. Sengupta, *Holographic Quantum Entanglement Negativity*, *JHEP* **05** (2018) 172, [1609.06609].

[256] O. Bohigas, M. J. Giannoni and C. Schmit, *Characterization of chaotic quantum spectra and universality of level fluctuation laws*, *Phys. Rev. Lett.* **52** (1984) 1–4.

[257] M. V. Berry, *Semiclassical theory of spectral rigidity*, *Proceedings of the Royal Society of London. A. Mathematical and Physical Sciences* **400** (1985) 229–251.

[258] S. Muller, S. Heusler, P. Braun, F. Haake and A. Altland, *Semiclassical foundation of universality in quantum chaos*, *Phys. Rev. Lett.* **93** (2004) 014103, [nlin/0401021].

[259] F. J. Dyson, *Statistical theory of the energy levels of complex systems. iii*, *Journal of Mathematical Physics* **3** (1962) 166–175.

[260] M. L. Mehta, *Random matrices*, Elsevier, 2004.

[261] F. Haake, *Quantum Signatures of Chaos*, Springer Berlin Heidelberg, 2010, 10.1007/978-3-642-05428-0.

[262] F. J. Dyson, *A class of matrix ensembles*, *Journal of Mathematical Physics* **13** (Jan., 1972) 90–97.

[263] T. Guhr, A. Muller-Groeling and H. A. Weidenmuller, *Random matrix theories in quantum physics: Common concepts*, *Phys. Rept.* **299** (1998) 189–425, [cond-mat/9707301].

[264] v. Lozej, G. Casati and T. Prosen, *Quantum chaos in triangular billiards*, *Phys. Rev. Res.* **4** (2022) 013138, [2110.04168].

[265] Y. Alhassid and N. Whelan, *Onset of chaos and its signature in the spectral autocorrelation function*, *Physical Review Letters* **70** (Feb., 1993) 572–575.

[266] E. Dyer and G. Gur-Ari, *2D CFT Partition Functions at Late Times*, *JHEP* **08** (2017) 075, [1611.04592].

[267] J. Maldacena, S. H. Shenker and D. Stanford, *A bound on chaos*, *JHEP* **08** (2016) 106, [1503.01409].

[268] I. García-Mata, R. Jalabert and D. Wisniacki, *Out-of-time-order correlations and quantum chaos*, *Scholarpedia* **18** (2023) 55237.

[269] A. Grabarits, K. R. Swain, M. S. Heydari, P. Chandarana, F. J. Gómez-Ruiz and A. del Campo, *Quantum Chaos in Random Ising Networks*, 2405.14376.

[270] E. J. Torres-Herrera, A. M. García-García and L. F. Santos, *Generic dynamical features of quenched interacting quantum systems: Survival probability, density imbalance, and out-of-time-ordered correlator*, *Physical Review B* **97** (Feb., 2018) , [1704.06272].

[271] E. Torres-Herrera, J. Karp, M. Távora and L. Santos, *Realistic many-body quantum systems vs. full random matrices: Static and dynamical properties*, *Entropy* **18** (Oct., 2016) 359, [1608.06636].

[272] R. N. Das, S. Dutta and A. Maji, *Late time dynamics in SUSY saddle-dominated scrambling through higher-point OTOC*, *Phys. Scripta* **99** (2024) 085246, [2010.07089].

[273] P. Richens and M. Berry, *Pseudointegrable systems in classical and quantum mechanics*, *Physica D: Nonlinear Phenomena* **2** (1981) 495–512.

[274] S. R. Jain and R. Samajdar, *Nodal portraits of quantum billiards: Domains, lines, and statistics*, *Reviews of Modern Physics* **89** (Dec., 2017) .

[275] R. Frigg, J. Berkovitz and F. Kronz, *The Ergodic Hierarchy*, in *The Stanford Encyclopedia of Philosophy* (E. N. Zalta, ed.), Metaphysics Research Lab, Stanford University, Fall 2020 ed., 2020.

[276] E. Ott, *Chaos in Dynamical Systems*, Cambridge University Press, Aug., 2002, 10.1017/cbo9780511803260.

[277] A. Vikram and V. Galitski, *Dynamical quantum ergodicity from energy level statistics*, *Phys. Rev. Res.* **5** (Aug, 2023) 033126.

[278] N. Jha and S. R. Jain, *Quantum mechanics of a rotating billiard*, in *Proceedings of the 12th Asia Pacific Physics Conference (APPC12)*, Journal of the Physical Society of Japan, Mar., 2014, 10.7566/jpscp.1.013116.

[279] S. R. Jain, *Proliferation law of periodic orbits of an integrable billiard as obtained from the eigenvalue spectrum*, *Phys. Rev. E* **50** (Sep, 1994) 2355–2356.

[280] R. Samajdar and S. R. Jain, *A nodal domain theorem for integrable billiards in two dimensions*, *Annals of Physics* **351** (Dec., 2014) 1–12.

[281] R. Samajdar and S. R. Jain, *Exact eigenfunction amplitude distributions of integrable quantum billiards*, *Journal of Mathematical Physics* **59** (Jan., 2018) .

[282] H. D. Parab and S. R. Jain, *Non-universal spectral rigidity of quantum pseudo-integrable billiards*, *Journal of Physics A: Mathematical and General* **29** (jul, 1996) 3903.

[283] D. Biswas and S. R. Jain, *Quantum description of a pseudointegrable system: The $\pi/3$-rhombus billiard*, *Phys. Rev. A* **42** (Sep, 1990) 3170–3185.

[284] S. Moudgalya, S. Chandra and S. R. Jain, *A finite-time exponent for random ehrenfest gas*, *Annals of Physics* **361** (2015) 82–90.

[285] R. B. d. Carmo and T. A. Lima, *Mixing property of symmetrical polygonal billiards*, *Phys. Rev. E* **109** (Jan, 2024) 014224.

[286] J. Chaika and G. Forni, *Weakly mixing polygonal billiards*, 2003.00890.

[287] S. Kerckhoff, H. Masur and J. Smillie, *Ergodicity of billiard flows and quadratic differentials*, *The Annals of Mathematics* **124** (Sept., 1986) 293.

[288] N. Chernov and S. Troubetzkoy, *Ergodicity of billiards in polygons with pockets*, *Nonlinearity* **11** (jul, 1998) 1095.

[289] C. Lozej and E. Bogomolny, *Intermediate spectral statistics of rational triangular quantum billiards*, 2405.05783.

[290] J. Wilkie and P. Brumer, *Time-dependent manifestations of quantum chaos*, *Physical Review Letters* **67** (Sept., 1991) 1185–1188.

[291] L. V. Iliesiu, M. Mezei and G. Sárosi, *The volume of the black hole interior at late times*, *JHEP* **07** (2022) 073, [2107.06286].

[292] H. A. Camargo, V. Jahnke, H.-S. Jeong, K.-Y. Kim and M. Nishida, *Spectral and Krylov complexity in billiard systems*, *Phys. Rev. D* **109** (2024) 046017, [2306.11632].

[293] Y. Sekino and L. Susskind, *Fast scramblers*, *JHEP* **10** (2008) 065, [0808.2096].

[294] D. A. Roberts, D. Stanford and L. Susskind, *Localized shocks*, *JHEP* **03** (2015) 051, [1409.8180].

[295] D. A. Roberts, D. Stanford and A. Streicher, *Operator growth in the syk model*, *JHEP* **06** (2018) 122, [1802.02633].

[296] A. Kar, L. Lamprou, M. Rozali and J. Sully, *Random matrix theory for complexity growth and black hole interiors*, *JHEP* **01** (2022) 016, [2106.02046].

[297] A. Dymarsky and M. Smolkin, *Krylov complexity in conformal field theory*, *Phys. Rev. D* **104** (2021) L081702, [2104.09514].

[298] J. Barbón, E. Rabinovici, R. Shir and R. Sinha, *On the evolution of operator complexity beyond scrambling*, *JHEP* **10** (2019) 264, [1907.05393].

[299] A. Avdoshkin and A. Dymarsky, *Euclidean operator growth and quantum chaos*, 1911.09672.

[300] S.-K. Jian, B. Swingle and Z.-Y. Xian, *Complexity growth of operators in the syk model and in jt gravity*, *JHEP* **03** (2021) 014, [2008.12274].

[301] S. He, P. H. C. Lau, Z.-Y. Xian and L. Zhao, *Quantum chaos, scrambling and operator growth in $t\overline{T}$ deformed syk models*, *JHEP* **12** (2022) 070, [2209.14936].

[302] M. J. Vasli, K. B. Velni, M. R. M. Mozaffar, A. Mollabashi and M. Alishahiha, *Krylov complexity in lifshitz-type scalar field theories*, *The European Physical Journal C* **84** (Mar., 2024) .

[303] E. Rabinovici, A. Sánchez-Garrido, R. Shir and J. Sonner, *Operator complexity: a journey to the edge of krylov space*, 2009.01862.

[304] A. Dymarsky and A. Gorsky, *Quantum chaos as delocalization in krylov space*, *Phys. Rev. B* **102** (2020) 085137, [1912.12227].

[305] A. Bhattacharya, P. P. Nath and H. Sahu, *Krylov complexity for nonlocal spin chains*, *Physical Review D* **109** (Mar., 2024) .

[306] V. Balasubramanian, J. M. Magan and Q. Wu, *Tridiagonalizing random matrices*, *Phys. Rev. D* **107** (2023) 126001, [2208.08452].

[307] V. Balasubramanian, J. M. Magan and Q. Wu, *Quantum chaos, integrability, and late times in the Krylov basis*, 2312.03848.

[308] A. N. Zemlyakov and A. B. Katok, *Topological transitivity of billiards in polygons*, *Mathematical Notes of the Academy of Sciences of the USSR* **18** (Aug., 1975) 760–764.

[309] V. I. Arnold, *Mathematical Methods of Classical Mechanics*, Springer New York, 1989, 10.1007/978-1-4757-2063-1.

[310] F. Valdez, *Infinite genus surfaces and irrational polygonal billiards*, *Geometriae Dedicata* **143** (May, 2009) 143–154.

[311] R. Artuso, G. Casati and I. Guarneri, *Numerical study on ergodic properties of triangular billiards*, *Physical Review E* **55** (June, 1997) 6384–6390.

[312] J. Wang, G. Casati and T. Prosen, *Nonergodicity and localization of invariant measure for two colliding masses*, *Physical Review E* **89** (Apr., 2014) .

[313] J. Huang and H. Zhao, *Ultraslow diffusion and weak ergodicity breaking in right triangular billiards*, *Physical Review E* **95** (Mar., 2017) .

[314] A. Miltenburg and T. Ruijgrok, *Quantum aspects of triangular billiards*, *Physica A: Statistical Mechanics and its Applications* **210** (Oct., 1994) 476–488.

[315] K. Życzkowski, *Classical and quantum billiards : integrable, nonintegrable and pseudo-integrable*, *Acta Physica Polonica B* **23** (1992) 245–270.

[316] T. Cheon and T. D. Cohen, *Quantum level statistics of pseudointegrable billiards*, *Phys. Rev. Lett.* **62** (Jun, 1989) 2769–2772.

[317] E. Bogomolny, *Formation of superscar waves in plane polygonal billiards*, *Journal of Physics Communications* **5** (May, 2021) 055010, [1902.02334].

[318] T. Gorin, *Generic spectral properties of right triangle billiards*, *Journal of Physics A: Mathematical and General* **34** (Oct., 2001) 8281–8295.

[319] J. Wiersig, *Spectral properties of quantized barrier billiards*, *Phys. Rev. E* **65** (Apr, 2002) 046217.

[320] H. P. Baltes, E. R. Hilf and J. L. Challifour, *Spectra of finite systems*, *Physics Today* **30** (Aug., 1977) 55–56.

[321] Y. Y. Atas, E. Bogomolny, O. Giraud and G. Roux, *Distribution of the Ratio of Consecutive Level Spacings in Random Matrix Ensembles*, *Phys. Rev. Lett.* **110** (2013) 084101.

[322] V. Oganesyan and D. A. Huse, *Localization of interacting fermions at high temperature*, *Phys. Rev. B* **75** (Apr, 2007) 155111.

[323] J. S. Cotler, G. Gur-Ari, M. Hanada, J. Polchinski, P. Saad, S. H. Shenker et al., *Black holes and random matrices*, *JHEP* **05** (2017) 118, [1611.04650].

[324] L. Leviandier, M. Lombardi, R. Jost and J. P. Pique, *Fourier transform: A tool to measure statistical level properties in very complex spectra*, *Physical Review Letters* **56** (June, 1986) 2449–2452.

[325] A. del Campo, J. Molina-Vilaplana and J. Sonner, *Scrambling the spectral form factor: unitarity constraints and exact results*, *Phys. Rev. D* **95** (2017) 126008, [1702.04350].

[326] J. Liu, *Spectral form factors and late time quantum chaos*, *Phys. Rev. D* **98** (2018) 086026, [1806.05316].

[327] J. T. Edwards and D. J. Thouless, *Numerical studies of localization in disordered systems*, *Journal of Physics C: Solid State Physics* **5** (apr, 1972) 807.

[328] G. Misguich, V. Pasquier and J.-M. Luck, *Inverse participation ratios in the xxz spin chain*, *Physical Review B* **94** (Oct., 2016) , [1607.01300].

[329] B. Bhattacharjee and P. Nandy, *Krylov fractality and complexity in generic random matrix ensembles*, 2407.07399.

[330] H. G. Menzler and R. Jha, *Krylov localization as a probe for ergodicity breaking*, 2403.14384.

[331] M. Alishahiha and M. J. Vasli, *Thermalization in Krylov Basis*, 2403.06655.

[332] P. Bocchieri and A. Loinger, *Quantum recurrence theorem*, *Phys. Rev.* **107** (Jul, 1957) 337–338.

[333] M. Doncheski and R. Robinett, *Quantum mechanical analysis of the equilateral triangle billiard: Periodic orbit theory and wave packet revivals*, *Annals of Physics* **299** (Aug., 2002) 208–227.

[334] C. Jung, *An exactly soluble three-body problem in one dimension*, *Canadian Journal of Physics* **58** (June, 1980) 719–728.

[335] A. Damle and A. Dougherty, *Understanding the eigenstructure of various triangles*, *SIAM Undergraduate Research Online* (2010) 187–208.

[336] A. Peres, *Quantum theory: Concepts and methods*, *Springer Dordrecht* (1993) .

[337] S. Dhar, S. Dasgupta and A. Dhar, *Quantum time of arrival distribution in a simple lattice model*, *Journal of Physics A: Mathematical and Theoretical* **48** (2013) , [1312.5923].

[338] S. Dhar, S. Dasgupta, A. Dhar and D. Sen, *Detection of a quantum particle on a lattice under repeated projective measurements*, *Physical Review A* **91** (2015) , [1410.8701].

[339] C. Anastopoulos and N. Savvidou, *Time-of-arrival probabilities and quantum measurements*, *Journal of Mathematical Physics* **47** (Dec., 2006) 122106–122106, [quant-ph/0509020].

[340] N. Erez, G. Gordon, M. Nest and G. Kurizki, *Thermodynamic control by frequent quantum measurements*, *Nature* **452** (Apr., 2008) 724–727, [0804.2178].

[341] H. Friedman, D. A. Kessler and E. Barkai, *Quantum walks: The first detected passage time problem*, *Phys. Rev. E* **95** (Mar., 2017) 032141, [1611.05676].

[342] C. Liu, H. Tang and H. Zhai, *Krylov complexity in open quantum systems*, *Phys. Rev. Res.* **5** (2023) 033085, [2207.13603].

[343] B. Skinner, J. Ruhman and A. Nahum, *Measurement-Induced Phase Transitions in the Dynamics of Entanglement*, *Phys. Rev. X* **9** (2019) 031009, [1808.05953].

[344] R. Suzuki, J. Haferkamp, J. Eisert and P. Faist, *Quantum complexity phase transitions in monitored random circuits*, 2305.15475.

[345] Y. Li, X. Chen and M. P. A. Fisher, *Quantum Zeno effect and the many-body entanglement transition*, *Phys. Rev. B* **98** (2018) 205136, [1808.06134].

[346] Y. Li, X. Chen and M. P. A. Fisher, *Measurement-driven entanglement transition in hybrid quantum circuits*, *Phys. Rev. B* **100** (2019) 134306, [1901.08092].

[347] S. Sang, Y. Li, T. Zhou, X. Chen, T. H. Hsieh and M. P. A. Fisher, *Entanglement Negativity at Measurement-Induced Criticality*, *PRX Quantum* **2** (2021) 030313, [2012.00031].

[348] E. C. G. Sudarshan and B. Misra, *The zeno's paradox in quantum theory*, *Journal of Mathematical Physics* **18** (april, 1977) 756–763.

[349] P. Facchi, V. Gorini, G. Marmo, S. Pascazio and E. Sudarshan, *Quantum zeno dynamics*, *Physics Letters A* **275** (2000) 12–19.

[350] P. Facchi and S. Pascazio, *Quantum zeno dynamics: mathematical and physical aspects*, *Journal of Physics A: Mathematical and Theoretical* **41** (oct, 2008) 493001, [0903.3297].

[351] S. W. Gaaf and E. Jarlebring, *The infinite bi-lanczos method for nonlinear eigenvalue problems*, *SIAM Journal on Scientific Computing* **39** (2017) S898–S919, [https://doi.org/10.1137/16M1084195].

[352] *Templates for the solution of algebraic eigenvalue problems: A practical guide*, Jan., 2000. 10.1137/1.9780898719581.

[353] M. Gruning, A. Marini and X. Gonze, *Implementation and testing of lanczos-based algorithms for random-phase approximation eigenproblems*, *Computational Materials Science* **50** (2011) 2148–2156.

[354] C. Zheng and D. Li, *Distinguish between typical non-hermitian quantum systems by entropy dynamics*, *Scientific Reports* **12** (2022) .

[355] V. Delgado and J. G. Muga, *Arrival time in quantum mechanics*, *Phys. Rev. A* **56** (Nov., 1997) 3425–3435, [quant-ph/9704010].

[356] L. Jin and Z. Song, *Solutions of PT symmetric tight-binding chain and its equivalent Hermitian counterpart*, *Phys. Rev. A* **80** (2009) 052107, [0904.1513].

[357] X. Zhang, X. Song, S. Zhang, T. Zhang, Y. Liao, X. Cai et al., *Solvable non-Hermitian skin effects and real-space exceptional points: Non-Hermitian generalized Bloch theorem*, 2, 2023.

[358] Q.-B. Zeng, *Non-Hermitian skin effect edge*, *Phys. Rev. B* **106** (2022) 235411, [2209.12534].

[359] R. Lin, T. Tai, L. Li and C. H. Lee, *Topological non-Hermitian skin effect*, *Front. Phys. (Beijing)* **18** (2023) 53605, [2302.03057].

[360] K. Kawabata, T. Numasawa and S. Ryu, *Entanglement Phase Transition Induced by the Non-Hermitian Skin Effect*, *Phys. Rev. X* **13** (2023) 021007, [2206.05384].

[361] Z.-X. Kong, J.-R. Li, S.-F. Zhang and L.-L. Zhang, *Impact of PT -symmetric imaginary potentials on edge states of one-dimensional rhombus lattice*, *Results in Physics* **39** (Aug., 2022) 105674.

[362] S. Yao and Z. Wang, *Edge states and topological invariants of non-hermitian systems*, *Physical Review Letters* **121** (Aug., 2018) , [1803.01876].

[363] S. Yao, F. Song and Z. Wang, *Non-hermitian chern bands*, *Phys. Rev. Lett.* **121** (Sep, 2018) 136802, [1804.04672].

[364] K. Pal, K. Pal, A. Gill and T. Sarkar, *Time evolution of spread complexity and statistics of work done in quantum quenches*, *Phys. Rev. B* **108** (2023) 104311, [2304.09636].

[365] C. Beetar, N. Gupta, S. S. Haque, J. Murugan and H. J. R. V. Zyl, *Complexity and operator growth for quantum systems in dynamic equilibrium*, 2023.

[366] E. M. Graefe, U. Günther, H. J. Korsch and A. E. Niederle, *A non-hermitian symmetric bose–hubbard model: eigenvalue rings from unfolding higher-order exceptional points*, *Journal of Physics A: Mathematical and Theoretical* **41** (may, 2008) 255206, [0802.3164].

[367] M. Alishahiha and S. Banerjee, *A universal approach to krylov state and operator complexities*, 2212.10583.

[368] M. M. Wilde, *From Classical to Quantum Shannon Theory*, 1106.1445.

[369] M. M. Wilde, *Quantum Information Theory*, Cambridge University Press, 2 ed., 2017.

[370] M. A. Nielsen and I. L. Chuang, *Quantum Computation and Quantum Information: 10th Anniversary Edition*, Cambridge University Press, June, 2012, 10.1017/cbo9780511976667.

[371] B. M. Terhal, M. Horodecki, D. W. Leung and D. P. DiVincenzo, *The entanglement of purification*, *J. Math. Phys.* **43** (2002) 4286–4298, [quant-ph/0202044].

[372] C. A. Agón, M. Headrick and B. Swingle, *Subsystem complexity and holography*, *Journal of High Energy Physics* **2019** (Feb., 2019) .

[373] H. A. Camargo, P. Caputa, D. Das, M. P. Heller and R. Jefferson, *Complexity as a novel probe of quantum quenches: Universal scalings and purifications*, *Physical Review Letters* **122** (Feb., 2019) .

[374] M. Ghodrati, X.-M. Kuang, B. Wang, C.-Y. Zhang and Y.-T. Zhou, *The connection between holographic entanglement and complexity of purification*, *JHEP* **09** (2019) 009, [1902.02475].

[375] H. A. Camargo, L. Hackl, M. P. Heller, A. Jahn, T. Takayanagi and B. Windt, *Entanglement and complexity of purification in (1+1)-dimensional free conformal field theories*, *Phys. Rev. Res.* **3** (2021) 013248, [2009.11881].

[376] S. S. Haque, C. Jana and B. Underwood, *Saturation of thermal complexity of purification*, *JHEP* **01** (2022) 159, [2107.08969].

[377] A. Bhattacharya, A. Bhattacharyya and S. Maulik, *Pseudocomplexity of purification for free scalar field theories*, *Phys. Rev. D* **106** (2022) 086010, [2209.00049].

[378] A. Bhattacharyya, S. Brahma, S. S. Haque, J. S. Lund and A. Paul, *The early universe as an open quantum system: complexity and decoherence*, *JHEP* **05** (2024) 058, [2401.12134].

[379] A. Bhattacharyya, T. Hanif, S. S. Haque and M. K. Rahman, *Complexity for an open quantum system*, *Phys. Rev. D* **105** (2022) 046011, [2112.03955].

[380] E. Cáceres, J. Couch, S. Eccles and W. Fischler, *Holographic Purification Complexity*, *Phys. Rev. D* **99** (2019) 086016, [1811.10650].

[381] E. Caceres, S. Chapman, J. D. Couch, J. P. Hernandez, R. C. Myers and S.-M. Ruan, *Complexity of Mixed States in QFT and Holography*, *JHEP* **03** (2020) 012, [1909.10557].

[382] S.-M. Ruan, *Purification Complexity without Purifications*, *JHEP* **01** (2021) 092, [2006.01088].

[383] G. Di Giulio and E. Tonni, *Complexity of mixed Gaussian states from Fisher information geometry*, *JHEP* **12** (2020) 101, [2006.00921].

[384] G. Di Giulio, *Circuit complexity and entanglement in many-body quantum systems*. PhD thesis, SISSA, Trieste, 2021.

[385] S. Chapman and G. Policastro, *Quantum computational complexity from quantum information to black holes and back*, *Eur. Phys. J. C* **82** (2022) 128, [2110.14672].

[386] A. Bhattacharya, A. Bhattacharyya, P. Nandy and A. K. Patra, *Islands and complexity of eternal black hole and radiation subsystems for a doubly holographic model*, *Journal of High Energy Physics* **2021** (May, 2021) .

[387] R.-Q. Yang, H.-S. Jeong, C. Niu and K.-Y. Kim, *Complexity of holographic superconductors*, *JHEP* **04** (2019) 146, [1902.07586].

[388] D. Wang, X. Qiao, M. Wang, Q. Pan, C. Lai and J. Jing, *Holographic entanglement entropy and subregion complexity for excited states of holographic superconductors*, *Nucl. Phys. B* **991** (2023) 116223, [2301.00513].

[389] K. Umemoto and Y. Zhou, *Entanglement of purification for multipartite states and its holographic dual*, *Journal of High Energy Physics* **2018** (Oct., 2018) .

[390] S. Lloyd, *Ultimate physical limits to computation*, *Nature* **406** (Aug., 2000) 1047–1054, [quant-ph/9908043].

[391] S. Dutta and T. Faulkner, *A canonical purification for the entanglement wedge cross-section*, *JHEP* **03** (2021) 178, [1905.00577].

[392] M. Alishahiha and S. Banerjee, *A universal approach to Krylov state and operator complexities*, *SciPost Phys.* **15** (2023) 080, [2212.10583].

[393] C. M. Caves and B. L. Schumaker, *New formalism for two-photon quantum optics. 1. Quadrature phases and squeezed states*, *Phys. Rev. A* **31** (1985) 3068–3092.

[394] Z. Y. Ou, S. F. Pereira, H. J. Kimble and K. C. Peng, *Realization of the Einstein-Podolsky-Rosen paradox for continuous variables*, *Phys. Rev. Lett.* **68** (1992) 3663.

[395] S. E. Aguilar-Gutierrez and A. Rolph, *Krylov complexity is not a measure of distance between states or operators*, 2311.04093.

[396] A. Srivastav, V. Pandey, B. Mohan and A. K. Pati, *Family of Exact and Inexact Quantum Speed Limits for Completely Positive and Trace-Preserving Dynamics*, 2406.08584.

[397] S.-M. Ruan, *Circuit Complexity of Mixed States*. PhD thesis, Waterloo U., 2021.

[398] E. H. Lieb and D. W. Robinson, *The finite group velocity of quantum spin systems*, *Commun. Math. Phys.* **28** (1972) 251–257.

[399] A. H. Karamlou et al., *Quantum transport and localization in 1d and 2d tight-binding lattices*, *npj Quantum Inf.* **8** (2022) 35, [2107.05035].

[400] K. Sanderson, *Quantum dots go large*, *Nature* **459** (2009) 760–761.

[401] H. Lin, O. Lunin and J. M. Maldacena, *Bubbling AdS space and 1/2 BPS geometries*, *JHEP* **10** (2004) 025, [hep-th/0409174].

[402] D. Berenstein, *A Toy model for the AdS / CFT correspondence*, *JHEP* **07** (2004) 018, [hep-th/0403110].

[403] G. 't Hooft, *A Planar Diagram Theory for Strong Interactions*, *Nucl. Phys. B* **72** (1974) 461.

[404] J. A. Minahan, *The q Schrodinger equation*, *Mod. Phys. Lett. A* **5** (1990) 2625–2632.

[405] D. E. Berenstein, J. M. Maldacena and H. S. Nastase, *Strings in flat space and pp waves from N=4 superYang-Mills*, *JHEP* **04** (2002) 013, [hep-th/0202021].

[406] S. Frolov and A. A. Tseytlin, *Multispin string solutions in AdS(5) x S**5*, *Nucl. Phys. B* **668** (2003) 77–110, [hep-th/0304255].

[407] M. Kruczenski, A. V. Ryzhov and A. A. Tseytlin, *Large spin limit of AdS(5) x S**5 string theory and low-energy expansion of ferromagnetic spin chains*, *Nucl. Phys. B* **692** (2004) 3–49, [hep-th/0403120].

[408] M. Kruczenski and A. A. Tseytlin, *Semiclassical relativistic strings in S**5 and long coherent operators in N=4 SYM theory*, *JHEP* **09** (2004) 038, [hep-th/0406189].

[409] A. A. Tseytlin, *Semiclassical strings in AdS(5) x S**5 and scalar operators in N=4 SYM theory*, *Comptes Rendus Physique* **5** (2004) 1049–1059, [hep-th/0407218].

[410] A. A. Tseytlin, *Semiclassical strings and AdS/CFT*, in *NATO Advanced Study Institute and EC Summer School on String Theory: From Gauge Interactions to Cosmology*, pp. 265–290, 9, 2004, [hep-th/0409296].

[411] J. A. Minahan, *Review of AdS/CFT Integrability, Chapter I.1: Spin Chains in N=4 Super Yang-Mills*, *Lett. Math. Phys.* **99** (2012) 33–58, [1012.3983].

[412] J. Erdmenger, M. Flory, M. Gerbershagen, M. P. Heller and A.-L. Weigel, *Exact gravity duals for simple quantum circuits*, *SciPost Phys.* **13** (2022) 061, [2112.12158].

[413] J. Erdmenger, M. Gerbershagen, M. P. Heller and A.-L. Weigel, *From complexity geometry to holographic spacetime*, 2212.00043.

[414] A. R. Brown, D. A. Roberts, L. Susskind, B. Swingle and Y. Zhao, *Holographic Complexity Equals Bulk Action?*, *Phys. Rev. Lett.* **116** (2016) 191301, [1509.07876].

[415] A. Belin, R. C. Myers, S.-M. Ruan, G. Sárosi and A. J. Speranza, *Complexity equals anything II*, *JHEP* **01** (2023) 154, [2210.09647].

[416] A. Belin, R. C. Myers, S.-M. Ruan, G. Sárosi and A. J. Speranza, *Does Complexity Equal Anything?*, *Phys. Rev. Lett.* **128** (2022) 081602, [2111.02429].

[417] A. Bhattacharya and A. Jana, *Quantum chaos and complexity from string scattering amplitudes*, 2408.11096.

[418] V. Balasubramanian, J. M. Magan, P. Nandi and Q. Wu, *Spread complexity and the saturation of wormhole size*, 2412.02038.

[419] A. M. Perelomov, *Coherent states for arbitrary lie group*, *Communications in Mathematical Physics* **26** (1972) 222–236.

[420] R. Gilmore, *Geometry of symmetrized states*, *Annals of Physics* **74** (1972) 391–463.

[421] A. Perelomov, *Generalized Coherent States and Their Applications*, Texts and Monographs in Physics, Springer, Berlin, Heidelberg, 1986, 10.1007/978-3-642-61629-7.

[422] A. Chattopadhyay, A. Mitra and H. J. R. van Zyl, *Spread complexity as classical dilaton solutions*, *Phys. Rev. D* **108** (2023) 025013, [2302.10489].

[423] V. Balasubramanian, M. Decross, A. Kar and O. Parrikar, *Quantum complexity of time evolution with chaotic hamiltonians*, *JHEP* **01** (2020) 134, [1905.05765].

[424] L. Frappat, P. Sorba and A. Sciarrino, *Dictionary on Lie superalgebras*, hep-th/9607161.

[425] J. R. Klauder, *Path integrals and stationary-phase approximations*, *Physical Review D* **19** (1979) 2349.

[426] J. R. Klauder and B.-S. Skagerstam, *Coherent states: applications in physics and mathematical physics*, World scientific, 1985.

[427] E. H. Fradkin, *Field Theories of Condensed Matter Physics*, vol. 82, Cambridge Univ. Press, Cambridge, UK, 2, 2013.

[428] D. Ge and G. Policastro, *Circuit complexity and 2d bosonisation*, *Journal of High Energy Physics* **2019** (Oct., 2019) .

[429] H.-y. Fan, Y. Fan and F. T. Chan, *Normally ordered unitary operator for multimode squeezed fermion states*, *Phys. Lett. A* **247** (1998) 267–272.

[430] B. Fatyga, V. A. Kosteleckỳ and D. R. Truax, *Baker–campbell–hausdorff relations for the orthosymplectic group osp (1/2)*, *Journal of mathematical physics* **30** (1989) 291–294.

[431] W. Mück and Y. Yang, *Krylov complexity and orthogonal polynomials*, *Nucl. Phys. B* **984** (2022) 115948, [2205.12815].

[432] R. Hernandez and E. Lopez, *The SU(3) spin chain sigma model and string theory*, *JHEP* **04** (2004) 052, [hep-th/0403139].

[433] S. Bellucci, P. Y. Casteill, J. F. Morales and C. Sochichiu, *SL(2) spin chain and spinning strings on AdS(5) x S**5*, *Nucl. Phys. B* **707** (2005) 303–320, [hep-th/0409086].

[434] I. Y. Park, A. Tirziu and A. A. Tseytlin, *Spinning strings in AdS(5) x S**5: One-loop correction to energy in SL(2) sector*, *JHEP* **03** (2005) 013, [hep-th/0501203].

[435] N. Beisert, *The Dilatation operator of N=4 super Yang-Mills theory and integrability*, *Phys. Rept.* **405** (2004) 1–202, [hep-th/0407277].

[436] R. Hernandez and E. Lopez, *Spin chain sigma models with fermions*, *JHEP* **11** (2004) 079, [hep-th/0410022].

[437] B. Stefanski, Jr. and A. A. Tseytlin, *Super spin chain coherent state actions and AdS(5) x S**5 superstring*, *Nucl. Phys. B* **718** (2005) 83–112, [hep-th/0503185].

[438] K. Adhikari, A. Rijal, A. K. Aryal, M. Ghimire, R. Singh and C. Deppe, *Krylov Complexity of Fermionic and Bosonic Gaussian States*, *Fortsch. Phys.* **72** (2024) 2400014, [2309.10382].